Karlsruhe Institute of Technology

Electric field simulations and electric dipole investigations at the KATRIN main spectrometer

Zur Erlangung des akademischen Grades eines

Doktors der Naturwissenschaften

von der Fakultät für Physik
des Karlsruher Instituts für Technologie
genehmigte

Dissertation

von

Dipl.-Phys. Daniel Franz Rudolf Hilk

aus Ehringshausen

Erstgutachter:	Prof. Dr. Guido Drexlin Institut für Experimentelle Kernphysik, KIT
Zweitgutachter:	Prof. Dr. Wim de Boer Institut für Experimentelle Kernphysik, KIT

Tag der mündlichen Prüfung: 20. Januar 2017

Declaration of authorship

I declare that I have developed and written the enclosed thesis in hand completely by myself, and have not used sources or means without any declaration in the text.

Erklärung der Selbstständigkeit

Hiermit versichere ich, die vorliegende Arbeit selbstständig angefertigt, alle dem Wortlaut oder Sinn nach entnommenen Inhalte anderer Werke an den entsprechenden Stellen unter Angabe der Quellen kenntlich gemacht und keine weiteren Hilfsmittel verwendet zu haben.

.....

Daniel Hilk

Karlsruhe, den 21. Dezember 2016

Zusammenfassung

Kern der vorliegenden Arbeit ist die Entwicklung von Feldberechnungsmethoden höchster Präzision und experimentelle Untergrundstudien mit der elektrischen Dipolmethode für das KATRIN Experiment. Beide Punkte sind für das Verständnis von Untergrundprozessen und das Erreichen des projektierten Untergrundsignals von 10 mcps zum Erreichen einer Neutrinomassen-Sensitivität von $m_{\overline{\nu}_e} = 200\,\mathrm{meV/c^2}$ mit 90 % C.L. unabdingbar.

Neutrinos stellen grundlegende Schlüsselteilchen der Astroteilchenphysik dar: Im Rahmen des Standardmodells der Teilchenphysik sind Neutrinos als schwach-wechselwirkende Teilchen klassifiziert, die in drei Flavor-Generationen unterteilt sind. Neutrinos als die leichtesten bekannten Elementarteilchen, treten in sehr großer Menge in unserem Universum auf (pro cm^3 befinden sich 336 Neutrinos aus dem Urknall). Ursprünglich wurden Neutrinos als masselose Teilchen angenommen, der Nachweis einer von Null verschiedenen Ruhemasse konnte durch Neutrino-Oszillationsexperimente erbracht werden. Diese bahnbrechende und wegweisende Entdeckung hat wesentlich zum Verständnis von massiven Neutrinos beigetragen. Daher wurde im Jahr 2015 der Nobelpreis für Physik an Arthur McDonald (SNO Experiment) und Takaaki Kajita (Super-Kamiokande Experiment) verliehen. Da Oszillationsexperimente nur sensitiv auf Differenzen von Neutrinomassen sind, ist die absolute Massenskala dieser Teilchen unbekannt. Die Bestimmung des zuletzt genannten Massenparameters wird einen erheblichen Einfluss auf die Elementarteilchenphysik, aber auch auf die Beschreibung von Strukturbildung in unserem Universum haben. Zur modell-unabhängigen Bestimmung der absoluten Neutrinomasse werden verschiedene experimentelle Ansätze verfolgt und realisiert. Die vielversprechendste Methode stellt die Spektroskopie des Energieendpunktes von Elektronen aus dem Tritium β-Zerfall dar. Für die weltweit präziseste Spektroskopie des Energieendpunktes aus dem Tritium β-Zerfall wurde das KATRIN-Experiment am Karlsruher Institut für Technologie (KIT) entwickelt und aufgebaut.

Für eine präzise β-Spektroskopie von Elektronen bei 18.6 keV Energie wird ein Spektrometer vom MAC-E Filter Typ von 24 m Länge und 10 m Durchmesser eingesetzt. Die Elektronen aus einer fensterlosen gasförmigen Tritiumquelle werden durch das Experiment adiabatisch geführt und in der sogenanten Analysierebene im Spektrometer bei einer Auflösung von $\Delta E = 0.93\,\mathrm{eV}$ nach ihrer kinetischen Energie selektiert.
Dabei darf eine Untergrundsignalrate von 10 mcps nicht überschritten werden, um eine Sensitivität von $200\,\mathrm{meV/c^2}$ der Neutrinomasse zu erreichen. Allerdings wurde im Rahmen von vorhergehenden Arbeiten eine nicht-reduzierbare Untergrundkomponente im KATRIN Hauptspektrometer identifiziert.
Im Rahmen dieser Arbeit ist dieses Problem über die erfolgreiche Anwendung von elektrischen Dipolpulsen am Hauptspektrometer im Detail untersucht worden. Vorhergehende Experimente zeigten bereits auf, dass das Anlegen von elektrischen Dipolpulsen erlaubt, Untergrundelektronen insbesondere hinsichtlich ihrer Speichereigenschaften genauer zu untersuchen. Im Kontext der vorliegenden Arbeit wurde diese Methode zur Charakterisierung und Reduzierung von Untergrundsignalen erstmalig am KATRIN Hauptspektrometer eingesetzt.

Die Herausforderung ist hier, geeignete Techniken und Methoden zur Modellierung und Optimierung des elektromagnetischen Feldlayouts zu bestimmen, um einen höchst möglichen Untergrund-Reduktionsfaktor durch elektrische Dipolpulse zu erreichen.

Für Hochpräzisions-β-Spektroskopie am Energieendpunkt von Elektronen aus dem Zerfall von molekularem Tritium, ist es unabdingbar, neben den Untergrundsignalen auch die Transmissionseigenschaften von Elektronen zu studieren. Zu diesem Zweck müssen elektrostatische Felder innerhalb des Spektrometers mit höchster Genauigkeit und Präzision berechnet werden. Die KATRIN Kollaboration setzt dazu das eigens entwickelte Softwareprogramm *KEMField* ein, welches auf der Randelementmethode basiert (engl. boundary element method, BEM).
Für die elektrische Potential- und Feldberechnung ist die Auswertung von zweidimensionalen Oberflächenintegralen notwendig, die in der Vergangenheit zu numerischen Fluktuationen und Ungenauigkeiten geführt hat. Dieser Fehler kann sich im ungünstigsten Fall direkt auf die Auswertung von physikalischen Ergebnissen als systematische Störung auswirken.

Im Rahmen dieser Arbeit wurden diese störenden Fluktuationen erfolgreich durch die Einführung einer numerischen Integration, der Gaußschen Kubatur, beseitigt. Erst diese Entwicklung ermöglicht es, korrekt elektrostatische Felder mit *KEMField* berechnen. Insbesondere für die Simulation des 70 m langen KATRIN Experimentes, wurden detaillierte Studien auf der Basis eines neuen, präzisen und hocheffizienten Elektrodenmodells des Hauptspektrometers durchgeführt. Durch diese Studien konnten die Ungenauigkeiten auf die numerische Präzision von 10^{-15} reduziert werden.

Der Einsatz von hochpräzisen Feldberechnungsmethoden ist insbesondere für die Simulation und das damit verbundene Verständnis von dreidimensionalen Dipolfeldern am KATRIN Hauptspektrometer von höchster Bedeutung. Letzteres wurde im Rahmen von umfangreichen Inbetriebnahmemessungen am Hauptspektrometersystem erstmals detailliert untersucht. Neben statischen Dipolfeldern wurden auch gepulste Dipolfelder am Hauptspektrometer angelegt, um die vorhergesagte Raten-Reduktion von Untergrundereignissen gespeicherter Teilchen zu untersuchen. Nachdem im Rahmen von ersten Messungen mit statischen Dipolfeldern die elektrostatische Konfiguration des Hauptspektrometersystems optimiert wurde, konnte durch die Anwendung von gepulsten elektrischen Dipolfeldern die erwartete Untergrundreduktion eindrucksvoll erstmals am KATRIN Hauptspektrometer gezeigt werden.

Diese grundlegenden theoretischen sowie experimentellen Resultate zur elektrischen Dipolmethode sind für das Verständnis des intrinsischen Untergrundes am KATRIN Hauptspektrometer unabdingbar. Nur auf diese Weise konnten die a priori unbekannten Speicher-Eigenschaften des Niederenergie-Untergrundes aus Ionisationsprozessen von H-Rydberg-Atomen charakterisiert werden. Diese Ergebnisse sind für die weitere Optimierung und somit das Erreichen der Sensitivität von $m_{\overline{\nu}_e} = 200\,\mathrm{meV/c^2}$ mit einem Untergrundniveau von 10 mcps essentiell.

Aufbau der Arbeit

Kapitel 1 gibt eine Einführung in das Gebiet der Neutrinophysik, beginnend mit der Entdeckung und Postulation dieses Teilchens im frühen 20. Jahrhundert, gefolgt von der Beschreibung verschiedener Experimente mit dem Ziel der Bestimmung seiner Eigenschaften. Als zweiter wichtiger Aspekt wird die Entdeckung von Neutrino-Oszillationen besprochen und deren Konsequenzen zur Beschreibung von nunmehr massebehafteten Neutrinos. Aufbauend auf diesen Ergebnissen wird der theoretische Rahmen zur Beschreibung von massiven Neutrinos im Standardmodell der Elementarteilchen diskutiert.

Kapitel 2 gibt eine umfassende Einführung in das KATRIN Experiment. Zu Beginn werden die charakteristischen Grundlagen des MAC-E Filters besprochen, dies umfasst neben der Diskussion von Transmissionseigenschaften insbesondere auch die Beschreibung von Untergrundprozessen durch gespeicherte Teilchen. Daran anschließend werden die verschiedenen Komponenten des 70 m langen Experimentaufbaus vorgestellt und in den Kontext der vorliegenden Doktorarbeit gestellt. Abschließend wird die Auswertung des Neutrinomassenparameters aus den experimentellen Daten detailliert besprochen.

Kapitel 3 diskutiert die Struktur und Funktionalität verschiedener Softwaremodule am KATRIN Experiment, die unter anderem zur Simulation von elektromagnetischen Feldern und von Teilchentrajektorien wichtig sind. Zusammen mit ausgewählten Beispielen dient dieses Kapitel als aktuelle Referenz zum Arbeiten mit den Softwarepaketen *KEMField* und *Kassiopeia*. Zusätzlich werden Softwaremodule besprochen, die zur Untersuchung von systematischen und statistischen Fehlern unabdingbar sind.

Kapitel 4 stellt einen zentralen Punkt dieser Arbeit dar. Hier wird die Auswertung von zweidimensionalen Oberflächenintegralen mit der Gaußschen Kubatur besprochen. Dazu werden gezielt grundlegende Beispiele diskutiert, die die Leistungsfähigkeit dieser Methode unterlegen. Des weiteren wird eine verbesserte Methode zur analytischen Integration besprochen, die im Falle einer Feldberechnung an speziellen Punkten notwendig wird. Zusammen mit der numerischen Metode kann die nun von KATRIN eingesetzte Software auf Basis dieser Ergebnisse eine Präzision im Rahmen von 10^{-15} erreichen. Abschließend wird der Einsatz dieser Methoden für das KATRIN Experiment an einem optimierten Modell gezeigt.

Kapitel 5 fasst die experimentellen Resultate der im Jahr 2015 erstmalig durchgeführten Messkampagne mit Dipolfeldern am KATRIN Hauptspektrometer zusammen. Durch die Messung mit statischen elektrischen Dipolfeldern wurde zunächst ein grundlegendes Verständnis der Auswirkung eines elektrostatischen Dipolfeldes auf Detektorsignaturen erworben und eine optimierte Feldkonfiguration bestimmt.
Mit diesen gewonnenen Resultaten, konnte ein gepulstes Dipolfeld zur Reduktion von Untergrundsignalen durch gespeicherte Teilchen mit höchsten Reduktionsfaktoren erfolgreich realisiert werden.

Kapitel 6 baut auf den in Kapitel 5 dargestellten Resultaten unmittelbar auf. Hier ist das Ziel, über vergleichende theoretische und experimentelle Untersuchungen auf der Basis von elektrischen Dipolpulsen den intrinsischen Untergrund am KATRIN Hauptspektrometer zu charakterisieren. Nachdem im Rahmen einer Langzeitstudie zunächst zweifelsfrei gezeigt werden konnte, dass der elektrische Dipol zu keinem Reduktionseffekt beim intrinsischen Untergrund aus Rydberg-Atomen führt, bestätigt diese Messkampagne die Theorie das neue Untergrundparadigma, dass der wesentliche Untergrund in einem hochauflösenden MAC-E Filter durch neutrale, instabile Atome (Radon und H-Rydbergzustände) entsteht.

Kapitel 7 fasst alle Ergebnisse dieser Arbeit zusammen und gibt einen Ausblick auf weitere konsekutive Studien.

Introduction

The thesis in hand deals with the development of high-accuracy electric field simulation methods and experimental background investigations with the electric dipole method for the KATRIN experiment. Both fields of work are of crucial importance to obtain the targeted background level of 10 mcps for the investigation of the absolute neutrino mass scale with a sensitivity of $m_{\overline{\nu}_e} = 200\,\mathrm{meV/c^2}$ at 90 % C.L.

Neutrinos play an essential role in the field of modern astroparticle physics: In the framework of the Standard Model of particle physics, neutrinos are described as weakly interacting particles, grouped in three flavor generations, representing the lightest and most abundant fermionic particles of the universe (each $\mathrm{cm^3}$ contains 336 neutrinos from the Big Bang). Formerly believed to be massless, neutrino oscillation experiments revealed a non-vanishing mass of these particles. In the year 2015, these investigations were distinguished with the Nobel prize of physics to the projects SNO headed by Arthur McDonald and Super-Kamiokande headed by Takaaki Kajita. While the massive nature of neutrinos has been uncovered through the detection of non-vanishing mass splittings, the absolute mass scale of these elusive particles is yet to be determined. The experimental determination of this parameter will have a significant impact on elementary particle physics, as well on the picture of the evolution of cosmological large-scale structures. Different experimental approaches are thus pursued in order to determine the absolute mass scale of the neutrino. The most promising method to determine this parameter in a model-independent way is based on the precise spectroscopy of the β-decay endpoint region of molecular tritium. Tailored for this purpose, the KATRIN experiment at the Karlsruhe Institute of Technology (KIT) will obtain an unprecedented sensitivity on the absolute neutrino mass scale by high-precision and high-statistics β-spectroscopy.

To enable high-precision β-spectroscopy at 18.6 keV electron energy, the experiment takes advantage of a very large spectrometer of the MAC-E filter type which has a length of 24 m and a diameter of 10 m. In the spectrometer electrons are guided adiabatically from the tritium source sided entry to the detector while the minimum electron energy is analyzed in the analysis plane of the spectrometer with unprecedented precision of $\Delta E = 0.93\,\mathrm{eV}$. A background signal of 10 mcps may not be exceeded in order to achieve the targeted design sensitivity of $200\,\mathrm{meV/c^2}$ on the neutrino mass. However, in context of previous works, a non-negligible intrinsic background component has been detected in the KATRIN main spectrometer.
In context of this thesis, this problem is investigated by means of the application of electric dipole fields in the main spectrometer for both background characterization and reduction. Past experiments revealed that the electric dipole method allows to investigate the storage behavior of the underlying background signal in detail. For the first time, the intrinsic background of the KATRIN main spectrometer has been studied by means of this technique. The objective of these studies was to characterize and to eliminate the intrinsic background in order to achieve the above mentioned targeted design goals. The challenge here is to develop suitable techniques to determine in advance the best electromagnetic dipole configurations to eliminate and to study different background classes.

For high precision β-spectroscopy at the tritium endpoint, it is indispensable to understand both the background processes and the transmission of signal electrons. For these requirements, electrostatic fields inside the spectrometer have to be simulated with highest accuracy and precision. The KATRIN collaboration takes advantage of the in-house developed software tool *KEMField* which is based on the boundary element method (BEM). For the electric field and potential computation, this software module incorporates various integration techniques which previously have suffered from numerical fluctuations which consequently can influence physical results. In the context of this work, these troublesome fluctuations were erased successfully by the means of a newly-adapted numerical integration technique based on the Gaussian cubature. The techniques now employed lead to fast and precise results allowing to make correct predictions and calculations of fields and potentials over the entire 70 m long KATRIN setup. For the latter task, a large variety of dedicated studies was carried out, based on a tailored electrode model of the main spectrometer.

Precise field calculations in three dimensions are of utmost importance in all configurations where the main spectrometer is operated in an electric dipole mode. This particular setup is expected to remove stored low-energy background electrons in the flux tube. However, prior to this thesis, it had not been applied to the KATRIN spectrometer system. This thesis discusses the first experimental application of electric dipole fields in this very large MAC-E filter system. In view of the rather complex geometry of the spectrometer, a detailed understanding of electrostatic fields is a prerequisite for later studies targeted at the dynamical removal of particles. As a first step, static fields were investigated with the help of the field simulation methods. Finally the removal efficiency of an optimized electric dipole field configuration was determined. In this way it could be shown that the sensitive flux tube volume of the main spectrometer can be emptied from stored particle background. For later tritium measurements the mitigation of stored particle background is essential in order to achieve the targeted sensitivity goals.

The pioneering results of the electric dipole method are thus crucial for the understanding of the intrinsic high-energy electron background component of the main spectrometer. As the electric dipole will remove stored electrons only this method was applied to the at present irreducible remaining intrinsic main spectrometer background featuring electrons with exceedingly small energies in the sub-eV range in order to characterize their storage behavior and energy scale.

Outline

Chapter 1 of this thesis gives a brief introduction to neutrino physics. A set of crucial experimental and theoretical achievements is highlighted, such as the postulation of the neutrino in the 1930s and its much later discovery in the 1950s. Next, the ground-breaking observation of neutrino flavor oscillations is presented in more detail, followed by a discourse on massive neutrinos with special focus on the physics of massive neutrinos.

The second chapter is devoted to a comprehensive presentation of the principles and components of the KATRIN experiment. The energy analysis of β-electrons by means of a MAC-E filter system is given an in-depth discussion. Each component, such as the ultraluminous molecular tritium source is explained in detail while emphasizing its particular purpose for the experiment. A dedicated section is devoted to more recent improvements and updates to individual sub-components in the context of the ongoing and previous commissioning measurements of the spectrometer and detector section. The chapter closes with a discussion on the determination of the experimental observable, the square of the neutrino mass.

Chapter 3 focuses on simulation and analysis tools which have been developed over many years in the KATRIN collaboration. Special emphasis is given to the different field calculation methods, as these play a crucial role for the understanding of transmission and background characteristics along the entire beam line of KATRIN. This part also serves as a brief tutorial for the KATRIN simulation tools, supplemented by exemplary excerpts from XML configuration files.

Chapter 4 presents a key field of work of this thesis, namely the improvement of the direct field calculation method with the Gaussian cubature. The advantages and the effect of numerical integration are discussed in the context of several validation results while the crucial elimination of rounding errors is detailed by dedicated chosen mathematical examples. The chapter closes by reviewing the adaption of the mathematical tools and methods for electrostatic field calculations for the KATRIN experiment.

The subsequent chapter 5 summarizes the experimental results of the spectrometer and detector section in 2015 obtained with an electric dipole configuration with the focus on commissioning results of the electric dipole system. The discussion of the measurements is subdivided into two main parts. First, a thorough understanding of electrostatic dipole fields in the KATRIN main spectrometer was obtained, whereas in a second phase dynamically pulsed electric dipole fields were applied together with an optimized electrostatic field setting in order to determine the maximal possible rate reduction for stored particles in the flux tube.

The following chapter 6 discusses the application of dipole fields to study the properties of intrinsic background in the main spectrometer volume. In doing so, the storage behavior of the intrinsic particle background is determined. For upcoming measurement campaigns, a strategy is developed in order to further characterize the intrinsic background with the electric dipole method.

Chapter 7 closes the thesis by summarizing the key facts of electric field calculations and experimental investigations of dipole fields and by pointing out several future improvements based on the results of this work.

Contents

CHAPTER 1

Introduction to neutrino physics

Since their postulation in the early 20th century by Wolfgang Pauli, neutrinos continue to play a central role in contemporary modern physics. In the last decades many discoveries have been made in this area of research. Key among them is the discovery of neutrino oscillations which implicates that neutrinos are not massless. This represents a crucial milestone beyond the Standard Model of particle physics which described neutrinos as massless particles. In 2015 T. Kajita and A. B. McDonald were awarded the Nobel prize of particle physics for this fundamental discovery with the Super-Kamiokande and SNO experiments. Neutrino physics will continue to be a key in order to explore physics beyond the Standard Model. Neutrinos interact very weakly with matter and are thus very difficult to detect. For the exploration of the properties of neutrinos, a large number of atmospheric, solar, reactor and accelerator experiments was carried out so far. Whereas these neutrino oscillation experiments depend on the values of the mass splittings Δm^2_{ij}, single beta decay experiments are indispensable in order to determine the absolute mass of this particle class. In the past, the experiments in Mainz and Troitsk have been able to constrain the mass to about 2 eV, which is about five orders of magnitude smaller than the electron mass. The thesis in hand has been written in context of the KATRIN experiment which pushes forward into a a new precision regime of single beta decay experiments to determine the neutrino mass scale in a model-independent way.

In the following chapter an outline on neutrino physics is given. In sec. 1.1 the discovery of neutrino physics is sketched pointing out important achievements in history. The experiments and the physics principle of neutrino oscillations is discussed in the following in sec. 1.2. Finally the theory of neutrino mass generation is discussed in light of different experimental approaches which tackle the determination of the neutrino mass in sec. 1.3.

1.1 Milestones of neutrino physics

In 1896 the phenomenon of radioactivity was discovered which has lead to an incredibly broad area of research in the following decades. Unstable nuclei can decay in three different processes which are labeled as α-, β- and γ-induced, depending on the emitted particle and its energy spectrum. Whereas the α- and γ-decay have a discrete energy spectrum, the β-decay is characterized by a continuous energy spectrum. In 1914, Chadwick discovered this continuous energy spectrum for the β-decay of radium (fig. 1.1).

1.1.1 Postulation of neutrinos

In order to solve the problem of energy and angular momentum conservation, 1932 Pauli extended the β-decay process with a third particle by the postulation of a spin-1/2 particle

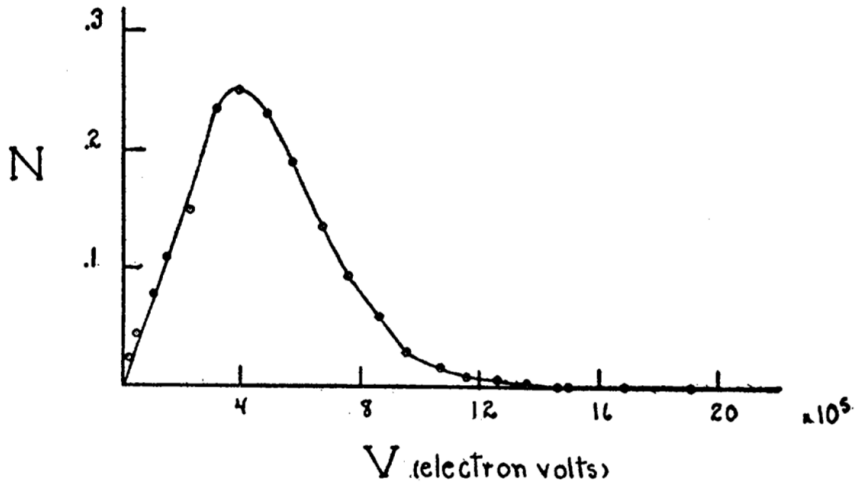

Figure 1.1: Energy distribution of radium β-decay. The measured β-decay energy spectrum is not discrete as expected, instead it is continuous. Figure from [Sco35].

which is stable, electrically neutral and of small rest mass. In 1934 Fermi developed a coherent theory which described the three-body β-decay as a point-like interaction between all involved fermions. Bethe and Peierls calculated the typical cross section for MeV-scale neutrino interactions to $\sigma \approx 10^{-44}\,\mathrm{cm}^2$. This small cross section implies a very weak interaction of neutrinos with matter.

1.1.2 Experimental discovery

It was thus more than 20 years later, in 1956, that the existence of neutrinos was finally proven in the series of *poltergeist* experiments by Cowan and Reines. They used the Savannah river reactor as intense neutrino source with an expected flux of $5 \times 10^{13}/(\mathrm{cm}^2\,\mathrm{s})$. The detector consisted of two tanks, which were filled with 200 ℓ water with 40 kg cadmium chloride dissolved. Both tanks were interleaved between scintillator layers with PMT readout. The detection is based on the 'classical' inverse beta decay reaction

$$\overline{\nu}_e + p \rightarrow e^+ + n. \tag{1.1}$$

Here, the detection of a neutrino is based on a delayed coincidence signal. Positrons slow down in the liquid and annihilate with free electrons to form a pair of 511 keV gammas which are emitted into opposite directions. The neutrons scatter off free protons in the target and, after being thermalized, they are captured by Cadmium within a few microseconds. The excited Cadmium nucleus Cd* decays into its ground state by emission of two gamma photons in the MeV range. Over a total measurement time of 1341 hours, three neutrino events were detected per hour. In this way, the cross section of inverse beta decay was determined to $\sigma = 6.3 \times 10^{-44}\,\mathrm{cm}^2$. In 1962 Ledermann, Schwartz and Steinberger detected the muon neutrino as the second neutrino flavor at the Brookhaven National Laboratory. There, the AGS particle accelerator was used to bombard a beryllium target with protons. The resulting pions decay via

$$\pi^+ \longrightarrow \mu^+ + \nu_\mu \qquad \text{and} \qquad \pi^- \longrightarrow \mu^- + \overline{\nu}_\mu. \tag{1.2}$$

The forward focused neutrino beam was then guided to a 10-ton Aluminum spark chamber, located behind a 13.5 m thick iron shield. No particle showers were observed as expected for electron type neutrinos. Instead straight tracks were recorded as predicted for muons from ν_μ-reactions. From this experimental observation it follows that ν_μs are a different

species. In 2001 the ν_τ was finally discovered by the DONUT experiment. To this end, 800 GeV protons from Fermilab were guided on a tungsten target. A particle shower was created with neutrinos being created from purely leptonic decays as well as semi-leptonic and hadronic decays. The tau leptons decay into ν_τ which interact in a detector consisting stainless-steel sheets interleaved with nuclear emulsion plates. With a shield of concrete, iron and lead against other particles produced from the initial proton interactions, it could be ensured that only ν_τ can pass through. The tau neutrino produces a tau lepton with a short lifetime and a short track in the emulsion, resulting in kink-like tracks. These results have confirmed the three flavor picture for neutral leptons, which earlier was established by the ALEPH experiment and others at the LEP collider at CERN. There the invisible width of the Z^0 resonance at 91 GeV proclaims three flavor states.

1.1.3 Neutrinos in the Standard Model

While measuring the neutrino flux from the sun, Davis also proved that neutrinos are different than their anti-particles because from antineutrino capture by chlorine no free electrons could be observed.
In 1958 Goldhaber proofed the left-handed nature of neutrinos by measuring the helicity in electron capture of metastable ^{152m}Eu and the consequent fast de-excitation of ^{152}Sm* in $\tau = 30$ fs.

$$\overline{\nu}_e + {}^{37}\mathrm{Cl} \not\rightarrow {}^{37}\mathrm{Ar} + e^- \ , \tag{1.3}$$

The helicity of the electron neutrino is equal to the helicity of the emitted photons. The measurement of the photon helicity delivered a value of $h = -1.0 \pm 0.3$. As a consequence the direction of the neutrino and the spin are in opposite direction, consequently the parity is maximally violated by the weak interaction process (as Wu discovered earlier). Within the Standard Model, the V-A theory describes massless, left-handed neutrinos and right-handed anti-neutrinos.
In order to further extend the picture of neutrinos, the Z^0 resonance width has been measured at four different experiments at LEP (ALEPH, DELPHI, L3 and OPAL). From this quantity, the number of generations of light active neutrinos has been determined to $N_\nu = 2.984 \pm 0.008$ [O$^+$14], consequently three active neutrino flavor generations have been proved.

The three different neutrinos $(\nu_e, \nu_\mu, \nu_\tau)$ form together with their leptonic partner a weak isospin doublet. Correspondingly the antiparticles form as well an isospin doublet.

1.2 Neutrino oscillations

The discovery of neutrino oscillations has far reaching consequences for both particle physics and cosmology. During the propagation of a neutrino as a mass eigenstate, the flavor eigenstates will oscillate, implying non-vanishing neutrino mass differences. As the Standard Model of particle physics describes neutrinos as massless particles, a strong motivation is raised to extend the existing description of fundamental particles. The following chapter discusses at first the solar neutrino problem and the original discovery of neutrino flavor oscillations followed by their theoretical description. The peculiarities of neutrino oscillations in matter are discussed separately and finally current experimental results are given.

1.2.1 The solar neutrino problem and discovery of oscillations

The *pp*- and CNO-cycles, which take place in the core of the sun, lead to proton fusion:

$$4p \rightarrow {}^4\mathrm{He} + e^+ + 2\nu_e + 26.73\,\mathrm{MeV}. \tag{1.4}$$

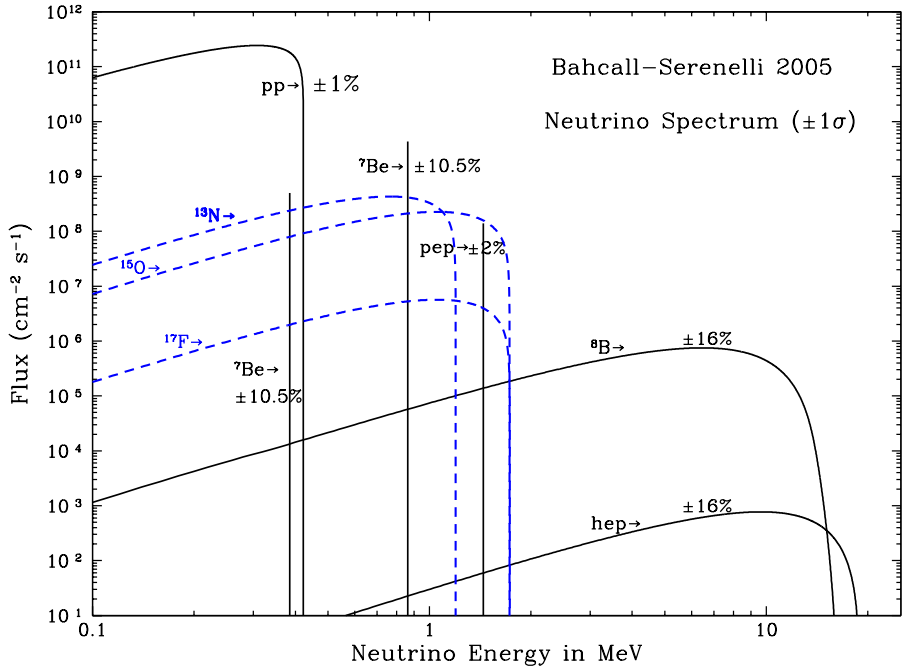

Figure 1.2: Solar neutrino spectrum as described by the SSM. The plot describes the energy dependent solar neutrino fluxes from the *pp*-chain (solid line) and the CNO cycle (dashed lines). The integral spectrum can be measured down to 0.2 MeV (GALLEX, SAGE) and the high-energy spectrum is measured differentially by the Borexino and SNO experiment. From [BSB05].

Within this process, electron neutrinos are emitted, their energy spectrum (fig. 1.2) is described by the Standard Solar Model (SSM). A total of 60 billion neutrinos per cm^2 and per second are expected here on earth. In the 1960s, the Homestake experiment was developed and setup in order to detect the solar neutrino flux and to confirm the SSM by Bahcall and co-workers. This experiment, led by the chemist Ray Davis, was based on a radiochemical detection technique. In order to take advantage of ^{37}Ar as target material, a tank of 600 t tetrachloroethylene was used. Neutrinos were detected by the following inverse beta decay reaction:

$$\nu_e + {}^{37}\mathrm{Cl} \underset{\text{capture}}{\overset{\text{decay}}{\rightleftharpoons}} {}^{37}\mathrm{Ar} + e^- \,.$$

After several weeks of measurement time, the few argon atoms produced in the tank were isolated. This decay back into an excited chlorine state can be recorded, as this state de-excites by release of an Auger electron with an energy of 2.8 keV, which is registered in a proportional counter. Since this radiochemical method is rather slow, no real-time information from the reactions can be gathered. Surprisingly, compared to the Standard Solar Model, the neutrino flux at the earth was about a factor of 1/3 lower than expected. The question at this point was whether the calculations of the SSM were correct, or if the neutrino flavors oscillate on their way from the sun to earth. Other experiments, based on gallium as target material and which were again only sensitive to electron neutrinos, confirmed the solar neutrino deficit. The Super-Kamiokande experiment was launched to primarily investigate atmospheric muon neutrinos. Whereas this experiment is sensitive to both ν_e and ν_μ at the GeV-scale, a deficit of atmospheric muon neutrinos was manifest. Finally, the oscillation of solar neutrinos into other active flavors was tested at the Sudbury neutrino observatory (SNO). This experiment used 1000 t heavy water as target material in order to measure ν-fluxes via neutral current (NC), charged current (CC) and electron

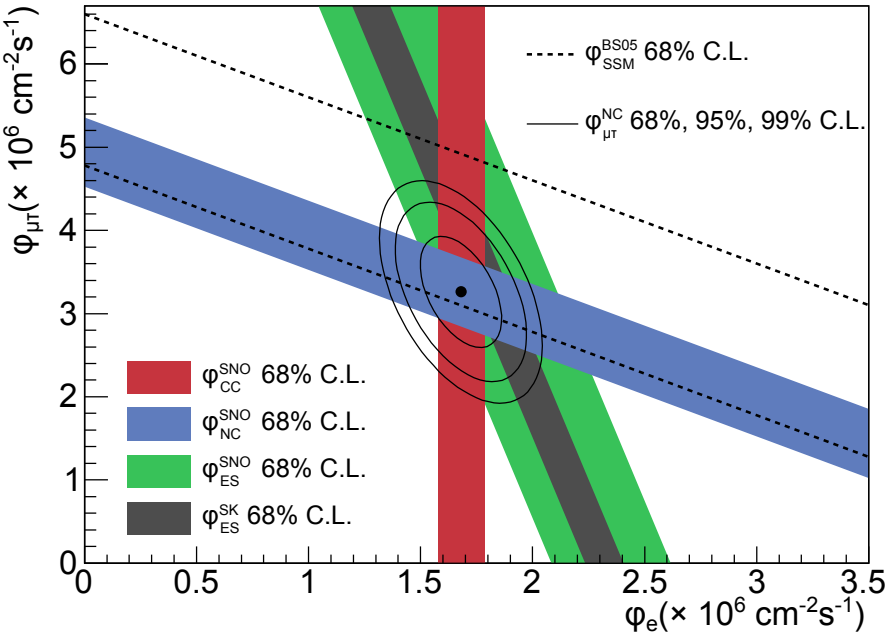

Figure 1.3: Flux of ^{8}B solar neutrinos from the SNO salt water phase. Measured flux $\phi_{\mu\tau}$, from tau and muon neutrinos, as function from measured flux ϕ_e from electron neutrinos, as determined by ES, NC and CC reactions of the SNO experiment and ES reactions of the Super Kamiokande experiment. The charged current reaction (red bar) determines the total neutrino flux. The intersection of the CC, NC and ES bands indicates that the flux is composed of 1/3 ν_e and 2/3 of ν_μ and ν_τ. Figure taken from [O+14].

scattering (ES) processes, where ν_x denotes neutrinos with all different kinds of flavors:

$$\nu_e + e^- \longrightarrow \nu_e + e^- \text{ (CC)} \tag{1.5}$$
$$\nu_e + D \longrightarrow \nu_e + p + p \text{ (CC)} \tag{1.6}$$
$$\nu_x + D \longrightarrow \nu_x + p + n \text{ (NC)} \tag{1.7}$$
$$\nu_x + e^- \longrightarrow \nu_x + e^- \text{ (ES)} \tag{1.8}$$

Figure 1.3 shows the results for the different fluxes of the neutrinos flvors.

1.2.2 Theoretical description

Two-generation neutrino oscillation

In the following, an oscillation between two neutrino flavors only is regarded. This simplified case is defined by a single mixing angle θ and contains of no CP-violating phase. Comparable to the Cabibbo matrix in the quark sector, the mixing of different mass eigenstates ν_1 and ν_2 results in well-defined flavor eigenstates ν_α and ν_β. Following matrix equation describes the mixing between the different states by a 2×2 rotation matrix U:

$$\begin{pmatrix} \nu_\alpha \\ \nu_\beta \end{pmatrix} = \begin{pmatrix} \cos\theta & \sin\theta \\ -\sin\theta & \cos\theta \end{pmatrix} \cdot \begin{pmatrix} \nu_1 \\ \nu_2 \end{pmatrix}. \tag{1.9}$$

The transition probability between two flavor eigenstates is given by:

$$P(\nu_\alpha \longrightarrow \nu_\beta) = P(\nu_\beta \longrightarrow \nu_\alpha) = P(\overline{\nu}_\alpha \longrightarrow \overline{\nu}_\beta) = P(\overline{\nu}_\beta \longrightarrow \overline{\nu}_\alpha) \tag{1.10}$$
$$= \sin^2(2\theta) \cdot \sin^2\left(\frac{\Delta m^2 c^3}{4\hbar}\frac{L}{E}\right) \tag{1.11}$$
$$= 1 - P(\nu_\alpha \longrightarrow \nu_\alpha). \tag{1.12}$$

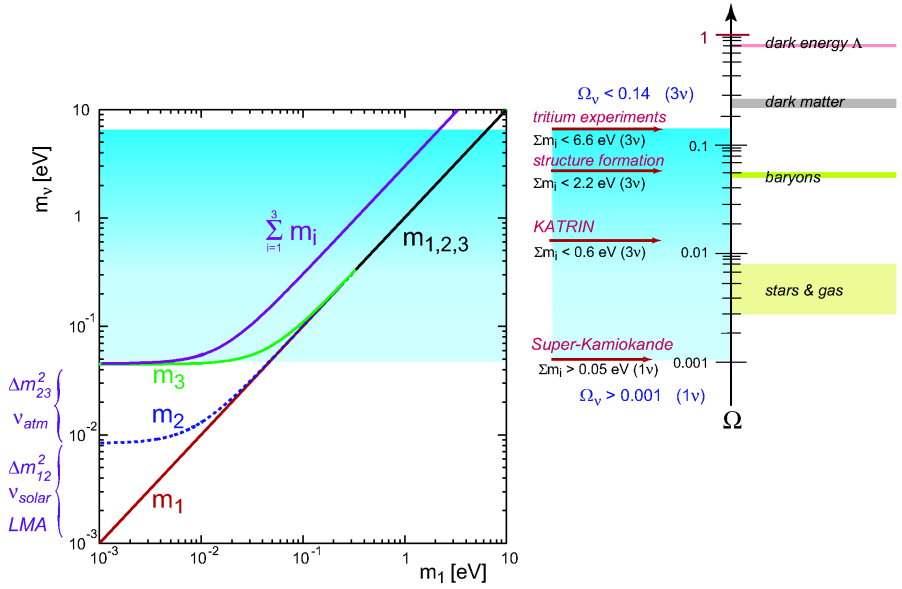

Figure 1.4: Neutrino mass eigenstates and contribution to the universe energy density. Left: Values of the neutrino mass eigenstates m_1, m_2 and m_3 as a function of the lightest mass eigenstate m_1. Either the eigenstates form a hierarchical set of eigenstates or a quasi-degenerate set. **Right: Neutrino contribution Ω_ν to the energy density of the universe in comparison to dark energy, dark matter and baryonic content.** The lower bound of Ω_ν results from the analysis of oscillations of atmospheric neutrinos. The upper bound is determined by tritium β-decay experiments. The KATRIN experiment will investigate the parameter space where relic neutrinos from the big bang act as hot dark matter. Figure from [A+04].

Here Δm^2 denotes the difference of squared masses, which is defined as $\Delta m^2 = m_1^2 - m_2^2$. From (1.11) it follows immediately that neutrino flavor oscillations can only occur, if the neutrinos have a non-vanishing mass and the Cabibbo angle is unequal to zero. The term $\sin^2(2\theta)$ defines the oscillation amplitude, L denotes the distance between neutrino source and detector (the baseline length) and E denotes the neutrino energy. In addition, a characteristic oscillation length L_0 is defined with:

$$L_0 = \frac{4\pi\hbar}{c^3}\frac{E}{\Delta m^2}. \tag{1.13}$$

In case of three-flavor oscillations additional mass differences and mixing angles have to be introduced. The detailled expressions can be found in [Zub11].

Oscillations in matter

Theoretical investigations have revealed, that the neutrino oscillation probability will change in matter, in particular in a dense plasma as the solar interior. This effect of matter enhanced oscillations is called MSW effect according to the initial theoretical formulation by Mikheyev, Smirnov and Wolfenstein [MS86, Wol78].
For the MeV-scale energies of solar neutrinos, neutral current reactions with electrons and nuclei will take place for all three flavor states. For electron neutrinos only, an additional charged current reaction can take place from which an effective potential

$$U = U(n_e) = \sqrt{n_e G_F} \tag{1.14}$$

is introduced, where U depends on the electron density in the matter. This additional potential also contributes to the Hamiltonian with an additional term:

$$H = H_0 + U = H_0 + \begin{pmatrix} U & 0 \\ 0 & 0 \end{pmatrix}. \tag{1.15}$$

Consequently the eigenvalue problem has changed and new eigenvectors and mass eigenvalues can be derived:

$$H\,|\nu_{M1}\rangle = m_{M1}\,|\nu_{M1}\rangle \quad \text{and} \quad H\,|\nu_{M2}\rangle = m_{M2}\,|\nu_{M2}\rangle \tag{1.16}$$

The flavor eigenstates can be obtained by a rotation in two-dimensional space (for simplicity two flavor eigenstates only are taken into account):

$$\begin{pmatrix}\nu_e\\ \nu_\mu\end{pmatrix} = \begin{pmatrix}\cos\theta_m & \sin\theta_m\\ -\sin\theta_m & \cos\theta_m\end{pmatrix}\cdot\begin{pmatrix}\nu_{M1}\\ \nu_{M2}\end{pmatrix}. \tag{1.17}$$

According to [Wol78], the mixing angle in matter θ_m can be expressed in terms of the mixing angle θ in vacuum. With L_0 denoting the vacuum oscillation length, the following abbreviations are introduced:

$$\kappa = \sqrt{1 \mp 2\left(\frac{L_0}{L_R}\right)\cos(2\theta) + \left(\frac{L_0}{L_R}\right)^2} \quad \text{and} \quad L_R = \frac{2\pi}{U}. \tag{1.18}$$

The mixing angle θ_m and oscillation length L_m in matter are given by [Wol78, Smi03]:

$$\sin(2\theta_m) = \frac{\sin(2\theta)}{\kappa} \quad \text{and} \quad L_m = \frac{L_0}{\kappa}. \tag{1.19}$$

Regarding these equations, the following statements can be drawn:

- The term L_0/L_R is proportional to the neutrino energy and the electron density in matter.
- The oscillation amplitude is given by $\sin\theta_m$ as in the case of vacuum oscillations.
- The oscillation in matter can even be amplified due to resonance effects.

Besides the Borexino experiment, the occurrence of matter effects of neutrino oscillations of ^{8}B neutrinos was studied by the SNO [A$^+$13] and KamLAND [A$^+$11b] collaborations. Also the Borexino project has beautifully confirmed the MSW effect for ^{7}B, ^{8}B and *pp* neutrinos from the sun. Figure 1.5 shows both the theoretical predictions together with experimental results by Borexino.

1.2.3 Overview of experimental techniques

The target of various experiments investigating neutrino oscillations is to determine the

- mixing angles θ_{12}, θ_{23} and θ_{13},
- mass square splittings Δm^2_{21} and Δm^2_{32},
- CP-violating phases.

Different experiments examine neutrino oscillation parameters either from natural (sun, atmosphere, astrophysical sources) or artificial sources (particle detectors, nuclear reactors). The different experiments can be distinguished with respect to the oscillation length and the neutrino energy. Commonly two different detection modes are realized:

- *Appearance channel:* Neutrino flavors which are absent in the primary source are detected, consequently the probability of occurrence of flavor type β from type is measured: $P(\nu_\alpha \longrightarrow \nu_\beta)$. This type of experiments features a small background signal and a sensitivity to small mixing angles.

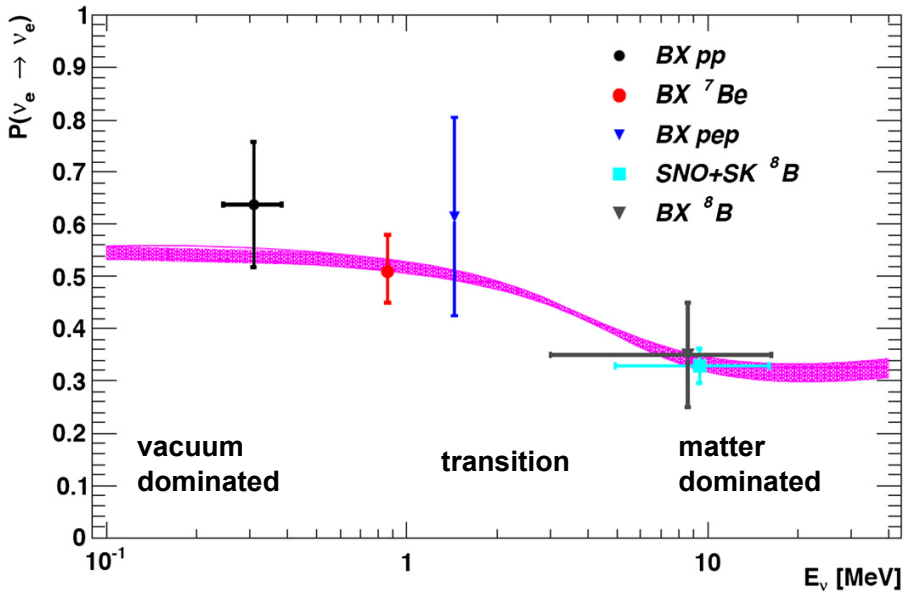

Figure 1.5: Survival probability of solar electron neutrinos together with the MSW prediction. The illustration depicts the survival probability of solar neutrinos with respect to their energy as determined by the Borexino collaboration. For low energies vacuum oscillations take place and for energies above $\approx 1.9\,\mathrm{MeV}$ matter effects dominate. The (central) light blue data point has been measured by SNO and Super Kamiokande respectively. The horizontal error indicates the energy band which has been used for analysis whereas the vertical band indicates a 1σ uncertainty. Figure adapted from [Bel16].

- *Disappearance channel:* Experiments, which have been setup for this mode measure the survival probability of the initial neutrino flavor α: $P(\nu_\alpha \longrightarrow \nu_\alpha)$. For this detection mode, the initial source activity has to be determined accurately. In general, these experiments thus consist of a near and a far detector. In the context of nuclear power plants the near detector measures the neutrino flux before an oscillation takes place in order to correlate recorded events at the far detector.

The neutrino probabilities $P(\nu_\alpha \longrightarrow \nu_\alpha)$ and $P(\nu_\alpha \longrightarrow \nu_\beta)$ depend on different parameters:

- The distance L between source and detector,
- the neutrino energy E,
- and the matrix elements $U_{\alpha i}$ of the PMNS matrix.

With respect to a possible observation of neutrino oscillations, three particular cases of the ratio L/E can be formulated (L_0 denotes the characteristic oscillation length):

- $\frac{L}{E} \ll \frac{1}{\Delta m^2}, L \ll L_0$: In this regime, the neutrino energy is too high or the detector is located too close to the source to observe oscillations.
- $\frac{L}{E} \approx \frac{1}{\Delta m^2}, L \approx L_0$: This is the most sensitive region in order to detect the sinusoidal oscillation pattern.
- $\frac{L}{E} \gg \frac{1}{\Delta m^2}, L \gg L_0$: Now the detector is too far away from the source or the neutrino energy is too low. Here, only an averaged transition probability can be measured.

From this pattern, the different mixing angles and the differences of squared masses can be determined by identifying the neutrino flavor, which is detected by observing the charged lepton in a charged current reaction [Zub11]:

$$\nu_l + N \longrightarrow l^- + X, \tag{1.20}$$

where N denotes the nucleus of the target material and X denotes the hadronic final state. In the following the different experimental techniques are sketched.

Accelerator neutrinos

Intense beams of neutrinos can be produced from particle accelerators via the collision of proton bunches onto a fixed graphite or beryllium target. Here, the protons produce new unstable particles, like kaons or pions. The latter are focused magnetically via a horn to a forward cone into a long decay tunnel. The pions or kaons will decay-in-flight into muons and neutrinos. Due to the relativistic boost, neutrinos have a large energy of $\mathcal{O}(\text{GeV})$. A block of concrete and steel slows down and absorbs the muons. After traveling distances of up to $\mathcal{O}(100\,\text{km})$, the neutrinos interact in a massive far detector. The neutrinos typically have a high energy of order 10 GeV, consequently only large mass splittings can be probed, e.g. $\Delta m^2_{32} \approx 10^{-3}\,\text{eV/c}^2$.

Reactor neutrinos

Nuclear power pants deliver an intense and isotropic source of electron anti-neutrinos. On average, a total of six neutrinos is produced per nuclear fission reaction. Each neutrino has an energy of a few MeV. The neutrino flux is thus proportional to the thermal power of the reactor. Since reactor neutrinos have a very low energy, this type of experiment is sensitive to electron type neutrinos only. Oscillation effects are thus measured in the disappearance channel, where the probability $P(\bar{\nu}_\alpha \longrightarrow \bar{\nu}_\alpha)$ is measured. As mentioned earlier the neutrino flux has to be known precisely. For this reason the experiments Daya Bay, RENO and Double Chooz take advantage of a near detector in order to measure the neutrino flux before oscillations can occur.
This experimental configuration allows to examine θ_{13}. Precision values for this parameter have been determined by RENO and Daya Bay, as well as by Double Chooz.

Atmospheric neutrinos

Atmospheric neutrinos result from the continuous interaction of high-energy cosmic rays (protons, α-particles and heavier nuclei) with the upper atmosphere of the earth. In this way broad showers of unstable particles (kaons, pions and muons) with high energy are produced.
The leptonic decay sequences will give rise to high-energy neutrinos:

$$\begin{array}{lll} K^+ \longrightarrow \mu^+ + \nu_\mu & \pi^+ \longrightarrow \mu^+ + \nu_\mu & \mu^+ \longrightarrow e^+ + \nu_e + \overline{\nu}_\mu \\ K^- \longrightarrow \mu^- + \overline{\nu}_\mu & \pi^- \longrightarrow \mu^- + \overline{\nu}_\mu & \mu^- \longrightarrow e^- + \overline{\nu}_e + \nu_\mu. \end{array} \tag{1.21}$$

The dominant contribution to atmospheric neutrinos results from the pion and muon decay chains, with the kaon decay chain representing an additional contribution with smaller probability. From the equations above, a 2:1 ratio between muon and electron neutrinos is expected for a broad energy range ($\mathcal{O}(\text{GeV})$).
The baseline of atmospheric neutrinos will vary from 10 km up to the diameter of the earth. The experiments are thus sensitive to squared mass differences of $\Delta m^2 > 10^{-4}\,\text{eV/c}^2$ [Zub11]. The Super-Kamiokande experiment thus could make the pivotal observation of a difference between the up and downward going muon neutrino flux. The muon neutrino deficit is found to be maximal for neutrinos traveling through the earth implying a $\Delta m^2 \approx 2.5 \times 10^{-3}\,\text{eV}^2$.

Solar neutrinos

As outlined earlier, electron neutrinos are produced mainly via *pp* fusion in the core of the sun:

$$p + p \longrightarrow \mathrm{D} + e^+ + \nu_e + 0.42\,\mathrm{MeV}\ . \tag{1.22}$$

The CNO cycle contributes only with 1.6 % due to the low solar core temperature. The solar neutrinos have either a monoenergetic or a continuous energy spectrum with a maximal energy of about $\mathcal{O}(15\,\mathrm{MeV})$ (fig. 1.3). The energies are described by the SSM, which can be found in [BSB05].
Neutrinos from the sun are of electron-type, so their energies are too low in order to produce other charged leptons than electrons in CC reactions. Experiments with solar neutrinos thus are of the $P(\nu_e \longrightarrow \nu_e)$ disappearance type, which however is sensitive to very small mass splittings Δm^2_{12}.

Solar neutrinos were discovered at first with radiochemical experiments and observed a deficit of solar neutrinos, the famous solar neutrino problem. Experiments of this class were the Homestake, GALLEX and SAGE experiments. Commonly, the detection principle is based on the neutrino capture by nuclei, where the unstable daughter nuclei of solar ν-interactions are extracted and their interaction rate is measured. In this way information on the neutrino flux can be gathered.

Real-time experiments deliver timing and spectral information on the neutrino flux. In this case, neutrinos can be detected via charged current and neutral current reactions. The scattering off electrons, protons, deuterons or nuclei will lead to distinct kinematics which help to identify specific reaction types. Fast charged leptons can be traced by the occurrence of Cerenkov radiation or by scintillation light.
Cerenkov detectors have a rather large energy threshold of typically $\approx \mathcal{O}(3.5\,\mathrm{MeV})$, consequently *pp* or ^{7}B neutrinos are not detected.
The use of organic liquid scintillators delivers no directional information, however the energy information is much better than in a Cerenkov detector. Also, the low energy threshold of $< 1\,\mathrm{MeV}$ allows to detect neutrinos from the *pep* and *pp* chains.

Experimental results

The parameter space given by neutrino oscillations is given in the following from a global three flavor analysis, taken from [GGMS16]. The sign of the parameter Δm^2_{23} defines the type of hierarchy, either normal or inverted.

1.3 Massive neutrinos

1.3.1 Theoretical description

In the Standard Model of particle physics, no formalism is embedded to describe massive neutrinos. However, the experimental evidence for neutrino oscillations clearly requires the introduction and theoretical description of at least two massive neutrino eigenstates. Since neutrinos are about five orders of magnitude lighter than their charged leptonic partners, the mass generation mechanism is expected to be different from the standard Higgs formalism. Consequently, the introduction of massive neutrinos inevitably leads to physics beyond the Standard Model.
Starting from the discussion of different mass terms in a Lagrangian describing massive neutrinos, finally possible mass eigenvalues of neutrinos are then presented and discussed in the following.

Table 1.1: Three-flavor oscillation parameters from global three flavor fit. From [GGMS16].

	Normal hierarchy ($\pm 1\sigma$)	Inverted hierarchy ($\pm 1\sigma$)
$\sin^2\theta_{12}$	$0.304^{+0.013}_{-0.012}$	$0.304^{+0.013}_{-0.012}$
θ_{12}	$33.48^{+0.78}_{-0.75}$	$33.48^{+0.78}_{-0.75}$
$\sin^2\theta_{23}$	$0.452^{+0.052}_{-0.028}$	$0.579^{+0.025}_{-0.037}$
θ_{23}	$42.3^{+3.0}_{-1.6}$	$49.5^{+1.5}_{-2.2}$
$\sin^2\theta_{13}$	$0.0218^{+0.001}_{-0.001}$	$0.0219^{+0.0011}_{-0.001}$
θ_{13}	$8.50^{+0.2}_{-0.21}$	$8.51^{+0.2}_{-0.21}$
$\Delta m^2_{21}/10^{-5}\,\mathrm{eV}^2$	$7.50^{+0.19}_{-0.17}$	$7.50^{+0.19}_{-0.17}$
$\Delta m^2_{3x}/10^{-3}\,\mathrm{eV}^2$	$2.457^{+0.047}_{-0.047}$	$-2.449^{+0.048}_{-0.047}$

Mass terms in the Lagrangian are always quadratical in the given fields. While neutrinos are described within weak isospin doublets, all possible spinor field combinations have to be Lorentz invariant and Hermitian.
A Dirac mass term is given by the following expression, where the fields have been subdivided into their chiral components ψ_L and ψ_R:

$$\mathcal{L} = m_D \left(\overline{\psi}_L \psi_R + \overline{\psi}_R \psi_L \right). \tag{1.23}$$

This mass term requires both the left- and the right-handed neutrinos to generate mass. Because only left-handed neutrinos exist in the Standard Model, neutrinos as described by this term stay massless, consequently.

Further possible spinor field combinations can be constructed with the charge conjugated field ψ_c, allowing additional Lorentz invariant terms in the Lagrangian. The following field combinations, noted here in chiral representation, are allowed and lead to the following Lagrange densities:

$$\mathcal{L}^L = \frac{1}{2} m_L (\overline{\psi}_L \psi^c_R + \overline{\psi}^c_R \psi_L) \text{ and} \tag{1.24}$$

$$\mathcal{L}^R = \frac{1}{2} m_R (\overline{\psi}^c_L \psi_R + \overline{\psi}_R \psi^c_L), \tag{1.25}$$

where m_L and m_R represent real valued Majorana neutrino masses.
Both Dirac and the Majorana Lagrange densities can be expressed in terms of a single Dirac-Majorana mass matrix M:

$$2\mathcal{L} = \begin{pmatrix} \bar{\psi}_L & \bar{\psi}^c_L \end{pmatrix} \underbrace{\begin{pmatrix} m_L & m_D \\ m_D & m_R \end{pmatrix}}_{M} \begin{pmatrix} \psi^c_R \\ \psi_R \end{pmatrix} + h.c. \tag{1.26}$$

The Lagrangian describing Dirac and Majorana masses has following properties:

- The CP conservation leads to real matrix entries of matrix M.
- Only the two Weyl spinors ψ_L and ψ^c_R contribute to the weak interaction. These two fields describe *active neutrinos*.
- The fields ψ_R and ψ^c_L do not contribute to the weak interaction and are called *sterile neutrinos*.

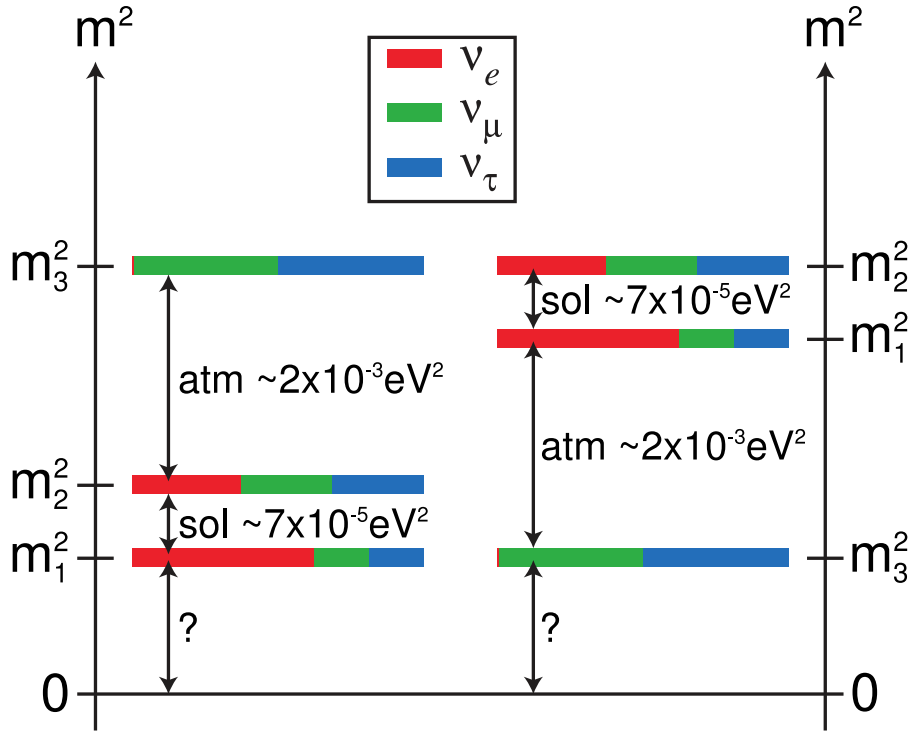

Figure 1.6: Illustration of neutrino mass hierarchies. The figure illustrates the normal (left) and inverted (right) hierarchy and the corresponding flavor mixing by different color bars (red for electron, green for muon and blue for tau flavor). The differences of squared masses have been measured with $\Delta m^2_{21} \approx 7.5 \times 10^{-5}\,\mathrm{eV}^2$ and $|\Delta m^2_{32}| \approx 2.3 \times 10^{-3}\,\mathrm{eV}^2$. Figure from [KL13].

The diagonalization of the matrix M leads to the mass eigenvalues, which are given as follows:

$$\epsilon_k m_k = \frac{1}{2}\left[(m_L + m_R) \pm \sqrt{(m_L - m_R)^2 + 4m_D^2}\right]. \tag{1.27}$$

The parameter $\epsilon_k = \pm 1$ has been introduced in order to always guarantee positive mass eigenvalues [GK90]. While ψ_L and ψ_R describe chiral interaction eigenstates to the real Majorana masses m_L and m_R, two Majorana fields with ϕ_1 and ϕ_2 as mass eigenstates are introduced:

$$\phi_1 = \phi_{1L} + \epsilon_1 \phi^c_{1R} = \cos\theta(\phi_L + \epsilon_1 \phi^c_R) - \sin\theta(\phi^c_L + \epsilon_1 \phi_R) \tag{1.28}$$

$$\phi_2 = \phi_{2L} + \epsilon_2 \phi^c_{2R} = \sin\theta(\phi_L + \epsilon_2 \phi^c_R) + \cos\theta(\phi^c_L + \epsilon_2 \phi_R). \tag{1.29}$$

The parameter ϵ_k is furthermore the CP eigenvalue of the Majorana neutrino ϕ_k: $\phi^c_k = \epsilon_k \phi_k$ and the mixing angle is defined as

$$\tan(2\theta) = \frac{2m_D}{m_R - m_L}. \tag{1.30}$$

Together with the above introduced expressions, the Lagrange density function can be expressed as

$$2\mathcal{L} = m_1 \bar{\phi}_1 \phi_1 + m_2 \bar{\phi}_2 \phi_2. \tag{1.31}$$

Finally three particular mass configurations are discussed briefly:

1. *Dirac neutrino with $m_L = m_R = 0$:*
   Two degenerated Majorana fields ϕ_1 and ϕ_2 result in a Dirac neutrino field which result in the Dirac mass term $\mathcal{L} = m_D \bar{\phi}\phi$.

2. *Majorana neutrino with $m_D = 0$:*
   In this case $m_{1,2}$ is equal to $m_{L,R}$. The fields $\phi_{1,2}$ are defined by the Majorana fields: $\phi_1 = \psi_L + \psi_R^c$ and $\phi_2 = \psi_R + \psi_L^c$.

3. *See-saw neutrino model with $m_L = 0, m_R \gg m_D$:*
   This scenario results in a light active neutrino with mass $m_1 = \frac{m_D^2}{m_R}$ and $m_2 \approx m_R$. The Majorana field $\phi_1 \approx \psi_L - \psi_R^c$ represents the (light) active neutrino, whereas $\phi_2 \approx \psi_L^c - \psi_R$ represents a heavy sterile neutrino.

1.3.2 Experimental approaches

Cosmology

Until 0.1 s after the Big Bang, neutrinos were in thermal equilibrium with the radiation bath by means of different weak interaction processes. At a temperature of around 1 MeV [LP14], the neutrino interaction rate dropped below the Hubble expansion rate of the universe, hence neutrinos decoupled from the cosmic plasma. The subsequent expansion of the universe has led to a strong red shift of primordial neutrinos. The free streaming length and the energy density of neutrinos are important parameters which strongly depend on the neutrino mass scale. Due to this very large free streaming length, neutrinos can carry energy out of dense regions. Their propagation with relativistic velocities and thus results in a wash-out of dense structures. In this context neutrinos are labeled as hot dark matter, with specific imprint on the structure formation of the early universe. From the measurement of the comic microwave background and the number density of photons, the present temperature of neutrinos is given as $T_\nu = 1.95\,\mathrm{K}$, the number density of a single neutrino flavor state is $(n_\nu + n_{\bar{\nu}}) = 112\,\mathrm{cm}^3$ [A$^+$11a]. The given temperature leads to a mean kinetic energy of $\langle E_{\mathrm{kin}} \rangle = 0.168\,\mathrm{meV}$. Due to this very low kinetic energy, it is very difficult to detect neutrinos. Neutrinos contribute in a specific way to the total energy-matter density of the universe:

$$\sum_i m_i = 93 \Omega_\nu h^2\,\mathrm{eV}. \tag{1.32}$$

From the Planck satellite and other cosmological data, the following model-dependent limits have been set for the sum of all different neutrino flavors [A$^+$16a]:

$$\sum_i m_i \leq 0.23\,\mathrm{eV}\ (95\,\%\ \mathrm{C.L.}) \tag{1.33}$$

For this analysis, the energy density and the Hubble constant have been assumed to be

$$\Omega_\nu h^2 \approx 0.025, \tag{1.34}$$

$$\text{and } H_0 = (67.7 \pm 0.6)\ \mathrm{km/(s\,Mpc)}, \tag{1.35}$$

with the Hubble parameter h being defined as $h = H_0/(100\,\mathrm{km/(s\,Mpc)})$. In the context of the determination of the above mentioned parameter, different experimental results from other astrophysical experiments have been taken into account, leading to a very constrained parameter set: Information from baryon acoustic oscillation measurements (BAO), joint-light curve analysis (JLA) from different supernovae and the number of active neutrino flavor generations, rendering this upper limit model-dependent.

Detection of supernova neutrinos with Time-Of-Flight method

Supernovae represent an intense transient source of neutrinos at the MeV-scale. The 10 s ν-pulse can thus be analyzed the Time-Of-Flight method to derive the squared neutrino mass

m_ν^2 (like β-decay experiments). The energy-dependent time-of-flight of a single neutrino with mass m_ν, energy E_ν and momentum p_ν is defined as follows:

$$T = \frac{L}{v} = \frac{L}{c} \cdot \frac{E_\nu}{p_\nu c} = \frac{L}{c} \cdot \frac{E_\nu}{\sqrt{E_\nu^2 - m_\nu^2 c^4}} \approx \frac{L}{c} \cdot \left(1 + \frac{m_\nu^2 c^4}{2E_\nu^2}\right). \tag{1.36}$$

The Taylor expansion in the last calculation step requires the rest mass of the neutrino to be much smaller than the kinetic energy. In order to be able to register time differences of order $\mathcal{O}(\mathrm{s})$ for neutrinos with a mass difference of $\mathcal{O}(10\,\mathrm{eV})$, the supernova needs to be at a distance of about 10 kpc [Kra92].

The quantity to be measured is the time difference which is given as

$$\Delta t = t_2 - t_1 = \Delta t_0 + \frac{L m_\nu^2}{2c} \left(\frac{1}{E_1^2} - \frac{1}{E_2^2}\right). \tag{1.37}$$

Whereas Δt, E_1 and E_2 are measured at the detector located on earth, the distance L between earth and supernova stems from astrophysical observations. The parameter Δt_0 describes the time difference of the neutrino emission at the supernova. This particular parameter depends however from the a priori unknown supernova emission parameters [Zub11].

From the type-II supernova SN1987A a total of 19 neutrinos within a time range of 13 s were detected by the IMB [B$^+$87] and Kamiokande [H$^+$87] experiments. The analysis, which is performed in context of [LL02], yields a mass limit of

$$m_\nu < 5.7\,\mathrm{eV} \quad (95\,\%\ \mathrm{C.L.}). \tag{1.38}$$

Neutrinoless double beta-decay

For nuclei with an even number of neutrons N and an even atomic number A, single β-decay is forbidden by energy conservation, this is also valid for odd configuration of A and N. Instead a double β-decay can occur as a second-order weak process. According to the pairing-term in the Bethe-Weizsäcker mass parabola, the even-even configuration is energetically preferred. In total 35 nuclei exist with the even-even configuration. The double β-decay is described as follows:

$$2n \longrightarrow 2p + 2e^- + 2\overline{\nu}_e \quad (2\nu\beta^-\beta^-) \tag{1.39}$$

$$2p \longrightarrow 2n + 2e^+ + 2\nu_e \quad (2\nu\beta^+\beta^+) \tag{1.40}$$

$$\tag{1.41}$$

Nucleons with an even mass number A result in a degenerate mass parabola. Either the number of neutrons N and the charge number Z are both even, which results in a higher binding energy or both values have an odd value, which results in a lower binding energy. In this particular nuclear configuration, single β-decay is forbidden, whereas the double β-decay is allowed. This decay mode has exceedingly long half-lifes. In the case of a Majorana nature of the neutrino, particle and anti-particle states are described as the same state, hence a Majorana neutrino can be exchanged. Besides the Majorana nature of the neutrino, a 'helicity' flip is required to 'fuse' the opposite helicity states of the two neutrinos. In the decay process the resulting charged leptons acquire the full Q-value (assuming the nuclear recoil can be neglected). Consequently, in the spectrum a discrete line will appear at the Q-value. Most importantly, this process violates lepton number conservation by two units.

The effective Majorana neutrino mass can be expressed in terms of a coherent sum:

$$\langle m_{\beta\beta} \rangle^2 = \left| \sum_{i=1}^{3} U_{ei}^2 m_i \right|^2 = \left| \sum_{i=1}^{3} |U_{ei}|^2 \exp(\alpha_{i1}) m_i \right|. \tag{1.42}$$

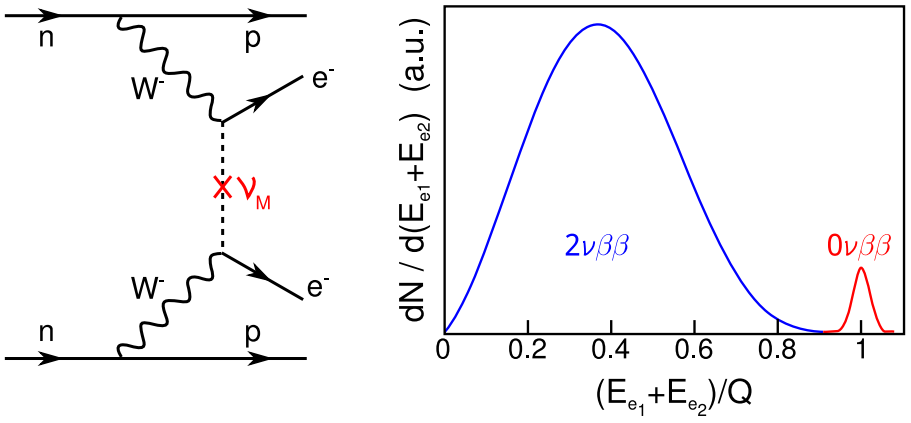

Figure 1.7: Depictions of the (neutrinoless) double β-decay. Left: Feynman diagram of the neutrinoless double β-decay. The simultaneous decay of two protons into two neutrinos requires the emission of two W bosons and the exchange of two Majorana neutrinos with opposite helicity. **Right: Energy spectrum of two emitted electrons from the $2\nu\beta\beta$- and $0\nu\beta\beta$-decay.** Whereas the double β-decay represents a three-body decay and leads to a continuous energy spectrum, the neutrinoless double β-decay (as a two-body decay) leads to an energy peak at the Q-value of the decay process. Illustrations adapted from [Wan13].

Kinematics of single β-decay

In the past, various properties of the weak interaction have been determined by investigation of various β-decay processes. This particular decay mode can also be used for the determination of the neutrino mass. There are three different modes of β-decay (A denotes the mass number and Z the atomic number):

$$(Z, A) \longrightarrow (Z+1, A) + e^- + \overline{\nu}_e \ (\beta^-) \tag{1.43}$$

$$(Z, A) \longrightarrow (Z-1, A) + e^+ + \nu_e \ (\beta^+) \tag{1.44}$$

$$(Z, A) + e^- \longrightarrow (Z-1, A) + \nu_e \ \text{(electron capture)} \tag{1.45}$$

The goal here is to deduce the electron energy spectrum from β^--decay and to obtain information on the neutrino mass parameter. The most important assumptions and calculation steps are shown in the following. For further details the reader is referred to the text book [Zub11].

The transition rate of the nuclear initial state i and final state f is described by Fermi's Golden Rule:

$$\Gamma_{i \longrightarrow f} = \frac{\mathrm{d}^2 N}{\mathrm{d}t \mathrm{d}E} = \frac{2\pi}{\hbar} \left| \langle f \,|\, H_{if} \,|\, i \rangle \right|^2 \rho(E_f). \tag{1.46}$$

The weak interaction is described by the Hamilton operator H_{if}, and $\langle f \,|\, H_{if} \,|\, i \rangle$ denotes the transition matrix element. The phase space density of the final states is given by $\rho(E_f)$.
To good approximation, the wave function of the electron and the neutrino is given commonly by

$$\phi_{e/\nu} = \frac{1}{\sqrt{V}}, \tag{1.47}$$

where V is the normalization volume of the wave function. However, the electron wave function needs to be modified due to the Coulomb interaction with the daughter nucleus, so that the finally the matrix element can be determined:

$$\left| \langle f \,|\, H_{if} \,|\, i \rangle \right|^2 \simeq \frac{g^2}{V^2} F(E, Z+1) |M_{if}|^2. \tag{1.48}$$

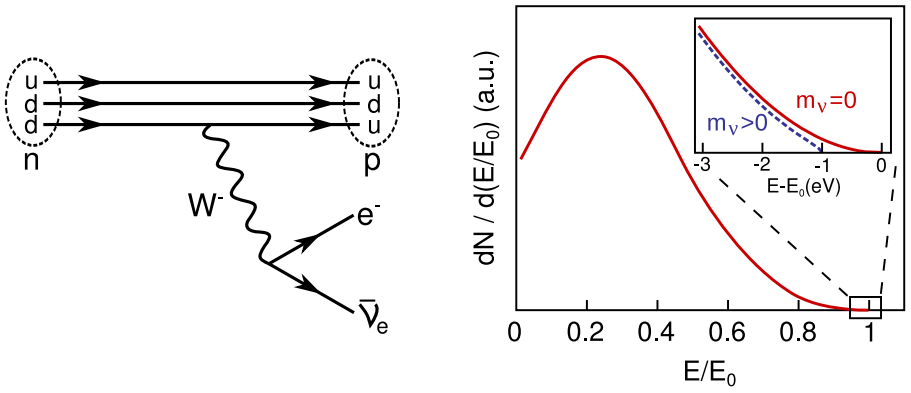

Figure 1.8: Feynman diagram and energy spectrum of single β-decay. Left: Single β-decay The Feynman diagram illustrates the transition of a down-quark into an up-Quark in a weak interaction process. Here the intermediate emission of a W^--boson is followed by the decay into an electron and an anti-neutrino. **Right: Differential electron energy spectrum.** The energy scale is normalized to the endpoint energy $E_0 \approx Q$. The spectral shape due to an electron with $E = 0\,\text{eV}$ and $E = 1\,\text{eV}$ is compared. Figure taken from [Sch13].

Here, $F(E, Z+1)$ has been introduced as the Fermi function M_{if} as the nuclear matrix element and g as the coupling constant. Together with the particle phase space density

$$\rho(E) = \frac{V^2 p_e E_e p_\nu E_\nu}{4\pi^4 \hbar^6}, \tag{1.49}$$

the final expression of the electron energy spectrum from β^--decay can be deduced to

$$\frac{\mathrm{d}N^2}{\mathrm{d}E\mathrm{d}t} = \frac{G_F^2 \cdot \cos^2\theta_C}{2\pi^3 c^5 \hbar^7} \cdot |\mathcal{M}|^2 \cdot F(Z+1, E) \cdot p \cdot (E + m_e c^2) \cdot \\ \cdot (E_0 - E) \cdot \sqrt{(E_0 - E)^2 - m_\nu^2 c^4} \cdot \theta(E_0 - E - m_\nu - c^2) \tag{1.50}$$

$$m_\nu^2 = \sum_{i=1}^{3} |U_{ei}^2| m_i^2 \tag{1.51}$$

Rhenium (β-decay) and holmium (electron capture) experiments

Both the β-decay of the rhenium isotope ^{187}Re and the electron capture of holmium ^{163}Ho have a very low Q-value each (the rhenium isotope has a Q-value of 2.87 keV and the holmium isotope of 2.8 keV). Both are thus well suited β-emitters for precision studies of the decay process at the endpoint, where the neutrino mass will modify the spectral electron energy shape. Because the signal fraction there decreases with E_0^{-3}, a low Q-value guarantees a sufficiently high signal rate. This however is counteracted by the overall decay rate which scales as E_0^{-5}.
The β-decay process of rhenium can be expressed as follows:

$$^{187}\text{Re} \longrightarrow ^{187}\text{Os}^+ + e^- + \overline{\nu}_e. \tag{1.52}$$

The electrons close to the β-end point energy of a few keV cannot be detected outside the source material. Consequently, the source was simultaneously used as detector material (cryogenic bolometer) and cooled down to cryogenic temperatures of $\mathcal{O}(\text{mK})$. In this way the energy of the β-decay can be measured via phonons, which results in a tiny temperature increase ΔT. The following generic relation between temperature increase and released energy by the β-decay

$$\Delta T = \frac{\Delta E}{C}, \tag{1.53}$$

calls for a small C, the heat capacity of the material. Since the detection of significant temperature increases requires small detectors of $\mathcal{O}(\mathrm{mg})$, multiple detector units have to be aligned together acting as a common detector array. In this way, systematical effects can be reduced.

This approach was realized in the MIBETA experiment which set an upper limit on the mass of the electron anti-neutrino of $m_{\overline{\nu}_e} < 15.6\,\mathrm{eV}$ at 90 % C.L. The successor experiment MARE was targeted to achieve a sensitivity of $\mathcal{O}(1\,\mathrm{eV})$ in the first and 0.2 eV in a second phase. However, this target had to be abandoned.

A complementary experimental approach is now being realized through the electron capture of holmium:

$$e^- + {}^{163}\mathrm{Ho} \longrightarrow {}^{163}\mathrm{Dy}^* + \nu_e \longrightarrow {}^{163}\mathrm{Dy}^* + Q. \tag{1.54}$$

This technique is realized in the ECHo experiment which targets a sensitivity in the sub-electronvolt regime and the HOLMES experiment aiming for a sensitivity of 1 eV.

Radio-frequency method

Instead of measuring the electron energy of β-decay by means of a MAC-E filter system, this approach targets to determine the kinetic electron energy from the energy-dependent cyclotron frequency of the electron in an external magnetic field B:

$$\omega(E) = \frac{\omega_0}{\gamma} = \frac{c^2}{2\pi}\frac{qeB}{E + m_e c^2}. \tag{1.55}$$

The non-shifted electron cyclotron radius is labeled as ω_0 and the Lorentz factor of the electron with mass m_e, kinetic energy E and charge q is denoted as γ. The radiation with frequency $\omega(E) \approx 27\,\mathrm{GHz}$ close to energy end point is detected for $B \approx 1\,\mathrm{T}$ by an antenna system. First tests of this experimental technique, as realized by the Project8 collaboration, can be found in [MF09, A$^+$15b].

CHAPTER 2

The KATRIN experiment

The goal of the KATRIN experiment is to measure the effective mass of the electron anti-neutrino with a sensitivity at 200 meV with 90 % C.L. (corresponding to 350 meV at 5σ) after three years of net measurement time. This design goal excels former limits by the Mainz [K$^+$05] and Troitzk Neutrino experiment [A$^+$11c] by a factor of ten (or a factor 100 for the observable, the square of the mass m_ν^2). Spectroscopy at the tritium end-point at $E_0 \approx 18.6\,\mathrm{keV}$, the very low rates (only 10^{-13} of the emitted electrons are expected to be at the last eV directly below the endpoint), have to be counterbalanced by an ultra-luminous ($A \approx 10^{11}\,\mathrm{Bq}$) tritium source. Since it is planned to measure up to 30 eV below the endpoint, a significant rate of electrons is expected to arrive at the detector. A spectrometer of the MAC-E type [P$^+$92, LS85] (magnetic adiabatic collimation combined with an electrostatic filter) with an unprecedented energy resolution of $\Delta E = 0.93\,\mathrm{eV}$ is thus essential to act as a high-pass filter for signal electrons to be counted at the detector.

This ambitious goal requires the setup of a complex system of different components for magnetic guidance and energy analysis of electrons from β-decay. The following chapter will explain the working principle of a MAC-E filter, as well as the different components of KATRIN from the tritium source to the silicon detector. Finally, the particular measurement configuration of the apparatus at the second commissioning phase of the main spectrometer and detector in 2015 will be outlined.

In section 2.1, first the principle of β-spectroscopy with MAC-E filters is explained. The technique of magnetic adiabatic collimation and electrostatic filtering is outlined in sec. 2.1.1, highlighting the key features of the KATRIN spectrometer. The rationale of why tritium has been chosen as source material is explained in section 2.1.4. The first part of this chapter closes with the presentation of the design goals of the KATRIN experiment as apparatus for high-precision β-spectroscopy.

In sec. 2.2, the different sub-modules of the experiment from the tritium source to the focal plane detector are explained, while the functionality of each component is presented and its importance for the complete experiment is emphasized.

For the investigation of electron transmission and background characteristics, measurement campaigns of the main spectrometer together with an attached electron gun system and detector system have been performed in context of dedicated measurement phases. The measurement setup is briefly abbreviated as SDS and stands for spectrometer and detector section, which is described in sec. 2.3.

The last part, sec. 2.4 focuses on key aspects in the determination of the neutrino mass. First, the design parameters will be discussed together with the expected systematical

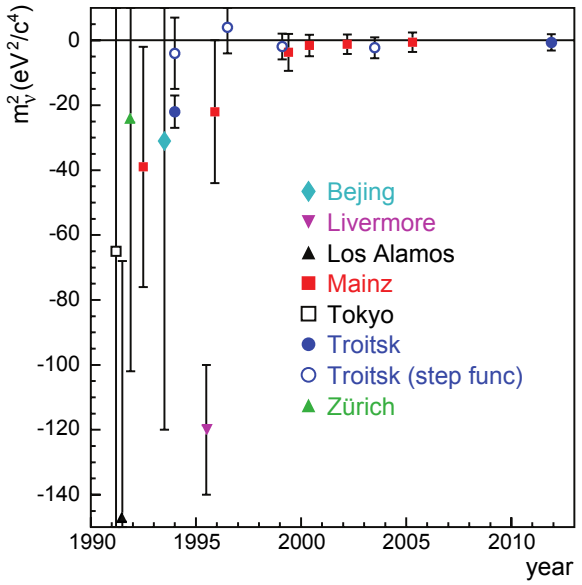

Figure 2.1: Results from former tritium β-decay neutrino experiments. Experiments in Bejing, Livermoore, Los Alamos, Tokyo and Zürich used magnetic spectrometers for the measurements. The experiments in Mainz and Troitsk have been the first who exploited the advantages of spectrometer of MAC-E filter type. Figure taken from [Sch14].

errors, followed by the determination of the neutrino mass sensitivity and a brief explanation of the optimization of the measurement time distribution. The chapter closes with an outlook on the measurement strategy and expected mass sensitivity in view of the current background level in the main spectrometer.

2.1 Tritium β-spectroscopy with MAC-E filters

The ideal combination of a high luminosity tritium source and a high-resolution MAC-E filter allows to investigate by kinematic means the end-point spectrum with yet unexplored sub-electronvolt ν-mass sensitivity. While the KATRIN experiment is pushing many technological components to their limit, the scientific outcome of a model-independent measurement of the absolute neutrino mass scale will be of key importance for astroparticle physics.

The deployment of MAC-E filters for β-decay studies, has been pioneered in the 1980s by groups in Mainz [P$^+$92] and Troitsk [LS85] independently. The experiments were able to push the neutrino mass limits to the few eV region. MAC-E filters have proven to be optimal for investigating the region around the energy end point (of tritium) with low count rates. In this way, the shape can be investigated with highest precision.

2.1.1 Principle of MAC-E filters

In preceding neutrino experiments in Mainz and Troitzk, spectrometers of MAC-E filter type have been instrumental in delivering important scientific data on the absolute neutrino mass scale. In the following, this working principle together with well-studied 'bottlenecks' of this particular spectrometer type are explained. Figure 2.2 illustrates the working principle of MAC-E filters.

Principle of magnetic guidance

Electrons from a β-emitter such as tritium are isotropically emitted and thus have to be guided on magnetic field lines on cyclotron paths from source to detector. Magnetic

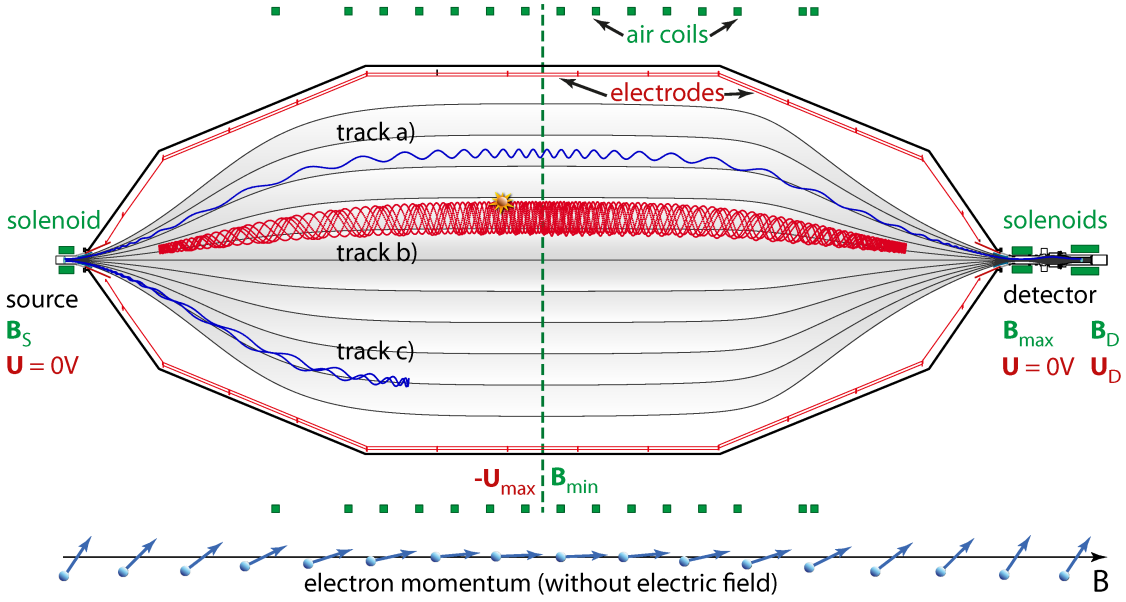

Figure 2.2: Measurement concept of MAC-E filters. Electrons are isotropically emitted at the source side (left) and guided adiabatically on cyclotron paths (blue) on magnetic field lines (black) to the detector side (right). The slow decrease of the magnetic field to the center of the spectrometer leads to an adiabatic transformation of transversal momentum to longitudinal momentum. The magnetic field is produced by superconducting magnets, located at both spectrometer ends, and fine-tuned by an air-coil system surrounding the spectrometer system. In the analyzing plane, the electrons are filtered by their longitudinal energy, since only electrons with a higher kinetic energy than the retarding potential U_0 can surpass the analyzing plane $E_\parallel > |qU_0|$. In this way the MAC-E filter system acts as an integrating high-pass filter. The remaining transversal momentum (relative to the magnetic field line) in the analyzing plane defines the energy resolution of the spectrometer, the KATRIN main spectrometer has a resolution of $\Delta E = 0.93\,\mathrm{eV}$ with default magnetic field settings. The electric field is produced by a sophisticated wire electrode system, installed at the inner vessel hull surface. Because the vessel hull will be hold on a slightly more positive potential, an outward pointing electric field shields the sensitive flux tube volume against low-energy secondary electrons from the inner surface. Illustration adapted from [A+16b].

guiding has the advantage of a high angular acceptance of almost 2π, which results in a high accepted solid angle.
The kinetic energy E_{kin} and the momentum $\boldsymbol{p}$ of an electron can be described by two components relative to the orientation of the magnetic field line: one component in the direction of the magnetic field line and one component perpendicular to the magnetic field line:

$$\boldsymbol{p} = \boldsymbol{p}_\parallel + \boldsymbol{p}_\perp \quad \text{and} \quad E_{\mathrm{kin}} = E_\parallel + E_\perp. \tag{2.1}$$

The momentum and the transversal energy (since $E \propto p^2$) can both be expressed in terms of a polar angle θ:

$$\boldsymbol{p}_\perp = \boldsymbol{p} \sin(\theta) \quad \text{and} \quad E_\perp = \boldsymbol{E}_{\mathrm{kin}} \sin(\theta)\,. \tag{2.2}$$

Accordingly, a maximal accepted starting polar angle can be derived for an electron starting in a source magnetic field of $B_s = 3.6\,\mathrm{T}$ and being transmitted through the strongest magnetic field of $B_{\mathrm{max}} = 6\,\mathrm{T}$ at the pinch magnet located at the exit of the main spectrometer. Under the assumption that the kinetic energy of an electron at the strongest magnetic field is equal to the transversal energy component (this implies the polar angle in this region to be $\theta_{\mathrm{max}} = 90°$), a maximal starting polar angle θ_s for an electron starting in the source magnetic field can be derived from conservation of the magnetic moment (in

order not to be trapped):

$$\frac{E_{\perp,s}}{B_s} = \frac{E_{\perp,\max}}{B_{\max}} \quad \Rightarrow \quad \theta_s = \arcsin\left(\sqrt{\frac{B_s}{B_{\max}}}\right) \approx 50.77^\circ \tag{2.3}$$

The underlying principle for the electron guidance is adiabatic invariance, which implies that the magnetic moment is constant along one single cyclotron turn:

$$\gamma\mu = \text{const.} = \frac{\gamma+1}{2} \cdot \frac{E_\perp}{B} \approx \frac{E_\perp}{B}, \tag{2.4}$$

where $E_\perp$ denotes the transversal kinetic energy. In case of a MAC-E filter operated with electrons from tritium β-decay with a low Q-value [OBW06, NFB+06, SEH+14], electrons with $E_{\text{kin}} \approx 18.6\,\text{keV}$ consequently result in a mild relativistic gamma factor of $\gamma \approx 1.04$ and thus can be treated in a first approximation as being non-relativistic. A MAC-E filter makes use of an electrostatic retarding potential to analyze the longitudinal energy part. For this reason the transversal energy has to be transformed into longitudinal energy. Since this transformation has to happen adiabatically, this implies that the magnetic field gradient and the electric potential gradient are sufficient small with:

$$\frac{\Delta U}{U} \ll 1 \quad \text{and} \quad \frac{\Delta B}{B} \ll 1. \tag{2.5}$$

For the neutrino mass analysis, only electrons with a kinetic energy of a few eV below the endpoint have to be considered. While collimating the electron momentum magnetically, the electric retarding potential has to be adjusted accordingly. The potential reaches its highest value of $U_{\text{ret}} \approx 18.6\,\text{kV}$ at the center plane of the spectrometer (also called analyzing plane), and thus filters electrons by their longitudinal energy. If an electron has a higher longitudinal energy than the retarding potential, it can surpass and reach the detector. This picture assumes that all transversal energy has been collimated into the longitudinal component. Since the magnetic field at the analyzing plane has a small non-zero value, a certain transversal energy will remain and stay hidden by the filter potential. Therefore a finite energy resolution ΔE is defined which describes the part of transversal energy which is not analyzed:

$$\Delta E = \frac{E_{\text{kin}}}{B_{\max}} B_{\min} = 0.93\,\text{eV}. \tag{2.6}$$

Here the KATRIN design values have been used, with $B_{\min} = 3 \times 10^{-4}\,\text{T}$ (mag. field in the analyzing plane), $B_{\max} = 6\,\text{T}$ (mag. field of the pinch magnet) and the maximal transversal electron energy at the pinch magnet $E_{\text{kin}} = 18.6\,\text{keV}$.

A more detailed discussion on the principle of adiabatic invariance can be found in appendix A.

Principle of electrostatic shielding and retardation

Whereas the source and the detector section of KATRIN are grounded, the inner electrode system of the retarding spectrometer is hold on a retarding potential U_0 close to the endpoint energy of tritium for the purpose of electrostatic energy analysis and block of low-energy electrons. The highest and most homogeneous potential is located in the center of the spectrometer. Together with the retarding potential, the longitudinal energy component of the β-electrons can be analyzed: Through the applied retarding potential, the kinetic energy of the signal electrons will be transformed into potential energy. If the starting energy is sufficient, electrons passing the location with highest electrostatic potential at the analyzing plane (central plane in the main spectrometer at $z = 0\,\text{m}$) are

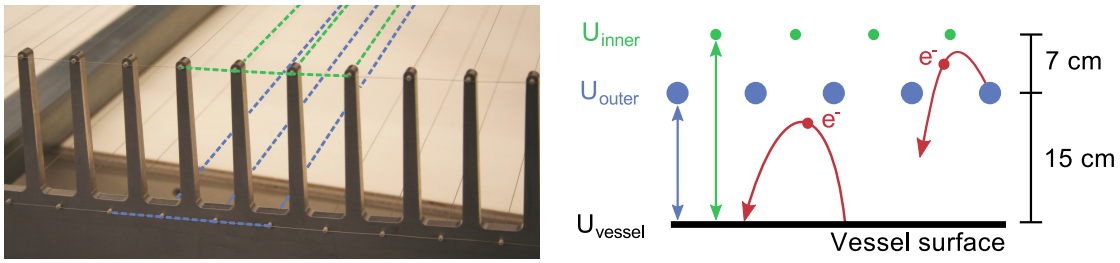

(a) Wire holding structure

(b) Shielding principle of secondary electrons

Figure 2.3: Concept of the dual-layer wire electrode. (a) Picture of the so-called combs, holding and aligning mechanically the dual wire layers. **(b)** Repel of secondary background electrons through a dual-layer wire electrode operated at different electrostatic potentials. Photograph from [Han07] and sketch from [Har15].

re-accelerated to their initial energy to impinge on the detector. If electrons have less energy, they are reflected back to the source.

The wire electrode can also shield against low-energy background electrons which are created at the wire holding structure or at the vessel wall, through dual wire layers held at two different potentials as illustrated by figure 2.3. The inner layer and the outer layer (together with the wire holding structure) are short-circuited while the vessel is kept at a more positive potential: $U_{\text{inner}} = U_{\text{outer}} < U_{\text{vessel}}$. By this configuration, an electric field pointing outwards establishes an $\boldsymbol{E} \times \boldsymbol{B}$ drift in order to drift background electrons radially out onto the vessel wall. As a further benefit, the more negative inner wire electrodes can shield electrostatically against the potential drop which is caused by the more positive wire holding structure. In this way the potential in the flux tube is more homogeneous. Further information on the wire electrode system is available in [Val10]. However, the excellent magnetic shielding far surpasses the above described electrostatic shielding due to its near-perfect axial symmetry.

2.1.2 Transmission and response function

Transmission function

The probability of transmission of electrons through a MAC-E filter depends on their starting kinetic energy and their starting polar angle. Electrons with a large starting angle need a specific amount of surplus energy $E_{\text{start}} - qU_0$ for transmission. Figure 2.4(a) shows the form of a generic transmission function, where the transmission probability increases with larger starting kinetic energy. It can be defined analytically as following step-wise function:

$$\mathcal{T}(E, U_0) = \begin{cases} 0 & \text{for } E < |qU_0| \\ \dfrac{1-\sqrt{1-\frac{E-qU_0}{E}\cdot\frac{B_S}{B_{\min}}}}{1-\sqrt{1-\frac{B_S}{B_{\max}}}} & \text{for } |qU_0| \leq E \leq |qU_0| + \Delta E \\ 1 & \text{for } E > |qU_0| + \Delta E \end{cases} \tag{2.7}$$

where B_S denotes the magnetic field in the source, and B_a in the analyzing plane.

Response function

The transmission function $\mathcal{T}$ describes the spectroscopic features of KATRIN in case of an ideal transmission of β-electrons, where no energy loss processes from the source to the analyzing plane have to be taken into account. However, the required rather high column

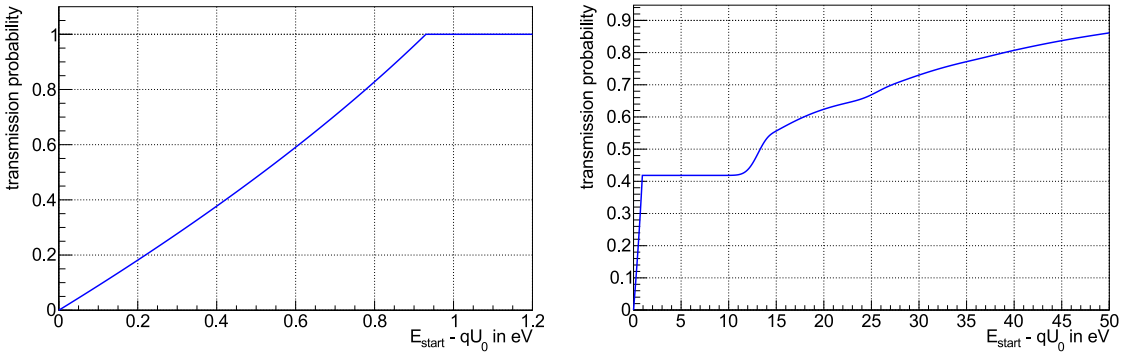

(a) Transmission function (b) Response function

Figure 2.4: Plots of the transmission and response function. (a) Transmission function for an isotropic source. The electron surplus energy is denoted on the x-axis. The retarding potential is $U_0 = -18.6\,\mathrm{kV}$, the source magnetic field strength is $B_S = 3.6\,\mathrm{T}$ and the field strength in the analyzing plane is $B_a = 3.0 \times 10^{-4}\,\mathrm{T}$. The maximal magnetic field at the detector pinch magnet with $B_{\mathrm{max}} = 6\,\mathrm{T}$. For larger surplus energies, even electrons with higher polar starting angles are transmitted until the full transmission with $E_{\mathrm{start}} - qU_0 \geq 0.93\,\mathrm{eV}$. **(b)** Response function for an isotropic β-electron source with maximal polar starting angle $\theta_{\mathrm{max}} = 50.77°$ and retarding potential $U_0 = -18.55\,\mathrm{kV}$. The inelastic cross section is $\theta_{\mathrm{inel}} = 3.4 \times 10^{-22}\,\mathrm{m}^2$ and the column density is $\rho d = 5 \times 10^{21}/\mathrm{m}^2$. 41.8 % of all β-electrons leave the source without inelastic scattering on tritium molecules. The response function stays constant until 10 eV surplus energy, which is the minimal energy loss due to inelastic scattering. At higher surplus energies more electrons can surpass the retarding potential after scattering on tritium molecules. Illustrations composed from [Gro15].

density in the WGTS will require the (normalized) energy loss function to be taken into account:

$$f(\Delta E) = \frac{1}{\sigma_{\mathrm{tot}}} \cdot \frac{\mathrm{d}\sigma}{\mathrm{d}\Delta E}, \tag{2.8}$$

where ΔE denotes the electron energy loss and σ_{tot} the total scattering cross section. The response function can be computed by convoluting the transmission function $\mathcal{T}$ with the energy loss function. Usually an n-fold scattering has to be taken into account:

$$\begin{aligned} f_{\mathrm{res}}(E, qU) &= T(E, qU) \otimes P_0 && (2.9)\\ &+ T(E, qU) \otimes P_1 \cdot f(\Delta E) && (2.10)\\ &+ T(E, qU) \otimes P_1 \cdot [f(\Delta E) \otimes f(\Delta E)] && (2.11)\\ &... && (2.12) \end{aligned}$$

Figure 2.4(b) shows an example of the response function. Inelastic processes invoke a minimal energy loss of 10 eV, hence the first section of the response function up to this value is identical to the transmission function. Implying that the retarding potential will be decreased, the value of $E - qU$ increases and the number of transmitted electrons will increase, namely those electrons who have had a higher kinetic energy and have experienced an energy loss due to inelastic scattering process. These electrons can also surpass the retarding potential.

2.1.3 Background processes in MAC-E filters

Several background processes can distort the measured β-electron energy spectrum, in particular background events can be produced from non-optimized electromagnetic setups of the spectrometer or from stored electrons in the magnetic bottle in its inner volume. The first issue can result in Penning traps, which after their ignition can lead to very

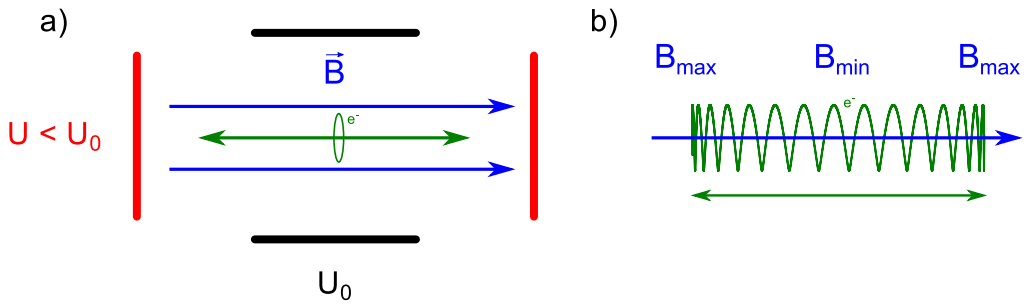

Figure 2.5: Electron trapping processes in a MAC-E filter. (a) Electron trapped on magnetic field line between two electric potential barriers which are hold on a more negative potential than the center potential U_0. **(b)** Magnetic bottle formed by two high magnetic field regions which act as a magnetic mirror. Electrons generated in the weak magnetic field region are reflected due to too large perpendicular velocity component $\boldsymbol{v}_\perp$ in the high magnetic field region. Figure from [Gro10].

high signal count rates, even leading to damage of hardware components. In context of [Frä10], the creation mechanism and the optimization of the electromagnetic design of the pre-spectrometer were discussed. The second large background source results from stored particles. Here, the α-decay of single ^{219}Rn and ^{220}Rn has been identified as the major source for stored electrons. More information on the identification and the properties of this type of background can be found in [Mer12, Wan13, Sch14, Har15].

Penning traps

A Penning trap formed in a localized volume, where charged particles are confined due to specific electromagnetic field configurations. In order to prevent the creation of Penning traps, a careful design of the electromagnetic components of the MAC-E filter and the corresponding field configuration is essential. Figure 2.5 illustrates the mechanism of a Penning trap: An electron is trapped between two electrodes which are set to a more negative potential. Due to its cyclotron motion along the magnetic field lines, a radial electron motion cannot occur. Hence the particle is reflected axially between the two electrodes. As the electron stays in the trap for extended periods of time, it can ionize residual gas molecules. As a result, positive ions, photons and secondary electrons will be produced. Positive particles and photons can leave the Penning trap and initiate ionization in the entire flux tube region. If the positive ions hit the cathode, even tertiary low-energy electrons can be created which lead to a creation of an unstable plasma which results in a vacuum breakdown. The risk and the characteristics of Penning traps have already been studied earlier and underline the necessity of a careful electromagnetic design of the components of a MAC-E filter.

Magnetic storage

A spectrometer of the MAC-E filter type allows spectroscopy of tritium β-decay with highest precision, but it will also act as a magnetic bottle and thus store a large part of all particles which are created in the sensitive flux tube volume. These electrons are guided adiabatically to the high magnetic field regions of the spectrometer while their longitudinal energy $E_\parallel$ is transformed into transversal energy $E_\perp$. If the increase of the longitudinal energy component due to the decrease of the electrostatic potential is too low, the transversal energy component will dominate. In this way, electrons are reflected and a stable storage condition is fulfilled. The mechanism is sketched in figure 2.5 (right). A maximal allowed transversal energy at the electron's starting position $\boldsymbol{x_s}$ can be defined

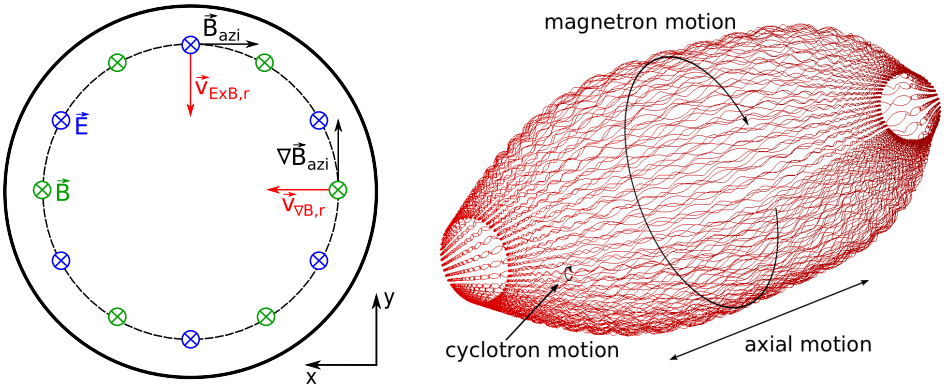

(a) Radial drift motion of electrons

(b) Electron storage

Figure 2.6: Radial drift motion and trajectories of stored electrons. **(a)** Radial drift motion of electrons due to $\boldsymbol{E} \times \boldsymbol{B}_{\text{azi}}$ and $\boldsymbol{\nabla}|\boldsymbol{B}_{\text{azi}}| \times \boldsymbol{B}_{\text{azi}}$ drift. An azimuthally directed magnetic field component due to an inhomogeneous field setup leads to a radial drift motion into the sensitive flux tube volume. **(b)** Motion of stored electrons in the main spectrometer. The electron trajectory of stored particles is composed of three different components. The cyclotron motion is the fastest motion with $t_{\text{cycl}} \approx 100\,\text{ns}$, the motion along the electron beam (z-axis) takes $t_{\text{ax}} \approx 10\,\mu\text{s}$ and the magnetron drift $t_{\text{mag}} \approx 100\,\mu\text{s}$. Illustration composed from [Wan13] (a) and [Mer12] (b).

which defines the onset of a stable storage condition:

$$E_{\perp,\max}(\boldsymbol{x_s}) = qU(\boldsymbol{x_s}) \cdot \frac{B(\boldsymbol{x_s})}{B_{\max}}. \tag{2.13}$$

As the retarding potential inside the spectrometer decreases to both ends, the longitudinal energy component of the electron is boosted, hence a higher electric potential will allow a higher transversal starting energy to be collimated (consequently also larger starting polar angles). While the maximal magnetic field in the magnetic trap (which is defined by the pinch magnet) transforms the longitudinal into transversal energy of the electron, the maximal allowed transversal energy is inverse proportional to the maximal magnetic field value. This statement is equal to the statement that electrons with a higher starting polar angle will have a larger storage probability.

Stored particles can originate from

- Nuclear decay of tritium or radon,
- Atomic De-excitation of atoms, and
- Ionization of residual gas molecules by positive ions.

The first item is discussed in more detail in context of active background mitigation with the electric dipole method in chapter 5.

To summarize: the storage behavior of an electron is defined by the energy resolution of the MAC-E filter system. If the electron has a higher transversal energy than the energy resolution of the spectrometer (in our case $\Delta E \approx 1\,\text{eV}$), the particle is stored.

2.1.4 Tritium as an optimal beta emitter

For the energy spectroscopy of β-decay electrons in the endpoint region, tritium is the candidate of choice due to numerous reasons which will be sketched in the following. Tritium decays via a semi-leptonic weak interaction process:

$$^3\text{H} \longrightarrow ^3\text{He}^+ + \text{e}^- + \overline{\nu}_e. \tag{2.14}$$

The following characteristics of tritium are major advantages in comparison to other β-emitters:

- **Short half-life:** With $\tau_{1/2} = (12.32 \pm 0.02)\,\mathrm{a}$, tritium can be used as a high-luminosity source while minimizing the amount of needed source material. By its high specific activity, or high decay rate per unit volume of source material, only a small amount of source material is required, which minimizes inelastic scattering processes.
- **Low endpoint energy:** A low end point at $E_0 \approx 18.6\,\mathrm{keV}$ is optimal for the technical feasibility of the retarding voltage applied to the spectrometer system. This endpoint requires the retarding voltage of the spectrometer to be set to $U = -18.6\,\mathrm{kV}$. As the absolute number of events scales $\propto E_0^5$, the rather high tritium endpoint compared to ^{163}Ho provides a relatively high rate at the endpoint region.
- **Super-allowed decay:** Since the mother and daughter nuclei represent mirror nuclei, the nuclear matrix element is energy-independent, resulting in a β-spectrum which is defined by the available kinematic phase space. The value of the matrix element is $|M|^2 = 5.55$ [Bel03], which is close to the value of a free neutron decay.
- **Constant recoil correction:** The kinematics of the tritium decay will be investigated in a region of up to 30 eV below the endpoint E_0. The correction for the tritium recoil energy to E_0 is almost constant over this range with variations in the order $\mathcal{O}(\mathrm{meV})$: $E_{\mathrm{rec}} = 1.72\,\mathrm{eV} \pm 3.5\,\mathrm{meV}$.
- **Simple atomic shell structure:** The simple shell structure of the mother and daughter nucleus do not require large corrections due to the final states or due to inelastic scattering processes in the T_2 source. Individual electronic excitations and their probabilities can be computed analytically. The Coulomb interaction between daughter nucleus and the emitted electron can be calculated on the basis of the Fermi function.

As KATRIN will take advantage of a windowless gaseous tritium source, no solid state effects (such as beta environmental fine structure) have to be taken into account.

2.2 Experimental setup of KATRIN

In the following, the sub-components of the KATRIN experiment from source to detector are discussed. Figure 2.7 illustrates the components of the KATRIN beam line together with a table of key experimental parameters.

2.2.1 Rear section

The rear section is located at the downstream end of the WGTS to control and monitor multiple source parameters by different components. The continuous control of these parameters is indispensable in order to achieve the targeted design sensitivity. The tritium activity will be monitored by Beta-Induced X-Ray Spectroscopy (BIXS) on the rear wall [R$^+$13]. In addition the electric potential of the source plasma will be controlled by this component [B$^+$12, Kuc16]. Most of the non-transmitted electrons (to the FPD) will be monitored at the rear wall. This is due to magnetic reflection and electrostatic reflection. The source column density can be measured periodically with the help of an installed high-intensity electron gun [Hug10, V$^+$11]. Furthermore, with the help of this device, the effect of inelastic scattering of β-electrons in the source can be determined. A magnetic dipole system installed at the DPS-1R and DPS1-F magnet systems allows to shift and center the electron beam, so that the entire beam tube cross section can be analyzed with the electron gun. Figure 2.8 shows a sketch of the rear section setup. Further information on the rear section can be found in [Bab14].

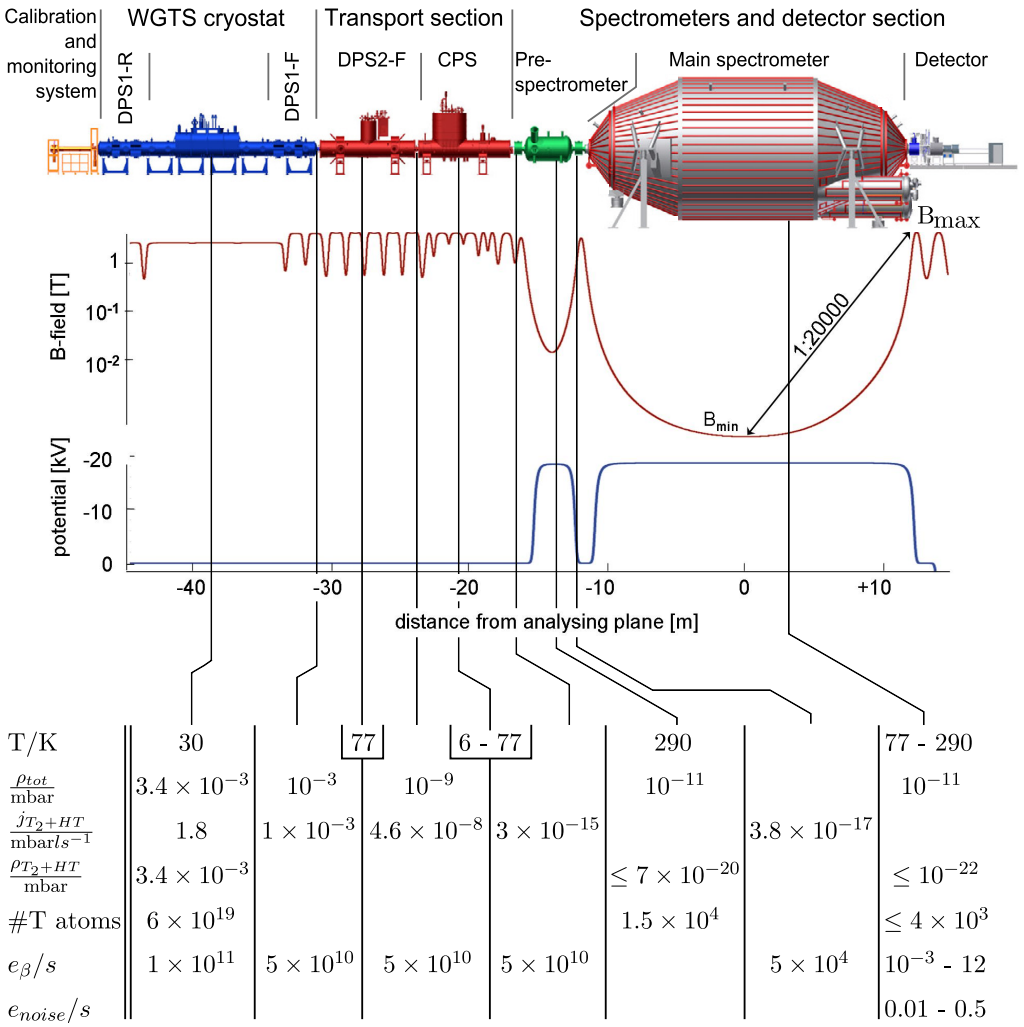

Figure 2.7: Overview of the complete KATRIN beam line. The picture illustrates the different components, which build up the 70 m-long KATRIN beam line with additional information on the inner beam tube temperatures, the total and partial tritium pressures and the expected count of signal and background electrons. Figure adapted from [Gos15].

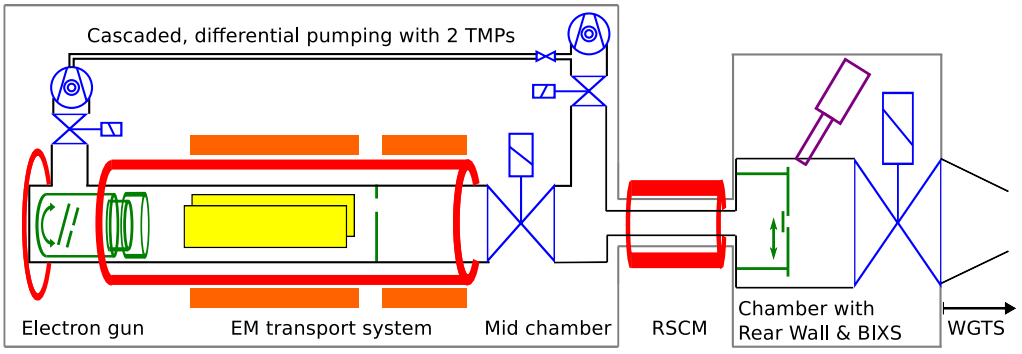

Figure 2.8: Schematics of the rear section. The measurement of the tritium activity will be done with the BIXS system and the rear wall defines furthermore the plasma potential (green, right). The electron gun (green, left) allows to investigate the source column density in well-defined measurement intervals. All components are connected to a primary vacuum system and a second containment. Installed valves and pumps are sketched in blue color and electromagnetic components are colored in orange (coils and solenoids) and yellow (electrodes). Picture from [Bab14].

2.2.2 Tritium source

KATRIN is equipped with a windowless gaseous tritium source (WGTS) which consists of a 10 m long beam tube with a diameter of 90 mm. High purity tritium with $\epsilon_T \approx 95\,\%$, gets injected with a flow rate of $q = 1.853\,\mathrm{mbar}\,\ell/\mathrm{s}$ at the center of the beam tube. Since fluctuations of the column density value will have a direct impact on the energies and rates of signal electrons due to different rates and probabilities of scattering processes, the column density has to be stabilized at the 10^{-3} level.

Located at the rear and front end of the WGTS, two differential pumping systems are installed (DPS-1R and DPS-1F), each equipped with six turbo molecular pumps each delivering a pumping speed of $2400\,\ell/\mathrm{s}$ for T_2 molecules. This results in a gas flow reduction factor about 100. The pumped-out tritium is fed into the inner loop system where the gas is processed and analyzed with respect to its isotopic ingredients by Laser Raman (LARA) spectroscopy. LARA is described in detail in the context of [Sch13, Fis14]. The reprocessed tritium is injected, resulting in a cycled throughput of tens of grams per day. The resulting β-decay activity in the source is $A = 10^{11}\,\mathrm{Bq}$.

Because the electron energies depend on the thermal velocities of the tritium molecules, a stable operating temperature at 30 K has to be guaranteed. For this reason a two phase neon cooling system has been installed, which stabilizes the beam tube temperature to a level of a few mK [SM17]. Before the final assembly of the WGTS, the cooling system was tested in a demonstrator experiment, in which context the temperature was successfully stabilized to $\pm 3.0 \times 10^{-4}$ (this recently has been repeated with the entire WGTS).

The WGTS cryostat is equipped with seven superconducting solenoids (fig. 2.9), which are driven by three power supplies, delivering a magnetic field strength of $B_R = 3.6\,\mathrm{T}$ at the center and rear side and $B_T = 5.6\,\mathrm{T}$ in the region facing the transport section, which guides the signal electrons. Since the magnet on the front side can deliver a higher magnetic field, electrons with a large polar angle will be prevented from entering the transport section. This fact is of high importance since these of electrons suffer from many scattering events and thus loose a large amount of energy which would lead to a non-negligible systematic error exceeding the targeted limits. To compensate a possible misalignment and plasma effects occurring close to the beam tube surface, the outer flux tube region will be note be transported through the system, so that only an effective source area of $A_S = 53\,\mathrm{cm}^2$ will contribute to the neutrino mass analysis with a guided magnetic flux of $\Phi = B \cdot A_S = 191\,\mathrm{T\,cm}^2$.

Positive ions are produced in the WGTS in large numbers through ionization of tritium molecules and subsequent chemical reactions. The different processes sum up to a positive ion current of $I_P = 27\,\mathrm{nA}$ and a smaller current of $I_N = 2\,\mathrm{nA}$ of negative ions [Kuc16, Kle17]. In the following the different components of the transport section are presented. These components are equipped with dedicated technologies in order to prevent tritium ions and molecules from entering the spectrometer and detector section.

2.2.3 Transport section

The design parameters of KATRIN require the neutral tritium flux to be reduced by 14 orders of magnitude from the WGTS point of injection while keeping the energy information of the emitted β-electrons undistorted. In this way the targeted background level and, consequently, the targeted sensitivity on the neutrino mass parameter can be maintained.

Differential pumping section

A dedicated DPS unit (fig. 2.10, left) has been installed as first component for tritium flow reduction. The goal is reduce the tritium flux in this component by five orders of

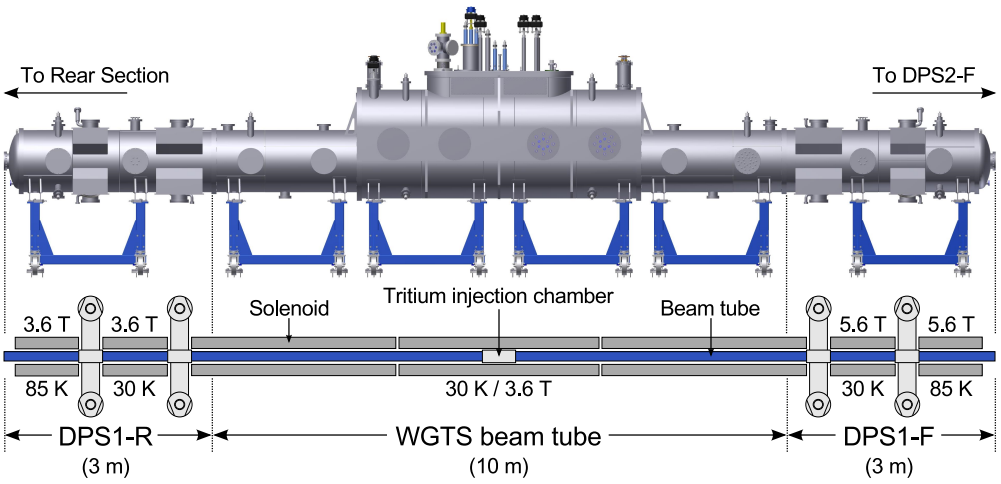

Figure 2.9: Illustration of the windowless gaseous tritium source (WGTS). The WGTS consists of a 10 m-long beam tube which is stabilized at 30 K. In its center, molecular tritium is injected at a constant flow rate. The β-electrons are guided magnetically to the rear and transport section. In order to pump neutral tritium molecules, differential pumping sections are installed directly at the rear and front end of the WGTS. Figure adapted from [Har15].

magnitude via four large turbomolecular pumps. Together with two additional turbo molecular pumps at the entry, the main differential pumping of tritium will be performed in this section with each TMP reaching a pumping speed of 2400 ℓ/s. The turbomolecular pumps are aligned in 20° chicanes at the beam line to suppress the molecular beaming effect by the tritium molecules so that the direct line of sight for neutral molecules is blocked. The following additional systems allow to suppress and to analyze the ion flux:

- Identification of the ion species with a dedicated Fourier Transform Ion Cyclotron Resonance (FT-ICR) unit. Since a special Penning trap configuration during these measurements is needed, this analysis can be only performed during a fixed time interval with no data-taking.
- Positive ions, which otherwise could enter the main spectrometer unimpeded, ring-shaped electrodes are elevated to $U = 100\,\mathrm{V}$ at the downstream end of the DPS.
- Dipole electrodes have been installed to drift ions onto the wall via an $\boldsymbol{E} \times \boldsymbol{B}$-drift. This technique prevents the pumping section and the WGTS from accumulating space charges due to remaining ions.

The beam tube elements are surrounded by five superconducting magnets, which guide the electrons adiabatically to the cryogenic pumping section. The remaining neutral atoms will be pumped out in the cryogenic pumping section.

Cryogenic pumping section

This second transport section (fig. 2.10, left) reduces the tritium flux by a further seven orders of magnitude. In order to work as a cryogenic pump, the beam tube elements have to be cooled down to a temperature of $T = 3\,\mathrm{K}$. The elements are covered by a thin argon frost layer with a high sticking probability for tritium molecules. This component is equipped with chicanes (15°) in order to ensure that the remaining tritium molecules will stick on the surface over several weeks. The concept of adsorption of tritium molecules on argon frost layers has been proven successfully in context of the TRAP experiment. For adiabatic guidance, the cryogenic pumping section houses a total of seven superconducting magnets.

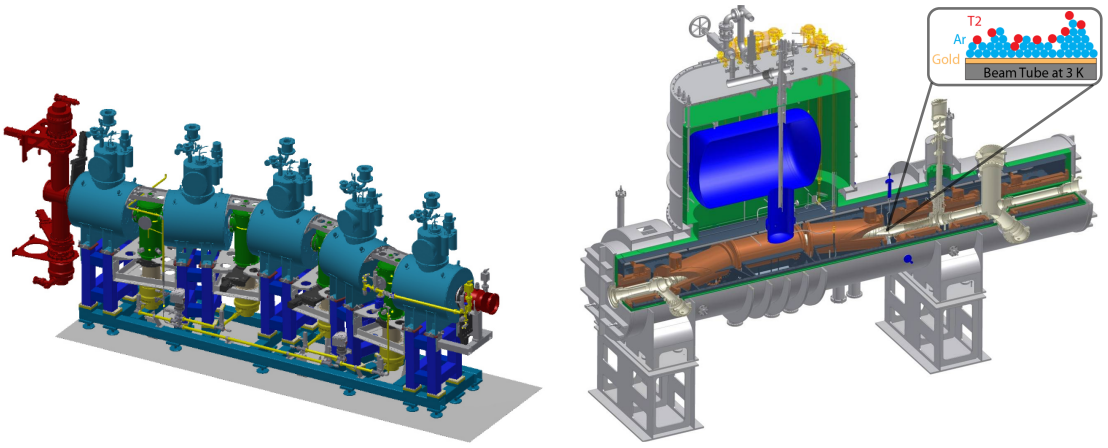

(a) DPS (b) CPS

Figure 2.10: Design of the differential and cryogenic pumping sections. (a) Setup of the DPS. Five superconducting magnets (colored in cyan) guide signal electrons adiabatically from the WGTS to the CPS. The pump ports are colored in green and the turbo-molecular pumps in yellow. The connections to pump port 0 from the WGTS and pump port 5 to the CPS are illustrated in red color. **(b)** Setup of the CPS. Electrons are guided through two chicanes produced by seven superconducting magnets. Tritium molecules stick on the 3 K cold beam tube surface, which is gold-plated and covered with an argon frost layer. Pictures from [Jan15] (DPS) and [Wan13] (CPS).

After three months of operation, the argon frost layer has to be regenerated, because an inventory of 1 Ci of T_2 molecules will have been accumulated on the surface. For this reason, the CPS has to be heated up to $T = 100\,\mathrm{K}$ by flushing with gaseous helium. Afterwards a new argon frost layer will be prepared.

The CPS is also equipped with a forward beam monitor which allows to measure the tritium activity in the source by counting β-electrons arriving in the outer flux tube region. A condensed krypton source is at present being installed at the CPS to serve as a calibration source for multiple issues, such as the measurement of the spectrometer transmission width or the work function of the main spectrometer [Dyb17, Res17].

2.2.4 Spectrometer systems

Main spectrometer

The main spectrometer is the largest single component of the KATRIN experiment (fig. 2.11, left) with a length of 23.6 m, a diameter of 10 m and a volume of 1250 m^3. The large diameter is necessary for the targeted energy resolution of 0.93 eV, whereas the length is required for the adiabatic transformation of transversal into longitudinal electron momentum. The main spectrometer filters β-electrons with unprecedented precision. The signal electrons are guided on magnetic field lines created by the superconducting solenoid at the pre-spectrometer side, PS2 magnet with 4.5 T field strength, and at the detector side, the pinch magnet with 6 T and detector magnet with 3.6 T. The magnetic field in the central parts is furthermore fine-shaped by a large volume air coil system (LFCS). In addition, the horizontal and vertical component of the earth magnetic field are compensated by a separate current system (EMCS). The main spectrometer vessel is on high potential and equipped with a complex wire electrode system on the inner surface (fig. 2.11, right). Together with the vessel, the wire electrodes can be operated on two different potentials creating an outward pointing electric field, which helps to shield background electrons created on the vessel surface. In order to limit scattering processes of residual gas molecules

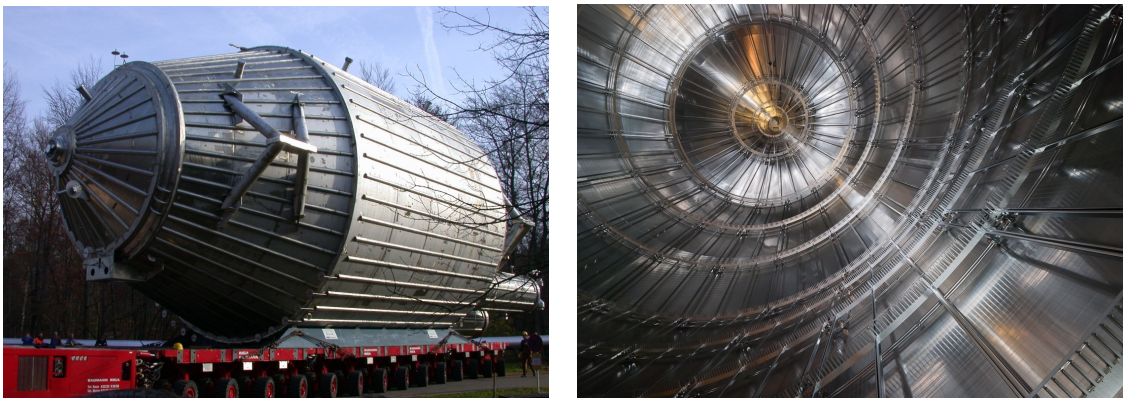

(a) Main spectrometer vessel (b) Wire electrode system

Figure 2.11: Photographs of the main spectrometer vessel exterior and interior. **(a)** Vessel transport to KIT campus north in November 2006. The main spectrometer vessel has a length of 23.6 m and a diameter of 10 m. **(b)** Wire electrode system in the main spectrometer. At the inner surface of the main spectrometer vessel 23,000 wire electrodes have been mounted. They have a diameter of 200 µm (inner wire layer) and 300 µm (outer wire layer). Two wire layers have been installed in order to shield against secondary emission from the tank wall. Photographs taken from [Val09] and [Sch14].

with signal electrons, the vessel will be operated at UHV conditions close to 10^{-11} mbar. For this reason the vessel has been equipped with a set of turbomolecular pumps and a large amount (≈ 2 km) of passive non-evaporable getter (NEG) strips located in the pump ports [A$^+$16b]. The technical details of the main spectrometer setup are discussed in the following section 2.3.

Pre-spectrometer

The pre-spectrometer is located between the CPS and the main spectrometer. This system (fig. 2.12) contains two magnets which generate a maximal field strength of 4.5 T in order to guide signal electrons adiabatically to the main spectrometer. Furthermore this spectrometer provides the option to act as a pre-filter in order to filter out low-energy electrons from the source. These electrons do not contain relevant information on the neutrino mass. For this reason a retarding potential of up to $U_0 = -18.3$ kV can be set. However, when the pre-spectrometer is elevated on high voltage, a large volume and very deep Penning trap between the two spectrometers will be created. There are multiple possibilities to avoid this Penning trap: While the spectrometer is at high voltage, a wire scanner could be used (either in a stationary or active mode) in order to empty the trapping volume from stored electrons [B$^+$10]. In order to operate the spectrometer permanently without distortion of the electro-magnetic configuration by a wire scanner, the pre-spectrometer can be hold on low potential while acting as a highly effective getter pump and acting as ion blocker.

Monitor spectrometer

The monitor spectrometer (fig. 2.12), formerly being used as the Mainz spectrometer, monitors the high voltage stability of the main spectrometer. Compared to the 70 m long beam line of the main spectrometer it features a much shorter beam line of 4.5 m. This spectrometer will continuously monitor the mono-energetic K-32 conversion line from a solid state krypton source via a silicon detector. It represents the world best high voltage calibration source [E$^+$14]. In order to protect the main beam line of KATRIN from magnetic stray fields of the monitor spectrometer setup, the latter has been installed in a separate building at 20 m distance from the main spectrometer.

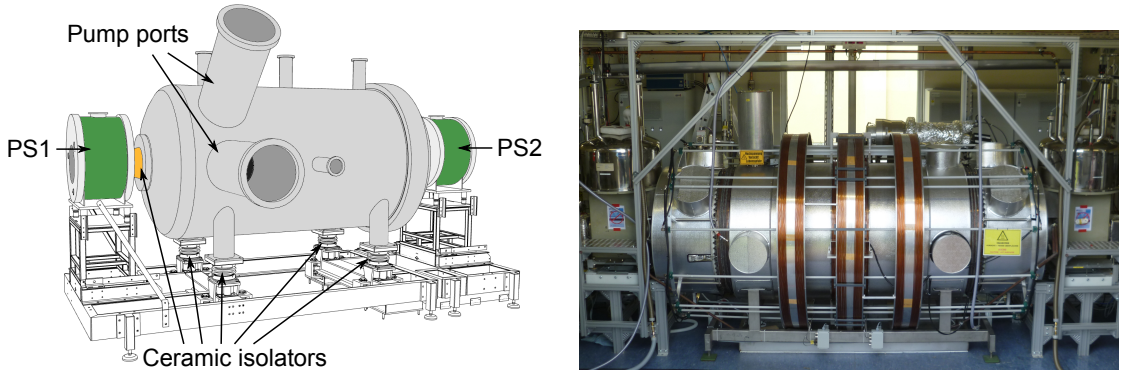

(a) Pre-spectrometer (b) Monitor spectrometer

Figure 2.12: Illustration and picture of the pre and monitor spectrometer. (a) The pre-spectrometer is mounted on a stainless-steel support structure, equipped with ceramic insulators. At each end, a superconducting magnet produces a magnetic field of $B = 4.5\,\mathrm{T}$ (labeled as PS1 magnet at upstream end and PS2 magnet at downstream end). The vessel and the inner electrodes are held on high potential $U_0 = -18.3\,\mathrm{kV}$ in order to filter low energetic β-electrons. The vessel is kept at UHV conditions at $p \approx 10^{-11}\,\mathrm{mbar}$. Sketch from [Frä10]. **(b)** A dedicated monitor spectrometer system has been installed in parallel to the KATRIN beam line in order to monitor precisely the high voltage at the main spectrometer system. This photo shows the separately installed monitor spectrometer system for KATRIN. Photo from [Erh12].

2.2.5 Focal plane detector

Transmitted electrons from the main spectrometer are counted with the focal plane detector (FPD) system (fig. 2.13) [A$^+$15a]. After passing the potential barrier at the analyzing plane, the particles are guided on magnetic field lines, produced by two super conducting magnets, onto a silicon PIN-diode wafer with a thickness of 503 µm and with a diameter of 125 µm. The dartboard pattern (fig. 2.13) of the wafer has a diameter of 90 mm, surrounded by a 2 mm guard ring and a 15.5 mm bias ring. A bias voltage of 120 V will be applied from the pixel side. The dead layer thickness of the wafer is $(155.4 \pm 0.5_{\mathrm{stat}} \pm 0.2_{\mathrm{sys}})\,\mathrm{mm}$ [A$^+$15a]. This array has been segmented into 148 pixels aligned into 12 rings in a bulls eye. The system has an energy resolution of $(2.2 \pm 0.2)\,\mathrm{keV}$ FWHM [Har15] and a timing resolution of 100 ns [Sch14].

Because a very low electron count rate is expected from the spectrometer, the detector system has been designed to feature a very low intrinsic background rate and a very high detection efficiency. After a careful selection of materials and extensive material screening, the detector background does not exceed the design goal parameter of $10^{-3}\,\mathrm{cps/keV}$ in the region of interest (ROI). Furthermore the system is shielded actively by a muon veto system and passively by a lead and copper shield.
In order to shift the electron energy spectrum into a region which is not dominated by the intrinsic detector background from fluorescence lines, and in order to reduce back scattering effects due to large electron angles, a dedicated post acceleration electrode (PAE) which is able to further accelerate the electrons by 10 keV.

To calibrate the system, this component is equipped with a ^{241}Am source and a UV-illuminated (240 nm) titanium disc. For the first source, the 59.54 keV γ peak can be used and for the latter, electrons with energies up to 20 keV can be produced as calibration source. In order to read out the pixel information, each pixel is connected via a pin to preamplifier modules. The signals are read out via plastic optic fiber from the detector electronics to the DAQ crate which converts these optical signals to electric signals. The computer running ORCA (object-oriented real-time control and acquisition) allows (beside

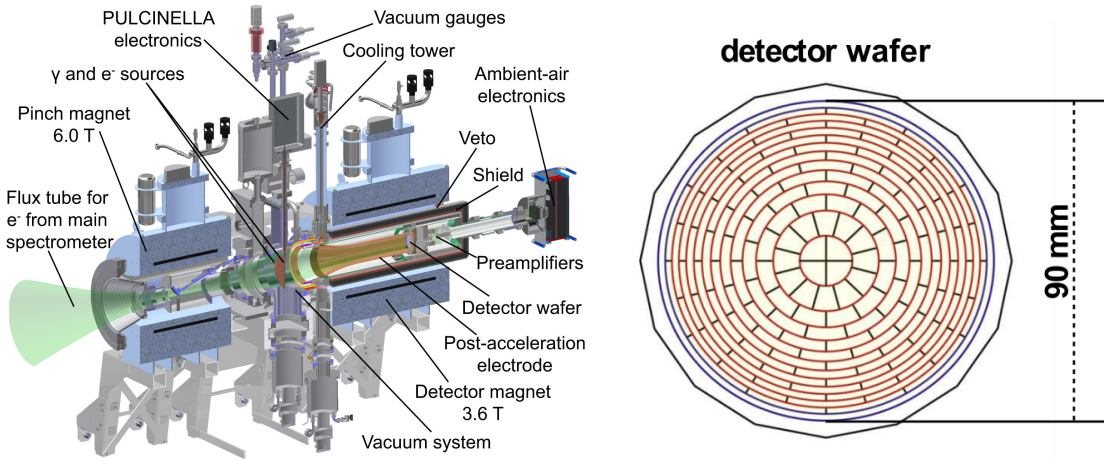

Figure 2.13: Sketch of the focal plane detector assembly and the layout of the wafer. Electrons from the main spectrometer are guided through the pinch magnet (6 T) and the detector magnet (3.6 T) onto the Si-PIN diode (right) which consists of 148 pixels of equal area (44.1 mm^2). Illustrations composed from [Frä10] and [A+15a].

low-level detector tests) the processing of input trigger signals, as well as the processing of signal rates and pixel views of the focal plane detector [A+15a]. Further information on the detector system can be found in [A+15a].

2.3 SDS measurement configuration

To investigate electron transmission systematics and background characteristics, a suite of measurements over several months of the main spectrometer together with an attached electron gun system and the detector system was performed. Initial investigations with the spectrometer and detector system (SDS) in the year 2013, in context of the first phase SDS-I, resulted in the apparatus to be optimized with respect to many items. In the frame of the second measurement phase, much more advanced studies regarding transmission of electrons and background characteristics could be performed. The second commissioning part consists of two phases: In the context of the first phase from October 2014 to March 2015, the main spectrometer was used as an un-baked system reaching a final vacuum pressure of $\mathcal{O}(10^{-10}\,\text{mbar})$. In this phase, for example the potential impact of cosmic induced muons was studied over a long-term run during the Christmas break. The main spectrometer then was baked out for the second measurement phase SDS-IIb, allowing to focus on the background characteristics in a more detailed way at a pressure of $\mathcal{O}(10^{-11}\,\text{mbar})$.

The following section highlights chosen main components of the (SDS) which are important in particular for the study of active background reduction with the electric dipole method, which is a key topic of the thesis in hand. In context of this thesis, the electron gun system is not discussed. Together with more details on the setup and operation of the e-gun at the SDS measurement phases, the reader is referred to [Beh16, Erh16, Kra16].

Section 2.3.1 presents the components of the magnet system comprising several superconducting magnets, a low-field correction system (LFCS) for shaping the magnetic flux tube and the earth magnetic field compensation system (EMCS). Furthermore the most relevant magnetic field setups of SDS-IIa and SDS-IIb are discussed here. Figure 2.14 illustrates the setup of the SDS components together with typically used magnetic field configurations.

The main spectrometer system is operated at UHV conditions which guarantees a very low distortion of the signal electrons due to residual rest gas molecules. In order to study

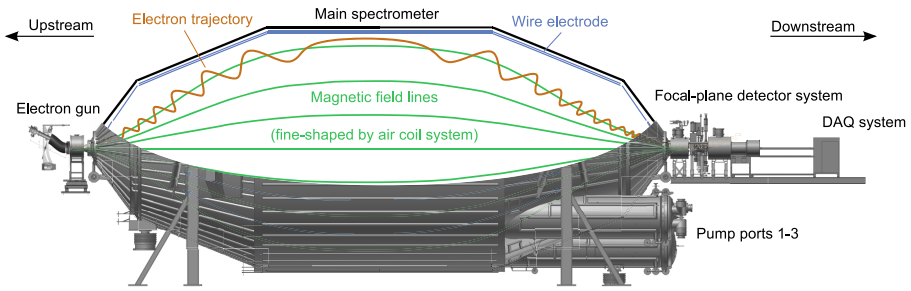

Figure 2.14: Layout of the SDS-IIa measurement setup. The electron gun is attached at the upstream end of the main spectrometer between the pre-spectrometer magnets (n.b. the PS1 magnet is not drawn here). An exemplary electron trajectory through the main spectrometer is drawn. The magnetic field lines fine-shaped by an air coil system which is shown in the next picture. At the downstream end, the detector system is attached to the UHV of the main spectrometer vessel. The UHV conditions are established by a sophisticated pumping system located in three pump ports. Sketch taken from [Har15].

the removal of stored electrons with the electric dipole method (ch. 5), a ^{220}Rn gas mantle was installed providing high statistics data sets of stored electrons. To this end, the vacuum system was equipped with a special container for artificial sources. Further key components of the vacuum system are shown in section 2.3.2.
Another major component of the KATRIN main spectrometer system its inner electrode system, which allows to fine shape the retarding potential in the analyzing plane. The inner electrode can be operated in various modes by a complex high-voltage distribution system. The hardware layout of this system is presented in section 2.3.3.
Finally this section closes with a brief sketch of the slow control and data management system in sec. 2.3.4.

2.3.1 Magnet system

The main propose of the magnet system is to adiabatically guide electrons from the main spectrometer to the detector system. The magnetic field plays a central role in context of a MAC-E filter system, since the energy resolution is directly determined by the ratio of the minimal and maximal magnetic field values. Also, in the context of the measurements presented in chapters 5 and 6, the applied magnetic field setup dictates whether a blocking potential will occur in case of an applied dipole potential configuration (cf. 5.2). In the SDS campaigns, the magnetic fields were produced by a total four superconducting solenoids located at the pre spectrometer position (PS1, PS2) and at the focal plane detector system (PCH, DET). The field is furthermore fine-shaped by normal conducting coils which surround the main spectrometer vessel (low field correction system, LFCS). In addition, the earth magnetic field is compensated by a dedicated coil setup at the before-mentioned position (earth-magnetic compensation system, EMCS). The applied magnetic fields can be monitored externally by multiple sensor systems. The setup and the performance of this system is documented in [Erh16].

Superconducting solenoids

The pre-spectrometer magnets PS1 and PS2 have a maximal magnetic field $B_{\mathrm{PS}} = 4.5\,\mathrm{T}$ each. Both coils have an inner radius of 227.5 mm and a length of 320 mm. The coils are operated at a base temperature of $T \approx 4.2\,\mathrm{K}$. Due to the operation of the electron gun in context of SDS-IIa, the PS1 was located 3.4 m from the coil center of the PS2 magnet. In this way an optimal transmission of the electrons from the electron gun was guaranteed. The e-gun system was dismounted for the SDS-IIb phase, hence the PS1 was then operated at its standard position in a distance of 16.5 m from the coil center to the analyzing plane.

At the downstream end, the pinch and detector magnets were operated to image electrons onto the focal-plane detector system. Along the entire KATRIN beamline, the pinch magnet with $B_{\mathrm{PCH}} = 6\,\mathrm{T}$ provides the strongest magnetic field. The detector magnet is located only 1.6 m in downstream direction and guides signal electrons directly onto the detector wafer, located 14 cm in downstream direction along the z-axis. In the standard configuration, the pinch and detector magnet are operated at $B_{\mathrm{PCH}} = 6\,\mathrm{T}$ and $B_{\mathrm{DET}} = 3.6\,\mathrm{T}$, the magnetic flux for this configuration is $\Phi = 210\,\mathrm{T\,cm^2}$. The coil of the pinch magnet has a length of 700 mm, the coil of the detector magnet is 900 mm long. The inner diameter of the pinch magnet coil is 454 mm, the coil of the detector magnet has a diameter of 540 mm. Both magnets are operated at $T \approx 4.2\,\mathrm{K}$. Because of multiple losses of the superconducting state (quench) of the pinch magnet before the first SDS measurement phase, the magnetic field of both the pinch and the detector magnet had to be reduced to $B_{\mathrm{PCH}} = 5\,\mathrm{T}$ and $B_{\mathrm{DET}} = 3\,\mathrm{T}$, respectively, with a resulting flux of $\Phi = 172\,\mathrm{T\,cm^2}$. After the maintenance break between SDS-IIa and SDS-IIb, the pinch magnet was replaced, so that the above mentioned design values were reached. For a magnetic field of 6 T, the pinch magnet has to be operated at 86.98 A, and the detector magnet at 56.15 A. Table 2.1 summarizes all configurations and current values.

Air coil system

Since the superconducting magnets as a stand-alone systems alone would not be able to guide electrons adiabatically from the electron gun to the detector, a large volume air coil system was installed to fine shape the magnetic flux tube between PS2 and the pinch magnet. This system has to fulfill certain requirements:

- *Magnetic guidance:* The electrons have to be guided adiabatically from the source (electron gun in SDS operation) to the detector.
- *Transmission condition:* The magnetic field has to fulfill the transmission condition, hence it has to be minimal at the center. Furthermore the magnetic field has to be maximal homogeneous to be able to define a transmission function.
- *Background:* In context of the SDS measurement phase, a volume-dependent background component was identified (cf. sec. 6.1). As a result, the volume of the flux tube, which can be controlled by the different air coil currents, is directly proportional to the background rate. In addition the magnetic field acts as the dominant shield against secondary particles produced at the vessel wall, since background electrons cannot easily travel on tracks perpendicular to the direction of the magnetic field lines.

To meet all requirements for the adiabatic transport of signal electrons, two independent air coil systems were installed, surrounding the main spectrometer vessel [GDL+13, Wan09]. Figure 2.15 shows a CAD-drawing of the main spectrometer including all air coil systems.

The earth magnetic field compensation system (EMCS) consists of two independent current loops in order to compensate the horizontal and vertical earth magnetic field component with $B_{\mathrm{hor}} = 5\,\mu\mathrm{T}$ and $B_{\mathrm{vert}} = 43.6\,\mu\mathrm{T}$. In order to produce a maximal homogeneous compensation, the current loops are arranged as cosine coil [GDL+13] which are operated in the course of SDS at 50 A and 9 A for the vertical and horizontal compensation of the earth magnetic field, respectively.

The second system is called low field correction system (LFCS) and fine shapes the magnetic flux tube further in order to prevent the magnetic field lines from the beam tube vessel wall components. The main spectrometer is surrounded by a total of 14 coaxially aligned coils with a diameter of $d = 12.6\,\mathrm{m}$. Each coil can be operated up to a current

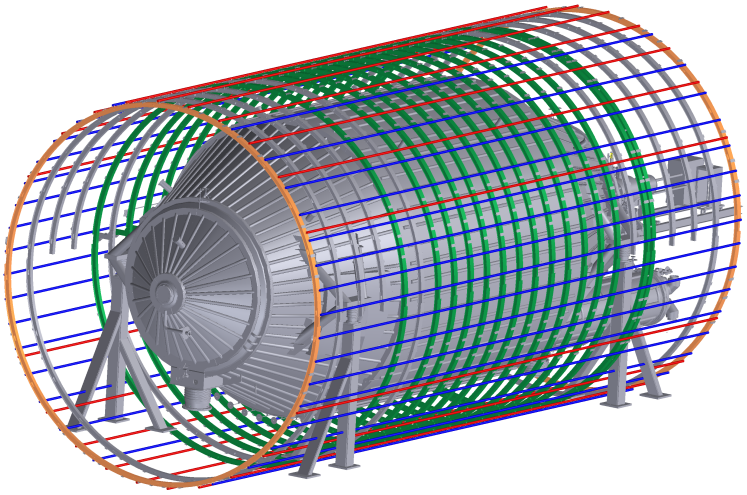

Figure 2.15: CAD-drawing of the main spectrometer system. The illustration shows the low-field correction system LFCS in green color and the two different the current loops of the earth magnetic field compensation system EMCS. The horizontal loops are colored in red and the vertical loops are colored in blue color. Drawing provided by [Rei12].

to 100 A allowing to adjust the minimal magnetic field in the flux tube from 0.33 mT to 1 mT. The magnetic field is directed in upstream direction, whereas coil no. 14 is operated in opposite current direction in order to balance the inequality between the PS2 (3.5 T) and pinch (6 T) stray fields.

The current of all coils is fed through a flip-box system with H-bridges, allowing to reverse the polarity of all coils within shortest time scales ($\mathcal{O}(10\,\mathrm{ms})$). In this way, the magnetic field lines can touch the vessel wall for a very short time scale. Besides the electric dipole method, stored particles can thus actively be removed from the flux tube. The realization and test of the flip box system in the context of the SDS measurements is documented in [Beh16].

In order to monitor the magnetic field, multiple sensor systems are installed surrounding the tank geometry. In this way, reliable and precise measurements of the applied magnetic field can be performed and the real-time value readout has been seamlessly integrated into the KATRIN software *Kasper*. The setup and investigation of magnetic field is discussed in [Erh16].

Magnetic field configurations

In the following the different magnetic field settings as used throughout this thesis are listed in table 2.1. For each setting the currents of the LFCS coils was optimized with the program *KTrap* from the Kasper simulation suite [Gro15]. The different settings either have a global minimum in the analyzing plane or have two global minima at $z < 0\,\mathrm{m}$ and $z > 0\,\mathrm{m}$. At $z = 0\,\mathrm{m}$ the two-minimum solutions have a local maximum [Wan13]. The two-minimum solution in general forms a more homogeneous flux tube: The field lines are more parallel to the vessel than in case of a corresponding one minimum solution which shields better against secondary electrons from the tank wall.

For fine shaping the magnetic flux tube, a total of 16 coils current values has to be set according to the desired flux tube geometry. The x- and y-components of the earth magnetic field compensation system have been chosen as common for all flux tube configurations. All settings in table 2.1 establish a symmetric magnetic flux tube.

Table 2.1: Overview of magnetic field settings used for this work. On top, the current of the superconducting solenoids are denoted, followed by the configuration of the air coil system. The number in brackets indicates if the configuration has a single global minimum (1) in the analyzing plane or has a dual field minimum (2) in the flux tube. Furthermore the configurations differ from the measurement phases SDS-IIa and SDS-IIb. All currents in this table are given in Ampere. Commonly for all configurations, the EMCS has been operated at 50 A vertical current and 9 A horizontal current.

Magnet	3.8 G (IIa, 1)	5 G (IIa, 2)	3.8 G (IIb, 2)	5 G (IIb, 2)
PS1	104.0	104.0	0.0	157.0
PS2	156.0	156.0	157.0	157.0
PCH	72.625	72.625	86.98	86.98
DET	46.795	46.795	56.154	56.154
LFCS coil 1	69.75	52.94	79.9293	52.942
LFCS coil 2	53.98	15.17	35.985	60.9684
LFCS coil 3	80.95	33.73	19.5684	33.8198
LFCS coil 4	54.88	34.47	22.0601	34.4713
LFCS coil 5	5.787	61.83	21.7321	61.8312
LFCS coil 6	8.284	75.65	34.7829	75.2128
LFCS coil 7	27.05	27.05	72.9043	27.0516
LFCS coil 8	4.018	49.49	64.2901	51.4924
LFCS coil 9	2.588	64.38	36.2351	66.3813
LFCS coil 10	39.16	46.64	26.7536	50.6413
LFCS coil 11	60.21	52.53	22.7623	54.5316
LFCS coil 12	39.16	29.78	33.2634	35.7811
LFCS coil 13	40.98	52.21	33.7738	56.1535
LFCS coil 14	-1.334	-47.82	-49.7485	-42.8211

2.3.2 Vacuum system

In order to provide an undistorted transmission of signal electrons, the pressure of the 1240 m^3 volume of the main spectrometer vessel has to be kept at the level of $\mathcal{O}(10^{-11}$ mbar). The main challenge arises from the outgassing of hydrogen from the large stainless steel surface making hydrogen the dominant part of rest gas species in the 23.2 m-long vessel. In context of [A+16b], the outgassing rate was estimated to be $1.4 - 2.5 \times 10^{-12}$ mbar ℓ/s. In order to maintain excellent UHV conditions, the main spectrometer vessel is equipped with three pump ports at the downstream side. Each port has a diameter of 1.7 m and a length of 3 m. Whereas the pump ports are installed in the bottom region of the main spectrometer, 11 additional ports are installed at the upper part of the vessel. These ports are used to provide electrical feedthroughs to the inner electrode system, vacuum gauges, a burst disc and a gas-inlet system. The detector system can be separated from the main spectrometer volume via the operation of a dedicated flapper valve without breaking UHV conditions. Because of a leak in the flapper mechanism prior to SDS-II, the valve had to be removed. Therefore, a bake-out at high temperatures of the main spectrometer vessel could not take place prior to SDS-IIa. As a consequence, the projected SDS-II measurement phase had to be separated into to two sub-phases: The first measurement campaign SDS-IIa was intended to perform measurements with a non-baked spectrometer, whereas after repair and re-installation of the before-mentioned flapper valve mechanism a bake-out of the system was performed prior to the SDS-IIb campaign.

In order to achieve UHV conditions in the main spectrometer vessel, an initial pump down

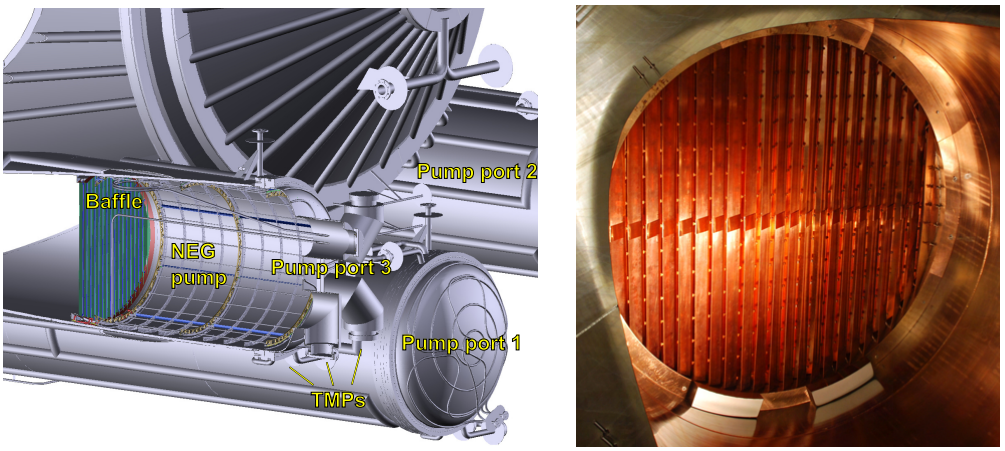

Figure 2.16: Photo and illustration of pump port 3 and baffle system. Left: The illustration shows a cross section of pump port 3, in particular the NEG pump and the baffles. **Right:** The photograph of the baffle system shows the 22 V-shaped copper stripes protecting the main spectrometer volume against Radon from the getter material.

sequence is performed with a temporarily installed screw pump with a speed of $630\,\mathrm{m}^3/\mathrm{h}$. Three additional vacuum pumps are operated successively to reach UHV conditions for the pump down of mainly hydrogen from the volume. The FPD system is equipped with its own set of cryogenic pumps in order to establish UHV and high vacuum conditions in different areas of the detector system.

Inside the pump ports 2 and 3 of the main spectrometer, a total of 1000 *SAES St707* non-evaporated getter strips, each 1 m long was installed. The getter material requires a thermal activation in advance to be fully operable at a pumping speed of $10^6\,\ell/\mathrm{s}$. Over the course of the first SDS phase in 2013, the entire vessel was baked at a temperature of $T \approx 300°C$. As a result, the getter stripes were activated via thermal radiation. During this operation several of the HV-carrying CuBe rods, installed to feed the inner electrode system, suffered from a thermal deformation. As a result, the vessel had to be baked out at a maximal temperature of $T \approx 200°C$ before SDS-IIb. Since this low temperature is not sufficient to activate the getter material, the strips were activated by a separated electrical heating system achieving temperatures of $T \approx 400°C$ by Ohmic resistance.
Unfortunately, the getter material emanates ^{219}Rn atoms which can enter the sensitive flux tube volume. In this region, the unstable atoms will undergo α-decay which is accompanied by electron emissions, resulting in a non-negligible background component due to stored particles. In order to prevent the atoms from entering the volume, a baffle system was installed between the vessel volume and the getter material [Gör14]. Figure 2.16 shows on the left side the design of the pump port region and on the right a photograph of the baffle system.
The baffle system consists of 22 V-shaped blades which are held at LN_2 temperature. The radon atoms are thus prevented from entering the flux tube by cryosorption and deliver a pumping speed of $3.75 \times 10^5\,\ell/\mathrm{s}$. Over the course of SDS-II, the baffle system was operated together with the inner electrode system on high voltage of the system was equipped with specific insulators.
Finally a pressure of up to $p \approx 3 \times 10^{-10}\,\mathrm{mbar}$ was reached over the course of SDS-IIa and $p \approx 6 \times 10^{-11}\,\mathrm{mbar}$ for SDS-IIb [Har15].

2.3.3 High-Voltage system

Over the course of neutrino mass measurements, the main spectrometer vessel is kept at high potential, whereas all beam-line elements up to the pre-spectrometer and the

detector are grounded. In order to fine shape the electric potential to obtain a perfect axially-symmetric electric potential and thus the best transmission characteristics, a wire electrode system is installed inside the vessel. A total of 248 wire electrode modules is installed, which in total have 23000 wires. Along the beam axis, the modules are aligned in 16 different rings. The flat cone and the cylindrical parts can be operated in a dual wire layer mode. The wires are quasi massless, with the inner wires having a diameter of 200 µm and the outer layer of 300 µm. The steep cone rings are equipped with a single wire layer. At both ends an anti-Penning and a ground electrode are installed. Both elements are formed as solid conical tubes. Unfortunately, during the bake out of SDS-I, a variety of short-circuits between the inner and outer wire layers appeared due to thermal deformation of the copper beryllium (CuBe) rods of the HV feedthrough system. Although several short-circuits could be repaired [D$^+$14], the main spectrometer has to be operated in a single wire-layer mode, also in the flat cone and cylindrical region. Due to the excellent magnetic shielding of the MAC-E filter, the shielding of the wire electrode system is no longer necessary to reduce wall background. Figure 2.17 shows the layout of the electrode system.

The high voltage is distributed by a dedicated system of multiple power supplies. A base power supply elevates the vessel and all electrode structures to a potential of up to −35 kV. In order to elevate the wire electrode system to a more negative potential than the surrounding vessel hull, a common power supply further elevates the potential by −2 kV on the vessel potential. Optionally, the inner electrode can be operated in a dipole mode. To this end, two independent power supplies for the dipole mode can lift the potential further by −1 kV, individually for the eastern and western electrode parts. Whereas the potentials typically will be applied statically to the electrodes, the dipole potentials can be operated in a pulsed mode for active background mitigation. The trigger signal for this mode will be optically fed to the FPD system for precise timing information. The optimization of the transmission characteristics of electrons require to fine tune the potentials in different modules. For this reason an individual offset potential of 500 V can be set to each ring individually for the east and west parts. Figure 2.18 illustrates the setup of the different power supplies [Kra16].

2.3.4 Slow control and data acquisition

The KATRIN data acquisition system processes experimental data from over of thousands of different sensors and control units in real time. The manifold sub-systems are managed by different slow-control systems: The Simatic PCS-7 system controls safety relevant systems, like different sensors for the main spectrometer vacuum or the LN_2-cooled baffle system. Compact field point devices running with LabVIEW applications, control other non-safety relevant systems, like the air coils or the magnetic field sensors. The high voltage system is controlled by both the PCS-7 system and compact field point devices. Whereas operators here can set here arbitrary values with the PCS-7 system, only defined values can be set with the compact field points. In this way the HV can be controlled safely without exceeding experimental boundaries. All different values can be set by the user via ORCA. This software is running on MacOS and allows the easy control and read-out of different sub-systems. Due to ORCA the experimentalist can easily automatize measurements by writing flexible scripts. The measured data is stored in multiple SQL-based data bases, which can be accessed either via the advanced-data extraction infrastructure (ADEI) or via the *KaLi* C++ library. The ADEI system extracts the data from the data base, reprocesses it and allows to access it via a web-based application. Whereas the ADEI system does not apply automatically calibration tables to data automatically, the data extraction via the KDBServer allows to automatically obtain calibrated data. This data can then be accessed via the *KaLi* library in context of a C++ program by the user.

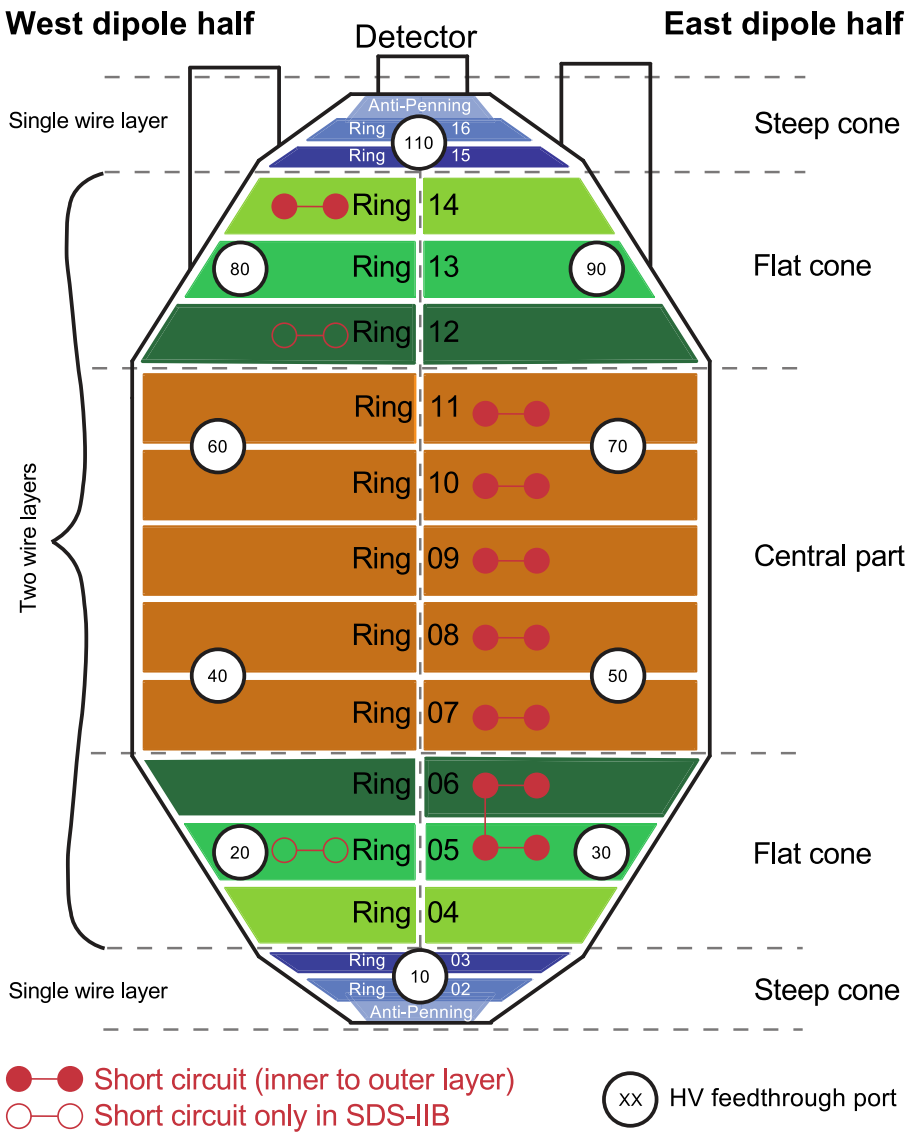

Figure 2.17: Sketch of the inner electrode system inside the main spectrometer. The 15 inner electrode modules are split in different rings along the beam axis. Whereas the steep cones are built with one single wire layer, all other electrode modules consist of two wire layers. In context of the vacuum bake-out before the SDS-I and SDS-IIb, several short circuits appeared mainly between inner and outer layer, but also between different rings. Figure taken from [Har15].

Figure 2.19 illustrates the data flow between slow control, data storage and extraction with the different systems [Kle14, CBKV10, H^+].

2.3.5 Summary of technical improvements for SDS

In the context of the second measurement phases SDS-IIa and SDS-IIb, the SDS apparatus was improved in the following areas: The air coil system was augmented by different field monitoring systems in order to set and check the different applied settings. In this way, a reliable magnetic field setup was established with a high traceability. The vacuum system was augmented by feedthroughs for the baffle system in order to profit from this very important passive reduction technique at high potentials. For the investigation of the efficiency of the baffle system and further active background reduction systems, a container for housing of artificial sources was attached to the vacuum system to artificially increase stored-particle background. In this way the effect of active mitigation strategies and the

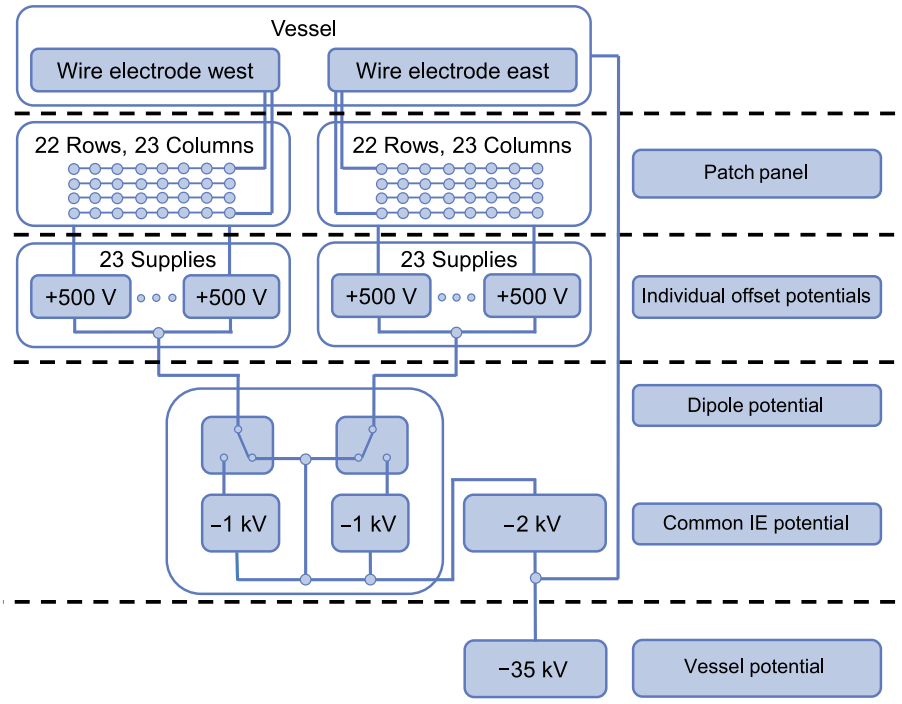

Figure 2.18: Voltage distribution for the inner electrode system. A dedicated high voltage power supply provides a voltage up to −35 kV to the main spectrometer vessel. An additional negative offset, which is based on the vessel potential, is applied to the entire inner electrode. Upon this potential further offsets can be applied to the eastern and western half of the inner electrode separately. Fine adjustments can be applied through positive offsets which can be set individually to the electrodes rings and to the different sides (east or west). Illustration adapted from [Kra16].

efficiency of the baffle system could be studied in great detail.
Furthermore the high voltage subsystems were augmented by a further common potential, which guarantees stable set points of the high voltage, which prevents from floating voltages.
In order to control the timing of the pulsed electric dipole mode, which is important in the context of active background reduction, the read back of the pulse signal is now fed into the DAQ systems via optical fibers in order to extract timing information of the dipole pulse with a very low latency.

2.4 Limit of the electron antineutrino rest mass

In the following, the extraction of a value (and uncertainty) for the squared anti-neutrino mass parameter from the observed shape of the β-electron energy spectrum close to the tritium end point region will be explained concisely. The topic is divided into three sections: First the design parameters of the experiment are discussed together with the expected systematical error contributions. This is followed by the concept of measurement time optimizations, to minimize the statistical error, before finally the estimation of the squared neutrino mass using χ^2 minimization is discussed. These two topics are crucial for a coherent summary of the analysis principle of the experimental data. The choice of a particular measurement strategy, which leads to an optimized sensitivity on the neutrino mass fit parameter given the recently investigated background level will be motivated in the following.

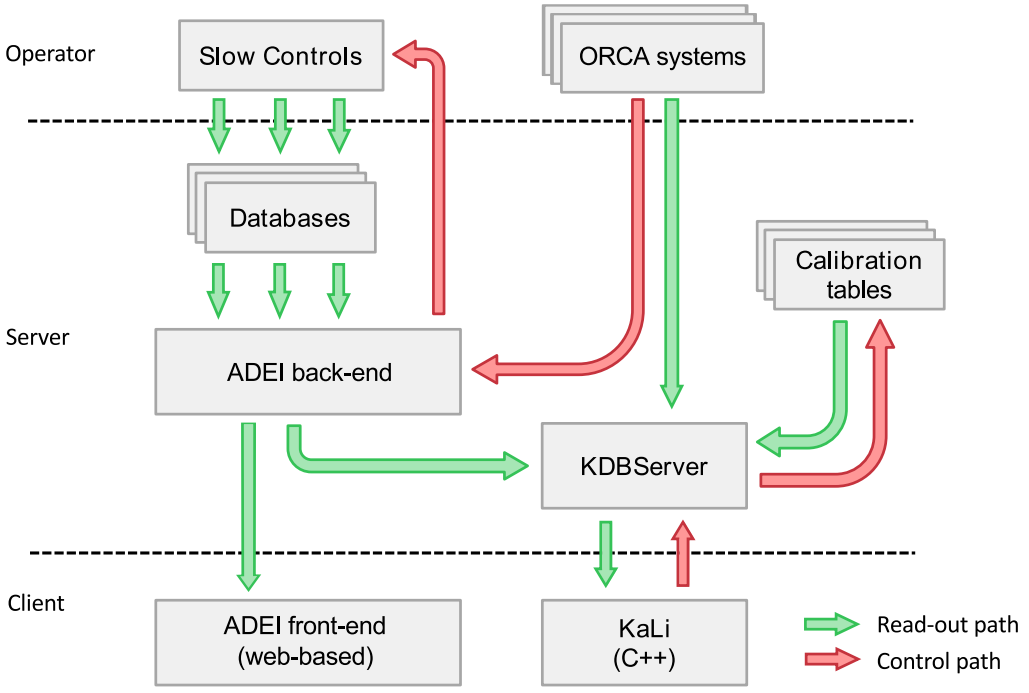

Figure 2.19: Sketch of SDS slow-control system and data paths. The measurement operator can set slow control values either via the ADEI system or ORCA. The experimental data is been stored on a server, where automatically the calibration values are applied. In order to access the measured data, either the ADEI web pages or the *KaLi* C++ library can be used. Sketch from [Har15].

2.4.1 Design parameter of the KATRIN experiment

The goal is to reach a sensitivity on the neutrino mass of 200 meV at 90 % confidence level (C.L.) after three years of net measurement time. This design goal exceeds the sensitivity of the former neutrino mass experiments in Mainz [K$^+$05] and Troitsk [A$^+$11c] by a factor of 10. For this challenging goal, several design parameters need to be fulfilled for the experimental operation. The following experimental key parameters will have a direct influence on the neutrino mass sensitivity:

1. **Source luminosity:** A high signal rate close to the tritium endpoint is needed, because the signal count rate of β-electrons with energy E close to the endpoint E_0 will decrease with $(E - E_0)^3$. A high signal electron number is directly proportional to the amount of tritium molecules. This value is proportional to the visible source area, the tritium purity and the column density. As described in [A$^+$04], the optimal value for the column density is $\rho d = 5 \times 10^{17} \frac{\text{molecules}}{\text{cm}^2}$ in order to keep both inelastic scattering probabilities and the following systematic uncertainties in the source small. The source is operated with a magnetic field is $B_S = 3.6\,\text{T}$, which in view of the maximal magnetic field strength is $B_{\text{max}} = 6\,\text{T}$, results in an effective visible source area of $A_S = 31.8\,\text{cm}^2$. The Tritium Laboratory Karlsruhe (TLK) is expected to provide a tritium gas purity of $\epsilon_t = 95\,\%$, which exceeds former tritium β-decay experiments significantly.

2. **Energy resolution:** In order to achieve the targeted design sensitivity of 200 meV, the energy resolution has to be improved by a factor of five compared to the former experiment in Mainz to $\Delta E = 0.93\,\text{eV}$ for an electron energy of $E = 18.6\,\text{keV}$, as the energy resolution given by $\frac{\Delta E}{E} = \frac{B_{\text{AP}}}{B_{\text{max}}} = \frac{1}{20000}$. From magnetic flux conservation considerations a spectrometer diameter of 10 m (including safety margins) is needed

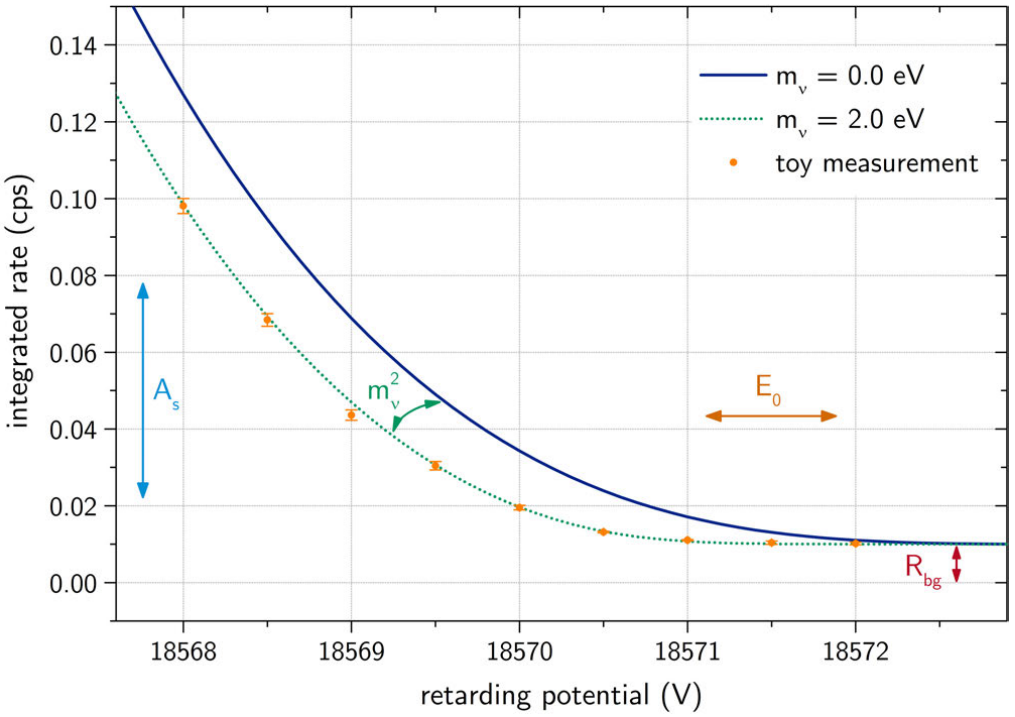

Figure 2.20: Illustration of the spectral fit due to the four free parameters E_0, $m^2_{\nu_e}$, R_S and R_b. Graph kindly provided by M. Kleesiek.

to fulfill the design requirements. Consequently, the analyzing plane covers a surface of 63.6 m^2.

3. **Background rate:** The goal of KATRIN is to obtain a 100 times larger signal electron rate at the endpoint than preceding experiments, together with a background rate of $R_{\mathrm{bg}} \leq 10\,\mathrm{mcps}$. The commissioning measurements however have revealed, that specific processes inside the large spectrometer volume of 1250 m^3 contribute a larger background, than anticipated (cf. ch. 6).

2.4.2 Sensitivity calculation

The KATRIN experiment will scan the endpoint region of tritium β-decay in an integrated mode. In this case, the measured total count rate depends on the retarding voltage U_0, the (constant) background rate $\dot{N}_{\mathrm{bg}}$, the value of the tritium endpoint E_0, and the squared mass of the electron anti-neutrino $m^2_{\overline{\nu}}$ (fig. 2.20). The total rate of measured signal electrons at retarding potential U_0 can then be analytically expressed as

$$\dot{N}_S(qU_0, E_0, m^2_{\overline{\nu}_e}) = N_{\mathrm{tot}} \cdot t_U \cdot \int_{qU_0}^{E_0} \frac{\mathrm{d}N}{\mathrm{d}E}(E_0, m^2_{\overline{\nu}_e}) \cdot R(E, qU_0)\mathrm{d}E, \tag{2.15}$$

where $N_{\mathrm{tot}} = A_S \cdot \rho d \cdot 2\epsilon_T$ denotes the number of tritium nuclei and $R(E, qU_i)$ the response function. An energy-independent Poisson-distributed background component $\dot{N}_{\mathrm{bg}}$ is added to the total signal electrons rate. With the multiplicative correction factors R_S and R_b, the theoretically expected total signal rate is given by

$$\dot{N}_{\mathrm{theo}}(qU_0, E_0, m^2_{\overline{\nu}_e}, R_S, R_b) = R_S \cdot \dot{N}_{\mathrm{S}}(qU_0, E_0, m^2_{\overline{\nu}_e}) + R_b \cdot \dot{N}_{\mathrm{bg}} \tag{2.16}$$

After multiplication of the theoretically calculated count rates with a specific measurement time, the mean counts for signal and background can be obtained. In general, an optimized measurement time distribution is used, which allocates the time interval spent at a specific

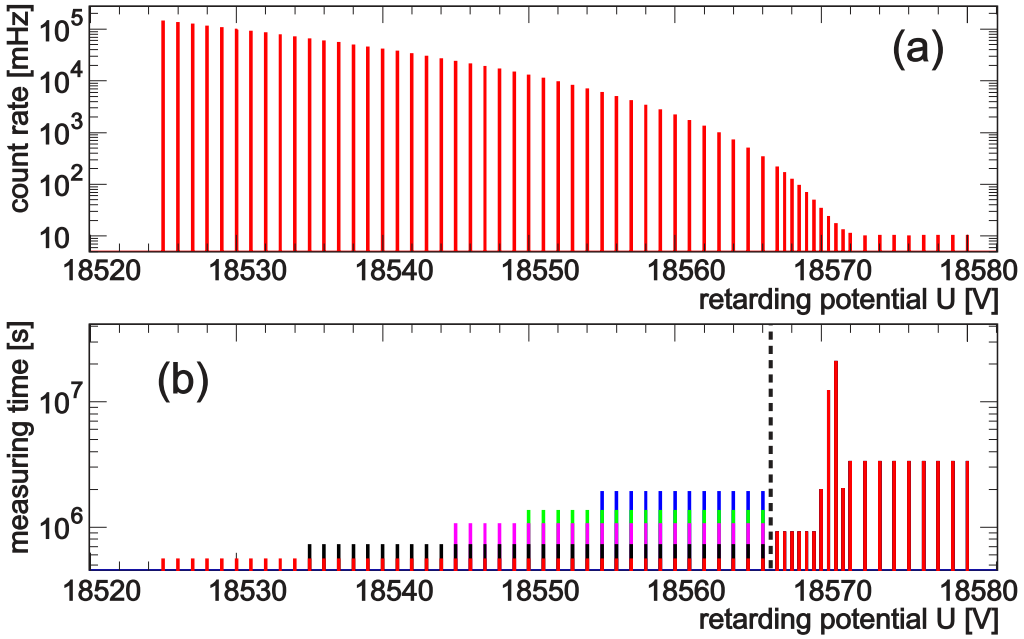

Figure 2.21: Plot of the measurement time distribution. The graphs shows measuring time at each retarding potential as proposed in [A+04] and the expected count rates. The measurement time distribution directly affects the statistical $m_{\overline{\nu}_e^2}$ uncertainties. From [A+04].

retarding potential. The resulting data set is analyzed in a χ^2-fit, where the quadratical differences between observed and theoretically predicted total event counts are minimized. This yields estimates for the four free fit parameters, namely the endpoint energy E_0, $m^2_{\overline{\nu}}$, and the normalization constants R_s and R_b for both signal and background electrons:

$$\chi^2(E_0, m^2_{\overline{\nu}_e}, R_S, R_b) = \sum_i \left(\frac{N_{\mathrm{meas}}(qU_i) - N_{\mathrm{theo}}(qU_i, E_0, m^2_{\overline{\nu}_e}, R_S, R_b)}{\sigma_{\mathrm{meas}}} \right)^2 . \tag{2.17}$$

Here a summation over all retarding potentials i as given by the measurement time distribution has to be performed. The quadratical differences are normalized to the variance of the measured counts with $\sigma_{\mathrm{meas}} = \sqrt{N_{\mathrm{meas}}}$. In the following the experimental data is denoted as N_{meas}.

The design goal of the KATRIN experiment is to investigate neutrino masses with a sensitivity of $m_{\overline{\nu}_e} = 200\,\mathrm{meV}$ at 90 % C.L.

The sensitivity follows from the statistical and systematical uncertainties on $m^2_{\overline{\nu}_e}$. For three years of net measurement time, the statistical uncertainty for nominal source and spectrometer settings is estimated to $\sigma_{\mathrm{stat}}(m^2_{\overline{\nu}_e}) = 18 \times 10^{-3}\,\mathrm{eV}^2$. Here, the measurement time distribution has a key influence on the statistical error. The equivalent budget of systematic uncertainties is expected to be constrained to be $\sigma_{\mathrm{sys}}(m^2_{\overline{\nu}_e}) = 17 \times 10^{-3}\,\mathrm{eV}^2$. Both errors are be summed up quadratically to the total uncertainty

$$\sigma_{\mathrm{tot}}(m^2_{\overline{\nu}_e}) = \sqrt{(\sigma_{\mathrm{stat}})^2 + (\sigma_{\mathrm{sys}})^2} = \sqrt{0.0017\,\mathrm{eV}^2 + 0.0018\,\mathrm{eV}^2}. \tag{2.18}$$

Since the expected value for the observable $m_{\overline{\nu}_e})^2$ is expected to show a Gaussian distribution (see sec. 3.5), the 90 % C.L. for $m_{\overline{\nu}_e}$ can be written in terms of the total uncertainty σ_{tot}:

$$S_{m_{\overline{\nu}_e}}(90\,\%) = \sqrt{1.645\ \sigma_{\mathrm{tot}}(m^2_{\overline{\nu}_e})}. \tag{2.19}$$

(The χ^2 function can either be minimized taking toy measurement data (cf. 3.5.2) or a experimental data set.)

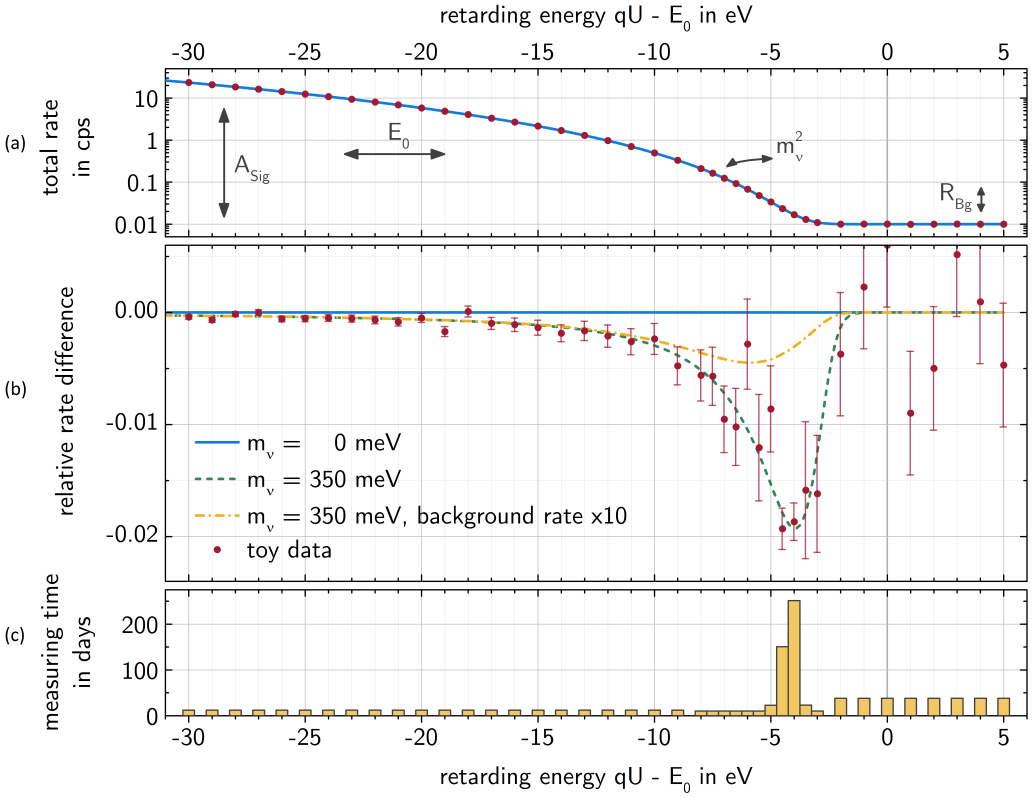

Figure 2.22: Effect of increased background in measurement time distribution. This plot shows the integrated spectrum fit (a), the fit of simulated data toy measurements (b) and the resulting measurement time distribution (c). The outcome of this calculation is that in case of an increased background level, the optimal scanning region is located deeper in the spectrum. Picture kindly provided by M. Kleesiek.

2.4.3 Measurement strategy and sensitivity optimization

Currently the experiment is facing a background level which is about a factor 50 above the design goal of 10 mcps. In general the effect of an increased background limit leads to a shift of the region where the signal-to-background ratio is maximal, and where the bulk of the measurement time should be spent. In figure 2.22 (b) the impact of a higher background is visible, the region where the spectral distortion is maximum then shifts further away from E_0, i.e. to lower energies.

The origin of this background has been reveled to be highly excited hydrogen atoms, which are produced at the spectrometer walls, and propagate into the sensitive flux tube. There the atoms are ionized by the thermal black body radiation resulting in low-energy electrons, which are indistinguishable from signal electrons. This topic is further discussed in [Dre17, Har15, Tro17]. In case the current background level would persist, a new measurement strategy will have to be adapted which results in a neutrino mass sensitivity of 240 meV in spite of the much elevated background level. The strategy consists of three steps:

1. As discussed in [OW08], the majority of the measurement time should be spent in a region with signal to background ratio of $\approx$ 2:1. After adjusting the measurement time distribution, a sensitivity of 290 meV can be achieved.
2. A further decrease of the statistical uncertainty can be achieved by enlarging the

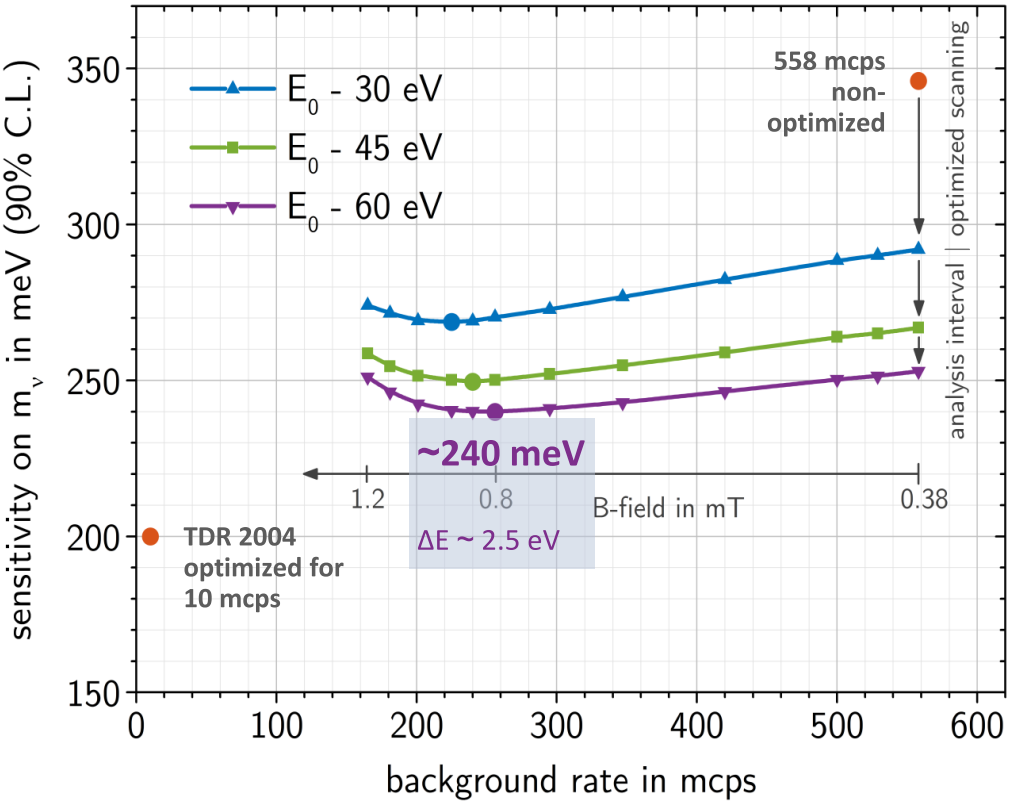

Figure 2.23: KATRIN sensitivity for elevated background level (factor 50) without active mitigation. Applying the design parameter to the statistical analysis, a sensitivity of 340 meV would be achieved. The plot shows how a lower sensitivity can be achieved by different mitigation strategies. (1) First the measurement time distribution in order to optimize for a signal to background ratio of 2:1, a sensitivity of 290 meV will be achieved. (2) The scanned energy spectrum will be enlarged, measurement points deeper in the spectrum will be analyzed. By this strategy, the statistical sensitivity will be decreased while the systematical uncertainty gets increased slightly. (3) The volume scaling of the background will be exploited and the sensitive flux tube volume will be decreased resulting in an increased energy resolution of $\Delta E = 2.5\,\text{eV}$. All individual modifications result in a final sensitivity of approximatively 240 meV under the assumption that the background cannot been actively reduced. Figure taken from [Val16].

analysis interval. The measurement interval then includes points deeper in the spectrum, as shown in figure 2.23. The increase of the systematic source errors due to electronic final states are expected to be compensated by a better source modeling.

3. Because the remaining background component correlates with the volume of the magnetic flux tube, a final sensitivity down to 240 meV can be achieved by compressing the active flux tube volume with a higher magnetic field value in the analyzing plane. However, as the error of the magnetic field is proportional to its strength, a better knowledge of the magnetic fields is required [Erh16, Ost16].

In general, the optimization of the neutrino mass sensitivity results from a trade-off between statistical and systematical errors. All above mentioned strategies are illustrated in figure 2.23.

CHAPTER 3

Simulation and analysis software

For the successful operation of the KATRIN experiment with its many diverse components, a solid body of software tools is indispensable to support the assembly and operation of the apparatus. A prime example is given by the challenge to compute and study electron trajectories through the entire beam line in order to understand and to optimize the transmission of signal electrons from the tritium source. Moreover, a large number of potential background processes have to be simulated to investigate and to solve the experimental signatures and underlying physical processes. For these purposes, the KATRIN collaboration has developed the open-source tracking software *Kassiopeia*, which can compute particle trajectories with highest precision in arbitrary complex geometries.

When computing particle trajectories over large distances in complex field geometries, it is essential to compute electromagnetic fields with highest accuracy and speed, either in two-dimensional approximated models or in realistic three-dimensional models. For this particular scope, the software tool *KEMField* has been developed. *KEMField* is based on the Boundary Element Method (BEM) which profits from the ability to compute electrostatic quantities from small-scale electrodes, which are embedded in large-scale structures in a highly efficient way. *KEMField* is furthermore equipped with the highly efficient Robin Hood algorithm [LSA06] which allows to solve higher dimensional linear BEM equation systems with a modest memory footprint while keeping a very high level of accuracy.

For tracking and field calculations with *Kassiopeia* and *KEMField*, a common geometry description of the different components of the KATRIN beam line is needed to guarantee consistent simulation results. The software module *KGeoBag* provides this ability by describing arbitrary geometries via XML input files and forwarding this information to either the navigation tools of particles within *Kassiopeia* or to the discretization tools which pack geometry input into small mesh elements for potential and field computations with *KEMField*.

All three presented tools are incorporated into the global KATRIN simulation and analysis package *Kasper*, which consists of programs for the analysis of detector data [Not14], the management of the KATRIN data base with slow control and run data and the execution of Monte Carlo toy measurements to investigate the influence of different experimental and physical parameters on the neutrino mass sensitivity [Kle14].

The first part of this chapter introduces the different software elements of the *Kasper* framework and gives an overview of their main features. Chapter 3.2 describes the particle tracking software *Kassiopeia* and its key features. This is followed in section 3.3 by an in-depth description of the definition and management of geometry models provided by the software *KGeoBag*, together with chosen examples. Special emphasis in this chapter is

given to the electromagnetic field calculation: Beginning with the concept behind magnetic field computation in section 3.4.1, the numerical computation of electric fields is detailed in sections 3.4.4 and 3.4.5. After discussing complex electromagnetic field calculations, the speed up of electrostatic field computation through code execution of special parallelized kernels on graphical processor units is reviewed in 3.4.6. The chapter closes by outlining the remaining software tools, in particular the calculation of the β-decay spectrum and Monte Carlo toy measurements. These packages are essential for a reliable estimate of the neutrino mass sensitivity in section 3.5.
All code examples and explanations mentioned in this chapter refer to the software code which is provided in the branch `dhilk_thesis` in the KATRIN GIT Repository[1]. In future the code will be incorporated into the main develop branch of this repository.

3.1 Overview of the software toolset

The common software framework *Kasper* is based on the C++ language and has recently been augmented with features from the C++11 standard. All elements of *Kasper* run on MacOS as well as on Linux operating systems and can be compiled individually with the CMake build system [MH03]. For specific tasks, external libraries have to be linked against the software: For linear algebra routines or unit testing for example, the boost library [DAR14] can be used. The ROOT data analysis library [A$^+$09] is used for storing experimental and simulated data as well as for the two-dimensional visualization of geometries and particle tracks. The three-dimensional visualization of simulated particle tracks or geometry models is bases on the Visualization Toolkit (VTK) library [SML06]. Furthermore, *Kasper* allows to exploit capabilities of parallel platforms ([NBGS08, SGS10, MPI94]) in order to boost computation speed. In the framework of *Kasper*, each module can be compiled and linked separately, even without external libraries. This feature is very important in order to compile *Kasper* on computers without libraries. As briefly mentioned in the introduction, each submodule of *Kasper* fulfills a specific task related to the simulation of the experiment and the analysis of data. In the following all submodules and their main features will be listed:

- Kommon: Collection of libraries for reading input and writing output files, for definition of mathematical and physical constants, for flexible random number generation and further mathematical utilities, like numerical integrators.
- KGeoBag: Organization of geometrical shapes to navigate particle trajectories in complex geometries and computation of electromagnetic fields [Cor14].
- KEMField: Library for the computation of electromagnetic potentials and fields [Cor14].
- Kassiopeia: Monte Carlo simulation program for particle tracking [Fur15, Gro15].
- KSC: Package containing different KATRIN-specific code additions for several modules, like geometry definitions or special extensions for the tracking module.
- SSC: Computation of differential and integrated β-decay spectra of gaseous tritium [Höt12].
- KaFit: Collection of statistical tools and minimizers for investigation of the neutrino mass sensitivity [Kle14].
- KaLi: Data library for KATRIN slow control and run data by a web service layer [Kle14].

[1] `https://nuserv.uni-muenster.de:8443/`

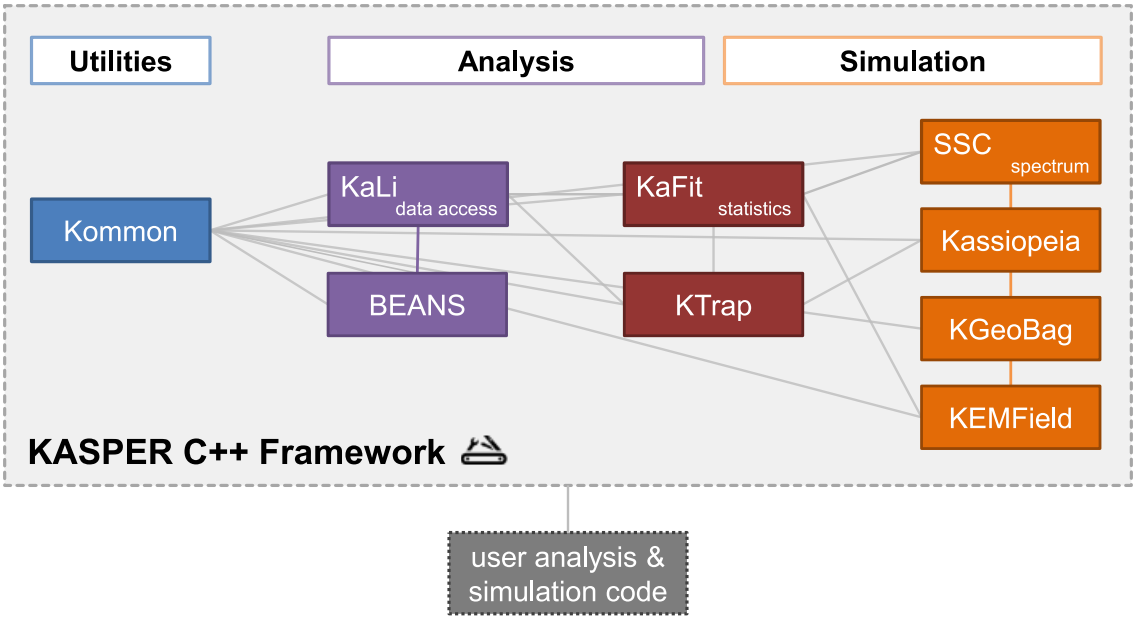

Figure 3.1: Overview of all *Kasper* submodules. The interdependence between the modules is indicated by lines. Figure kindly provided by M. Kleesik.

- BEANS: Toolset for the readout and analysis of data by the focal plane detector [Not14].
- KTRAP: Collection of programs for the analysis and simulation of the spectrometer transmission properties [Gro15].

Through the overlaying *Kasper* framework, the different submodules closely work together. Figure 3.1 illustrates the relation between the various subcomponents and groups their tasks into the three different main categories utilities, analysis and simulation.

3.2 Particle tracking simulations with *Kassiopeia*

To provide a reliable tool for tracking of low-energy electrons, different members of the KATRIN collaboration have developed the software tool *Kassiopeia*. This highly versatile tool allows to compute particle trajectories in the different components of KATRIN taking into account a variety of underlying physical processes: Different effects have to be taken into account for the electron interaction in gaseous tritium, electron propagation through the transport section and the spectrometers, up to the detection of electrons impinging on the Si-PIN diode of the focal plane detector. For a realistic simulation, experimental settings can be fed directly into the simulation program via XML input files, e.g. currents of solenoids or voltages from power supplies of the electrodes. In this way the physics simulation can be directly compared to the experimental data. Recently the latest version of *Kassiopeia* has been released with various additional features providing an easy way to control the simulation input with XML input files. Furthermore *Kassiopeia* is built up in a modular fashion, making it easy to extend the software with user-specific classes. Beginning with a short description on the organization of *Kassiopeia*, the principle of particle tracking is emphasized in context of this section. Finally the concept behind the XML user interface is shortly sketched. For a more detailed and comprehensive overview of *Kassiopeia*, the reader is referred to the works of the main authors of the software [Fur15, Gro15].

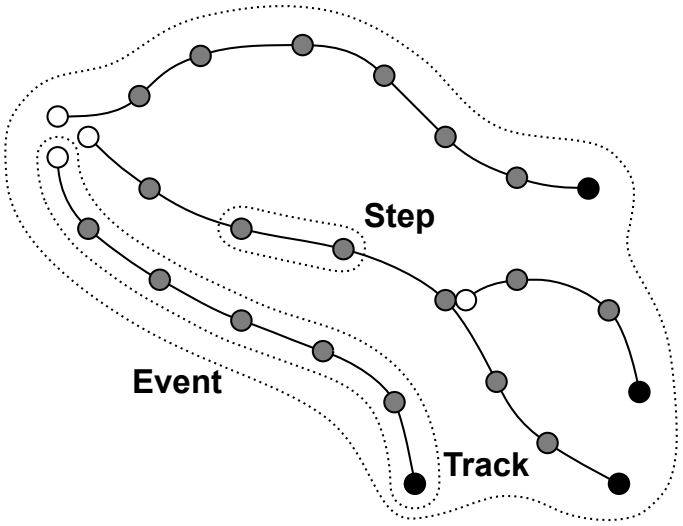

Figure 3.2: Schematic overview of the structure of an event consisting of four tracks and multiple steps. The figure illustrates three primary tracks, the center track contains an additional secondary track. White circles indicate the start point of a track, gray an intermediate step and black the final position. Figure adapted from [Fur15].

3.2.1 Organization of the software

Kassiopeia is able to simulate particle trajectories through complex electro-magnetic fields. Whereas a particle is defined as usual its static properties such as mass and charge, other properties like time, position and momentum are evaluated dynamically. The output data are organized in four hierarchic levels: A generic simulation structure contains runs, which consist of individual events and these are broken down in tracks and steps.

- **Step:** A step represents the smallest hierarchic element in the data structure of *Kassiopeia* and consists of an initial and a final particle state. For the evolution of the trajectory, the equation of motion has to be solved. Charged particles in electromagnetic fields are described for example by the Lorentz equation. Furthermore continuous processes like emission of synchrotron radiation, as well as discrete measures such as particle interactions or dedicated navigation commands will be taken into account during the computation of single steps.
- **Track:** Multiple steps are merged into a track as the logical connection between the generation and the termination of a specific particle consisting of multiple steps. Both start and stop of a track can be controlled directly by the user or indirectly by assigning dedicated interaction processes.
- **Events:** An event consists of multiple tracks, which originate either as a primary or as a secondary track from an interaction process within a dedicated particle step.
- **Run:** A run incorporates multiple events and represents a single particle track simulation. Multiple simulation runs can be merged into a single output file.

More detailed descriptions on the design and structure of *Kassiopeia* can be found in [Fur15, GF$^+$16]. As explained in the previous paragraph, the lowest level of organization represents a step, as at this level the evolution of the physical state of the particle takes place.

3.2.2 Physical state evolution

In the following, the computation and evolution of the physical state of a particle will be explained in more detail. In context of a particle track simulation, the generation of a

Table 3.1: Overview of available particle types in *Kassiopeia*.

Particle		ID	Particle		ID
Electron	e^-	11	Neutron	n	2112
Positron	e^+	-11	Tritium	T^+	31
Myon	μ^-	12		T_3^+	33
Anti-Myon	μ^+	-12		T_5^+	35
Proton	p	2212		T^-	-31
Anti-Proton	p^-	-2212	Rydberg states		10000

particle, the calculation of its trajectory and interactions and finally its termination will be discussed.

Particle generation

Kassiopeia is able to handle various particle types, as shown in table 3.1. The intrinsic properties of the particles are identified with a PDG-based numbering scheme [O+14]. Before initialization of an event, a set of particles has to be created each with a well-defined particle ID and intrinsic properties, like mass or charge.

For the dynamic properties the software contains four generators, defining the start time, start position, initial kinetic energy and finally the direction. The generator values can be defined as a single value or as a set of multiple values. Furthermore, it is possible to dice the starting position of a particle over a fixed geometric volume or an 'abstract' volume, defined by the magnetic flux tube.

Particle trajectory calculation

The propagation of a charged particle in electromagnetic fields is described through the Lorentz equation and its state is defined by the time t, the position $\boldsymbol{r}$ and the momentum $\boldsymbol{p}$. The corresponding first order differential equations are defined as follows:

$$\frac{\mathrm{d}t}{\mathrm{d}t} = 1 \tag{3.1}$$

$$\frac{\mathrm{d}\boldsymbol{r}}{\mathrm{d}t} = \frac{\boldsymbol{p}}{\gamma m} \tag{3.2}$$

$$\frac{\mathrm{d}\boldsymbol{p}}{\mathrm{d}t} = q\left(\boldsymbol{E} + \frac{\boldsymbol{p}\times\boldsymbol{B}}{\gamma m}\right). \tag{3.3}$$

A further continuous process, the emission of synchrotron radiation, can be added as an additional term to the above differential equations. The computation and derivation of this additional term is described in [Fur15, GF+16]. In case, where the electric and magnetic fields remain approximatively constant over a single cyclotron turn of an electron, the adiabatic invariant $\gamma\mu$ stays constant. Correspondingly the 'adiabatic trajectory' class allows particle propagation with larger step sizes while profiting from a significant speed increase. For the important case of adiabatic approximation, only the guiding center position of the particle has to be calculated. The exact position of the particle will be computed in a next step. In this case the physical state is represented by the time t, the guiding center position $\boldsymbol{r}_c$, the (transverse) momentum $\boldsymbol{p}_\perp$ perpendicular and $\boldsymbol{p}_\parallel$ parallel

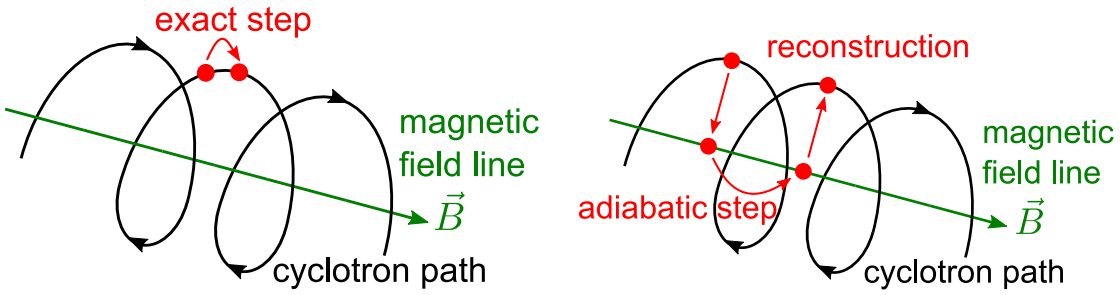

Figure 3.3: Sketch of different trajectory types. Each cyclotron step of the particle is computed for the exact trajectory. The adiabatic trajectory class computes the guiding center position of the particle and the exact position of the particle is reconstructed afterwards. Figure adapted from [Gro15].

to the magnetic field line.

$$\frac{\mathrm{d}t}{\mathrm{d}t} = 1, \tag{3.4}$$

$$\frac{\mathrm{d}\boldsymbol{r_c}}{\mathrm{d}t} = \frac{p_\parallel}{m\gamma}\frac{\boldsymbol{B_c}}{B_c}, \tag{3.5}$$

$$\frac{\mathrm{d}p_\parallel}{\mathrm{d}t} = -\frac{p_\perp^2}{2\gamma m B_c}\boldsymbol{\nabla} B_c + q\boldsymbol{E_c}\cdot\frac{\boldsymbol{B_c}}{B_c}, \tag{3.6}$$

$$\frac{\mathrm{d}p_\perp}{\mathrm{d}t} = \frac{p_\perp p_\parallel}{2\gamma m B_c}\boldsymbol{\nabla} B_c\cdot\frac{\boldsymbol{B_c}}{B_c} \tag{3.7}$$

The first term of equation 3.6 describes the magnetic mirror effect, whereas the second term describes the longitudinal acceleration due to the electric field along the magnetic field lines. Furthermore a gyration phase ϕ of the electron has to be taken into account due to the cyclotron motion and a drift motion due to the $\boldsymbol{E}\times\boldsymbol{B}$- and $\nabla\boldsymbol{B}$-drift. The gyration is defined by the cyclotron frequency of the particle:

$$\frac{\mathrm{d}\phi}{\mathrm{d}t} = \frac{qB_c}{m\gamma}. \tag{3.8}$$

The differential equation for the adiabatic motion including gyration and drift motion is defined as follows:

$$\frac{\mathrm{d}\boldsymbol{r}_\mathrm{c}}{\mathrm{d}t} = \frac{\boldsymbol{E}_\mathrm{c}\times\boldsymbol{B}_\mathrm{c}}{B_\mathrm{c}^2} + \frac{2p_\parallel^2 + p_\perp^2}{qm(\gamma+1)B_\mathrm{c}^3}\boldsymbol{B}_\mathrm{c}\times\boldsymbol{\nabla}B_\mathrm{c}\frac{\boldsymbol{B}_\mathrm{c}}{B_\mathrm{c}} \tag{3.9}$$

Figure 3.3 illustrates the difference between the different trajectory types and the method of step calculation.

Further information on the adiabatic motion of charged particles can be found in the literature [Nor61, Nor63, Thü02, Fur13].

Particle interactions

Particle interaction processes can occur in matter-filled space with a certain probability $P(t)$, or they can happen once the particle propagating in empty space reaches a surface. Assuming that the particle travels through a dense medium with number density n, an interaction occurs with the probability $P(t)$ after a time t:

$$P(t) = 1 - \exp\left(-\frac{t\cdot v}{\lambda}\right), \tag{3.10}$$

Table 3.2: Overview of available terminator classes in *Kassiopeia*. Adapted from [GF+16].

Terminator Name	Description
min/max z	bound on the z-position of the particle
min/max r	bound on the radial position of the particle
min distance	bound on the distance to defined geometry surfaces or spaces
min/max kin. energy	bound on the kinetic energy value
secondaries	stops track if the particle is a secondary particle
trapped	bound on the count of sign changes of longitudinal momentum
max time	bound on time of a particle track
max length	bound on length of a particle track
max steps	bound on maximal number of steps to be computed
death	generic terminator if it is active
output	range for the value of a specified arbitrary output variable

where the mean free path is defined as $\lambda = \frac{1}{n \cdot \sigma}$. The parameters density, velocity and cross section are taken as a mean value between initial and final value of a step. The value for the medium density is extracted from a separate density module and the final cross section taken into account includes all individual cross sections, such as elastic or inelastic cross sections. After rearranging equation 3.10, the time between two scattering events can be calculated:

$$t_{\text{scat}} = -\ln(1 - P_{\text{input}}) \cdot \frac{\lambda}{v}. \tag{3.11}$$

First the value P_{input} will be diced uniformly between 0 and 1. If the scattering time is smaller than the time between Runge Kutta steps $t_{\text{scat}} < t_{\text{steps}}$, then the step is recomputed with respect to a step size which is identical to the scattering time. If the scattering time is larger than the computed step time, no scattering occurs.
A surface interaction process is triggered when a particle crosses a particular surface. In general this will lead to a change of particle properties and result in a change of angular momentum and energy. This process typically occurs if an electron from the vacuum region of the spectrometer reaches the boundary of the silicon wafer of the detector system.

Particle termination

The termination classes allow a trajectory calculation to be stopped. There are different types of terminators, so that a particle trajectory can be stopped depending its position, like the minimal distance to geometric elements, or a termination can be initiated by physical quantities such as kinetic energy (low-energy cut-off). Table 3.2 gives an overview of all available terminators in *Kassiopeia*.

3.2.3 User interface and control

Kassiopeia is controlled by an input file in the XML format [BPSM+08]. A configuration input file contains a manifold of information which is important for the particle tracking simulation: The geometry to compute electromagnetic fields and for navigation, as well as information on different physical processes that have to be taken into account. Furthermore the input file contains information on the generation of particles with respect to their start point and direction, the type of trajectory and the required termination of the particle states. To this end, it has been equipped with an XML parser which benefits from different processors with extended features, like the processing of formulas or access to slow control data via *KaLi*. By using the XML processors, complex input, like geometries, can be

conveniently written down. Examples for all different processor types can be found in [Gro15]. The following example, taken from [GF+16], illustrates the use of variables, conditions, includes and loops in an XML file.

```
<!-- definition of path variable -->
<define name="path" value="/path/to/file"/>

<!-- inclusion of geometry xml file -->
<include name="[path]/CoilGeometry.xml"/>

<!-- condition if coils should be used -->
<if condition="[use_coils]">

  <!-- loop to add an individual current to a total of 5 coils -->
  <loop variable="i" start="1" end="5" step="1">
      <!-- the total current added to each coil is the product -->
      <!-- of its real current and its number of turns -->
      <electromagnet spaces="coil_[i]" current="{[[i]_current]*[[i]_turns]}"/>
  </loop>

</if>
```

3.3 *KGeoBag* - A geometry library for tracking and field simulations

The computation of electromagnetic fields and simulation of particle tracks requires different kinds of geometric information as input: The electromagnetic field software *KEMField* requests discretized surface mesh elements with defined electric potentials to compute electrostatic fields, as well as 'abstract' spaces in which a coil or solenoid is tagged with specific current values and winding numbers for the computation of magnetic fields. The particle tracking software *Kassiopeia* needs information on the geometric shapes, where particles can be generated or terminated. It also profits from the ability of *KGeoBag* to dice arbitrary vector points on abstract surfaces or spaces. This feature is important for Monte Carlo simulations: Here particle tracks are based upon random start points and directions. All above-mentioned features are combined in the program *KGeoBag*, which serves as a big tool to define and to manage arbitrary geometries commonly used by *Kasper* programs.

3.3.1 Definition of geometry elements

KGeoBag contains different classes to define geometric objects, these can be either three-dimensional surface- or space-objects, each possessing a well-defined macroscopic shape. The majority of objects is defined in two dimensions by their axial and radial coordinates. The user also has the ability to apply specific translations and rotations to each object afterwards in order to place the elements correctly in a three dimensional coordinate system. In addition to several rotationally-symmetric elements, *KGeoBag* has been augmented by shell areas in context of this work [Com15]. For example, this element class allows to easily model dipole electrodes being used in different components of the KATRIN experiment. The different types of shell areas and their definition in the XML language is shown in appendix B. Thus, arbitrary geometry objects can comfortably be used to define composed geometries, and are manipulated and placed via user-defined coordinate frames. Finally, *KGeoBag* allows to build a geometry assembly within a stand-alone C++ program by directly using different abstract class objects. The following extract from an XML file shows how a rotated poly-line will be defined:

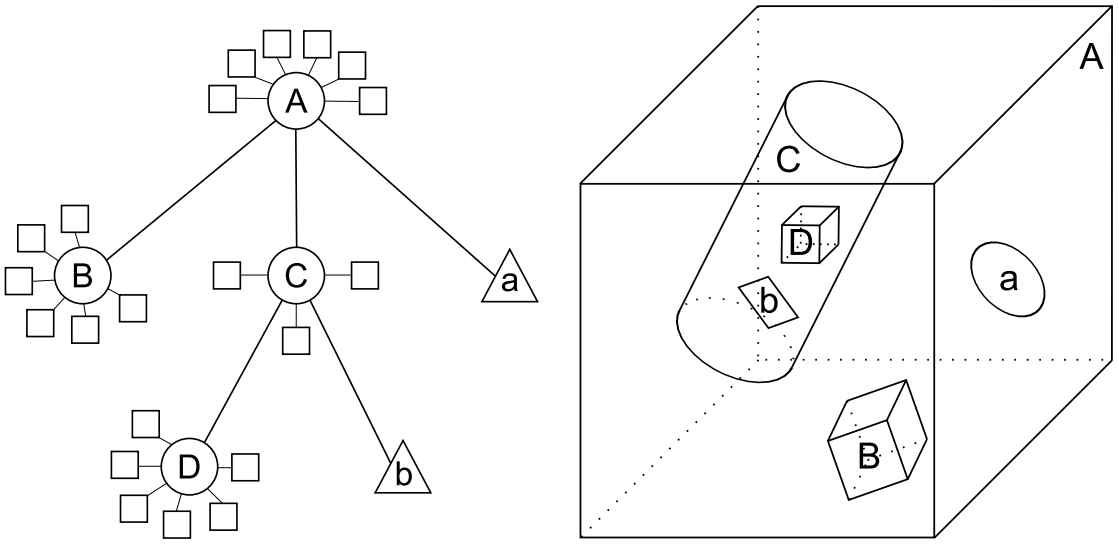

Figure 3.4: Organisation of geometric elements within *KGeoBag*. The left sketch shows how different space and surface objects can be located within a parent space. The right sketch illustrates the hierarchic organization of different geometry objects below a parent space. Pictures adapted from [Gro15].

```
<rotated_poly_line_surface name="rotated_poly_line_forward_surface"
    rotated_mesh_count="32">
    <poly_line>
        <start_point x="0.2" y="0.3"/>
        <next_line x="0.1" y="0.1"
        line_mesh_count="18" line_mesh_power="2."/>
        <next_arc x="-0.1" y="0.1"
        radius="0.2" right="true" short="true" arc_mesh_count="18"/>
        <next_line x="-0.2" y="0.2"
        line_mesh_count="18" line_mesh_power="2."/>
        <next_line x="-0.3" y="0.1"
        line_mesh_count="18" line_mesh_power="2."/>
    </poly_line>
</rotated_poly_line_surface>
```

A single surface or space can thus be placed into a space recursively. This feature allows to define arbitrary complex geometries and to align objects with respect to each other. Figure 3.4 shows the hierarchic organization of geometric objects in *KGeoBag*.

3.3.2 Extension system for electromagnetic calculations

Upon the definition of geometric elements, *KGeoBag* provides the ability to automatically mesh the geometry into small triangles, rectangles or line segments and forwards this piece of information to the program *KEMField*. Each mesh element will be assigned a constant charge density (zero-th order collocation scheme) by *KEMField*, hence the count of mesh elements directly influences the accuracy of the computed electric potential and field values. Especially in high field regions at corners or sharp edges, many mesh elements have to be used in order to obtain reasonable field and potential values. For this reason, all geometry classes are equipped with additional parameter for the mesh generation, such as power factors or linear mesh counts.

But before the mesh elements are generated, a current or potential has to be assigned to a (macroscopic) geometric element in advance:

```
<electrostatic_dirichlet
    surfaces="axial_pre_spec_assembly/@wire_electrode_tag"
    value="{[ps_inner_electrode_potential]}"
/>

<electromagnet
    spaces="magnet_ps_assembly/ps_2"
    current="[ps_2_current]"
    scaling_factor="[ps_2_turns]"
    direction="counter_clockwise"
/>
```

In order to extend the geometry with a subdivision into smaller triangular, rectangular or linear mesh elements, which then can be used by the field calculation program *KEMField*, a mesh object has to be created beforehand. The user can choose between axially symmetric, discrete rotational or non-axial mesh elements. The mesh extension will automatically be created with the following XML statement:

```
<!-- mesh for axially symmetric solid electrodes -->
<axial_mesh name="axial_mesh" surfaces="model_assembly/@electrode_tag"/>

<!-- mesh for discrete rotationally symmetric eletrodes, -->
<!-- the total count of objects around axis has to be defined -->
<!-- optionally an offset angle can be added -->
<discrete_rotational_mesh name="drmesh" count="1200" angle="0.5"/>


<!-- mesh for non axial electrodes -->
<mesh name="nonaxial_mesh" surfaces="model_assembly/@electrode_tag"/>
```

3.3.3 Visualization

KGeoBag is equipped with different programs for the visualization of defined geometries as well as of axially symmetric or non-axial mesh elements. The non-meshed geometry can easily be visualized with the program `GeometryViewer`. The executable requires two input arguments, namely the XML geometry input file, and the internal path to the objects:
`GeometryViewer /path/to/input.xml geometry_assembly/electrode_structure/#`
By this example command, the file `input.xml` will be opened and all geometric elements below the sub-space `electrode_structure` will be displayed due to the closing hash tag. After executing this program, a VTK visualization window will be displayed, rendering the chosen geometric elements. Furthermore the VTK output will be written into VTP files, located in the output folder for later visualization with ParaView. Similar to this program, non-axial and discrete rotational mesh elements can be visualized with the `MeshViewer` and axially-symmetric ones with the program `AxialMeshViewer`. The same input parameters have to be given as mentioned above. It is important to note that this kind of visualization does not contain any information about the applied potentials or currents. These programs are recommended for geometric inspection only. For the purpose of electrostatic analysis, a separate program of *KEMField* will be presented in 3.4.7. The software program `GeometryViewerROOT` can be used for two-dimensional visualization onto a ROOT TCanvas object.

3.4 Electromagnetic field computations with *KEMField*

For the investigation of electromagnetic configurations of the entire KATRIN setup and for particle tracking simulations (these require the numerical solution of the Lorentz equation),

the precise and fast calculation of electromagnetic fields is indispensable. Since commercial programs, like COMSOL, are limited by accuracy and computation speed [Wul14, Röt16] as needed for particle tracking simulations, the software *KEMField* has been developed. This is a object-oriented toolkit written in C++ language for solving time-independent electromagnetic problems allowing to solve electro-magnetic problems with highest accuracy and speed for arbitrary complex geometries. This program is based upon the solution of linear equation systems in context of the Boundary Element Method (BEM). Starting with the release of *KEMField* version 2.0, the input of electromagnetic quantities and the solution of linear algebra equations has internally been decoupled through modern template meta programming [Ale01]. This particular software design allows to apply the mathematical algorithms of *KEMField* not only for electromagnetic problems itself, but also for other mathematical problems in a flexible way.

KEMField consists of many different modules e.g. for the input processing of geometric elements, the parallel solution of linear equation systems and the VTK-based visualization of output data. The following list summarizes a choice of the most important modules and features of *KEMField*:

- **Surface libraries** serve as a common definition of all triangular, conical and rectangular surfaces with respect to unit normal vectors, areas, center points, solid angles, etc. Also line segments, which represent wires, are defined as a separate class.
- **Boundary integral libraries** contain different algorithms in order to perform a two-dimensional integration over a triangular or rectangular BEM surface element or a one-dimensional integration over a line segment. This topic will be discussed in more detail in chapter 4 of the thesis in hand.
- **Linear algebra solver:** *KEMField* has been specialized in version 2.0 for the possibility of the iterative solution of large equation systems. The Robin Hood solver algorithms play an essential role for this purpose. This will be discussed in section 3.4.3. Besides the highly efficient iterative algorithms, the linear algebra classes consist of Gauss-Jordan algorithms and different preconditioners.
- **Field solver:** For the fast evaluation of two-dimensional electromagnetic problems, a solver class based on the Zonal Harmonic expansion can be used. For the solution of three-dimensional problems, either an integrating field solver or a solver based on fast Fourier multipole methods can be used.
- **Plugins for parallel computation:** In order to exploit the capabilities of modern CPU- and GPU-based parallel architectures, *KEMField* is equipped with a CUDA(TM)[2] plugin for the code execution on NVidia(R) GPU devices and an OpenCL(TM)[3] plugin for CPU- and GPU devices of multiple vendors.
- **Visualization classes:** Three-dimensional geometries, field distributions, convergence plots, etc. can be visualized with a VTK-based plugin.
- **Math utilities:** Generic numerical integration routines, vector algebra classes and the definition of constants are consolidated here.
- ***KEMField* stand-alone applications**: For the test and validation of single classes, as well as the analysis and modification of *KEMField*-produced results, dedicated applications are provided.

[2]NVIDIA, NVIDIA Tesla, and NVIDIA CUDA are trademarks or registered trademarks of NVIDIA Corporation in the United States and other countries.
[3]OpenCL is a trademark of Apple Inc., used under license by Khronos.

- **External field library:** The definition of fields, which are not defined by BEM techniques, so-called external fields, like constant fields or fields from Biot Savarts law, are defined in this library.
- **Data organization:** *KEMField* stores the data on the geometric elements and the computed values, like charge densities in a binary data format. Several algorithms are provided to process these in manifold ways.

The following section focuses first on the magnetic field computation for axially symmetric coil geometries and non-axial line current segments. This is followed by a detailed discussion of the boundary element method for the solution of electrostatic problems. The computation of charge densities and the presentation of different electrostatic field computation methods are discussed afterwards. The section closes with a brief outline of the embedded parallelization and visualization techniques in *KEMField*.

3.4.1 Magnetostatic field calculations

The KATRIN experiment exploits more than 30 axially symmetric coils and a system of non-axial currents forming the earth magnetic field compensation system for particle guiding. *KEMField* allows to calculate magnetostatic fields in this complex setup with highest precision and speed. In order to initiate the magnetic field computation routines of *KEMField* by *Kassiopeia*, a corresponding field object has to be created containing common information on the settings and parameters of the magnetic field solver. In the following this is explained by detailing XML input files.

User interface

The `ksfield_electromagnet` object provides a magnetic field to be computed from a *KGeoBag* input geometry with *KEMField*. The geometry may either be axially symmetric, with the option of more than one symmetry axis, or be completely non axial without symmetry axis. For the field object, a name has to be defined, whereas the definition of a directory is optional. If this parameter is not defined, the default *KEMField* cache directory will be chosen. Furthermore a file name has to be defined, where *KEMField* stores the information on the input geometry and the solution. The option `system` allows the user to define an individual coordinate system, which will be used for computation. The geometry of the magnet system will be forwarded as a node of a *KGeoBag* surface or space.

```
<ksfield_electromagnet
    name="field_name"
    directory="locationforkbd"
    file="filename.kbd"
    system="coordinate_system"
    surfaces="EMsurfaces"
    spaces="EMSpaces">

    <!-- definition of one field solver -->

</ksfield_electromagnet>
```

Axially symmetric magnetic fields

Axially symmetric fields are realized over most parts of the KATRIN beamline. The magnetic fields by the different solenoids can either been taken as ideally axial or the geometry input data can be equipped with a specific tilt of a coil sharing even different symmetry axes. The latter is indispensable for the precise study of the flux tube alignment.

Individual magnets of major components such as the WGTS or CPS do not necessarily have to share the same symmetry axis, in this case axially computation methods, together with dedicated geometric transformations, can be applied. The papers [Glü11b, Glü06] detail the axial magnetic field calculation and how different symmetry axes of different magnets will be identified and computed commonly.

Elliptic integrals

The method of computing magnetic fields with elliptic integrals is valid in all space regions and the corresponding value can be taken as a reference. As this method suffers from a lack of speed, it is not recommended for particle tracking simulations. In case elliptic integrals are applied for the computation of magnetic fields [Gar63], the different coils have to be taken as a thin current loop, hence the complete coil has to be computed as a superposition of multiple coils. For the magnetic field computation, the elliptic integrals of first $K(k)$, second $E(k)$ and third kind $\Pi(c,k)$ are needed:

$$K(k) = \int_0^{\pi/2} \frac{\mathrm{d}\phi}{\sqrt{1-k^2\sin^2\phi}} \tag{3.12}$$

$$E(k) = \int_0^{\pi/2} \mathrm{d}\phi \sqrt{1-k^2\sin^2\phi} \tag{3.13}$$

$$\Pi(c,k) = \int_0^{\pi/2} \frac{\mathrm{d}\phi}{(1-c^2\sin^2\phi)\sqrt{1-k^2\sin^2\phi}} \tag{3.14}$$

For the calculation of a realistic coil, an integration along the axial and the radial component is required. The magnetic field can be expressed in terms of all mentioned elliptic integrals (3.12 - 3.14):

$$B_z = \hat{B}_z(Z_{\max}) - \hat{B}_z(Z_{\min}), \tag{3.15}$$

$$B_r = \hat{B}_r(Z_{\max}) - \hat{B}_r(Z_{\min}), \tag{3.16}$$

with

$$\hat{\mathbf{B}}_z(Z) = -\frac{\mu_0\lambda}{\pi} \cdot \frac{(z-Z)R}{(R+r)S}\left[K(k) + \frac{R-r}{2R}(\Pi(n,k) - K(k)\right], \tag{3.17}$$

$$\hat{\mathbf{B}}_r(Z) = -\frac{\mu_0\lambda}{\pi} \cdot \frac{R}{S}\left[2\frac{E(k)-K(k)}{k^2} + K(k)\right], \tag{3.18}$$

and

$$S = \sqrt{(r+R)^2 + (z-Z)^2}, \quad k = 2\frac{\sqrt{Rr}}{S}, \quad n = 2\frac{\sqrt{Rr}}{R+r}. \tag{3.19}$$

The axial and radial magnetic field components are expressed in polar coordinates while $\lambda = \frac{\mathrm{d}I}{\mathrm{d}z}$ represents the linear current density, z the axial position and r the radial position of the field point to be calculated. Furthermore $Z \in [Z_{\min}, Z_{\max}]$ denotes axial thickness of the coil and $R \in [R_{\min}, R_{\max}]$ the radial thickness of the coil. The integrals can be solved with arithmetic-geometric mean (AGM) method or the Chebychev approximation method [Glü16]. Alternatively Carlson's elliptic integrals [PTVF07] can be used for integration. As outlined above the computation of fields with this technique is not recommended for tracking simulations. Instead, another method gaining a speed up factor of 100 is strongly recommended, the zonal harmonic expansion.

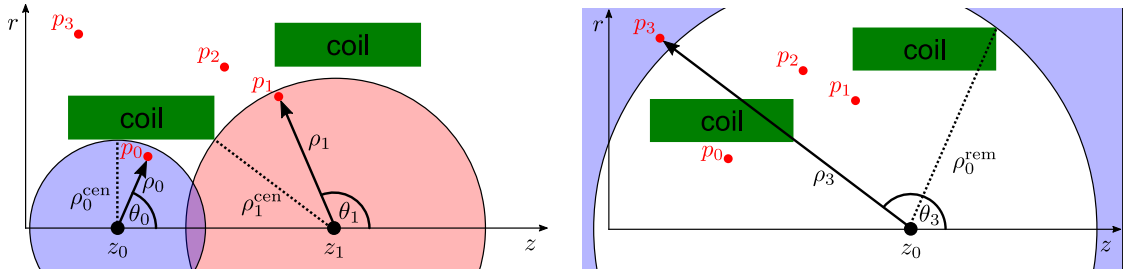

Figure 3.5: Sketch of different convergence areas of the zonal harmonic expansion. Left picture: Two different expansions at the two source points z_0 and z_1 are defined covering two different convergence areas with radii ρ_0^{cen} and ρ_1^{cen}. The field point p_2 is located outside of the convergence radii and the field computation with the given source points is not valid. In this case a remote expansion has to be applied, which is sketched on the **right picture:** Here the point p_3 can be computed, but the computation of the centrally located points p_0, p_1 and p_2 are not valid by using the remote expansion with convergence radius ρ_0^{rem}.

Zonal harmonic expansion

When simulating electron motion in the magnetic flux tube of the KATRIN experiment, the magnetic field can be expanded into Legendre polynomials in most cases. This statement is valid for all field points which are not located too close to the coil geometry. The magnetic field can then be expressed in terms of Legendre polynomials and their derivatives at fixed source points. There are two different expansion types to be used, depending from the field point location. If the field point is located on a sphere with $\rho < \rho_0^{\text{cen}}$ at the symmetry axis below the coil geometry, the central expansion in terms of the spherical coordinates ρ, θ and ϕ can be used:

$$B_r = -\sin(\theta) \sum_{n=1}^{\infty} \frac{B_n^{\text{cen}}}{n+1} \left(\frac{\rho}{\rho_{\text{cen}}}\right)^n P_n'(\cos(\theta)) \tag{3.20}$$

$$B_\phi = 0 \tag{3.21}$$

$$B_z = \sum_{n=0}^{\infty} B_n^{\text{cen}} \left(\frac{\rho}{\rho_{\text{cen}}}\right)^n P_n(\cos(\theta)) \tag{3.22}$$

In case the field point is located in the exterior region of a coil, a remote expansion has to be computed, where field points with $\rho > \rho_{\text{rem}}$ are valid. The magnetic field is given as

$$B_r = -\sin(\theta) \sum_{n=2}^{\infty} \frac{B_n^{\text{rem}}}{n} \left(\frac{\rho_{\text{rem}}}{\rho}\right)^n P_n(u) \tag{3.23}$$

$$B_\phi = 0 \tag{3.24}$$

$$B_z = \sum_{n=0}^{\infty} B_n^{\text{rem}} \left(\frac{\rho_{\text{rem}}}{\rho}\right)^n P_n'(\cos(\theta)) \tag{3.25}$$

The number and the location of the source points can be chosen arbitrarily and will be explained in the context of the XML input parameter definition.
Further information on the magnetic field computation implemented in *KEMField* can be found in [Glü11b].

User interface

The parameter `number_of_bifurcations` defines the number of elements that a single axially defined coil has to be split into. An expansion into source points can be omitted when the quotient of the distance between field point and source point over the convergence

radius exceeds the given `convergence_ratio`. The `convergence_parameter` is defined as the quotient of the five last expansion terms over the entire sum of the expansion. Once this value is smaller than the pre-defined value, the series is flagged as converged. The expansion will include a single term with no convergence check when the ratio between the distance from field to source point over the convergence is smaller than the value defined as `proximity_to_source_point`. The parameters `number_of_central_coefficients` and `number_of_remote_coefficients` allow to control the number of central and remote coefficients separately. The value behind `central_source_point_spacing` is defined as the minimal space between the source points. Equally this parameters exists for the case of remote source points. The source point start and end value is defined with respect to the z axis of the system. For the central source point a fractional spacing can additionally be defined (`use_fractional_central_sourcepoint_spacing`). In this case the spacing between source points will be given as a fraction of the previous convergence radius. In summary the following XML extract shows all above mentioned parameters:

```
<zonal_harmonic_field_solver
    number_of_bifurcations="-1"
    convergence_ratio=".999"
    convergence_parameter="1.e-14"
    proximity_to_sourcepoint="1.e-12"
    number_of_central_coefficients="3000"
    coaxiality_tolerance="1.e-8"
    use_fractional_central_sourcepoint_spacing="true"
    central_sourcepoint_fractional_distance="1.e-2"
    central_sourcepoint_spacing="1.e-2"
    central_sourcepoint_start="1.e-2"
    central_sourcepoint_end="1.e-2"
    number_of_remote_coefficients="300"
    remote_sourcepoint_start="5.e-2"
    remote_sourcepoint_end="5.e-2"
/>
```

Computation of non-axial magnetic fields with Biot Savarts law

The computation of magnetic fields in three-dimensional geometries is indispensable for numerous components of the KATRIN experiment, in particular the EMCS [GDL+13] or the rear section [Hei15]. To that end, *KEMField* has been equipped with dedicated discrete methods which allow to compute the magnetic field of arbitrary complex geometries by subdivision of arbitrarily shaped current segments into smaller linear shapes. The number of discretized linear elements is proportional to the accuracy and the computation speed. The magnetic field of an infinitesimal small current line segment is defined by the Biot Savart's law in differential form as follows:

$$\mathrm{d}\boldsymbol{B}(\boldsymbol{r}) = \frac{\mu_0}{4\pi}\frac{I\mathrm{d}\boldsymbol{s}\times\boldsymbol{r}}{r^3}, \tag{3.26}$$

where I denotes a constant electric current over the line segment $\mathrm{d}\boldsymbol{s}$ and μ_0 denotes the magnetic permeability of vacuum. The magnetic field of a single linear element can be obtained after (path) integration over this segment [Lei14]. For a complex shape, which is discretized into N linear elements, all contributions of each element have to be summed up:

$$\boldsymbol{B}_{\mathrm{sum}} = \sum_{i=1}^{N} \boldsymbol{B}_i. \tag{3.27}$$

User interface

In an XML configuration file for the *KGeoBag* package, a single line current can be defined as a rod space consisting of two vertices. It is important to note that the rod space has to be placed in global space. The following example, containing a rod space, illustrates that multiple line elements can be defined as a single rod object consisting of more than two vertices:

```
<space name="global_space">
    <rod_space name="example_rod">

    <rod radius="0.005" longitudinal_mesh_count="20" axial_mesh_count="10">
        <vertex x="-1." y="-1." z="-1."/>
        <vertex x="0." y="0." z="0."/>
        <vertex x="1." y="1." z="1."/>
    </rod>

    </rod_space>
</space>
```

It is important to note, that all line current elements have to be defined in the technical direction of the electric current (as defined by flow of positive charges). For the field computation, the mesh counts, as well as the radius will have no effect. After the definition of the line current elements, the element has to be flagged as an electromagnetic object and a current has to be defined on the element, as shown in the following extract of an XML configuration file:

```
<electromagnet
    spaces="global_space/example_rod"
    current="10."
/>
```

The current has to be defined in the SI unit (Ampere). The computation of the magnetic field can then be triggered with a *Kassiopeia* XML file. This requires the definition of an integrating field solver object in the corresponding field definition:

```
<ksfield_electromagnet
    name="field_biotsavart"
    file="magfield.kbd"
    system="global_space"
    spaces="global_space/example_rod"
    >
    <integrating_field_solver/>
</ksfield_electromagnet>
```

3.4.2 Principle of electrostatic field calculations with BEM

Electric potential and field calculations require more computational efforts than the computation of magneto-static fields. Since magnetic fields are produced by electric currents, which are directly measurable, electrostatic potentials and fields result from charge distributions, which depend on the voltage applied to the electrodes and on the specific electrode geometry. Common methods to solve for electrostatic problems are the finite element [DR06, Jin14] and the finite difference methods [LeV07]. Both require to mesh the entire region in order to numerically solve Maxwell's equation on the user given field point. For example, the main spectrometer incorporates small-scale wire structures $\mathcal{O}(100\,\mu\text{m})$ embedded in a large vessel with volume of $1200\,\text{m}^3$. For this kind of electrode geometries, characterized by large dimensional differences, it is advantageous to profit again from the

boundary element method (BEM) [HK89, Szi88]. The BEM technique requires only the electrodes to be discretized whereas FEM- or FDM-based methods require even the empty space between the electrodes to be discretized, leading to a very high allocation of memory and consumption of computation time. In addition, the boundary element method delivers more accurate potential and field solutions within a given time [CLRZ99] while allowing to describe open electrode systems, without the need of discretization of potentials at vacuum boundaries.

In a first step, the surface of the electrode has to be meshed into a finite number of small patches. In principle, the form of the electrode shape can be defined arbitrarily, however usually triangular and rectangular shapes are chosen. The accuracy of the computed fields and potentials directly depends on the number of discretized elements N, with N being proportional to the amount of required computer memory and time for further computation steps.

$$S = \sum_{j=1}^{N} S_j \tag{3.28}$$

For each mesh element S_j, the charge density is assumed to be constant. This quantity is unknown to the user. Hence the following linear equation system has to be solved, which sets the known electrode voltage in relation to the unknown charge density:

$$U_i = \sum_{j=1}^{N} C_{ij}\sigma_j. \tag{3.29}$$

The equation above contains the so called Coulomb matrix element C_{ij}, which represents the potential at the center of the element i (also called as collocation point) with respect to the contribution by element j. For the potential contribution by element j, a surface integration over the geometrical shape of the mesh element has to be performed. The development of precise and fast integration methods for the evaluation of the following integrals is one of the key topics of this thesis in hand and can be found in chapter 4.

$$C_j(\boldsymbol{r_i}) = C_{ij} = \frac{1}{4\pi\varepsilon_0} \int\limits_{S_j} \frac{1}{|\boldsymbol{r_i} - \boldsymbol{r_S}|} \mathrm{d}^2\boldsymbol{r_S} \tag{3.30}$$

In a first step equation 3.29 has to be solved to obtain the charge densities σ_j. This can be done for example with the Gauss-Jordan method, where computation time and memory scale with $\mathcal{O}(N)$ however. If an electrode system is meshed into 10000 single mesh elements, approximately 2.5 h and 1.8 GB RAM for the computation of the charge densities are required. For electrode geometries which do not exhibit any type of symmetry which usually allows to reduce the mesh count, novel iterative solver methods like the Robin Hood method [LSA06, LSA08, FLC+12] are required to decrease the amount of calculation time and computer memory. The Robin Hood method will be discussed in section 3.4.3, and the evaluation of potentials and fields on arbitrary space points will be explained in section 3.4.5.1 (after the charge densities have already been computed).

A more detailed mathematical description of the boundary element method can be found in [Cor14, Gos15].

User interface

To solve for charge densities, potentials or fields in case of a discretized geometry based on *KGeoBag* with the *KEMField* package, the XML configuration file has to set up the electrostatic solver as given in the example below. The main `ksfield_electrostatic` object has to contain exactly one charge density solver and one field solver. Both objects

will be discussed later in this chapter. In order to address the field object within *Kassiopeia*, an object name has to be given, followed by a directory and file name where the computed charge densities have to be stored. The system property requires a path to a *KGeoBag* space defining a root coordinate frame where the electrode geometry is located. The path to the *KGeoBag* geometry equipped with a mesh extension is given in the following property surfaces. The symmetry option can be used to control how the input electrode will be treated and how charge densities and fields will be computed. The possible options are `none` for 3-D computations, `axial` for ring-like solid electrodes and `discrete_axial` for rotationally symmetric electrodes which do not necessarily need to be solid rings. It is important to adapt the chosen symmetry option to the defined mesh extension in the geometry XML definition:

```
<ksfield_electrostatic
    name="field_electrostatic"
    directory="/path/to/dir"
    file="Electrodes.kbd"
    system="assembly"
    surfaces="assembly/@electrode_tag"
    symmetry="axial"
>
    <!-- definition of one charge density solver -->

    <!-- definition of one field solver -->

</ksfield_electrostatic>
```

3.4.3 Charge density computation with the Robin Hood method

The prime goal in electrostatics is to solve for the unknown charge densities σ_j. Whereas the corresponding equation system 3.29 can be solved via Gauss-Jordan or LU (lower-upper) decomposition, it turns out that for large geometries these methods are rather impracticable. The so called 'Robin Hood' method, which is an adaption of the Gauss-Seidel method, is more advantageous, since it allows to handle arbitrarily large equation systems without suffering from limitations of computer memory. The Robin Hood method achieves both high accuracy and fast convergence of the solutions. The method can solve for Neumann and Dirichlet boundary conditions, and it scales with $\mathcal{O}(N)$ instead of $\mathcal{O}(N^2)$ (as in case of the non-iterative Gauss-Jordan algorithm). Since this method invokes only a modest memory footprint, also higher dimensional linear equations can been solved without running into memory limitations. As a further benefit, the Robin Hood method can exploit parallel computing capabilities of modern platforms. All these benefits allow to solve three-dimensional electrostatic problems with both highest accuracy and unprecedented speed in contrast to standard solving techniques. Further information on this algorithm can be found in the paper of the main authors of the Robin Hood method [LSA06, LSA08, FLC+12].

Principle

Whereas the Robin Hood method can also be applied to problems involving dielectric boundaries, the main concept of the algorithm is discussed for the case of isolated conductors. The electrostatic model here is a cube and its surface has been discretized into smaller patches. In general these elements are represented by triangular or rectangular surfaces. Each surface element is assigned an initial charge distribution. In reality, this system will try to acquire an equipotential surface. In our example we have not yet achieved an equipotential surface given the chosen (initial) charge distributions. The goal of our method is to obtain an equipotential surface by redistributing charges. For this

reason, two sub-elements whose electric potentials differ most strongly from the average potential will be selected first. Now the charges will be redistributed so, that both surface elements maintain the same potential. As can be seen at this stage, the algorithm follows the principle observed in real conditions to obtain an equipotential surface. The amount of charge to be redistributed between the surfaces m and n is given by:

$$\delta\sigma = \frac{U_m - U_n}{C_{mm} + C_{nn} - C_{mn} - C_{nm}}, \tag{3.31}$$

where C_{ij} denotes the Coulomb matrix element as defined in eq. 3.30. The new potential of the corresponding surfaces is now defined as

$$U'_m = U_m - C_{mm}\delta\sigma + C_{mn}\delta\sigma \tag{3.32}$$
$$U'_n = U_n + C_{nn}\delta\sigma - C_{nm}\delta\sigma \tag{3.33}$$

The charges will be redistributed until an equipotential on the surface is reached up to an user-defined accuracy limit.

User interface

The following extract of an XML configuration file contains an object for the Robin Hood charge density solver. The solver can either be used with analytical or numerical urface integration methods (`robin_hood_bem_solver` or `robin_hood_numeric_bem_solver`). The different parameters control both the accuracy and speed of the algorithm. The tolerance is equal to the infinity norm of the charge density vector to be computed. The parameter `check_sub_interval` defines a number of iterations after the convergence is checked. The `display_interval` value is equal to the number of iterations between the update of the terminal output message. The `write_interval` value defines the frequency of writing solutions into a file. Correspondingly, the `plot_interval` value relates to the number of iterations between an update of the convergence plot. It is highly recommended to cache matrix elements instead of recomputing them at each iteration step, but this option is recommended especially for smaller electrostatic problems consisting of less than 20000 elements since the caching mechanism always requires a certain amount of allocated computer memory. The last two options allow to control the algorithm to be executed on a GPU device (`use_opencl`), its number (`opencl_device_id`) and if a convergence plot with VTK should be drawn:

```
<ksfield_electrostatic
    name="robin_hood_bem"
>
    <robin_hood_bem_solver
        tolerance="1.e-10"
        check_sub_interval="100"
        display_interval="1"
        write_interval="1"
        plot_interval="0"
        cache_matrix_elements="true"
        use_opencl="false"
        opencl_device_id="0"
        use_vtk="false"
    />
</ksfield_electrostatic>
```

3.4.4 Electric field solving methods for axisymmetric electrodes

The computation of axially symmetric conic electrodes can be performed with the zonal harmonic expansion as outlined in section 3.4.1. Also in this case the computation region

will be split into a central and a remote region with different source constants. The most important difference to the magnetic field calculation is the use of only one symmetry axis. As multiple symmetry axes of the electrodes will be used, asymmetric charge distributions are induced. This leads to a non-axial problem to be solved with 3-D methods as described in section 3.4.5.

Elliptic integrals

To very good approximation, the electrodes of the KATRIN main spectrometer can be described as rotational symmetric conical electrodes. This fact is important, as it reduces the problem to two dimensions [Glü11a]. In order to compute fields and potentials, the electrodes have to be approximated first as thin charged rings [Lei14]. The potential at an arbitrary field point (z, r) in space can thus be expressed as [Glü16]:

$$\Phi(z,r) = \frac{Q}{2\pi^2\varepsilon_0}\frac{K(k)}{S}. \tag{3.34}$$

The geometric sizes of a charged ring are defined by its axial coordinate Z and its radial coordinate R. The total charge assigned to the ring surface is Q while $K(k)$ (3.12) denotes the first elliptic integral. The conical electrodes carry homogeneous charge distributions and have to be expressed by an integration over multiple thin charged rings. The electrode is finally represented in the (z, r) plane by a parametrized curve, which reads as follows:

$$Z(p) = z_a + (z_b - Z_a)\cdot\frac{p}{L} \tag{3.35}$$

$$R(p) = r_a + (r_b - r_a)\cdot\frac{p}{L}. \tag{3.36}$$

The path length of the curve is represented by the parameter p. The infinitesimal charge $\mathrm{d}Q$ sitting on the electrode surface is expressed in terms of the charge density $\sigma(p)$:

$$\mathrm{d}Q = 2\pi\sigma(p)R(p)\mathrm{d}p. \tag{3.37}$$

After numerical integration of equation 3.37 over the total curve length from $p = 0$ to $p = L$, the potential of a charged conical electrode can be calculated [Glü16]:

$$\Phi(z,r) = \frac{\sigma}{\pi\varepsilon_0}\int_0^L \mathrm{d}p\frac{R(p)K(k)}{S}. \tag{3.38}$$

Divergences of this integral can be avoided by subdividing the integration interval into smaller sub-intervals.

Zonal harmonic expansion

The evaluation of electric potentials and fields by elliptic integrals typically requires too much computation time for efficient particle tracking simulations. Since a field interpolation method would still require a considerable amount of time to prepare field maps, the zonal harmonic expansion will now be also applied to axisymmetric electrode geometries allowing a fast and accurate evaluation of fields and potentials. The electric potential and field can be expressed in terms of Legendre polynomials and their derivatives as follows:

$$\Phi(z,r) = \sum_{n=0}^{\infty}\Phi_n^{\mathrm{cen}}\left(\frac{\rho}{\rho_{\mathrm{cen}}}\right)P_n(\cos(\theta)) \tag{3.39}$$

$$E_z(z,r) = -\frac{1}{\rho_{\mathrm{cen}}}\sum_{n=0}^{\infty}\Phi_{n+1}^{\mathrm{cen}}\cdot(n+1)\left(\frac{\rho}{\rho_{\mathrm{cen}}}\right)^n P_n(\cos(\theta)) \tag{3.40}$$

$$E_r(z,r) = \frac{\sin(\theta)}{\rho_{\mathrm{cen}}}\sum_{n=0}^{\infty}\Phi_{n+1}^{\mathrm{cen}}\left(\frac{\rho}{\rho_{\mathrm{cen}}}\right)^n P_n'(\cos(\theta)) \tag{3.41}$$

Here, the coefficients have the dimension of an electric potential and represent the potential at the source point $S(z_0, 0)$ on axis. These central source constants represent the electric field sources (charges, dipoles) in the central region of the electrodes. The parameter Φ_n^{cen} is proportional to higher derivatives of the on-axis potential function $\Phi_0(z)$ at the source point $S(z_0)$:

$$\Phi_n^{\text{cen}} = \Phi_n^{\text{cen}}(z_0) = \frac{\rho_{\text{cen}}^n}{n!}\Phi_0^{(n)(z_0)}. \tag{3.42}$$

Accordingly, the expansion is only valid for field points located at $\rho < \rho_{\text{cen}}$. For field points located in the other outer regions of the electrodes, a remote expansion has to be used. As well as in the central case, the source coefficients have the dimension of an electric potential:

$$\Phi(z, r) = \sum_{n=0}^{\infty} \Phi_n^{\text{rem}} \left(\frac{\rho_{\text{rem}}}{\rho}\right) P_n(\cos(\theta)) \tag{3.43}$$

$$E_z(z, r) = \frac{1}{\rho_{\text{rem}}} \sum_{n=1}^{\infty} \Phi_{n-1}^{\text{rem}} \cdot n \left(\frac{\rho_{\text{rem}}}{\rho}\right)^{n+1} P_n(\cos(\theta)) \tag{3.44}$$

$$E_r(z, r) = \frac{\sin(\theta)}{\rho_{\text{rem}}} \sum_{n=1}^{\infty} \Phi_{n+1}^{\text{rem}} \left(\frac{\rho}{\rho_{\text{rem}}}\right)^{n} P_n'(\cos(\theta)) \tag{3.45}$$

The remote zonal expansion even corresponds to the multipole expansion of the electric potential and field (the first term represents the electrode charge, whereas the second represents an electric dipole, etc.). If the field point is located too close to the electrode geometry, elliptic integrals have to be computed. Further information on the zonal harmonic expansion can be found in the paper [Glü11a].
The user interface is similar to the magnetic field solver.

3.4.5 Electric field solving methods for non-axial electrodes

Several components in the KATRIN beam line produce non-axial electrostatic fields, which need to be studied either in the context of detailed Monte Carlo tracking simulations or dedicated field simulations. Both require to compute charge densities and field values for three-dimensional geometries, where no symmetry can be exploited, resulting in a high discretization number. Three different methods to compute field values in case of complex geometries will be highlighted in the following. The detailed discussion of each method regarding accuracy, speed and computer memory is continued in chapter 4.

3.4.5.1 Direct summation of Coulomb matrix elements

The slowest, but most accurate results are obtained by direct summation of the individual potential and field contributions of each discretized element. The electric potential and field value at a field point $\boldsymbol{r}$ read as follows:

$$U(\boldsymbol{r}) = \frac{1}{4\pi\varepsilon_0} \sum_{i=1}^{N} \sigma_i \int_S \mathrm{d}\boldsymbol{r}_i \frac{1}{|\boldsymbol{r} - \boldsymbol{r}_i|} \tag{3.46}$$

$$\boldsymbol{E}(\boldsymbol{r}) = \frac{1}{4\pi\varepsilon_0} \sum_{i=1}^{N} \sigma_i \int_S \mathrm{d}\boldsymbol{r}_i \frac{\boldsymbol{r} - \boldsymbol{r}_i}{|\boldsymbol{r} - \boldsymbol{r}_i|^3}. \tag{3.47}$$

The charge density σ_i of each element i remains constant, hence N two-dimensional integrations have to be performed. This method is recommended for studying potentials and fields with highest precision, since each contribution will be summed up directly without further approximation. It thus follows that the total computation time will increase linearly with the number of discretized elements. In chapter 4 various two-dimensional integration techniques over triangular and rectangular surface patches is discussed in detail.

User interface

The user can choose between two different solver types, either the surface integrations will be evaluated only by analytical integrals (`integrating_field_solver`), or numerically in combination with a new analytical approach for triangular and rectangular mesh elements (`numeric_integrating_field_solver`). The following example illustrates how to define a field solver with the XML interface. Please note that only a single field solver can be defined in the `ksfield_electrostatic` tag:

```
<integrating_field_solver use_opencl="true" opencl_device_id="0">

<numeric_integrating_field_solver use_opencl="true" opencl_device_id="1">
```

Both field calculation modules profit from the parallel execution of the code on OpenCL platforms. In this case, internally the direct summation will be replaced by a parallel reduction ([Cat10, Har07]), which can decrease the computation time up to a factor of 1000, depending on the hardware. For the distribution of different simulations to multiple devices, the device number (`opencl_device_id`) can be assigned accordingly.

3.4.5.2 Cubic interpolation of potential and field grid points

A further possibility to compute electric potentials and fields for three-dimensional problems represents the spline interpolation [PTVF07]. In the most easiest case an arbitrary function $f(x)$ and its derivative is given in the interval $[0; 1]$. This function can be approximated by a cubic polynomial function $p(x) = ax^3 + bx^2 + cx + d$. After plugging in corresponding values into the function and the derivative, the coefficients can be determined:

$$a = 2f(0) - 2f(1) + f'(0) + f'(1) \tag{3.48}$$
$$b = -3f(0) + 3f(1) - 2f'(0) - f'(1) \tag{3.49}$$
$$c = f'(0) \tag{3.50}$$
$$d = f(0). \tag{3.51}$$

Usually the function values have to be interpolated between arbitrary intervals instead of the unit interval. In this case the derivative has to be computed between the previous and the next point. Assuming that the function values p_0, p_1, p_2 and p_3 are given at the points $x = -1$, $x = 0$, $x = 1$ and $x = 2$ with grid spacing $\Delta x = 1$. Consequently the given function values can be used in order to obtain the values for the coefficients:

$$a = -\frac{p_0}{2} + \frac{3p_1}{2} - \frac{3p_2}{2} + \frac{p_3}{2} \tag{3.52}$$
$$b = p_0 - \frac{5p_1}{2} + 2p_2 - \frac{p_3}{2} \tag{3.53}$$
$$c = -\frac{p_0}{2} + \frac{p_2}{2} \tag{3.54}$$
$$d = p_1. \tag{3.55}$$

After combination of the obtained results, the complete cubic interpolation formula can be written down [Bre]:

$$f(p_0, p_1, p_2, p_3, x) = \left(-\frac{p_0}{2} + \frac{3p_1}{2} - \frac{3p_2}{2} + \frac{p_3}{2}\right) x^3 + \left(p_0 - \frac{5p_1}{2} + 2p_2 - \frac{p_3}{2}\right) x^2 + \left(-\frac{p_0}{2} + \frac{p_2}{2}\right) + p_1 \tag{3.56}$$

The implementation together with performance issues of this method have been investigated extensively in context of [Ste16].

A more advanced method is the Hermite interpolation [Lei14], which allows to obtain precise results with even higher grid spaces. In general, more exact results can be computed by using higher order derivatives.

3.4.5.3 Fast Fourier transformation on multipoles

Following the well-motivated principles of the boundary element method, electric potentials and fields can be computed as shown in the previous section by direct summation over the discretized elements for all cases where the geometry does not offer an exploitable symmetry. Then, for each mesh element a surface integration has to be performed, which in the case of a high discretization number can lead to a large amount of computation time ($\mathcal{O}(30\,\mathrm{ms})$ for a single field point). *Kassiopeia* employs the Runge Kutta method at 8th order which typically needs for a single particle step 13 field evaluations, which makes this ansatz impracticable. Consequently the direct field solving method by integration is strongly not recommended for the usage with particle tracking. For the purpose of very fast field computation, a special version of the fast Fourier transformation on multipoles (FFTM) has been developed for *KEMField* [Bar16]. The main principle here is to replace the summation over N surface mesh elements by a summation over a collection of multipole moments comprising fewer terms and delivering equal potential and field values as the direct method. In the following, the theory behind multipole and local expansions is sketched shortly in the beginning, followed by a depiction of the algorithm as implemented in *KEMField* and the user-controllable parameters by XML input files.

Multipole and local expansions

In general, the electric potential induced by surface charge densities can be expressed as a multipole expansion of degree p as follows [Jac99]:

$$\phi(r,\theta,\phi) = \frac{1}{4\pi\varepsilon_0}\sum_{l=0}^{p}\sum_{m=-l}^{m=l}\frac{M_l^m Y_l^m(\theta,\phi)}{r^{l+1}}. \tag{3.57}$$

Here, the multipole moments M_l^m can be computed in terms of a surface charge density:

$$M_l^m = \int_S \sigma(x) r'^l(x) Y_l^{-m}(\theta'(x),\phi'(x))\mathrm{d}s_x. \tag{3.58}$$

In Cartesian multipole expansions the term in first order corresponds to the scalar net charge of the charge distribution, the term in second order is equal to the dipole moment and is a vectorial size. The term in the next order is the quadrupole moment and is denoted in matrix form. However in general the spherical harmonics are referred to as spherical tensors, where the value of the degree l is the rank, i.e. rank=0 is a scalar, rank=1 is a vector and rank=2 is a matrix. With this expansion it is possible to decouple the value of the electric potential and field from the number of discretized elements. Depending from the charge to field point distance, more or less moments have to be taken into account in order achieve a certain potential and field accuracy for all field points which are not enclosed by the charges.

The error estimation for the multipole expansion can be defined with the help of circular regions. The multipole expansion holds valid in a region which is outside of the charge distribution and the expansion origin. The valid evaluation region is located in the exterior region of a circle, which surrounds a forbidden tolerance zone as well as the charge regions (figure 3.6, left). Consequently potentials and fields can be evaluated only far outside of the electrode regions. The idea is now to compute multiple multipole expansion for the different charge regions. A potential or field value could be computed as the superposition

of different multipole expansions. By the `neighbor_order` parameter (to be explained later in detail in this section), the area where a direct field evaluation by integration is necessary, can be defined. The `neighbor_order` parameter is proportional to the area of the forbidden zone for the error band. In a first step, the algorithm applies furthermore a multipole-to-multipole (M2M) transition. Here the information on many multipole grids will be merged into one bigger multipole comprising smaller multipoles. In this way the number of multipole expansions will be drastically reduced. By doing this, the computation effort and scaling can be decreased from order $\mathcal{O}(N^2)$ to order $\mathcal{O}(N \log N)$.

If field points have to be evaluated inside of electrode regions (e.g. between wires of the main spectrometer, sketched in figure 3.6, right), the field has to be evaluated from a local expansion. The local expansion can be defined analogously to the multipole moments (3.58) with following formula:

$$\phi(r, \theta, \phi) = \frac{1}{4\pi\varepsilon_0} \sum_{j=0}^{p} \sum_{k=-j}^{k=j} L_j^k Y_j^k(\theta, \phi) \cdot r^j. \tag{3.59}$$

With the help of a Fourier transformation, in a second step, the local expansion can directly been extracted from the multipole expansion (M2L) [GR88] by following convolution

$$L_j^k = \sum_{n=0}^{\infty} \sum_{m=-n}^{n} M_n^m \cdot T_{j,n}^{m,k}(\rho, \alpha, \beta), \tag{3.60}$$

where $T_{j,n}^{m,k}(\rho, \alpha, \beta)$ is the response function. This particular step is specific to the implementation in *KEMField* as it will be discussed in the following. More mathematical details can be found in [Bar16, Gos15]. After the translation to local moments has been done, the local moments from merged multipoles will be translated to different electrode regions by the local-to-local conversion (L2L).

Algorithm in KEMField

The algorithm which has been implemented into *KEMField* [Bar13, BFC15] relies on an hybrid of the fast Fourier transformation on multipoles (FFTM) and the fast multipole method (FMM) [GR97]. In a first step, the entire space has to be subdivided into a grid which defines the regions, containing the multipole moments. In this step, FMM profits from an adaptive octree partitioning. This feature is indispensable for KATRIN, since the main spectrometer electrodes consist of small-scale wires which are embedded into a large (empty) tank. Consequently for the charge regions near the electrodes, the algorithm allows a finer partition to be applied and the large empty space of the tank region can be subdivided into a more coarse grid. In a next step, the multipole moments are computed according to equation (3.58). In this way, the multipole to local conversion (M2L) can be handled in a very efficient way. Whereas the original FFTM algorithm applies only constant grid sizes to arbitrary electrode geometries, the multipole to local conversion in *KEMField* profits from the convolution theorem in combination with applied adaptive cube sizes. The following list comprises the different computation steps of the *KEMField* FMM-FFTM hybrid algorithm in chronological order and refers to the explanations given in the text before and in figure 3.7.

1. Construction of an adaptable cubic tree (FMM).
2. Calculation of multipole moments from charge sources (discretized mesh elements).
3. Gathering of multipole moments leads to smaller collection multipole moments (M2M conversion, FMM).

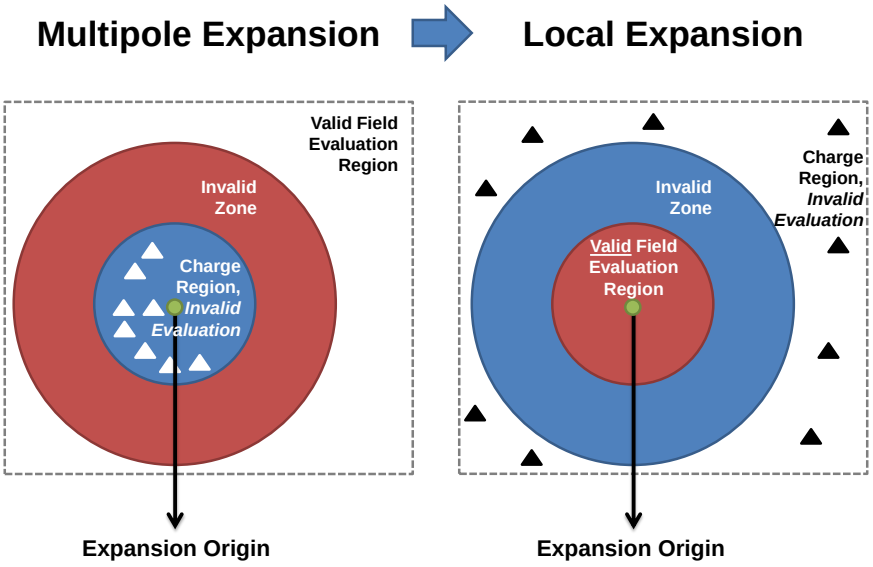

Figure 3.6: Schematics of the difference between multipole and local expansion. Whereas the region where the multipole expansion converges is outside of the electrodes, field points around the electrodes can be evaluated with the local expansion. At the invalid zone and at regions where charges are present, the expansion does not converge.

4. Transformation of multipole moments to local moments using fast Fourier transformation (M2L conversion, FFTM).
5. Gathering and assignment of local moments (L2L conversion, FMM).

User interface

In general, *KEMField* will apply an adaptive sub-divison of a world cube into smaller cubes. The multipole expansions will be computed around the cube center and describe the far field contributions of the source elements to the potential and field values. For the description of potential and field inside a cube, the multipole expansion is transformed into a local expansion. Nearby elements will be evaluated with the direct method. In the following it is shown how the FFTM field solver can be used with XML input files. The subsequent XML extract shows a configuration which can be used on CPUs with maximal 4 GB RAM. The configuration ensures the calculation of electric fields with minimal accuracy of $\mathcal{O}(10^{-9})$ (tested with a non-axial main spectrometer model, [Ste16]).

```
<fast_multipole_field_solver
    top_level_divisions="8"
    tree_level_divisions="2"
    expansion_degree="13"
    neighbor_order="3"
    maximum_tree_depth="6"
    region_expansion_factor="1.1"
    use_region_size_estimation="true"
    use_opencl="false"
/>
```

- The `top_level_divisions` parameter is equal to the subdivision number of the top level box, covering the entire world space.

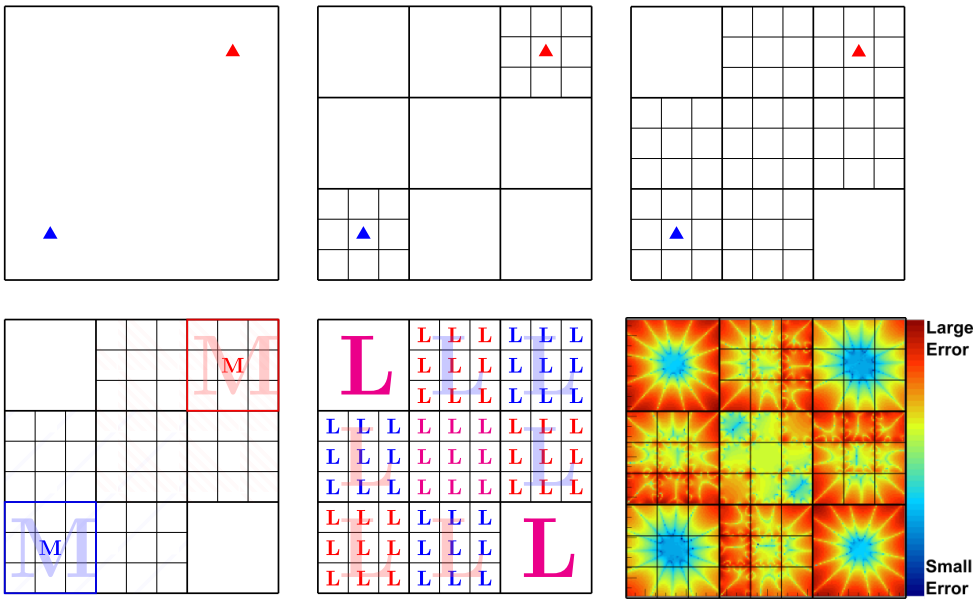

Figure 3.7: Sequence of the multipole transformation in *KEMField* (from left to right, from top to bottom). Beginning with a region containing two electrode groups (blue and red triangle), the root region is subdivided into child regions and the two child regions which contain the electrode groups are subdivided further in nine child sub-regions. Unless the maximal tree depth is reached, as defined by the user, also the neighbors have to be subdivided further into sub-regions (3rd picture). The number of neighbor elements to be taken into account is given as well by a user controllable parameter. In a next step, the multipole moments for the different electrode regions will be calculated and the merge (upward pass) of the multipole moments will be performed until the root node (M2M). The different colors indicate the different electrode regions to which the multipole moments belong to. The faded large M indicates the corresponding moment of the parent region. Afterwards the transformation from multipole to local coefficients (M2L) will be calculated by a convolution at each expansion point and the distribution of the parental local coefficients to the child is performed (local-to-local conversion, L2L). The last picture illustrates the field errors in the different regions. Figure adapted from [Bar13].

- The `tree_level_divisions` parameter controls the count in how many lower level boxes a box will be subdivided. Its value is equal to the number of boxes along one side. If this parameter is equal to two, a box will be subdivided into eight smaller boxes.
- The maximal order of the multipole and local expansion factors are defined as the parameter `expansion_degree`. For precise results, parameter values in the range from 10 to 13, combined with a `neighbor_order` of 3, is recommended.
- The `neighbor_order` (also called zero mask size) defines which boxes are considered as neighbor. If this value is equal to 1, considering a primary cubic region, boxes in the same level and sharing one side, corner or edges are declared as neighbor. In total this primary box own 26 neighbors. In general a `neighbor_order` n implies that all same level boxes inside a cube with side length of $2n+1$ boxes are considered as neighbor. If a field point has to be evaluated in the primary node, the neighbor regions will be evaluated directly. In this way the before mentioned 'forbidden tolerance zone' is defined. The higher this value, the slower the algorithm will work due to an increased amount of necessary direct field evaluations.
- The `maximum_tree_depth` describes the maximal depth in which cubes are subdivided. The tree size is proportional to the computation time of local moments and

limits the time needed for direct field evaluations.

- The `region_expansion_factor` scales the estimated world size by the given factor.

3.4.6 Parallelization of *KEMField* subcomponents

In order to further accelerate the computation of electrostatic potentials and fields, the *Kasper* module *KEMField* can run special code on graphic processor units (GPUs) profiting from a highly parallel execution of mathematical operations, general-purpose computing on graphics processing units is abbreviated as GPGPU. In contrast to non-parallelized applications on CPUs, GPGPU facilitates a large variety of computationally intensive tasks and achieves speed-up factors of up to 1000. Today many computations take advantage of this technology (e.g. [RS05, Hwu11]) and even one of the ten fastest supercomputers is accelerated with GPUs (Supercomputer *Titan* at Oak Ridge National Laboratory).

Technique

The traditional purpose of GPUs is to render detailed graphics in real time. For this purpose many mathematical operations like coordinate transformations or light reflexions have to be performed in parallel. In contrast to CPUs, GPUs have been optimized since their early days for parallel floating-point operations, whereas the layout of CPUs has been focused on intelligent cache mechanisms and complex flow control mechanisms. To be able to profit from parallel GPGPU computing, the code has to be revised and adapted to the given GPU hardware layout.

Hardware layout and data pattern

A GPU acts as a co-processor for the CPU and computation data have to be copied to the device before the computation and back afterwards, there is no direct access, neither to the RAM nor to the mass storage of the host system from the GPU code. This particular interplay between CPU and GPU is labeled as heterogeneous or hybrid system.

Before the computation, the input data has to be chopped and distributed over different cores of the GPU. A single work item can be regarded as a single pixel, that the GPU has to be compute. Each work item is identified by an index. In the case of mathematical operations, a single work item can stand for a matrix element. The many different work items have to be grouped into blocks, which share a common memory on the GPU. The number and the size of the blocks have to be optimized in order to fully exploit the hardware capabilities, making this task highly vendor-dependent. The main difference regarding CPUs is that each core has to perform the same operation, whereas a CPU can assign different cores with different tasks.

Applications and user interface

In general a GPU code is written in kernels, which will be executed on the device in parallel. The most prominent languages for GPU code are CUDA and OpenCL. *KEMField* has been equipped with both kernel languages for field solving by parallel reduction and charge density computation with the Robin Hood method. Whereas CUDA currently can be used for *KEMField* stand-alone applications, the computations based on OpenCL can be triggered directly with the XML user interface. As OpenCL supports heterogeneous platforms, also other device types such as multi-core CPUs or accelerators can be used in parallel besides graphic cards. Before compiling *KEMField*, the options for parallel computing can be chosen in the CMake configuration dialog. After the code compilation, *KEMField* offers multiple applications which directly profit from parallel computing platforms. Charge density and field solving classes are equipped with corresponding CUDA and OpenCL kernels. In the following a short list of programs for charge density solving of the 3-D KATRIN main spectrometer model is presented.

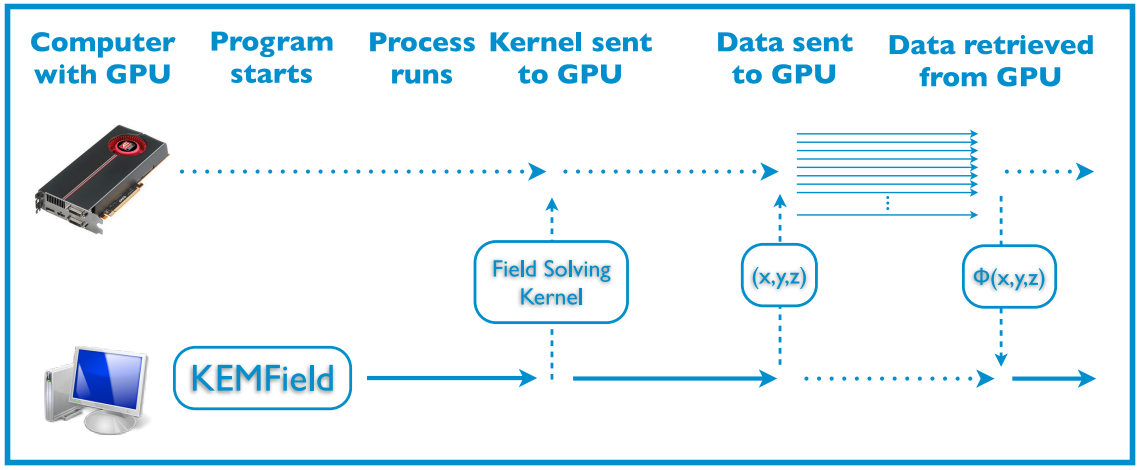

Figure 3.8: Depiction of the field calculation method with *KEMField*. After the start of the *KEMField* program, in a first step the GPU code (also called kernel) will be transferred onto the chip. Afterwards the computation data to be processed in parallel is copied on the GPU. After the computation, the results are copied back onto the host system. Illustration taken from [Cor11].

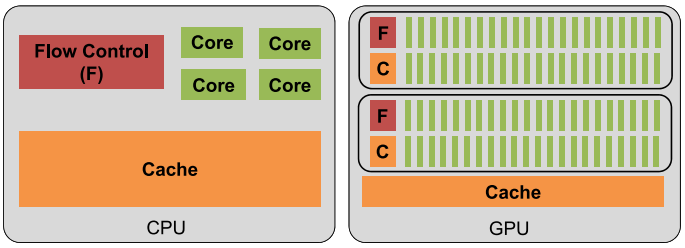

Figure 3.9: Sketch of the different hardware architectures. Whereas the CPU is equipped with additional cache and flow control units allowing the execution of different tasks on a few cores, the GPU can execute a single piece of code on hundreds of cores. Here the cache and flow control units are smaller.

Usage of multiple devices

A further boost of computation efficiency can be achieved by using multiple GPUs via the MPI standard. The parallelization of *KEMField* with the MPI package can be activated, likewise to OpenCL, via the CMake configuration menu. The combination of both techniques, OpenCL and MPI, can be used for charge density solving of the main spectrometer. The KATRIN-specific software module (KSC) is equipped with the following MPI- and OpenCL-aware programs for charge density solving:

- `AssemblyChargeDensity` computes the charge density for the 3-D main spectrometer from a given XML input file.
- `MainSpectrometerChargeDensityAnalytic` computes the charge density with analytic surface integrators.
- `MainSpectrometerChargeDensity_FastMultipole` computes charge densities using fast Fourier multipole methods.
- `MainSpectrometerChargeDensityNumeric` computes the charge density with numeric surface integrators.
- `MainSpectrometerChargeDensityNumeric_CUDA` computes the charge density with numerical integrator on single CUDA devices.

3.4.7 Visualization of BEM elements

In order to display and visualize electromagnetic quantities such as the electric potential, the charge density or the field-generating currents inside a geometry, the *KEMField* application `VisualizeEMGeometry` can be used. This tool takes advantage of the VTK tool chain as used in *KGeoBag*, but it can assign further electromagnetic data as calculated by *KEMField* for visualization coloring. Instead of plain geometry XML files, electromagnetic and geometric data in the binary data format of *KEMField* serve as a input. Each meshed geometry is merged into a surface container. The name of the surface container has to be forwarded to the visualization tool in order to create VTP output files. It will be read out with the program `InspectEMFile` via the following command: `InspectEMFile NameOfKbdFile.kbd`

```
<!-- readout of Robin Hood convergence -->
<Key>
    <0>(std::string)ResidualThreshold_a27a8d59743d2d7bd6d52b4237c296ca<\0>
    <1>(std::string)ResidualThreshold<\1>
    <2>(std::string)b4faf1d73e2fdbc8d7d2b829515bb6ae<\2>
    <3>(unsigned int)4<\3>
    <4>(std::string)ResidualThreshold<\4>
    <5>(std::string)36fb72b0830ef636e774375e3ffeb7dc<\5>
    <6>(std::string)716348640f9c8e31fe2f58105c4da4e9<\6>
    <7>(std::string)a27a8d59743d2d7bd6d52b4237c296ca<\7>
    <8>(unsigned long)260<\8>
    <9>(unsigned long)44<\9>
<\Key>
<!-- readout of surface container identification -->
<Key>
    <0>(std::string)SurfaceContainer_a27a8d59743d2d7bd6d52b4237c296ca<\0>
    <1>(std::string)SurfaceContainer<\1>
    <2>(std::string)a27a8d59743d2d7bd6d52b4237c296ca<\2>
    <3>(unsigned int)2<\3>
    <4>(std::string)SurfaceContainer<\4>
    <5>(std::string)a27a8d59743d2d7bd6d52b4237c296ca<\5>
    <6>(unsigned long)489<\6>
    <7>(unsigned long)157869518<\7>
<\Key>
```

The name is given as the first entry of the second tag:
`SurfaceContainer_a27a8d59743d2d7bd6d52b4237c296ca`

In a next step the visualization has to be triggered with the command:

```
VisualizeEMGeometry NameOfKbdFile.kbd
-n SurfaceContainer_a27a8d59743d2d7bd6d52b4237c296ca
```

A VTP file will be created to be visualized with ParaView for example.

3.5 Beta spectrum calculation and study of statistical and systematic uncertainties

In the following, the concepts behind two further software tools will be highlighted: Tritium β-decay spectra can be calculated with *SSC* and together with the tool *KaFit* the effect of different experimental parameters on the neutrino mass sensitivity can be studied.

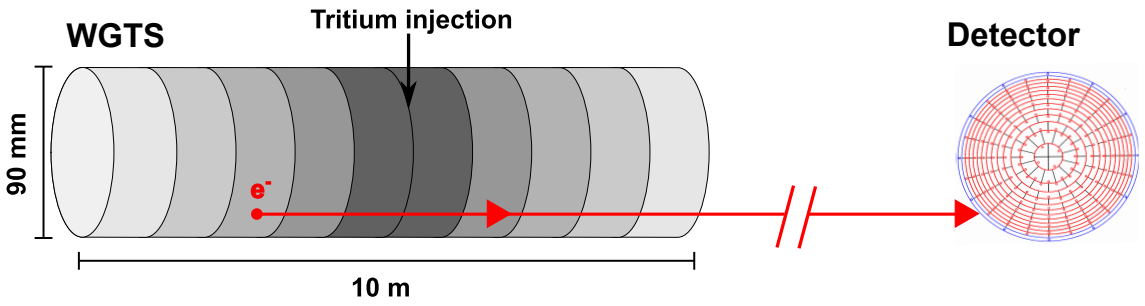

Figure 3.10: Subdivision of the WGTS beam line segment into voxels. The voxels are linearly segmented in beam line direction and, according to the segmentation of the focal plane detector, as well azimuthally and radially into 148 segments. Inhomogeneities of magnetic field strengths, temperature or densities can be taken into account. Figure adapted from [Höt12].

3.5.1 Analytical beta spectrum computation with *SSC*

The program *SSC* computes the energy spectrum of electrons from tritium β-decay. Close to the energy endpoint of tritium all physical processes have to be simulated and taken into account to yield a precise simulation result on the neutrino mass. In addition to source-related effects, *SSC* incorporates the transmission and response function of the spectrometers to calculate the integral electron rate, which is also the quantity experimentally observed by KATRIN. The source and spectrum calculation code *SSC* is based upon analytical calculations without Monte Carlo techniques. The analytical results can be forwarded to *Kassiopeia* for further particle tracking simulations.

Electrons generated in the source region are affected by inhomogeneities in the source, resulting from variations of the local potential (plasma effects), the magnetic field strength, gas densities, and finally beam tube temperatures:

- The irregular shape of the magnetic field directly influences the visible source area. Electrons from outer flux tube radii have higher polar starting angles and suffer from a higher energy loss due to scattering. The design requirement of $\Phi = 191\,\mathrm{T\,cm^2} = B \cdot A$ for the transported flux results in a maximal visible source area of $A = 53\,\mathrm{cm^2}$. Besides scattering probabilities of β-electrons, the maximal accepted polar starting angle is defined by the magnetic field in the source.
- The gas density and the velocity distribution are proportional to the number of injected tritium molecules, which depends on further parameters like the inlet pressure or the pumping speed, and control the source activity.
- The temperature profile of the WGTS beam tube has a direct influence on the thermal movement of the tritium molecules and which causes Doppler broadening [Höt12].

In order to model these (inhomogeneous) physical quantities in the source in a correct manner, *SSC* profits from the voxelization concept as illustrated in figure 3.10. For each volume segment, the temperature, density, bulk velocity and field (and potentials) can be defined individually [Höt12].

Differential beta spectrum

The calculation of the differential spectrum of β-electrons is given to first order by the well known formula by Fermi (see eq. 1.50). In the context of sub-eV scale neutrino mass measurement, additional effects have to be taken into account for a correct source model. The Fermi function describes the interaction of the emitted electron with the daughter

nucleus. In case of the β^--decay, the spectrum is shifted towards energies below the endpoint, because the electron is attracted by the positive charge and consequently looses energy. Further terms which cause energy loss due to radiative corrections also have to be taken into account [Höt12, Kle14]. The recoil of the daughter nucleus $(^3\mathrm{HeT})^+$ leads to a typical energy loss of approximately $E_{\mathrm{rec}} \approx 1.7\,\mathrm{eV}$ for electrons close to E_0. Another energy shift results from the fact that daughter molecules can have rotational, vibrational and electronic excitations, with each state being characterized by an excitation energy E_F populated by a probability P_f, giving individual β-spectra for each decay branch [Höt12]. For a comprehensive description of the beta decay spectrum, the excitation spectrum has to be convoluted with a Gaussian distribution for incorporating the Doppler broadening due to thermal velocities of the gas molecules. For a more detailed discussion the reader is referred to [Höt12].

Integrated beta spectrum

SSC can also generate an integrated β-decay spectra which can be used as an input for the χ^2-function in order to determine m_ν^2 as a fit parameter. For each voxel in the source, the signal count rate is computed individually. Different voxels contributing to the same detector pixel can be summed up to obtain realistic count rates expected on pixel j of the focal plane detector:

$$\dot{N}_{\mathrm{S}}^j(qU, E_0, m_{\overline{\nu}_e}^2) = N_{\mathrm{T}}^j \cdot \epsilon_{\mathrm{det}}^j \cdot \frac{\Omega^j}{4\pi} \cdot \int_{qU}^{E_0} \frac{\mathrm{d}\dot{N}}{\mathrm{d}E}^j (E_0, m_{\overline{\nu}_e}^2) \cdot R^j(E, qU)\mathrm{d}E. \tag{3.61}$$

Here, N_{T}^j represents the number of tritium nuclei, projected onto a pixel, which depends from provided tritium purity ϵ_T and the column density ρd. Also the maximal solid angle accepted has to be calculated for each pixel individually: $\Omega^j = 2\pi(1 - \cos\theta_{max}^j)$. Other parameters like the detector pixel efficiency $\epsilon_{\mathrm{det}}^j$ and the effective response function $R^j(E_0, qU_0)$ have to be defined for each pixel separately, too. The differential count rates $\frac{\mathrm{d}\dot{N}}{\mathrm{d}E}$ contain information on the source properties as discussed in the paragraph above. By varying source-related parameter, the study of their effect on the integral spectrum can be investigated either per detector pixel or based upon a total count rate.

3.5.2 Statistical analysis of neutrino mass sensitivity with *KaFit*

To evaluate statistical and systematical uncertainties on the neutrino mass parameter for a specific measurement setup after a pre-defined measurement time distribution (MTD), the software tool *KaFit* allows to execute ensemble simulations of the KATRIN experiment [Kle14]. Besides generated toy measurements in context of ensemble simulations, this program is able to estimate the mass parameter also from real data.

Simulation of a KATRIN toy measurement

In the previous paragraph it has been described, how integrated rates and expected detector counts will be computed analytically with SSC. Here it is motivated how a realistic data set incorporating different spectra at different retarding potentials can be obtained. But, in order to mimic a real measurement, the theoretically computed expectation values have to be replaced with a random value drawn from a Poisson distribution. Further, a Poissonian distributed background component must be added. In the following equation, $\dot{N}_{\mathrm{bg}}$ denotes the expected mean background rate at pixel j. Finally the number of counted background events at a given measurement time t_{qU_0} is given as:

$$N_{\mathrm{bg}}^j = \mathrm{Poisson}(t_{qU_0} \cdot \dot{N}_{\mathrm{bg}}^j). \tag{3.62}$$

The expected count rate $N^j_{\mathrm{toy}}(qU_0)$ of a toy measurement is composed of a signal and a background count rate:

$$N^j_{\mathrm{toy}}(qU_0) = \mathrm{Poisson}(\hat{N}_S(qU_0)) + N_{\mathrm{bg}}, \tag{3.63}$$

where the expectation value of the Poisson distribution is $\hat{N}_S(qU_0)$. The standard deviation of the count rate is defined as $\sigma = \sqrt{N^j_S(qU_0) + N^j_{\mathrm{bg}}(qU_0)}$, since signal and background are both assumed to be distributed purely Poissonian.

χ^2-Function for the KATRIN four-parameter fit

In order to gather the neutrino mass squared as fit parameter, the quadratical difference between theoretical and simulated count rate distribution has to be minimized in context of a χ^2-minimization. First the theoretical spectrum has to be computed accordingly to equation 3.61, additionally two unknown normalization constants R_S and R_b have to be taken into account for both the signal and background component:

$$N^j_{\mathrm{theo}}(qU_0, E_0, m^2_{\overline{\nu}_e}, R_S, R_b) = (R_S \cdot \dot{N}^j_{\mathrm{S}}(qU_0, E_0, m^2_{\overline{\nu}_e}) + R_b \cdot \dot{N}^j_{\mathrm{bg}} \cdot t_{qU_0} \tag{3.64}$$

It is important to highlight that the measured count rate of the KATRIN experiment incorporates four parameters: E_0, $m^2_{\overline{\nu}_e}$ and R_S together with R_b. The χ^2-function needs to be minimized to obtain the best fit estimator $\hat{m}^2_{\overline{\nu}_e}$ in order to extract the information on the neutrino mass parameter:

$$\chi^2(E_0, m^2_{\overline{\nu}_e}, R_S, R_b) = \sum_{i,j} \left(\frac{N^j_{\mathrm{toy}}(qU_i) - N^j_{\mathrm{theo}}(qU_i, E_0, m^2_{\overline{\nu}_e}, R_S, R_b)}{\sigma_{\mathrm{toy}}} \right)^2, \tag{3.65}$$

where $N^j_{\mathrm{toy}}(qU_i)$ can be replaced by count rates $N^j_{\mathrm{meas}}(qU_i)$ from real measurements. The summation over the index j comprises all 148 detector pixels, whereas i denotes the different retarding voltages. In [A+04] 41 different retarding potentials are projected in the KATRIN neutrino measurement campaign, consequently the sum will consist of 6068 different terms in order to finally determine the neutrino mass parameter.
For the technical realization of the minimization routine, the *KaFit* software comprises of different minimization algorithms like Minuit from the data analysis package ROOT [A+09] or different Markov Chain Monte Carlo algorithms [Kle14].

Measurement time distribution

The mean signal count on the detector at a given retarding potential qU can be calculated by multiplying the integrated signal count rate, as computed with SSC (eq. 3.61), with the given time t_{qU} spent at the retarding potential U:

$$N_S(qU) = \dot{N}^j_{\mathrm{S}}(qU, E_0, m^2_{\overline{\nu}_e}) \cdot t_{qU}. \tag{3.66}$$

An example of MTDs can be found in chapter 2 in figures 2.21 and 2.22. A complete KATRIN measurement, covering three years of net measurement time (five calendar years including calibration and maintenance time), the β-spectrum will be scanned by applying different retarding potentials U at a given time t. Following, an entire KATRIN tritium measurement campaign is characterized by a MTD, which defines how many time will be spent at a certain retarding potential. The sum of all times $\sum t_{qU_0}$ covers in general the projected net measurement time, but it can be adapted to individual and more realistic time intervals. The MTD influences the statistical uncertainty of the neutrino mass estimate. The measurement time has to be focused at the endpoint area, where the greatest distortion due to $m_{\overline{\nu}_e} \neq 0$ is expected. Up to this point, the calculation of the integrated rate and the expected counts (with *SSC*) is purely based on analytical formulas.

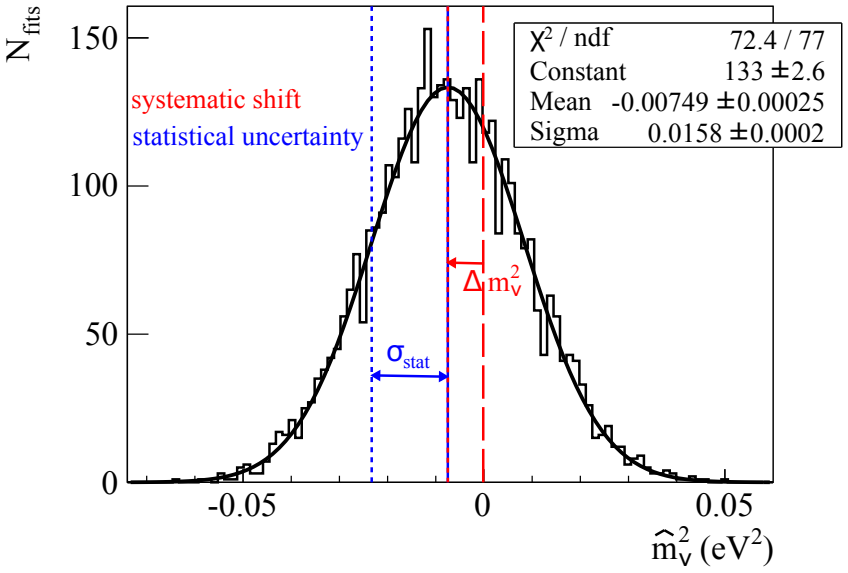

Figure 3.11: Gaussian distribution of m_ν^2 best-fit values of 4000 KATRIN measurements. The simulated measurement time was three years. The systematic shift in the m_ν^2 parameter was induced by using a different column density for toy measurement and simulation. The standard deviation is quantity for the statistical deviation. Graph taken from [Höt12].

Sensitivity studies with ensemble simulations

The purpose of ensemble simulations is to obtain the effect on statistical and systematical uncertainties of the neutrino mass parameter due to the variation of physical (input) parameters. Following, an ensemble of multiple KATRIN measurements with a given MTD is simulated and for each simulated measurement, the parameter $m_{\overline{\nu}_e}^2$ is estimated. This Monte Carlo approach estimates the variance of the neutrino mass squared estimates. Figure 3.11 shows the shift of the neutrino mass parameter in context of 4000 KATRIN measurements with three years measurement time. For each measurement the theoretical spectrum has been fitted to the simulated measurement in order to gather the best-fit value $m_{\overline{\nu}_e}^2$. From the ensemble of different $m_{\overline{\nu}_e}^2$ estimates, the mean value $\overline{m}_{\overline{\nu}_e}^2$ and the standard deviation σ_{stat} can be extracted. The standard deviation σ_{stat} describes the variation of statistical parameters, different measurement time distributions or backgrounds. The projected statistical uncertainty by the experiment is $\sigma_{\mathrm{stat}} = 0.018\,\mathrm{eV}^2$. By varying the before-mentioned parameters, the effect on the target design sensitivity can be investigated. The systematic shift of the mean value to the mass input parameter $\Delta m_{\overline{\nu}_e}^2 = \overline{m}_{\overline{\nu}_e}^2 - m_{\overline{\nu}_e}^{2,\mathrm{sim}}$ describes the systematic uncertainty of $m_{\overline{\nu}_e}^2$. Statistical and systematical shifts are summed up quadratically, delivering the targeted design sensitivity of the experiment. 90 % C.L. sensitivity translate as

$$S_{m_{\overline{\nu}_e}}(90\,\%) = \sqrt{1.645\sigma_{m_{\overline{\nu}_e}^2,\mathrm{tot}}}\ , \text{ with } \sigma_{m_{\overline{\nu}_e}^2,\mathrm{tot}} = \sqrt{\sigma_{\mathrm{stat}}^2 + \sigma_{\mathrm{sys}}^2}. \tag{3.67}$$

The presented techniques and tools will be applied in app. F, where the effect of an imprecise simulation on the retarding potential due to analytical integration algorithms is investigated. For further information on the statistical evaluation of the neutrino mass parameter as well as the software implementation of statistical methods and fitting algorithms, the reader is referred to [Kle14, Höt12, Käf12].

3.6 Summary

In this chapter different major components of the simulation and analysis software toolkit *Kasper* have been discussed. In context of the assembly and the operation of the KATRIN experiment which contains different components, highly versatile software tools are required to compute particle trajectories precisely (3.2), electro-magnetic fields with highest numerical precision and speed (3.4) or analytical tritium source spectra together with expected signal rates (3.5.1). For the organization of different geometric models of the experiment, an integrated software tool (3.3) manages and maintains the geometric components of the experiment in a consistent way, so that different simulation programs can access to commonly organized geometric data of the apparatus. Furthermore with dedicated statistical minimization algorithms (3.5.2), the effect on the neutrino mass sensitivity by individual experimental parameters can be studied.

As it represents one key topic of this thesis, the electrostatic field computation with *KEMField* has been emphasized in context of this chapter. The boundary element method is a corner stone for fast field computations as they are required by particle trajectory calculations in realistic geometries. In addition, several fast field computation methods for three-dimensional problems, like FFTM or the interpolation with cubic splines have been discussed since these are essential for the simulations in context of chapters 5 and 6.

CHAPTER 4

Potential and field computation of charged BEM triangles and rectangles

Triangles and rectangles have many applications in mathematics, engineering and science. The finite element method [Hue75, Seg84, CMP89, Gup99] (FEM) and the boundary element method [Gup99, Kyt95, GKW03, BSD08, BTW84, BD92, Cor09] (BEM) rely especially heavily on triangles and rectangles as basic elements for their discretization procedure. In order to obtain the system of equations with the nodal function values of the elements in FEM and BEM, numerical or analytical integrations over the elements are needed.

The main subject of the following chapter is the three-dimensional electric potential and field calculation of charged triangular and rectangular BEM elements. Electric field calculation is important in many areas of physics: electron and ion optics, charged particle beams, charged particle traps, electron microscopy, electron spectroscopy, plasma and ion sources, electron guns, etc. [Szi88, HK89]. A special kind of electron and ion energy spectroscopy is realized by the MAC-E filter spectrometers, where the integral energy spectrum is measured by the combination of electrostatic retardation and magnetic adiabatic collimation. Examples are, besides the KATRIN pre- and main electron spectrometers [A$^+$04, PRG$^+$12, A$^+$16b] (cf. ch. 2), the Mainz and Troitsk electron spectrometers [K$^+$05, Lob03] and the aSPECT proton spectrometer [G$^+$05, B$^+$08]. High accuracy electric field and potential computations are indispensable for precise and reliable charged particle tracking calculations for these experiments. For this purpose the open source C++ codes *KEMField* [Cor14] and *Kassiopeia* [Fur15, GF$^+$16, Gro15], as described in chapter 3, are used in both the KATRIN and aSPECT experiment.

For electric potential and field computation with BEM [Szi88, HK89, CS00, Cor09], the surface of the electrodes is discretized by many small boundary elements, and a linear algebraic equation system is obtained for the unknown charge densities of the individual elements. To solve these equations, either a direct or an iterative method is used. When the charge densities are known, the potential and field at an arbitrary point (called field point) can be computed by summing the potential and field contributions of all elements. The electric potential and field of a single charged element at the field point can be expressed by analytical or numerical integration of the point-charge Coulomb formula times the charge density over the element surface. In the simplest case of constant BEM elements, the charge density is assumed to be constant over the element surface.

The following chapter focuses on analytical and numerical integration techniques over triangular and rectangular surfaces. First, a very efficient analytical surface integration method, based on RWG basis functions [HTS06], is derived for electrostatic potential and

field functions in sections 4.1.2 and 4.1.3. Compared to the ansatz chosen in [Cor09, Cor14, FLC+12], this method does not contain more than two transcendental functions and allows furthermore to compute the potential and field in a single computation step. A careful treatment of special field point locations has been implemented; the field point can be located directly even on or between meshed electrode elements giving reasonable results without canceling the computation. Here the analytical method [Cor09] suffered from incorrect results, which led to wrong charge density and field values.

After the discussion of the potential and field results, the evaluation of special field points and the implementation of the method are discussed.

The analytical integration method for field points far from the elements leads to numerical problems. In some special cases, however, numerical integration can be more advantageous than analytical integration. In section 4.2 this benefit is demonstrated for the case of electric potential and field computation of charged triangles and rectangles applied in the boundary element method (BEM). Analytical potential and field formulas are rather complicated (even in the simplest case of constant charge densities) compared to numerical formulas, and have usually larger computation times, furthermore at field points far from the elements they suffer from large rounding errors. On the other hand, Gaussian cubature, which is an efficient numerical integration method, yields simple and fast potential and field formulas that are very accurate far from the elements. The simplicity of the method is demonstrated by the physical picture: the triangles and rectangles with their continuous charge distributions are replaced by discrete point charges, whose simple potential and field formulas explain the higher accuracy and speed of this method. The main principle of Gaussian cubature is explained in section 4.2.2, followed by the investigation of the numerical accuracy of single triangular and rectangular elements in sec. 4.2.3.

Sec. 4.3 contains results for accuracy comparisons of potential and field simulations with two complex electrode geometries containing 1.5 million triangles and 1.5 million rectangles, respectively. The table in this section shows that the relative errors of the Gaussian cubature calculations are much smaller than the errors of the analytical calculations. In fact, the Gaussian cubature relative error values are close to 10^{-15}, i.e. the best accuracy that is possible to obtain with the double precision arithmetic that is used in these computations. Sec. 4.4 presents an additional advantage of the Gaussian cubature method: the potential and field calculations with low-N cubature formulas are significantly faster than the corresponding simulations with analytical integration. E.g. the 7-point cubature method in CPU computations is about five times faster than the analytical integration method as explained in sec. 4.1 and more than ten times faster than the analytical integration method of ref. [Cor14]. The larger speed of the Gaussian cubature method is due to its simplicity: it needs the evaluation of only one square root and one division operation for each Gaussian point, in addition to multiplications and additions, while the analytical integration methods need many time consuming transcendental function evaluations (like *log*, *atan2* etc.). Of course, for the elements with smaller distance ratios the cubature formulas with larger number of points (e.g. 12, 19 or 33) have to be used (to get an acceptable accuracy level), and they are slower (although still faster than the analytical methods). Nevertheless, the distance ratio distribution plots in sec. 4.3 show that for most of the elements of a typical electrode geometry the fast 7-point cubature method can be used.

This chapter closes with sec. 4.5, where the computation of potentials and fields is applied for the particular case of very fast computations for particle-tracking in non-axial electric dipole fields. The electrode model is discussed regarding accuracy and speed itself, followed by the incorporation of the numerical integration techniques into the fast multipole field solver code. Finally the code is validated by dedicated accuracy and speed comparisons.

4.1 Analytical computation of fields and potentials for triangles and rectangles

Up to now, surface integrals of meshed surface elements have been evaluated analytically. The calculation of the integrals is needed either by the calculation for potential and fields at arbitrary space points (cf. sec. 3.4.5.1) or in context of the solution of charge densities [FLC+12]. The analytical computation method [Cor09, Cor14, FLC+12] (labeled in the following as "analytical 1") suffers unfortunately from very long computation times and the need of many transcendental functions, which can lead to numerical instabilities as will be explained later. Furthermore, potential and field values cannot be calculated in a single computation step, leading to an increased computation time.

In addition to the large relative potential and field errors, the analytical 1 method of refs. [Cor14, FLC+12] has the following problem for the field computation of triangles: depending from the electrode geometry, at some very sharply defined field points (e.g. $\mathbf{P} = (0, 0, 0)$) the relative field error is extremely large (more than 10), i.e. the field value is completely wrong, and in some cases one gets *nan* or *inf* results (with C++ compiler). Only a few triangles (from the 1.5 million) are responsible for these wrong field values. Also, electric field values located in the same plane of triangles are wrong. The latter issue is important for calculating the charge at dielectric surfaces [Wul14].

New integral formulas for the analytical calculation of electrostatic potentials and fields has been studied in context of [HTS06]. The goal is to derive in the following compact analytical expressions for the surface integrals of polygons over the potential and field function.

4.1.1 RWG basis functions

The presented ansatz comes from the numerical solution of electrodynamic scattering problems. The most common method to solve these integrals is the Method of Moments (MoM). In this case, the goal is to calculate unknown electric or magnetic surface current distribution. Equally to the electrostatic BEM problem, the surface is meshed into small triangular mesh elements while the currents on these elements can then be approximated by an expansion in corresponding basis functions depending from the mesh shape [RWG82]. Usually triangular and rectangular patches are the most commonly used mesh shapes, but in the following triangular shapes will be regarded only. Always a pair of two adjacent triangles will be defined as can be seen in figure 4.1. Both triangles share a common edge I_n with length L. Let A^+ and A^- be the area of the two triangles and $\boldsymbol{p}^+$ and $\boldsymbol{p}^-$ are the vertices to the corner points of each triangle. The corresponding basis function reads as follows:

$$\boldsymbol{f}_n(\boldsymbol{r}') = \begin{cases} \frac{L}{2A^+}(\boldsymbol{r}' - \boldsymbol{p}^+), & \text{if } \boldsymbol{r}' \in T^+ \\ \frac{L}{2A^-}(\boldsymbol{r}' - \boldsymbol{p}^-), & \text{if } \boldsymbol{r}' \in T^- \\ 0, & \text{otherwise.} \end{cases} \tag{4.1}$$

Applying these basis functions to surface integral expression leads to double integrals with singular kernels. Mostly the singularity subtraction method will be applied here in order to obtain a closed form of the integral equations. In the following, a solution for the integrals for the potential as well for the fields is derived. Mainly important are the following two functions:

$$K_1^q(\mathrm{spt}(\boldsymbol{f}_n)) = \int_{\mathrm{spt}} R^q \left(\nabla' \cdot \boldsymbol{f}_n(\boldsymbol{r}')\right) \mathrm{d}S' \tag{4.2}$$

$$\boldsymbol{K}_3^q(\mathrm{spt}(\boldsymbol{f_n})) = \int_{\mathrm{spt}} \nabla' R^q \mathrm{d}S', \tag{4.3}$$

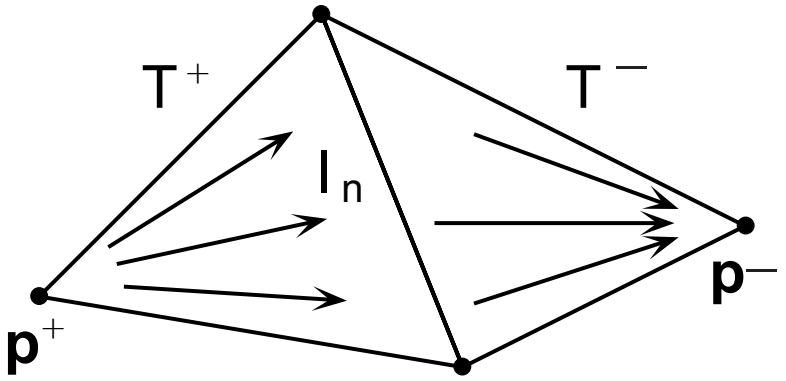

Figure 4.1: RWG basis functions for a pair of triangular surfaces and illustration of surface currents. Both triangles share a common edge I_n and the vertices $\boldsymbol{p}^+$ and $\boldsymbol{p}^-$ label the edges opposite to the common edge I_n. The arrows indicate the direction of RWG basis functions $\boldsymbol{f}_n(\boldsymbol{r})$ Adapted from [HTS06].

where R is define as $R^q = |\boldsymbol{r} - \boldsymbol{r'}|^q$ and spt denotes the support of the corresponding function. They directly define the electric potential and field for the case $q = -1$ and are solved in the following. For more detailed information on this topic the reader is referred to [HTS06]. Whereas in this case surface currents are defined onto a discretized triangular or rectangular geometry, the formulas can be applied very well to electrostatic problems with constant charge densities, too. The electric potential $U(\boldsymbol{r})$ and field $\boldsymbol{E}(\boldsymbol{r})$ are given as follows with constant charge density σ:

$$U(\boldsymbol{r}) = \frac{\sigma}{4\pi\varepsilon_0} K_1^q(\mathrm{spt}(\boldsymbol{f}_n)) \tag{4.4}$$

$$\boldsymbol{E}(\boldsymbol{r}) = \frac{\sigma}{4\pi\varepsilon_0} \boldsymbol{K}_3^q(\mathrm{spt}(\boldsymbol{f_n})). \tag{4.5}$$

4.1.2 Integral solution for potential function in RWG basis

The goal is to derive analytic surface integrals for polygons which avoid transcendental functions as much as possible. Green's function is replaced by the series expansion of the differential operator. First the surface divergence of

$$\nabla'_s \cdot \left((\boldsymbol{r} - \boldsymbol{r'}) R^q \right) = \left(\nabla'_s \cdot (\boldsymbol{r} - \boldsymbol{r'}) \right) R^q + (\boldsymbol{r} - \boldsymbol{r'}) \cdot (\nabla'_s R^q) \tag{4.6}$$

is computed. After applying the product rule, the surface divergence as well as the surface gradient has to be computed. Beginning by computing the surface gradient $\nabla'_s R^q$ which is defined in general as

$$\nabla'_s R^q = \nabla' R^q - \hat{\mathbf{n}} \left(\hat{\mathbf{n}} \cdot \nabla' R^q \right). \tag{4.7}$$

As it can be seen by the formula, the surface gradient is equal to the gradient subtracted with the normal component. In a next step the gradient

$$\nabla R^q = \nabla |\boldsymbol{r} - \boldsymbol{r'}| \tag{4.8}$$

$$= -q |\boldsymbol{r} - \boldsymbol{r'}|^{q-2} (\boldsymbol{r} - \boldsymbol{r'}) \tag{4.9}$$

$$= -q R^{q-2} (\boldsymbol{r} - \boldsymbol{r'}). \tag{4.10}$$

is evaluated. After putting all previous results together and defining the height between surface of the polygon and the field point as $|h|$ with

$$h = \hat{\mathbf{n}} \cdot (\boldsymbol{r} - \boldsymbol{r'}), \tag{4.11}$$

one gets

$$(\boldsymbol{r}-\boldsymbol{r'})\cdot\nabla'_s R^q = -qR^q + h^2 qR^{q-2}. \tag{4.12}$$

It remains to compute

$$\nabla'_s\cdot(\boldsymbol{r}-\boldsymbol{r'}) = -2. \tag{4.13}$$

This value results from setting $\nabla = \nabla_s + \nabla_n$. Since one only wants to obtain the surface divergence, ∇_n can be set to zero.

Putting all terms together the final result reads as:

$$\nabla'_s\cdot\left((\boldsymbol{r}-\boldsymbol{r'})\,R^q\right) = -2R^q - qR^q + qR^{q-2}h^2 \tag{4.14}$$

The integrand R^q can now be written as

$$R^q = \frac{q}{q+2}h^2R^{q-2} - \frac{1}{q+2}\nabla_s\left((\boldsymbol{r}-\boldsymbol{r'})\,R^q\right). \tag{4.15}$$

Next the surface integral is taken over each term:

$$\int_P R^q \mathrm{d}S' = \frac{qh^2}{q+2}\int_P R^{q-2}\mathrm{d}S' - \frac{1}{q+2}\int_P \nabla'_s\left((\boldsymbol{r}-\boldsymbol{r'})\,R^q\right)\mathrm{d}S' \tag{4.16}$$

For the integral over the surface divergence, Gauss' theorem in two dimensions is needed:

$$\int_P \nabla'_s\left((\boldsymbol{r}-\boldsymbol{r'})\,R^q\right)\mathrm{d}S' = \int_{\partial P}\hat{\mathbf{m}}\cdot(\boldsymbol{r'})(\boldsymbol{r}-\boldsymbol{r'})R^q\mathrm{d}l'. \tag{4.17}$$

$\hat{\mathbf{m}}_i(\boldsymbol{r'})$ denotes the outward directed unit normal vector which remains constant for all vectors $\boldsymbol{r'}$ in the i'th side ∂P_i of the polygon surface P. The projection t_i is defined as

$$t_i = \hat{\mathbf{m}}_i(\boldsymbol{r'})\cdot(\boldsymbol{r}-\boldsymbol{r'}), \tag{4.18}$$

and one obtains after abbreviating the surface integral over R^q by $I_q^S(P)$ following recursive formula:

$$I_q^S = \frac{qh^2}{q+2}I_{q-2}^S(P) - \frac{1}{q+2}\sum_{i=1}^{m} t_i I_q^L(\partial P_i). \tag{4.19}$$

For the electrostatic potential it is necessary to set $q=-1$, this results in following final recursive formula:

$$I_{-1}^S = \int_P R^q\mathrm{d}S' = -h^2 I_{-3}^S(P) - \sum_{i=1}^{m} t_i I_q^L(\partial P_i) \tag{4.20}$$

Evaluation of line integral I_{-1}^L

For the computation of $\int_P R^q\mathrm{d}S'$ a further line integral has to be calculated:

$$I_{-1}^L(\partial P_i) = \int_{\partial P_i}\frac{1}{R}\mathrm{d}l' = \int_{s^-}^{s^+}\frac{1}{\sqrt{s^2+R_0^2}}\mathrm{d}s \text{ , with} \tag{4.21}$$

$$R_0^2 = t^2 + h^2. \tag{4.22}$$

Here the line integral has been expressed in terms of the orthogonal components $\boldsymbol{s}$, $\boldsymbol{t}$, and $\boldsymbol{h}$, which are sketched on figure 4.2 In addition, the constants s^+ and s^- are defined:

$$s^+ = (\boldsymbol{p_2}-\boldsymbol{r})\cdot\hat{\mathbf{s}}, s^- = (\boldsymbol{p_1}-\boldsymbol{r})\cdot\hat{\mathbf{s}}, \tag{4.23}$$

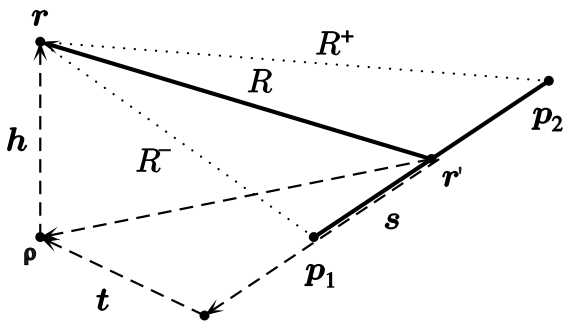

Figure 4.2: Sketch of the integral along the line ∂P_i. The vector $\boldsymbol{r}-\boldsymbol{r'}$ can be expressed in terms of three orthogonal components $\boldsymbol{s}$, $\boldsymbol{t}$ and $\boldsymbol{h}$. The vector $\boldsymbol{r'}$ resides on the line ∂P_i between the end points of the line $\boldsymbol{p_1}$ and $\boldsymbol{p_2}$. Illustration taken from [HTS06].

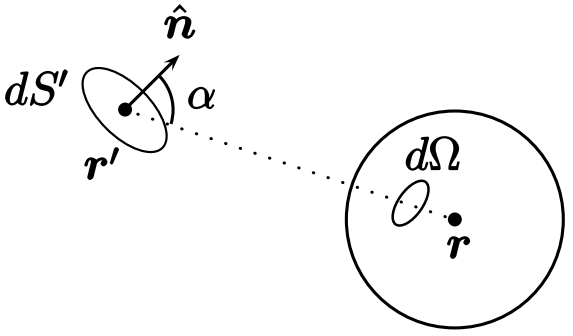

Figure 4.3: Projection of a surface element as described by the spanned solid angle. The projection of the surface element $\mathrm{d}S'$ as seen from r' is described by the solid angle $\mathrm{d}\Omega$ and depends on the angle α between the normal vector $\hat{\mathbf{n}}$ and the vector $r - r'$. Illustration taken from [HTS06].

with

$$\hat{\mathbf{s}} = \frac{(\boldsymbol{p_2} - \boldsymbol{p_1})}{|(\boldsymbol{p_2} - \boldsymbol{p_1})|}. \tag{4.24}$$

The solution of the following integral can be taken for example from [BS79]:

$$\int_{s^-}^{s^+} \frac{1}{\sqrt{s^2 + R_0^2}} \mathrm{d}s = \ln\left(s^+ + \sqrt{(s^+)^2 + R_0^2}\right) - \ln\left(s^- + \sqrt{(s^-)^2 + R_0^2}\right) \tag{4.25}$$

If the field point is located on a side line, this integral the expression $s^- + \sqrt{(s^-)^2 + R_0^2}$ gets zero and leads to a division through zero or $\ln(0)$. In order to prevent the code from delivering invalid results in that particular case, the latter term will be expressed in a Taylor expansion:

$$s^- + \sqrt{(s^-)^2 + R_0^2} \approx -|s^-| + |s^-| \left(1 + \frac{1}{2}\left(\frac{R_0}{s^-}\right)^2\right) \tag{4.26}$$

Evaluation of surface integral I^S_{-3}

For the electric field and the potential formulas, the surface integral of the function $\frac{1}{R^3}$ has to be computed. Beforehand the quantity $h = \hat{\mathbf{n}}(\boldsymbol{r'}) \cdot (\boldsymbol{r} - \boldsymbol{r'})$ is defined, where $\hat{\mathbf{n}}$ is the right-handed unit normal vector of the polygon P. The magnitude $|h|$ is the distance of the field point to the plane of the polygon P. In a first step the integral is multiplied

with h and in a second step the integrand is expressed as a gradient:

$$hI^S_{-3}(P) = h\int_P \frac{1}{R^3}\mathrm{d}S' = \int_P \frac{\hat{\mathbf{n}}\cdot(\boldsymbol{r}-\boldsymbol{r'})}{R^3}\mathrm{d}S' \tag{4.27}$$

$$= -\int_P \hat{\mathbf{n}}(\boldsymbol{r'})\nabla'\frac{1}{R}\mathrm{d}S' \tag{4.28}$$

The angle α between the normal vector and the connecting line between the center point of the polygon and the field point $(\boldsymbol{r}-\boldsymbol{r'})$ is $\hat{\mathbf{n}}(\boldsymbol{r'})\cdot(\boldsymbol{r}-\boldsymbol{r'}) = R\cos(\alpha)$. The orthogonal projection of the surface element $\mathrm{d}S'$ of the polygon P onto the plane which is perpendicular to the vector $\boldsymbol{r}-\boldsymbol{r'}$ is equal to $|\cos(\alpha)|dS'$. In this way the infinitesimal solid angle can be defined by

$$\mathrm{d}\Omega = \frac{\cos(\alpha)}{R^2}\mathrm{d}S' = \frac{\hat{\mathbf{n}}(\boldsymbol{r'})\cdot(\boldsymbol{r}-\boldsymbol{r'})}{R^3}\mathrm{d}S' = \frac{h}{R^3}\mathrm{d}S'. \tag{4.29}$$

The infinitesimal solid angle is integrated afterwards over the surface:

$$\Omega = \int_P \mathrm{d}\Omega = \int_P \frac{h}{R^3}\mathrm{d}S'. \tag{4.30}$$

After setting this result equal to 4.27, the surface integral I^S_{-3} can be expressed in terms of the solid angle Ω, which can be seen as the shadow projection of the polygon on a unit sphere.

$$I^S_{-3}(P) = \frac{1}{h}\Omega \tag{4.31}$$

Computation of solid angle with Euler-Erikksons formula for triangles

In principle the solid angle of any polygon can be computed using Girard's spherical excess formula, but in context of the realization of triangular and rectangular shapes, the simpler Euler-Erikkson formula for the solid angle of triangles will be used, since arbitrary polygons can be expressed as triangles.

α_n is the angle between two polygon side lines which are projected on the unit sphere.

$$|\Omega| = \sum_{n=1}^{m}\alpha_n - (m-2)\pi \tag{4.32}$$

m is the number of the polygon sides, the unit sphere is centered at r'. Any polygon can be subdivided into a finite number of triangles. As already mentioned, the much simpler Euler-Eriksson formula can be used:

$$|\Omega| = 2\arctan(y/x), \tag{4.33}$$

with

$$x = 1 + \boldsymbol{a_1}\cdot\boldsymbol{a_2} + \boldsymbol{a_1}\cdot\boldsymbol{a_3} + \boldsymbol{a_2}\cdot\boldsymbol{a_3} \tag{4.34}$$

$$y = |\boldsymbol{a_1}\cdot(\boldsymbol{a_2}\times\boldsymbol{a_3})|. \tag{4.35}$$

Here, $\boldsymbol{a_n}$ is defined as a unit vector from the field point to n'th vertex point of the triangle:

$$\boldsymbol{a}_n = \frac{\boldsymbol{p}_n - \boldsymbol{r}}{|\boldsymbol{p}_n - \boldsymbol{r}|}. \tag{4.36}$$

The vertex points are denoted in positive rotation order with respect to the unit normal vector perpendicular to the triangle surface.

4.1.3 Integral solution for field function in RWG basis

In a first step the gradient operator is expressed as a sum of a surface and a normal part. Likewise in the previous case the integrals are computed over a general polygon surface.

$$\int_P \nabla' R^q \mathrm{d}S' = \int_P \nabla'_s R^q \mathrm{d}S' + \int_P \nabla'_n R^q \mathrm{d}S'. \tag{4.37}$$

In a first step the normal gradient is computed:

$$\nabla'_n R^q = \hat{\mathbf{n}}(\boldsymbol{r}')(\hat{\mathbf{n}}(\boldsymbol{r}') \cdot \nabla')R^q = -\hat{\mathbf{n}}(\boldsymbol{r}')hqR^{q-2} \tag{4.38}$$

The product $\phi = R^q\hat{\mathbf{m}}$ is assumed to be constant for the side i of the polygon. For this special case the Gaussian theorem reads as follows:

$$\int \nabla \boldsymbol{A} \cdot \mathrm{d}S = \int_{\partial S} (\boldsymbol{A}\hat{\mathbf{n}})\mathrm{d}l. \tag{4.39}$$

If the vector field $\boldsymbol{A}$ can be expressed as $\boldsymbol{A} = \phi\boldsymbol{c}$, then

$$\int_S \nabla\phi \mathrm{d}S' = \int_{\partial S} \phi\hat{\mathbf{n}}\mathrm{d}l. \tag{4.40}$$

In this way the integral over the surface gradient transforms as:

$$\int_P \nabla'_S R^q \mathrm{d}S' = \sum_{i=1}^{m} \hat{\mathbf{m}}_i \int_{\partial P} R^q \mathrm{d}l' \tag{4.41}$$

After summing up the two terms, one obtains a recursive formula for the electric field of arbitrary polygons:

$$\boldsymbol{K}_3^q = \int_P \nabla' R^q \mathrm{d}S' = \sum_{i=1}^{n} \hat{\mathbf{m}}_i I_q^L(\partial P_i) - hq\hat{\mathbf{n}} I_{q-2}^S(P) \tag{4.42}$$

Setting again $q = -1$ for electrostatics leads to the final expression for the electric field:

$$\boldsymbol{K}_3^{-1} = \sum_{i=1}^{n} \hat{\mathbf{m}}_i I_{-1}^L(\partial P_i) + h\hat{\mathbf{n}} I_{-3}^S(P). \tag{4.43}$$

4.1.4 Code implementation and optimization for BEM

In the following, the code realization of the potential and field function in terms of the line integral I_{-1}^L and the surface integral I_{-3}^S is discussed. Figure 4.4 shows the flow and the interplay of the different functions. One key benefit of this method is the ability to compute the electric potential and field simultaneously, since both the electric potential and field are dependent from the integrals I_{-1}^L and I_{-3}^S in the same fashion, they only differ by the prefactors. Consequently, a dedicated function has been provided for the simultaneous evaluation of potential and field. In order to guarantee correct results on the surface of mesh elements, the code checks if the field point is located on a vertex point of an element or if the field point is located on the side-line of an element. For example the field values are not defined at these special points, at the edges of a polygon te field values have a logarithmic singularity [Dur64]. For all cases the corresponding distances from field point to the mesh element are calculated. As already discussed, if the field point is on the side line, a Taylor expansion will be calculated. If the field point is on a edge the field point will be pushed in the direction which is perpendicular to the element's surface and recalculated. In context of charge density solving algorithms of BEM, like the Robin Hood algorithm [FLC+12], the potential and the electric field has to be evaluated at the

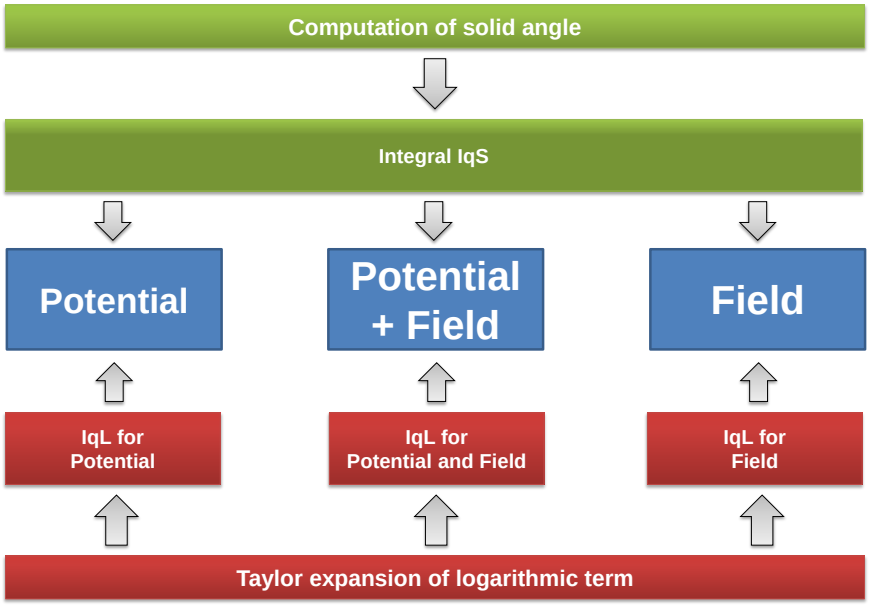

Figure 4.4: Schematic representation of code structure of analytic integrators. The diagram represents the code structure for the calculation potentials and fields of triangular and rectangular mesh elements equally.

center of an element (at the so-called collocation point). If meshed geometry elements do not overlap (without setting vertices), the above mentioned checks are note necessary [Bar15]. Especially for the GPU code realization these checks lead to a code overhead an a slight decrease of computation time. Following in the software, the user can exclude these checks if no field point has to be evaluated at side lines or edges. In order to avoid further code overhead, the solid angle and the logarithmic expansion are computed centrally for the corresponding shape type.

4.1.5 Comparison of analytic electrostatic potential and field computations

In the following the formulas which have been deduced in the previous sections are compared with the integrator classes as described in [Cor09, Cor14]. This short study focuses on the accuracy comparison of potentials and fields of triangles. For this reason, the averaged relative error of the potential and field of diced triangle geometries is plotted against the distance ratio from 2 to 10000 in 1000 steps. Latter is defined as the distance of the field point to the center of the element geometry over the average side length of the triangle. The averaged errors have been determined by comparison against a two-dimensional numerical Gauss-Legendre integration as reference value which is close to the floating-point accuracy of $\mathcal{O}(10^{-15})$. Further details on the realization of the applied error computation together with corresponding formulas can be found in section 4.2.1.

Figures 4.5 and 4.6 show clearly that the analytical value as obtained by the above-mentioned integration techniques is characterized by less fluctuations. Especially in the case of very low distance ratio values a relative error of the field of $\mathcal{O}(10^{-14})$ can be obtained while the RWG potential computations achieve especially in low distance ration regions an accuracy of nearly $\mathcal{O}(10^{-15})$. Both plots indicate clearly that the fluctuations increase by higher distance ratio values. This fact is discussed in the following section 4.2 in context of the technique of numerical integration together with further accuracy and speed studies in secs. 4.3 and 4.4.

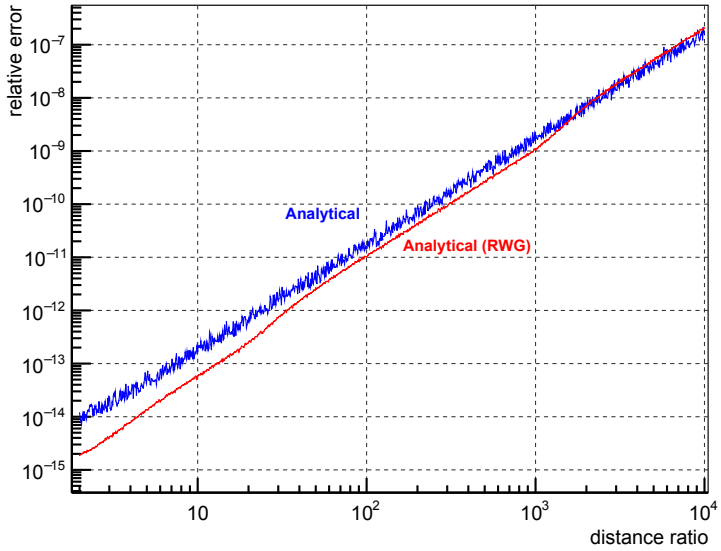

Figure 4.5: Comparison of analytically computed triangle potentials. The averaged relative error of the potential of diced triangle geometries is plotted against distance ratio values from 2 to 10000.

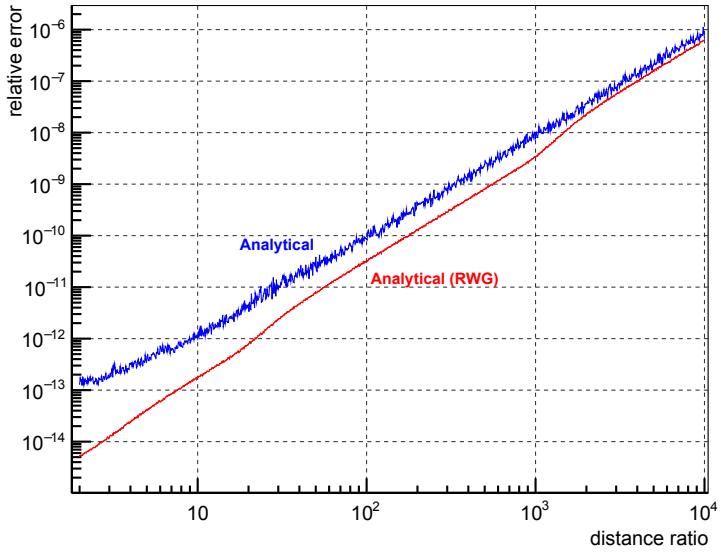

Figure 4.6: Comparison of analytically computed triangle fields. The averaged relative error of the field of diced triangle geometries is plotted against distance ratio values from 2 to 10000.

4.2 Numerical computation of fields and potentials for triangles and rectangles

It is a general belief that analytical integration is more accurate than numerical integration. This is in many cases true, but not always. A simple example with one-dimensional integral and small integration interval (sec. 4.2.1) shows that analytical integration can have a large rounding error, due to the finite arithmetic precision of the computer [Übe97, Gol91], while a simple numerical integration achieves in this case a much higher accuracy. Analytically calculated electric potential and field formulas of charged triangles and rectangles show a similar behavior for large distance ratios. Sec. 4.2.1 presents a few plots for the

relative error of the analytical potential and field of triangles and rectangles as a function of the distance ratio. One can see that for field points far from the element the analytically computed potential and field values have significant rounding errors that are much higher than the machine epsilon of the corresponding arithmetic precision [Übe97, Gol91] that is used for the computation. The analytical integration formulas of refs. [Cor14, FLC+12] and [HTS06] (also: sec. 4.1 of this thesis) have been used used for these plots. There are many other published analytical integration results for potential and field calculation of triangles and rectangles [RGWV79, OH82, DH89, THT02, MM07, LPPM11, Car13, Dur64, BMB73a, BMB73b, Eup85], and these suffer probably from the same rounding error that increases with the distance ratio. The rounding errors are caused by the transcendental functions (e.g. *log*, *atan2* etc.) in the analytical formulas and by the well-known subtraction cancellation problem of finite-digit floating-point arithmetic computations. Another disadvantage of the analytical integrations is that the analytical potential and field formulas are rather complicated, and consequently the calculations are rather time consuming.

According to the aforementioned simple example with one-dimensional integration, one can eliminate the rounding error problem of the analytical potential and field calculations by using numerical integration. The two-dimensional numerical integration could be performed by two subsequent one-dimensional integrations, using e.g. the efficient Gauss-Legendre quadrature method with 16 nodes for each dimension [Eva93, KS05]. If the field point is not too close to the triangle or rectangle, this bi-quadrature method results in very accurate integral values. In fact, we use this method as a reference integration in order to define the errors of the other integration methods. Nevertheless, if the goal is also to minimize the computation time, then it is more expedient to use the Gaussian cubature method for two-dimensional numerical integration, because it has fewer function evaluations for a targeted accuracy. In sec. 4.2.2 a short overview is given about the numerical integration of an arbitrary function over a triangle or a rectangle with Gaussian cubature. The integral is approximated by a weighted sum of the function values at a given number of Gaussian points. The accuracy of this approximation is defined by the degree of the cubature formula, which usually increases with the number N of Gaussian points. Appendices C and D contain ten tables of the Gaussian points and weights of five different Gaussian cubature formulas for triangles and rectangles. These formulas have various number of Gaussian points (from $N = 4$ to $N = 33$) and degrees of accuracy (from 3 to 13).

In sec. 4.2.3 we apply the general Gaussian cubature formulas for electric potential and field calculation of triangles and rectangles with constant charge density. The mathematical formalism of the Gaussian cubature integration is illustrated by a nice physical picture: the triangles and rectangles with continuous charge distribution are replaced by discrete point charges, and the complicated two-dimensional integration of the potential-field calculation is substantially simplified by using the potential and field formulas of point charges. The figures in sec. 4.2.3 reveal that for field points far from the elements the Gaussian cubature method has high accuracy and is exempt from the rounding error problem of the analytical integrations. The relative error of the potential and field calculation with a given Gaussian cubature formula is about 10^{-15} above some distance ratio limit (with double precision computer arithmetics), and increases with decreasing distance ratio below this limit, which decreases with increasing number of Gaussian points (i.e. for more accurate cubature formulas). For small distance ratios, e.g. DR < 3, the Gaussian cubature formulas are not accurate enough, and analytical integration should be used in this region.

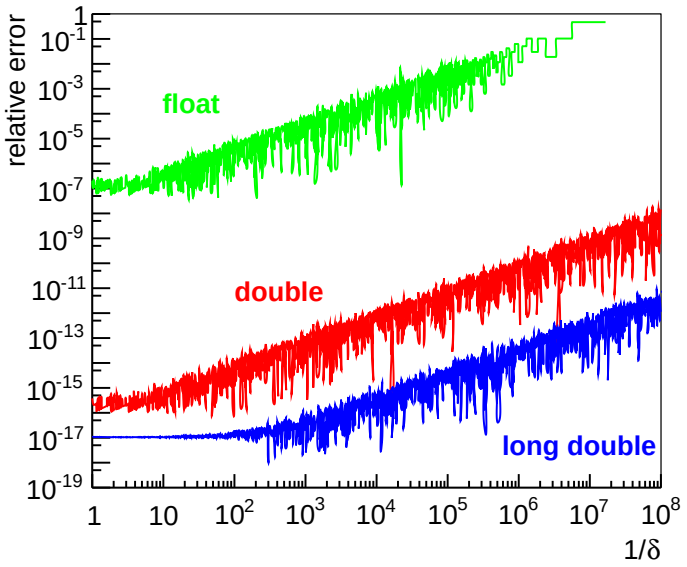

Figure 4.7: Relative error of the one-dimensional analytical integral $\exp(1+\delta) - \exp(1)$ **as function of** $1/\delta$**, for float, double and long double C++ arithmetic types.**

4.2.1 Reevaluation of analytical surface integration

In the beginning, a simple one-dimensional integral of the function $\exp(x)$ from 1 to $1+\delta$ is considered. The analytical result from the Newton-Leibniz formula is $\exp(1+\delta) - \exp(1)$, and this is for small δ a typical example for loss of accuracy (digits) when subtracting two almost equal numbers. The problem is that the computer stores in a floating-point arithmetic number always a finite number of digits [Übe97, Gol91], and a few of them can disappear at subtraction. Therefore, the relative error of the above integral for small δ is much larger than the machine epsilon of the floating-point number system that is used for the computation.

If a high accuracy is required for the integral value with small δ, it is better to use numerical integration, e.g. Gaussian quadrature. With double precision arithmetic and with Gauss-Legendre quadrature [Eva93, KS05] using 16×16 integration nodes, the relative error of the integral is smaller than 10^{-15}, i.e. the numerical integration has the maximal precision that is possible to achieve with the corresponding floating-point number system. One can see this by the independence of the integral value on the number of integration nodes, or by comparing with a higher precision (e.g. long double) computation. Due to this fact, we can get the accuracy of the analytical integral values by comparing them with the numerical quadrature values: $\mathrm{err}(I_{an}) = |(I_{an} - I_{num})/I_{num}|$.

Fig. 4.7 presents the relative error $\mathrm{err}(I_{an})$ of the analytical integral above as a function of $1/\delta$, for three different C++ floating-point arithmetic types: float, double and long double. The relative error increases with $1/\delta$ and decreases with increasing precision of the floating-point arithmetic. It is then obvious that the analytical integration has a rounding error which can be for small integration interval size δ much larger than the precision of the floating-point arithmetic type that is used for the calculation. The numerical integration (like Gaussian quadrature) is, however, devoid of this precision loss problem.

The above-mentioned issue has to be discussed in context of electric potential and field computation of triangles and rectangles with constant charge density σ.
The potential Φ and field $\mathbf{E}$ at field point $\mathbf{P}$ can be generally written (in SI units) as

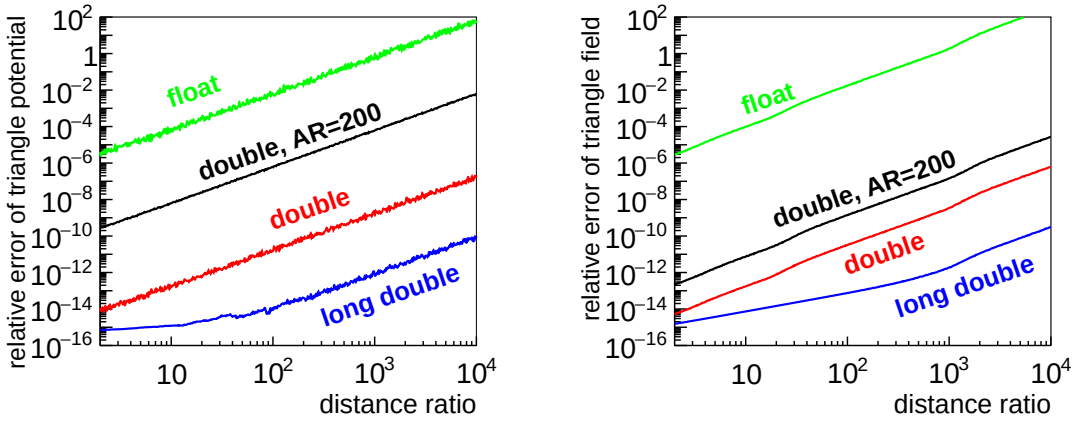

(a) Averaged relative error of triangle potential (b) Averaged relative error of triangle field

Figure 4.8: Averaged relative error of the analytically computed triangle potential (refs. [Cor14, FLC+12], left) and triangle field (ref. [HTS06], right), as a function of the distance ratio, for float (green), double (red) and long double (blue) C++ arithmetic types (with low aspect ratio triangles), and with double precision and high aspect ratio (AR=200) triangles (black).

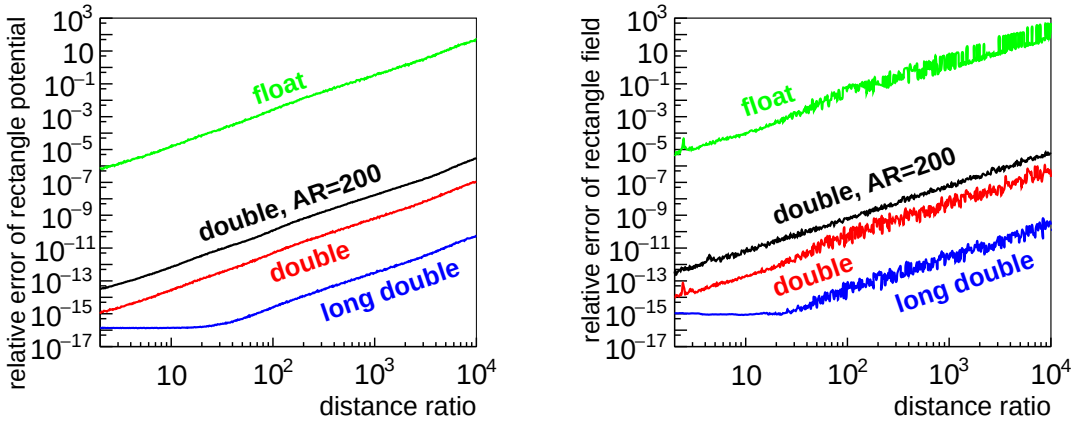

(a) Averaged relative error of rectangle potential (b) Averaged relative error of rectangle field

Figure 4.9: Averaged relative error of the analytically computed rectangle potential (ref. [HTS06], left) and rectangle field (Ref. [Cor14], right), as a function of the distance ratio, for float (green), double (red) and long double (blue) C++ arithmetic types (with low aspect ratio rectangles), and with double precision and high aspect ratio (AR=200) rectangles (black).

surface integrals over the element:

$$\Phi(\mathbf{P}) = \frac{\sigma}{4\pi\varepsilon_0} \int\limits_{\text{element}} \mathrm{d}^2\mathbf{Q} \cdot \frac{1}{|\mathbf{P}-\mathbf{Q}|}, \qquad \mathbf{E}(\mathbf{P}) = \frac{\sigma}{4\pi\varepsilon_0} \int\limits_{\text{element}} \mathrm{d}^2\mathbf{Q} \cdot \frac{\mathbf{P}-\mathbf{Q}}{|\mathbf{P}-\mathbf{Q}|^3}, \tag{4.44}$$

where $\mathbf{Q}$ denotes the integration point on the element surface. The distance between the field point $\mathbf{P}$ and the center point (centroid) $\mathbf{Q}_{\text{cen}}$ of the triangle or rectangle is defined as: $D = |\mathbf{P} - \mathbf{Q}_{\text{cen}}|$, and L is the average side length of the triangle or rectangle (e.g. $L = (a+b+c)/3$, with triangle side lengths a, b and c). In the following, the distance ratio of the element and field point combination is defined as $\mathrm{DR} = D/L$; this corresponds to the $1/\delta$ parameter of the one-dimensional integral described above. In order to investigate the potential and field calculation of triangles and rectangles, the following procedure has been carried out. First, the corner points of triangles or rectangles have been diced inside

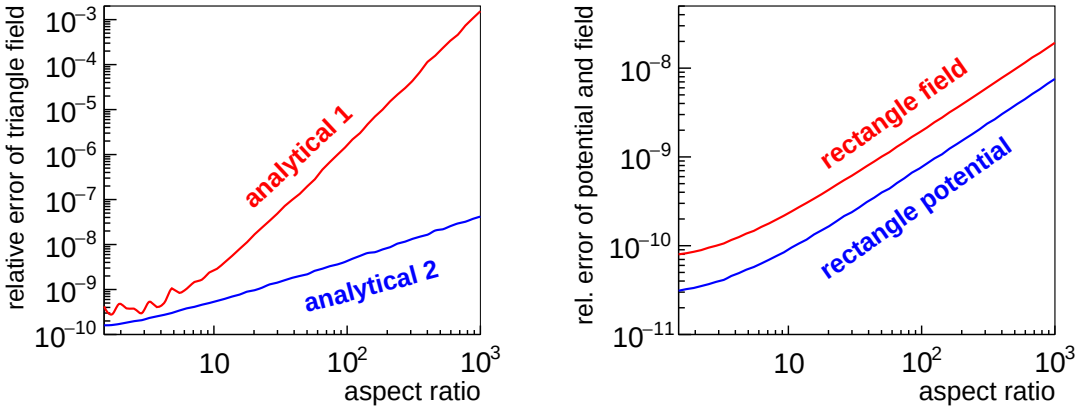

(a) Averaged relative error of analytical triangle field

(b) Averaged relative error of rectangle potential and field

Figure 4.10: Averaged relative error of the analytically computed triangle field (left, 1 (red): ref. [Cor14], 2 (blue): ref. [HTS06]), and rectangle potential and field (right, ref. [HTS06]; ref. [Cor14] is similar), as a function of the aspect ratio, with fixed distance ratio DR=300.

a cube with unit lengths as well as the direction unit vector of the field point has been diced relative to the triangle or rectangle centroid. Then, for a fixed distance ratio both the element (triangle or rectangle) and the field point are defined. The potential and field of the element with unit charge density is computed at the field point by two different analytical integration methods: first, with refs. [Cor14] (App. A and B) and [FLC+12] (App. A), and second, with ref. [HTS06] (eqs. 63 and 74) and section 4.1 of this thesis. In order to obtain the error of the analytical integrals, we also calculated the potential and field by numerical integration, using two successive one-dimensional Gauss-Legendre quadratures (GL2) [Eva93, KS05] with $n_{GL2} = 16$ integration nodes for both integrations. If the field point is located not too close to the element (i.e. for distance ratio above two), the latter method yields a relative accuracy which is close to the precision of the applied floating-point arithmetic type (e.g. order of 10^{-15} for double precision in C++). One can check that the GL2 integral values do not change if the discretization number n_{GL2} is changed, and possible rounding errors can be tested by comparing double and long double calculations. The relative error of the analytically computed potential is then: $\mathrm{err}(\Phi_{an}) = |(\Phi_{an} - \Phi_{GL2})/\Phi_{GL2}|$. For the field $\mathbf{E}$ the relative error is defined in the following way: $\mathrm{err}(\mathbf{E}_{an}) = \sum_{j=x,y,z} |\mathbf{E}_{j,an} - \mathbf{E}_{j,GL2}|/|\mathbf{E}|_{GL2}$, where the sum goes over the components x, y and z. 1000 elements and field point direction vectors are generated for each distance ratio, and the average of the above defined relative error values is taken. In this case the triangles and rectangles have small (mainly below ten) aspect ratios (AR). The triangle aspect ratio is defined as the longest side length divided by the corresponding height. Similarly, the rectangle aspect ratio is the longer side divided by the shorter side. Figures 4.8 and 4.9 present the above defined averaged relative errors for triangle and rectangle potential and field, computed by the analytical integration formulas of refs. [Cor14, FLC+12, HTS06], as a function of the distance ratio, for three different floating-point arithmetic types (float, double and long double of the C++ language) with low aspect ratio elements, and also for larger (AR=200) aspect ratio elements. For small distance ratio (below five), the relative error values are close to the corresponding floating-point arithmetic precision. Note that the used Gauss-Legendre quadrature implementation has double precision accuracy, therefore the relative error in case of long double precision is not smaller than 10^{-15} or so. Furthermore, the plots show that the relative error of the analytical integrals increases with the distance ratio and also with the aspect ratio, while it decreases with increasing precision of the floating-point arithmetic type.

It is obvious that the analytical integrals have significant rounding errors for large distance ratio. These potential and field errors are even much larger for triangles and rectangles with large aspect ratio, as one can see in Fig. 4.10. It can be conjectured that all other analytically integrated potential and field formulas in the literature (refs. [RGWV79, OH82, DH89, THT02, MM07, LPPM11, Car13, Dur64, BMB73a, BMB73b, Eup85]) suffer from similarly large rounding errors for field points located far from the elements.

4.2.2 Numerical integration with Gaussian cubature

The rounding error problem of the analytical integration can be solved by using numerical integration for field points far away from the element. Gaussian quadrature and cubature are efficient numerical integration techniques [Eva93, KS05, Str71, Eng80, EMU96] which can yield high accuracies with a minimal number of nodes (function evaluation points).

The integral of an arbitrary function f over a surface element can be generally approximated by Gaussian cubature as

$$\int_{\text{element}} \mathrm{d}^2\mathbf{Q} \cdot f(\mathbf{Q}) = \mathcal{A} \cdot \sum_{i=1}^{N} w_i \cdot f(\mathbf{Q}_i) + \mathcal{R}, \qquad \sum_{i=1}^{N} w_i = 1, \tag{4.45}$$

where $\mathbf{Q}_i$ and w_i are the Gaussian points (nodes, knots) and weights, respectively, and $\mathcal{A}$ denotes the area of the element. The remainder $\mathcal{R}$ is the absolute error of the Gaussian cubature integral formula.

To parametrize the Gaussian points $\mathbf{Q}_i$, it is expedient to use local coordinates: they rely on the element geometry for their definition and are generally called natural coordinates [Hue75, CMP89, Seg84]. In the case of rectangles, it is advantageous to use a local coordinate system whose axes are parallel with the side unit vectors $\mathbf{u}_x$ and $\mathbf{u}_y$ of the rectangle. An arbitrary point $\mathbf{Q}$ on the plane of the rectangle can be parametrized by the local natural coordinates x and y:

$$\mathbf{Q} = \mathbf{Q}_{\text{cen}} + \frac{a}{2}\, x\, \mathbf{u}_x + \frac{b}{2}\, y\, \mathbf{u}_y, \tag{4.46}$$

where $\mathbf{Q}_{\text{cen}}$ denotes the rectangle center, and a and b are the two side lengths; see Fig. 4.11(a). For $|x| \leq 1$ and $|y| \leq 1$ the point $\mathbf{Q}$ is inside the rectangle, otherwise it is outside.

For the parametrization of points in a triangle it is advantageous to use the so-called barycentric or area coordinates. An arbitrary point $\mathbf{Q}$ on the plane of the triangle can be written as a linear combination of the triangle vertex vectors $\mathbf{A}$, $\mathbf{B}$ and $\mathbf{C}$:

$$\mathbf{Q} = \lambda_A \mathbf{A} + \lambda_B \mathbf{B} + \lambda_C \mathbf{C}, \quad \text{with} \quad \lambda_A + \lambda_B + \lambda_C = 1, \tag{4.47}$$

where λ_A, λ_B and λ_C are the barycentric coordinates. They are all less than 1 if the point $\mathbf{Q}$ is inside the triangle. For $\lambda_A = 1$, $\lambda_B = \lambda_C = 0$: $\mathbf{Q} = \mathbf{A}$, and for $\lambda_A = 0$ the point $\mathbf{Q}$ is on the line $\mathbf{BC}$. $\lambda_A = \lambda_B = \lambda_C = 1/3$ corresponds to the centroid of the triangle. The coordinate λ_A is equal to the ratio of the triangle areas $\mathbf{QBC}$ and $\mathbf{ABC}$ (and similarly for λ_B and λ_C), as one can see in Fig. 4.11(b). Due to this property, the barycentric coordinates are also called area coordinates (see Refs. [Hue75, Seg84, CMP89]). The computation time of a Gaussian cubature formula is proportional to the number of Gaussian points (nodes) N. A good formula has small error (remainder $\mathcal{R}$ in Eq. 4.45) with small N. Usually, a two-dimensional Gaussian cubature formula is constructed so that it is exact (with $\mathcal{R} = 0$) for all possible monomials $f(x, y) = x^n y^m$ with $0 \leq n+m \leq d$, but for $n + m > d$ the remainder $\mathcal{R}$ is not zero. The integer d is called the degree of the cubature formula. A large degree d corresponds to high accuracy, but the number of nodes N, and so the computation time, also increases with d.

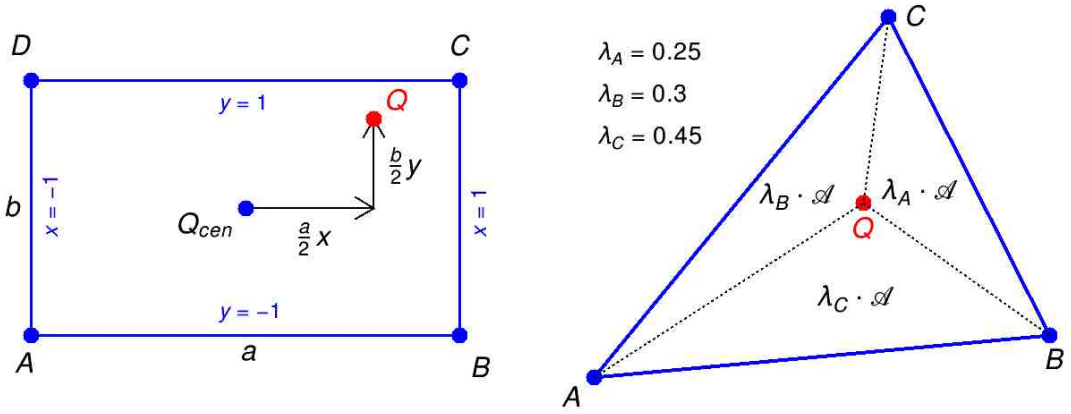

Figure 4.11: Natural local coordinates on a rectangle (left) and barycentric (area) coordinates on a triangle (right).

The definition of the degree above makes it plausible how to determine the nodes and weights for two-dimensional Gaussian cubature formulas: first, one calculates the integral (analytically or numerically) on the left-hand side of Eq. 4.45 for several different monomial functions $f(x, y) = x^n y^m$ (with $n + m \leq d$). Then, each integral value is set equal to the cubature sum formula on the right-hand side of Eq. 4.45 (with $\mathcal{R} = 0$). One obtains then the nodes and weights by solving this nonlinear equation system, which is obviously a difficult task, especially for large N and d. It is expedient to have all weights positive (to reduce rounding errors) and all nodes inside the element.

Gaussian point coordinates and weights for triangles and rectangles with various N and d values can be found in several books [Str71, Eng80, EMU96] and in many publications [Rad48, HS56, HS58, HMS56, Gat88, LJ75, Pap15, AC58, Tyl53, Möl76, CH88, RR69, OS06, Dun85, HP76, HP77, LG78, WX03, ZCL09]. Examples for very high degree cubature formulas are: $N = 175$, $d = 30$ for triangles in [WX03], and $N = 100$, $d = 23$ for rectangles in [OS06]. There are several review papers about the subject in the literature [CR93, LC94, Coo99, Coo02, Coo03, Coo].

In app. C barycentric coordinates and weights of five different Gaussian cubature formulas are presented for triangles: $N = 4$, $d = 3$ (Table C.1), $N = 7$, $d = 5$ (Table C.2), $N = 12$, $d = 7$ (Table C.3), $N = 19$, $d = 9$ (Table C.4) and $N = 33$, $d = 12$ (Table C.5). app. D contains Cartesian natural coordinates and weights of five different Gaussian cubature formulas for rectangles: $N = 4$, $d = 3$ (Table D.6), $N = 7$, $d = 5$ (Table D.7), $N = 12$, $d = 7$ (Table D.8), $N = 17$, $d = 9$ (Table D.9) and $N = 33$, $d = 13$ (Table D.10). In most cases, one row in a table corresponds to several nodes with equal weights: the coordinates of the other nodes can be obtained by various permutations or sign changes of the given numbers (see the table captions for detailed explanations). Figures 4.12 and 4.13 show a few examples for the Gaussian points of a triangle and a rectangle. In Fig. 4.12(a), point 1 corresponds to the first row in Table C.2 (this is the centroid of the triangle). Points 2 to 4 correspond to the second row: for point 2 $\rightarrow \lambda_A = t + 2ts$, for point 3 $\rightarrow \lambda_B = t + 2ts$, and for point 4 $\rightarrow \lambda_C = t + 2ts$ (the other barycentric coordinates are $t - ts$). Similarly, points 5 to 7 correspond to the third row in that table. These figures can be useful to understand the multiplicity structure of the tables in app. C and D.

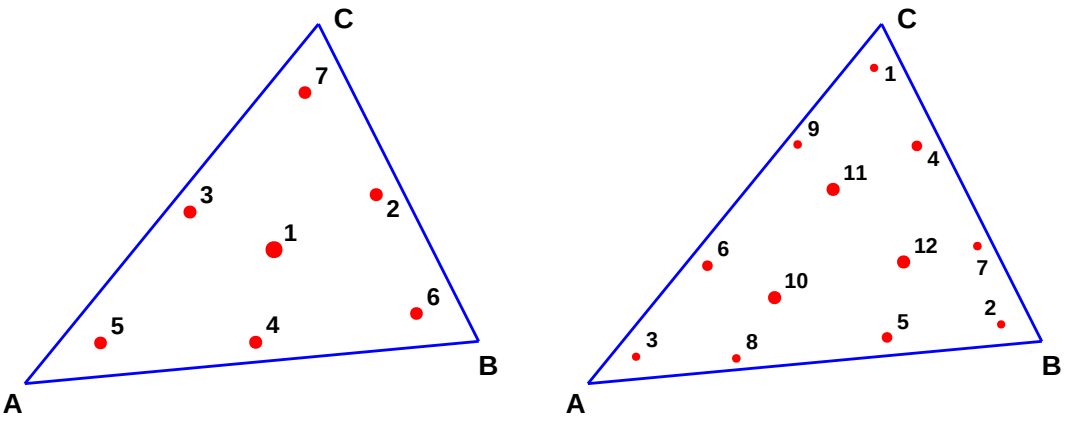

(a) Triangle 7 point (b) Triangle 12 point

Figure 4.12: Gaussian points of the 7-point (left) and the 12-point (right) cubature formula for triangle. The numbers are the indices of the Gaussian points. The surfaces of the red circles are proportional to the corresponding weights.

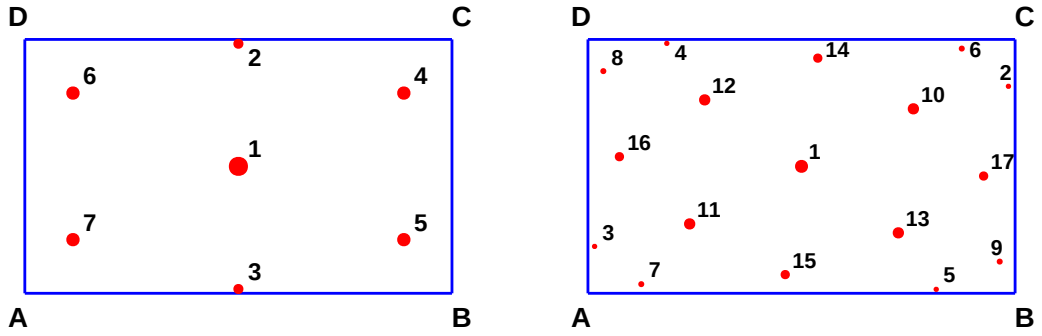

(a) Rectangle 7 point (b) Rectangle 17 point

Figure 4.13: Gaussian points of the 7-point (left) and the 17-point (right) cubature formula for rectangle. The numbers are the indices of the Gaussian points. The surfaces of the red circles are proportional to the corresponding weights.

4.2.3 Potential and field calculation for single BEM elements

The electric potential and field of an arbitrary constant BEM element (with constant charge density σ) at a field point $\mathbf{P}$ can be approximated by Gaussian cubature as:

$$\Phi(\mathbf{P}) \approx \frac{1}{4\pi\varepsilon_0} \sum_{i=1}^{N} \frac{q_i}{|\mathbf{P}-\mathbf{Q}_i|}, \qquad \mathbf{E}(\mathbf{P}) \approx \frac{1}{4\pi\varepsilon_0} \sum_{i=1}^{N} q_i \frac{\mathbf{P}-\mathbf{Q}_i}{|\mathbf{P}-\mathbf{Q}_i|^3}, \tag{4.48}$$

where $q_i = w_i q$ denotes the charge of point i, and $q = \sigma\mathcal{A}$ is the total charge of the element. The physical picture of the Gaussian cubature formalism is nice and intuitive: the BEM element with continuous charge density is replaced by discrete point charges, whereas the charge q_i at the Gaussian point $\mathbf{Q}_i$ is proportional to the Gaussian weight w_i, and the sum of the individual charges q_i is equal to the total charge of the element (see eq. 4.45). Obviously, it is much more easier to compute the potential and field produced by point charges instead of continuous charge distributions. As we will see below, the point charge method is not only easier but also more precise, at least for field points which are not too close to the element. In addition, the point charge calculation

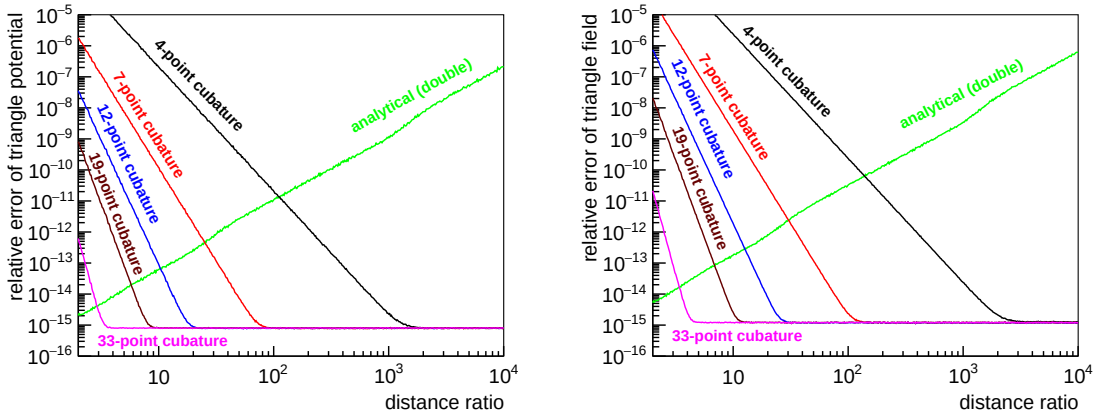

(a) Relative potential error of triangles

(b) Relative field error of triangles

Figure 4.14: Averaged relative error of the triangle potential (left) and field (right) for the five Gaussian cubature approximations of app. C, as a function of the distance ratio. For comparison, the averaged relative error of the triangle potential and field computed by analytical integration (ref. [HTS06] and sec. 4.2) is also shown.

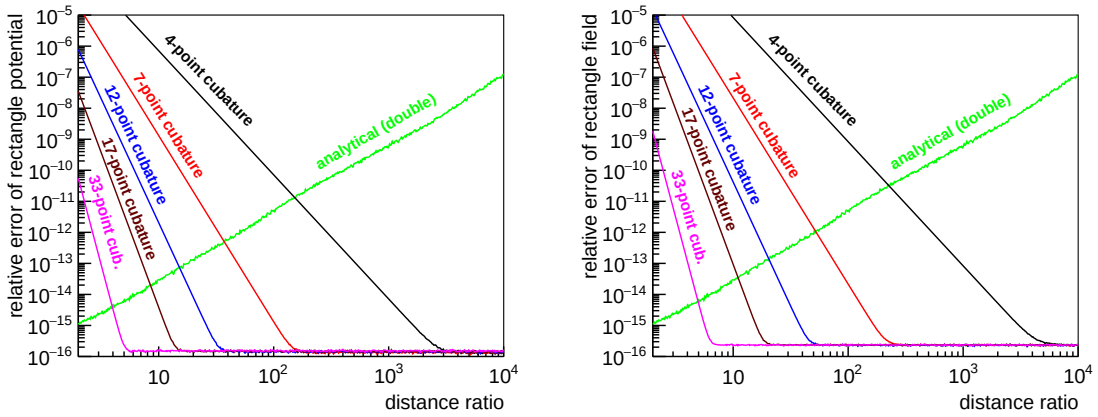

(a) Relative potential error of rectangles

(b) Relative field error of rectangles

Figure 4.15: Averaged relative error of the rectangle potential (left) and field (right) for the five Gaussian cubature approximations of app. D, as a function of the distance ratio. For comparison, the averaged relative error of the rectangle potential and field computed by analytical integration (ref. [HTS06] and sec. 4.2) is also shown.

is typically faster than the analytical integration with continuous charge distribution (see sec. 4.4). In order to investigate the performance of the Gaussian cubature or point charge approximation for potential and field calculation of triangles and rectangles, the same procedure that is described in sec. 4.2.1 has been used. First, for a fixed element and field point, the relative error of the potential computed by Gaussian cubature is defined as: $\mathrm{err}(\Phi_{cub}) = |(\Phi_{cub} - \Phi_{GL2})/\Phi_{GL2}|$, where Φ_{GL2} is computed by two-dimensional Gauss-Legendre integration. A similar formula holds for the field error (see in sec. 4.2.1). Then, 1000 elements and field point directions are randomly generated for a fixed distance ratio, and the averages of the relative error values are calculated for 500 different distance ratio values from 2 to 10000.

Figures 4.14 and 4.15 present the averaged relative error of the potential and field for triangles and rectangles as a function of the distance ratio, for the ten Gaussian cubature approximations described in app. C and D, together with the relative error of the analytical

integration described in ref. [HTS06] and sec. 4.1 (with double precision arithmetic type). While the relative error of the analytical integration is small for field points close to the element (small distance ratio), and it increases with the distance ratio, the behavior of the Gaussian cubature error is just the opposite: it is large for field points near the element, and it decreases with the distance ratio. In fact, the accuracy of the Gaussian cubature at high distance ratio is limited only by the finite-digit computer arithmetic precision. Therefore, it seems that the analytical and numerical integration methods complement each other: to get high accuracy everywhere, one should use analytical integration for field points close to the element and numerical integration farther away.

It is also conspicuous from the figures that the cubature formulas with more Gaussian points N have higher accuracy and can be used also for field points closer to the elements to obtain a given accuracy level (e.g. 10^{-15}). The computation time for the potential or field simulation by Gaussian cubature is approximately proportional to N, therefore, in order to minimize the computation time, it is expedient to use several different cubature formulas: for large distance ratio DR one can use a cubature formula with smaller N, and for smaller DR one should use a formula with larger N. E.g. to obtain $2 \cdot 10^{-15}$ relative accuracy level for the triangle potential, one should use the following cubature formulas in the various distance ratio intervals: $N = 4$ for DR > 1500, $N = 7$ for $80 <$ DR < 1500, $N = 12$ for $20 <$ DR < 80, $N = 19$ for $8 <$ DR < 20, $N = 33$ for $3 <$ DR < 8, and analytical integration for DR < 3. In the case of triangle field these limits are slightly higher. If both the potential and the field has to be computed for a field point in one computation step, then one should use the limits defined by the field; namely, in this case the same Gaussian points and weights can always be used for both calculations.

In Sec. 4.2.1 it has been showed that the relative error of the analytically computed potential and field increases with the triangle and rectangle aspect ratio. Also for the Gaussian cubature the aspect ratio dependence has been investigated. Fig. 4.16 presents the error of the 7-point Gaussian cubature field as a function of the aspect ratio, for DR=300 distance ratio; the potential error and higher-order Gaussian cubatures have a similar behavior. The triangle potential and field error of the Gaussian cubature increases with the aspect ratio. Therefore, a large number of triangles with high aspect ratios should be avoided in BEM calculations, if high accuracy computations are required. On the other hand, the Gaussian cubature potential and field calculations of rectangles seem not to be sensitive to the rectangle aspect ratio. Alternatively a triangle can be mapped into a rectangle by the Duffy transformation [Duf82, LC94], therefore the numerical integration over a triangle by Gaussian cubature can also be done by using the Duffy transformation in conjunction with the Gaussian cubature formulas for rectangles of app. D, instead of the triangle formulas of app. C. In this case, however, much larger errors for the potential and field of triangles are obtained than by using the Gaussian cubature formulas for triangles. E.g. the relative error of the triangle field at DR=100 with the Duffy transformation and the 7-point rectangle cubature formula is about 10^{-8}, in contrast with the few times 10^{-15} error of the triangle 7-point Gaussian cubature formula (see Fig. 4.14(b)).

4.3 Accuracy comparisons with complex electrode assemblies

The main goal of potential and field calculation of charged triangles and rectangles is to apply these elements for electric potential and field computations of complex electrode systems with BEM. Therefore, it is important to compare the accuracy of the analytical and numerical integration methods not only for individual elements, but also for electrode systems with many elements. In this section, results for two electric field simulations are presented: one of them contains only triangles as BEM elements, the other one only rectangles. For this purpose, the main spectrometer vessel and inner electrodes of the

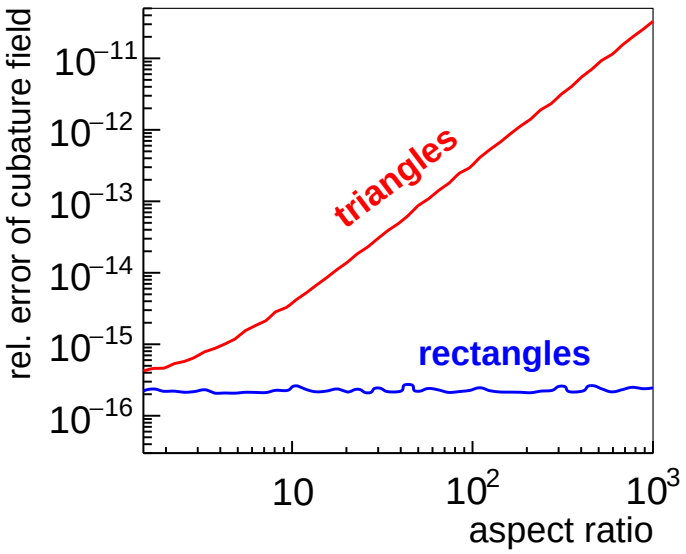

Figure 4.16: Averaged relative error of the 7-point Gaussian cubature field for triangles and rectangles as a function of the aspect ratio, for a fixed distance ratio DR=300.

KATRIN experiment have been discretized first by 1.5 million triangles and second by 1.5 million rectangles, using a dipole electrode potential configuration. The triangle model will be explained in more detail in section 4.5.1. The KATRIN main spectrometer inner electrode system is equipped with a sophisticated wire electrode system [Han07, Val10], but in both models the wire electrodes are replaced by full electrode surfaces. Further details about the KATRIN main spectrometer can be read in chapter 2 of the thesis in hand. As a further example for complex electrode geometries, in appendix E potentials and fields of the analytically calculable spherical capacitor are compared against numerical values by RWG and cubature methods.

Figure 4.17 presents the aspect ratio distribution of the two models (left: triangles, right: rectangles). One can see that especially the triangle model consists of many triangles with large (AR > 20) aspect ratios. Figure 4.18 shows the distance ratio distributions for these two models for the central field point $\mathbf{P} = (0, 0, 0)$. Due to the large number of elements and the small element sizes (relative to typical field point – element distances), most of the distance ratio values are above 100, where the fast 7-point cubature method can be applied. The electrode discretization has been assembled with the C++ library *KGeoBag* (cf. sec. 3.3) and the charge density and field computation have been performed throughout this chapter with *KEMField* (cf. sec. 3.4). With the computed charge density values (cf. sec. 3.4.3), the electric potential and field at an arbitrary field point can be calculated by summing the potential and field contributions of the individual elements (cf. sec. 3.4.5.1). In order to compare the relative errors of the various field computation methods, 3000 field points inside a cylinder with 9 m length and 3.5 m radius have been generated randomly (centered at the KATRIN main spectrometer vessel center), and the average of the relative errors defined in secs. 4.2.1 and 4.2.3 have been computed. As reference potential and field values, the Gauss-Legendre bi-quadrature method described in sec. 4.2.1 has been used. Table 4.1 summarizes the results for two different analytical methods and for Gaussian cubature. In the case of triangles, two calculations have been performed: first, with all triangles, and second, using only the small aspect ratio (AR < 10) triangles (since it has been showed in secs. 4.2.1 and 4.2.3 that both the analytical and the Gaussian cubature calculations for triangles are sensitive to the aspect ratio).

In table 4.1 the following features can be seen:

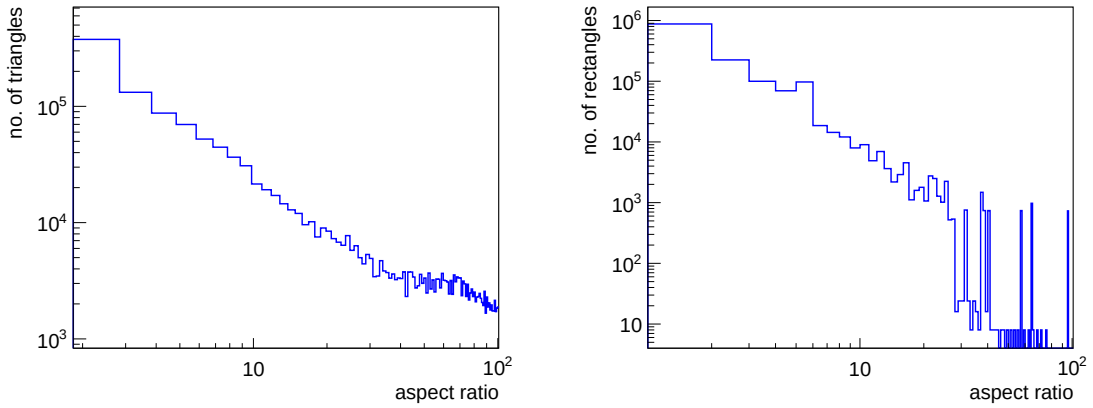

(a) Aspect ratio distribution of triangles

(b) Aspect ratio distribution of rectangles

Figure 4.17: Aspect ratio distribution of triangles (left) and rectangles (right) of two different discretization models of the KATRIN main spectrometer electrode system with electric dipole field. Vertical axis: number of elements per bin, with constant bin size 1.

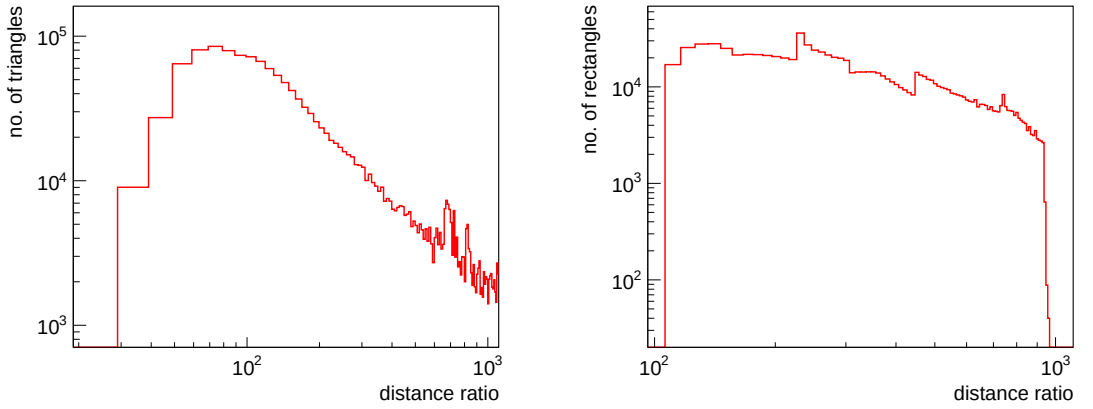

(a) Distance ratio distribution of triangles

(b) Distance ratio distribution of rectangles

Figure 4.18: Distance ratio distribution of triangles (left) and rectangles (right) of the two discretization models of the KATRIN main spectrometer electrode system with electric dipole field, at field point $\mathbf{P} = (0, 0, 0)$ (center of spectrometer). Vertical axis: number of elements per bin, with constant bin size 10.

1. The Gaussian cubature integration method has much smaller relative errors than both analytical integrations: the potential error is practically double precision, while the field error is somewhat larger, but also close to the double precision level.
2. The analytical method 2 (ref. [HTS06]) has smaller errors than the analytical method 1 (refs. [Cor14, FLC+12]).
3. The potential errors are in all cases smaller than the field errors.
4. In case of using only smaller aspect ratio triangles, the errors are smaller than with all (i.e. also large aspect ratio) triangles.

Furthermore the reduction of the potential and field rounding errors of the 1.5 million elements by Kahan summation [Übe97, Kah65] has been tried, but with no success.

In addition, the implementation of the RWG and cubature integration techniques have been validated in context of the calculation of the analyzing plane potential of a very

Table 4.1: Average relative error of potential and field simulation of triangles and rectangles at 3000 field points, computed with two different analytical methods and with Gaussian cubature. Analytical 1: Refs. [Cor14, FLC+12]; Analytical 2: Ref. [HTS06] and sec. 4.1.

	Analytical 1	Analytical 2	Gaussian cubature
Potential error (triangles)	$7.1 \cdot 10^{-9}$	$4.6 \cdot 10^{-12}$	$4.9 \cdot 10^{-16}$
Field error (triangles)	$1.8 \cdot 10^{-6}$	$3.2 \cdot 10^{-9}$	$4.5 \cdot 10^{-14}$
Potential error (triangles, AR < 10)	$1.8 \cdot 10^{-11}$	$2.0 \cdot 10^{-12}$	$3.2 \cdot 10^{-16}$
Field error (triangles, AR < 10)	$1.4 \cdot 10^{-7}$	$6.7 \cdot 10^{-10}$	$2.4 \cdot 10^{-14}$
Potential error (rectangles)	$2.6 \cdot 10^{-11}$	$1.7 \cdot 10^{-11}$	$1.1 \cdot 10^{-16}$
Field error (rectangles)	$6.3 \cdot 10^{-7}$	$5.2 \cdot 10^{-9}$	$1.7 \cdot 10^{-14}$

complex three-dimensional main spectrometer electrode model [Cor14]. Differences have been computed to the analytical integration techniques [Cor09] and fed into a *KaFit* sensitivity simulation in order to determine the effect on the neutrino mass parameter through numerical potential inhomogeneities due to analytical integration. The discussion of the results will be continued in app. F.

4.4 Computation time with CPU and GPU

In the following, the computer speed of the Gaussian cubature and the analytical integration methods is compared on CPU (C++) and GPU (OpenCL) [SGS10, Hwu11]. For this purpose, the electric potential and field have been calculated of the two electrode models, as described in the previous section, which contain 1.5 million triangles (cf. sec. 4.5.1) and 1.5 million rectangles, respectively.

Table 4.2 presents the CPU computation time values for 100 field points and five different calculation types: two analytical (refs. [HTS06, Cor14, FLC+12]) and three Gaussian cubature methods. At the cubature method, the Gaussian points are calculated from the individual element geometry before each potential / field calculation. One can see that the Gaussian cubature methods (especially those with 7 and 12 points) are significantly faster than the analytical calculations. The computation time of the Gaussian cubature formulas increases almost linearly with the number of Gaussian points. The triangle and the rectangle integrations have approximately the same speed. Table 4.3 shows the time comparisons on a GPU with OpenCL, with two different analytical methods (refs. [HTS06, Cor14, FLC+12]) and with a distance ratio dependent cubature integrator incorporating the 7-point, 12-point and 33-point cubature methods. Also on this platform the cubature is much faster than analytical methods and can deliver a speed up of almost an order of magnitude for triangles.

The possible time benefit by saving the Gaussian points for all elements into heap memory in advance has been investigated, too. The storage of the Gaussian points can require a lot of memory (e.g.: 800 MB for 5 million elements and 7 points for each element), depending from the number of meshed electrode elements. In the following, the 7-point and 12-point cubature are compared against the analytical method as discussed in [HTS06]. As shown in table 4.4, again a speed increase up to factor five by using the Gaussian cubature versus the analytical 2 method of [HTS06] is achieved. Since the Gaussian points are computed on the fly in the fast stack memory, the non-cached variant of the cubature code is only marginally slower than the code version with precomputed Gaussian points.

Table 4.2: Computation time values and speed increase factors (relative to analytical speed) for cubature implementation on CPU, with field and potential of 1.5 million triangles and rectangles computed at 100 field points. Analytical 1: Refs. [Cor14, FLC+12]; Analytical 2: Refs. [HTS06]. SF1: (time of analytical 1)/time; SF2: (time of analytical 2)/time.

Element type	Computation method	Time (s)	SF1	SF2
Triangles	Analytical 1	161	1	0.44
	Analytical 2	70	2.3	1
	7-point cubature	15.7	10.3	4.5
	12-point cubature	25.5	6.3	2.7
	33-point cubature	61	2.6	1.1
Rectangles	Analytical 1	140	1	0.56
	Analytical 2	79	1.8	1
	7-point cubature	18	7.7	4.4
	12-point cubature	28	5.1	2.8
	33-point cubature	70	2.0	1.1

Table 4.3: Computation time values and speed factors for cubature implementation on GPU, with field and potential computed at 10000 field points. Analytical 1: Refs. [Cor14, FLC+12]; Analytical 2: Refs. [HTS06]. In the case of distance ratio dependent computation the 7-point, 12-point and the 33-point cubature methods and the analytical method 2 are used.

Element type	Computation method	Time (s)	Speed increase factor (relative to analytical 1)
Rectangles	Analytical 1	82.7	1
	Analytical 2	81.7	1.01
	7-point cubature	27.8	3
	Distance ratio dependent	64.8	1.3
Triangles	Analytical 1	258	1
	Analytical 2	80.2	3.2
	7-point cubature	28.3	9.1
	Distance ratio dependent	97	2.7

Table 4.4: Speed test with 1.5 million triangles, 100 field points, precomputed vs. non-precomputed Gaussian points.

Computation method	Time (s)	Speed increase factor (relative to analytical 2)
Analytical 2	60.7	1
7-point cubature, precomputed	12.7	4.8
7-point cubature, non-precomputed	14.5	4.2
12-point cubature, precomputed	19.9	3
12-point cubature, non-precomputed	23	2.6

During the realization of the code it has been clearly visible that the Gaussian cubature computation time depends very much on implementation details. In the C++ codes of the above described calculations, double arrays have been used for the representation of the Gaussian point, field point and electric field components. In another calculation, the `TVector3` class of the *ROOT* data analysis code package [A+09] has been used. The code layout is more elegant and clean by using the `TVector3` class, but in this case the computation is four times slower than by using double arrays. Interestingly, the cubature computation is about two times slower even if the `TVector3` header are included in the main C++ functions while they are not used for the calculations.

GPU architectures profit from a high degree of parallelism, even though the clock speed is not that high as on CPUs. In order to guarantee a highly parallel execution of the code, the used data fragments may not be too large, hence large double arrays have to be avoided, because using too large data arrays results in a lower degree of parallelism (and hence less speed) (e.g. for the 33-point cubature the array containing the Gaussian points is 99-dimensional). This is the reason why saving data in large arrays due to limitation of register memory on GPU chips has been avoided. Instead, mainly double variables are used, resulting in a very highly parallel execution of the code.
Technical information on used hardware and software equipment can be found in appendix G.

4.5 Adaptations for simulations with electric dipole fields

In the previous parts mathematical techniques and software tools (ch. 3) have been presented for computing electric potentials and fields for three-dimensional electrostatic problems with unprecedented accuracy up to the machine epsilon of the floating-point number system (for double precision $\mathcal{O}(10^{-15})$). In order to prepare for fast electron tracking in electric dipole fields, this chapter presents an optimized three-dimensional electrode model of the main spectrometer and the validation results of potential and field accuracy studies.

There are many components of the KATRIN apparatus, which are studied in context of tracking simulations with 3-D electrostatic fields, like the rear-section e-gun system [Hei15], the dipole electrode system of the differential pumping section [Com15], the pre- and the main spectrometer [Cor14, Bar16, Gos15] and finally the detector system [Cor14]. All mentioned electrode models suffer from a large number of discretized elements. For example the main spectrometer model [Cor14] consists of $\mathcal{O}(5 \times 10^6)$ discretized elements. Commonly this huge number requires a large amount of computer memory in order to load and to compute numerical field values. In sec. 4.5.1 a new electrode model, specially tailored for the fast computation of three-dimensional fields and potentials in the KATRIN main spectrometer, is presented. This model profits from a lower discretization count and consequently requires a smaller amount of computational memory. Together with a speed test, the new model is validated against potential and field values from the accurate proven CAD-based main spectrometer assembly [Cor14].

Monte-Carlo simulations of electron trajectories with 3-D electrostatic geometries require a further boost of the field computation time. Besides an optimized electrode model, a very efficient field solving technique itself is indispensable (a single cyclotron turn of an electron needs up to 13 field evaluations). For this purpose, potentials and fields are computed by numerical integration techniques (cf. sec. 4.2.2) in combination with the fast Fourier transformation on multipoles (FFTM) (sec. 3.4.5). The alternative usage of a cubic interpolation instead of FFTM is discussed in [Ste16]. In order to improve FFTM, the integration techniques by RWG and the Gaussian cubature have been integrated into the code part and replace former analytical methods (within the FFTM code) for several reasons:

- In regions, which are not populated by many electrode elements (like the flux tube of the main spectrometer), the very rapid FFTM technique will be used for field calculation during electron tracking, whereas in the region very close to the electrodes, FFTM cannot compute anymore accurate values, and numerical integration techniques will be applied for potential and field calculation.
- As described in sec. 4.2.1, former analytical integration techniques lead to inconsistent results for dedicated mesh shape-field point combinations. This issue directly propagates to FFTM and leads consequently to inconsistent results during tracking.

In order to obtain the best accuracy and highest speed for tracking simulations, the interplay between FFTM and numerical integration technique with optimized FFTM field solver parameters are validated in sec. 4.5.2. Consequently, particle tracking simulations (ch. 5 and 6) for three-dimensional electrode configurations of the KATRIN main spectrometer are feasible in a realistic amount of time.

4.5.1 Optimized electrode model of the main spectrometer

In context of [Cor14], a very detailed electrode model of the main spectrometer, which is based on CAD drawings, has been developed (labeled in the following as *main spec assembly*). This model, which is built up of 5,079,848 discretized surface elements, is the basis for the computation of very accurate potentials and fields in the main spectrometer. Simulations with this accurate model is required especially by transmission studies [Gro15, Bar16, Erh16] while it is useful also for the study of other non-axial effects in the main spectrometer. Unfortunately, due to the very high count of mesh elements, together with a large amount of memory, this model suffers from very high computation times for charge densities and field values.

If potential and field values have to be computed mainly inside the magnetic flux tube of the main spectrometer, in context of trajectory calculations, the detailed wire electrode geometry, as modeled in the *main spec assembly*, has a negligible effect. Consequently a lean and fast main spectrometer model (labeled as *non-axial main spec model*) has been developed and optimized especially for simulations with electric dipole fields [Ste16]. Figure 4.19 illustrates the layout and the triangular mesh structure of the model. Additionally to apply different potentials to the electrode rings, the *non-axial main spec model* allows to assign different potentials to the eastern and western part of the electrode as well. In order to optimize the electrode model and to reduce the count of mesh elements, following main modifications have been applied:

- Reduction of mesh element count through replacement of the complex wire electrode system by (solid) conical electrodes.
- The model does not include an outer wire layer, since the inner electrodes are modeled as a full electrode.
- For a possible dipole configuration, these elements are separated by a gap of 25 mm ($\approx 0.3°$) in eastern and western direction.
- The geometry of the vessel hull has been reduced and covers, as needed, only the gaps between the electrode rings and the dipole half shells.
- The pump port geometries have been omitted.

Figure 4.19 shows the layout and the mesh structure of the *non-axial main spec model*. Further details on the model can be taken from [Ste16].

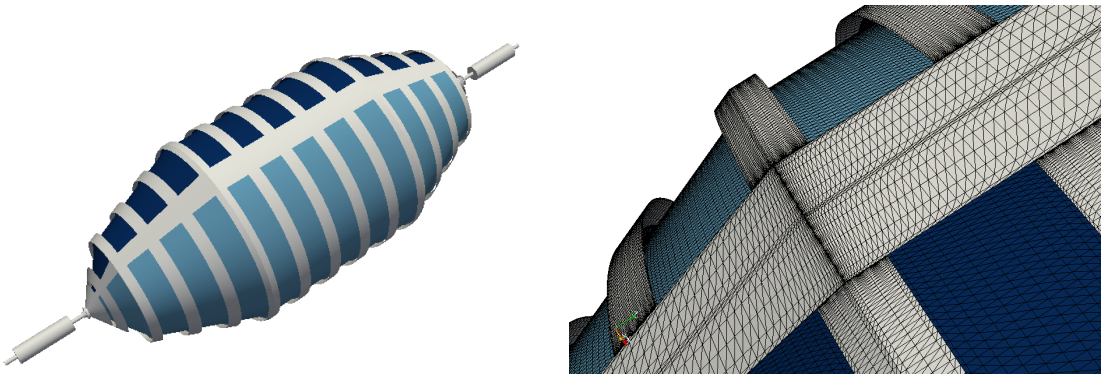

Figure 4.19: Layout of the non-axial main spec model and mesh structure of the electrode elements. Two different potentials can be assigned, either to the western or the eastern electrode half shell, as indicated by different colors on the pictures. From [Ste16].

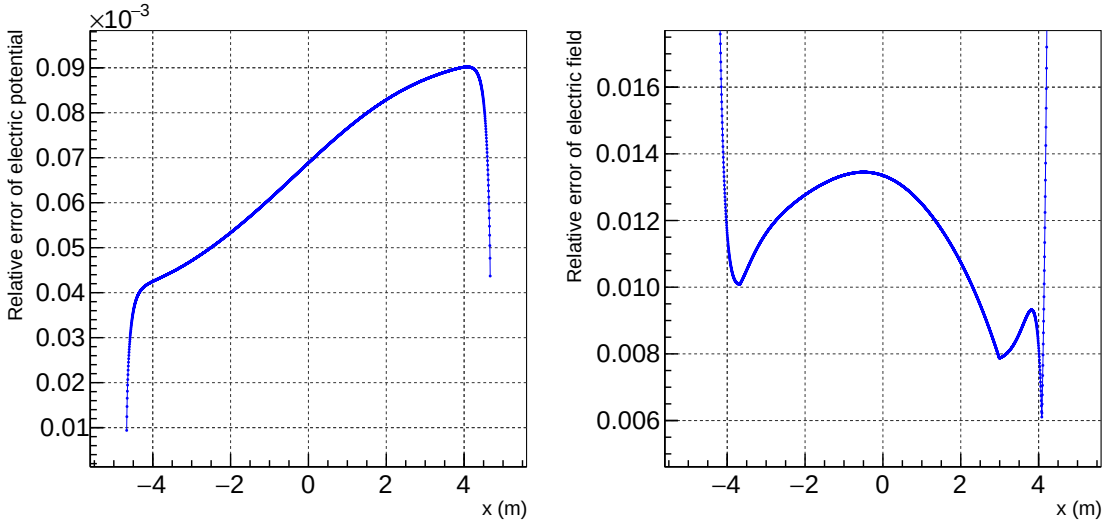

(a) Relative potential error

(b) Relative field error

Figure 4.20: Comparison of potentials and fields of different main spectrometer electrode models along the x-axis in the center at $y = z = 0\,\mathrm{m}$**. Left:** Relative potential error of the *non-axial main spec model* with respect to the CAD-based *main spec assembly*. **Right:** Relative electric field error.

Test of model errors

Surely, it is expected that the reduced electrode structure and the lower mesh element count leads to numerical deviations, compared to the three-dimensional *main spec assembly*. In order to justify the usage of this model for particle tracking simulations, the relative error between the *main spec assembly* and the approximative *non-axial main spec model* has been calculated by direct field solving methods (by numerical integration). Since this field solver achieves an accuracy of up to $\mathcal{O}(10^{-15})$, the computed relative errors only result from the electrode model itself. The relative errors have been computed for a dipole configuration of the main spectrometer along the x-axis from $x = -4.67\,\mathrm{m}$ to $x = 4.67\,\mathrm{m}$. Throughout this chapter the relative errors are defined as in sec. 4.2.1. The results are visualized in fig. 4.20. The 3.8 G flux tube has a radius of $r = 3.87\,\mathrm{m}$ in the cylindrical central part. At $x = -3.87\,\mathrm{m}$ the relative potential error is 4.3×10^{-5}, at $x = 3.87\,\mathrm{m}$, 4.3×10^{-5}. The different values at lower and higher x values can result from

Table 4.5: Overview of time and memory consumption of different 3-D main spectrometer electrode models. All values have been computed on a GPU with a direct field computation by (numerical) integration.

Parameter	Main spec assembly	Non-axial main spec model
Surface mesh elements	5079848	1517552
Computation times:		
- Model initialization	90 s	4 s
- Charge densities (approx.)	4 d (2 GPUs)	1 d (1 GPU)
- Single potential value	0.0174 s	0.0066 s
- Single field value	0.0203 s	0.0043 s
- Combined potential and field	0.0204 s	0.0076 s
Memory consumption:		
- Charge density file size	510 MB	158 MB
- RAM usage	> 4 GB	720 MB

non-axial elements of *the main spec assembly* (e.g. ports or deformations). The exact determination of this asymmetry is not part of this study. The relative field error also shows an asymmetry, at $r = 3.87$ m the error is 10^{-2} and at $r = 3.87$ m, 9.0×10^{-3}.

Time and memory consumption

Table 4.5 compares the different numeric values of computation time and memory consumption. All values have been evaluated with numerical integration techniques (on a GPU) as explained in chapter 4, which scales linearly with the number of mesh elements.

4.5.2 Test of FFTM field simulation parameter

As the solution of the Lorentz equation with Runge Kutta 86 [GF+16] algorithm requires up to 13 field evaluations per cyclotron step for the electron trajectory calculation, the field evaluation time has to be decreased further by taking advantage of a combination of direct field solving by numerical integration and the fast Fourier transformation on multipoles (sec. 3.4.5.3). The goal is to compute potentials inside the flux tube region with FFTM, whereas for the outer regions, where the multipole expansion can not be applied, the numerical methods as explained in ch. 4 are used. In the following the results of different numerical tests with an optimized FFTM configuration are presented. The following parameters have been chosen commonly throughout the different tests. Their detailed description can be found as well in sec. 3.4.5.3.

- `top_level_divisions = 6`
- `tree_level_divisions = 2`
- `expansion_degree = 13`
- `neighbor_order = 3`
- `maximum_tree_depth = 6`
- `region_expansion_factor = 1.1`

They have been selected by an experimental study regarding the memory consumption. The above mentioned parameters guarantee a computer RAM consumption with less than 4 GB. In this way, FFTM needs a very small amount of memory also for cache files and

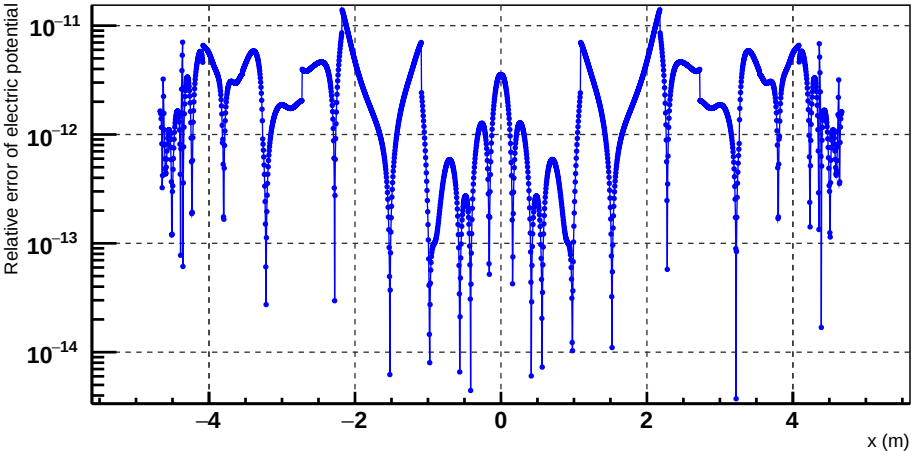

(a) Relative error of the electric potential by FFTM

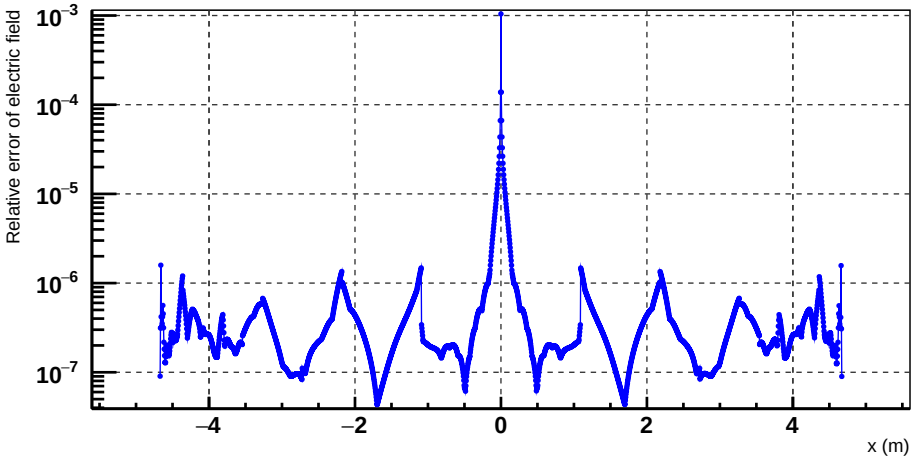

(b) Relative error of the electric field by FFTM

Figure 4.21: Relative error of the electric potential and field as computed with FFTM in the *non-axial main spec model*. The values have been computed at a straight line from $x = -4.67\,\mathrm{m}$ to $x = 4.87\,\mathrm{m}$ at $y = z = 0\,\mathrm{m}$.

smaller cluster computer can be used. Details on the different parameter are given in sec. 3.4.5.3. Whereas for the previous study all potential and field values have been computed by direct integration, now the FFTM method is compared to the integration with the common *non axial main spec model* in a dipole configuration. The relative potential and field errors are plotted in figure 4.21 on a line from $x = -4.67\,\mathrm{m}$ to $x = 4.87\,\mathrm{m}$ at $y = z = 0\,\mathrm{m}$. Mainly for all different x-values the accuracy of the potential is computed to the order $\mathcal{O}(10^{-11})$ and the field to $\mathcal{O}(10^{-6})$. The peaks arise from the location of the expansion origin, in this region, a higher accuracy is given. This is also shown by figure 3.7. Whereas the values have been computed on a fixed line, in a next step, 1000 field calculation points are diced within a cylinder volume, centered at $z = 0\,\mathrm{m}$ with a radial extend of $r < 2.5\,\mathrm{m}$ and a length of $|z| < 4.2\,\mathrm{m}$ in z-direction (calculation area denoted as *inner volume*). Separately, 1000 points have been computed on a cylindrical surface, which has been located close to the electrodes at $r = 4.67\,\mathrm{m}$ (calculation area denoted as *outer surface*). Table 4.6 summarizes the mean relative potential and field errors for the *inner volume* and *outer surface* computation region together with the statistical error σ_{stat}.

Table 4.6: Accuracy of potentials and fields as computed with FFTM for the non-axial main spec model.

	Mean	σ_{stat}
Inner volume		
- Potential	7.025×10^{-13}	3.865×10^{-13}
- Field	1.001×10^{-8}	2.684×10^{-8}
Outer surface		
- Potential	5.483×10^{-13}	3.088×10^{-13}
- Field	2.947×10^{-9}	8.139×10^{-9}

Speed test

Finally the speed of the FFTM algorithm with the given parameter set is tested against numerical integration methods. The potential, the field and a special method for the calculation of the field and the potential has been tested by the evaluation of 1000 field points in the inner volume and an outer surface close to the electrodes. In general, smaller computation times are expected for the inner volume than for the outer surface. In the latter case, FFTM has to use the field solving techniques by numerical integration as well, which are slower than the summation over multipole moments. The latter has no noticeable speed profit between CPU and GPU systems, since always the evaluation of the multipole moments will be handled by a CPU. Close to the electrodes a speed profit is especially on GPU platforms visible, since the numerical integration techniques are realized as well on GPUs. Table 4.7 summarizes all gathered results.

4.6 Summary

Integration over triangles and rectangles is important for many applications of mathematics, science and engineering, especially for FEM and BEM. In context of the evaluation of the nodal function, surface integrations have to be performed. In the beginning, a very lean and easy analytical ansatz based on RWG basis functions has been derived for the case of BEM with constant charge densities. While this particular method is perfect for the simultaneous computation of potentials and fields in order to save computation time, the derivation of the formulas is characterized by only a few transcendental functions. This fact results in a very high numerical stability and a small computation time, compared to other analytical integration formulas. Nevertheless, in some special cases the numerical integration has higher accuracy and also higher speed. It has been demonstrated successfully in the case of electric potential and field calculation of charged triangles and rectangles at points far from these elements, the Gaussian cubature numerical integration method is much more accurate and faster than some of the best analytical integration methods. Using the Gaussian cubature method, the triangles and rectangles with continuous charge distribution are replaced by discrete point charges, the potential and field of which can be computed by simple formulas. At field points far from the elements, the analytical methods have large rounding errors, while the accuracy of the Gaussian cubature method is limited only by computer arithmetic precision. Closer to the elements, a Gaussian cubature formula with higher number of Gaussian points (nodes) has to be employed, in order to obtain the maximal accuracy. Very close to the elements, the Gaussian cubature method is not precise enough, therefore analytical integration has to be used there. Nevertheless, for a typical BEM problem the field point is far from most of the elements, therefore the simple, fast and accurate Gaussian cubature method can be used for a large majority of the boundary elements.

Table 4.7: Chosen parameter of FFTM field solver. Speed comparison of field solving by direct numerical integration (combination of cubature and RWG) and fast Fourier transformation on multipoles with the non axial main spectrometer model in a dipole configuration. The time values are taken as a mean value from 1000 diced points, the rounding error is 10^{-4} s. All field points are located at $|z| < 4.2$ m. The inner volume is defined as a cylinder with $r = 2.5$ m and the outer surface as cylindric surface at $r = 4.67$ m.

Field solver type	Platform	Time (ms) *Inner volume*	Time (ms) *Outer surface*
Electric potential			
Numerical integration and RWG	CPU	416.6066	398.6896
	GPU	6.6539	6.8366
FFTM	CPU	0.0066	1.1217
	GPU	0.0050	0.1216
Electric field			
Numerical integration and RWG	CPU	437.9734	412.6221
	GPU	4.2929	4.4249
FFTM	CPU	0.0057	1.1758
	GPU	0.0055	0.1022
Electric field and potential			
Numerical integration and RWG	CPU	454.9548	429.1755
	GPU	7.5795	7.7954
FFTM	CPU	0.0108	2.0889
	GPU	0.0105	0.1882

The complex electrode examples described in sec. 4.3 illustrate that the Gaussian cubature method can be four to seven orders of magnitude more accurate than some of the best analytical methods that can be found in the literature. In addition, the examples in sec. 4.4 show that the potential and field computation with Gaussian cubature can be three to ten times faster than the analytical methods, both with CPU and with GPU. An additional advantage of the Gaussian cubature method is that accurate higher derivatives of the electric field can be relatively easily calculated analytically by point charges, while in the case of analytical integrations this is a rather difficult task. The higher derivatives can be useful for field mapping computations in conjunction with the Hermite interpolation method.

In context of this chapter, the Gaussian cubature method has been compared with analytical integration in the case of constant BEM elements (i.e. elements with constant charge density). Nevertheless, the Gaussian cubature method can be easily applied also for elements with arbitrary charge density function (e.g. linear, quadratic etc.). Most probably, the Gaussian cubature method is more accurate and faster than analytical integration also in the case of higher order charge density functions. The Gaussian cubature method presented here for electrostatics can also be applied for magnetostatics and time-dependent electromagnetic problems. E.g. magnetic materials can be computed by fictive magnetic charges, and the magnetic field in that case can be calculated by similar formulas than electric field of electric charges. It might be that the Gaussian cubature numerical integration method can also be used for the efficient computation of multipole moment coefficients of triangles and rectangles (see ref. [Bar16] for analytical integration results).

Finally the newly developed integration methods have been applied for the case of field calculation for particle tracking in a main spectrometer geometry. For an additional boost of fast tracking simulations a new, three-dimensional electrode model for the KATRIN main spectrometer has been developed (sec. 4.5.1), which profits from smaller computation times of field and potential values through a reduced mesh count. In order to check for the model quality, the relative potential and field error has been calculated by comparison with a CAD-based electrode model. The model quality is given by the relative field error, which is maximal 9.0×10^{-3}.

While the speed of computation has been improved by 37 % with the optimized electrode model, an appropriate field solving technique is chosen in order to further boost targeted tracking simulations. The accuracy has been determined by the calculation of the relative error along a straight line in the spectrometer, but also field points have been chosen randomly inside the main volume of the spectrometer geometry and in the region of the electrodes. Here, the quality of the fast multipole field solver is determined by the relative field error which is given by 10^{-9} in most regions of the electrode model. In face of the speed increase due to FFTM and the smaller amount of required memory, these results allow fast tracking inside the main spectrometer volume with a low memory footprint for following (dipole) simulations.

CHAPTER 5

Study of active mitigation of stored-electron background with the electric dipole method

In order to achieve the projected goal of a 10 mcps background signal, intelligent and smart background reduction strategies are required, which are able to reduce and to characterize background processes in the main spectrometer. In the context of [Mer12, Wan13] it has already been shown that an essential background contribution results from electrons released during the α-decay of ^{219}Rn. In the context of subsequent works [Gör14, Har15], it could be demonstrated that a liquid nitrogen cooled baffle system is able to reduce the stored particle background due to radon trapping by about 95 %. This particular system is based on the principle of cryosorption and thus works passively without the need to change the electro-magnetic field configuration of the MAC-E filter. All active reduction methods are based on a change of the field configuration over the shortest time scales possible. One big advantage of these active reduction techniques is their ability to reduce the background while also allowing to further characterize the energy scale or time constant of the corresponding background component by applying different field strengths. Of particular interest here is the study of novel background components, which can be characterized by the electric dipole technique (cf. ch. 6). In general, there are several methods in order to reduce the stored particle background by applying non-standard electromagnetic field configurations, like the electron cyclotron resonance [Mer12], the magnetic pulse [Beh16] or the electric dipole method, which is discussed in the following. In this thesis, Several tests of the electric dipole method were performed to scan different experimental parameters and to determine the optimal pulse setting for the most efficient background mitigation factor.

The fundamental properties of magnetic storage of particles in MAC-E filters are first discussed in sec. 2.1.3, while the principle of the electric dipole method is reviewed in sec. 5.1. Next, specific simulation results are presented which demonstrate that the electric dipole method is expected to efficiently remove stored electrons up to an energy of $\mathcal{O}(1\,\mathrm{keV})$. In the context of the second SDS measurement campaign, the dipole method was thoroughly tested and shown to be a very reliable method to reduce stored-particle background. Over the course of a first set of measurements, as described in sec. 5.2, static electric dipole fields were applied to define the best dipole mode with respect to the reference field of the main spectrometer. In the next measurement iteration, electric dipole pulses were applied over the shortest possible time scales. These measurements were carried out to determine the optimal pulse setting for background mitigation to be applied during a KATRIN measurement period. The measurement results for dipole pulses can

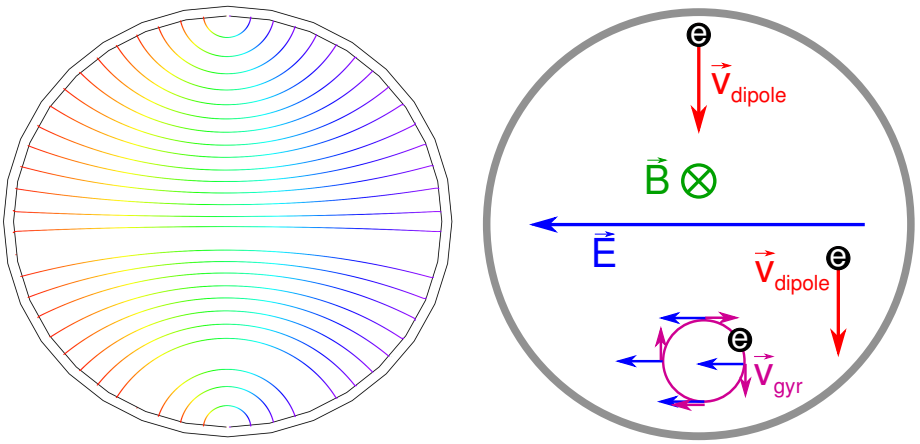

(a) Field lines formed by a 100 V electric dipole field in the main spectrometer

(b) Principle of outward pointing $\boldsymbol{E}\times\boldsymbol{B}$-drift from an electric dipole field

Figure 5.1: Concept of electron removal with an electric dipole field. (a) The figure shows the form of electric field lines in the main spectrometer for a 100 V electric dipole field. The field lines are almost linear in the center, whereas a high curvature can be seen close to the neighboring electrodes. The calculation of electric field lines has been carried out in context of [Ste16]. **(b)** Together with the magnetic guiding field pointing into the plane, an electric dipole creates an $\boldsymbol{E}\times\boldsymbol{B}$-drift. This drift can remove stored electrons onto the tank wall. Illustration taken from [Wan13].

be found in section 5.3.

5.1 Active removal of stored electrons with electric dipole fields

In the following the electric dipole method is reviewed in more detail as an powerful technique to reduce stored-particle background in MAC-E filters. The method has successfully been pioneered at the Mainz Neutrino mass experiment in the context of [Thü02, Mül02, Fla05]. In the following the theory for the removal of stored electrons (together with Monte Carlo simulations) from the KATRIN main spectrometer system is outlined. To create an electric dipole field in the main spectrometer, the eastern and western parts of the inner electrode have to be elevated to different potentials. This particular electrostatic setup evidently disturbs the transmission of signal electrons and thus can be applied during short off-beam times only. By design, the geometry of the inner electrode system is almost ideally axial symmetric, providing the possibility to set the eastern and the western half ring to different potentials by dedicated additional power supplies. Since the distance between two wire modules is of order $\mathcal{O}(25\,\mathrm{mm})$, the potential difference must not exceed $\Delta U = -1\,\mathrm{kV}$. The removal of stored electrons is based on the creation of an $\boldsymbol{E}\times\boldsymbol{B}$-drift velocity, which is defined as $\boldsymbol{v}_d = (\boldsymbol{E}\times\boldsymbol{B})/B^2$. Together with the magnetic guiding field lines this will induce a drift onto the vessel wall. Figure 5.1 illustrates the electric field lines in the main spectrometer for a 100 V dipole field (left) and the resulting outward-pointing drift velocity by the magnetic guiding field (right). The drift by the electric dipole fields is superimposed on the inherent magnetron motion of a stored electron, so that the guidance to the tank wall with $\boldsymbol{v}_d$ has to happen within one magnetron turn. The success of the electric dipole thus depends on the kinetic energy of the electron and the applied dipole field strength. Figure 5.2 illustrates a case where the electric dipole field is too weak so that the electron trajectory has not been pushed onto the tank wall within one magnetron turn. Also shown is the case where the dipole field is sufficiently strong to guide the electron onto the vessel wall.

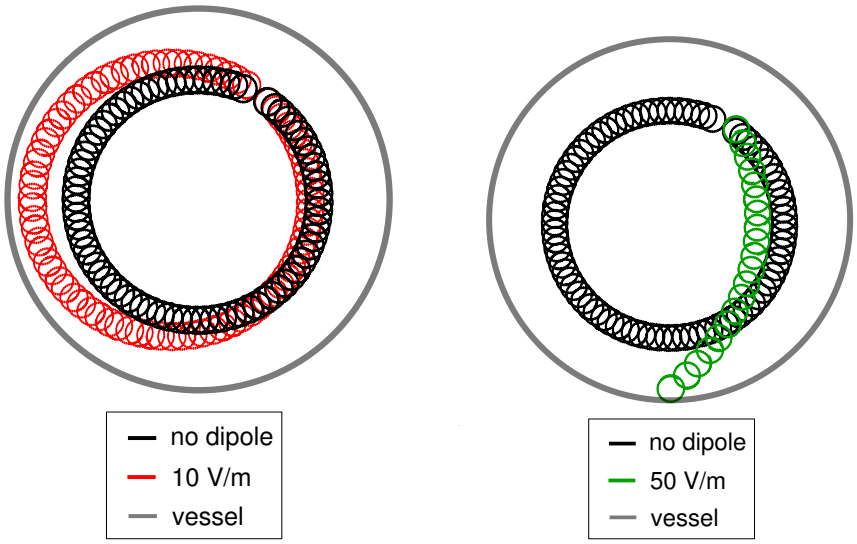

Figure 5.2: Influenced magnetron drift of a stored electron due to an electric dipole field. Left: A dipole field of $E = 10\,\mathrm{V/m}$ is to weak in order to move the electron onto the vessel wall within one magnetron turn. **Right:** The electron can be removed by applying a stronger electric field of $E = 10\,\mathrm{V/m}$. Figure from [Wan13].

This limitation of the electric dipole method mainly results from the proportionality of the kinetic energy of the electron and the magnetron drift velocity. While the latter will grow with the kinetic starting energy, the dipole drift velocity is limited due to the maximal field strength that can be applied. Also, high-energetic electrons which are closer to the tank wall cannot be removed easily, since the magnetron drift velocity also grows for higher radii. In order to investigate the removal efficiency, a in-depth simulation of the trapping probability was carried out in context of [Ste16]. Here, the trapping probability for twelve different electron starting kinetic energies was investigated for four different dipole field strengths. The simulation was carried out in the framework of a full three-dimensional main spectrometer model and the field solvers described in sec. 4.5. The following electromagnetic configuration was commonly chosen for all following simulations:

- Vessel voltage: $U = -18.5\,\mathrm{kV}$
- Inner electrode: $U = -18.6\,\mathrm{kV}$
- Dipole voltages: $0\,\mathrm{V}$, $-100\,\mathrm{V}$, $-500\,\mathrm{V}$ and $-1000\,\mathrm{V}$
- $5\,\mathrm{G}$ magnetic field configuration

Figure 5.3 confirms the above mentioned principles: The dipole field can efficiently remove low-energy stored particles, whereas electrons above a certain energy threshold remain trapped even in the presence of the non-axial component. This energy threshold is different for specific dipole field configurations. A potential drawback of this technique is, however, the fact that secondary particles from the vessel wall then can drift into the sensitive flux tube volume during the short (or longer) time period of the application of the dipole fields. In the context of measurements, this effect will be studied first for static electric dipole fields. In case where an electric dipole field is operated in a pulsed mode during very short time scales, this effect can be neglected. As a result, the dipole field technique then can be used to investigate the fraction of stored particles of the standard background. Furthermore dipole fields are sensitive to the kinetic energy of the electrons, so the dipole configuration can be used to investigate the electron spectrum of background electrons.

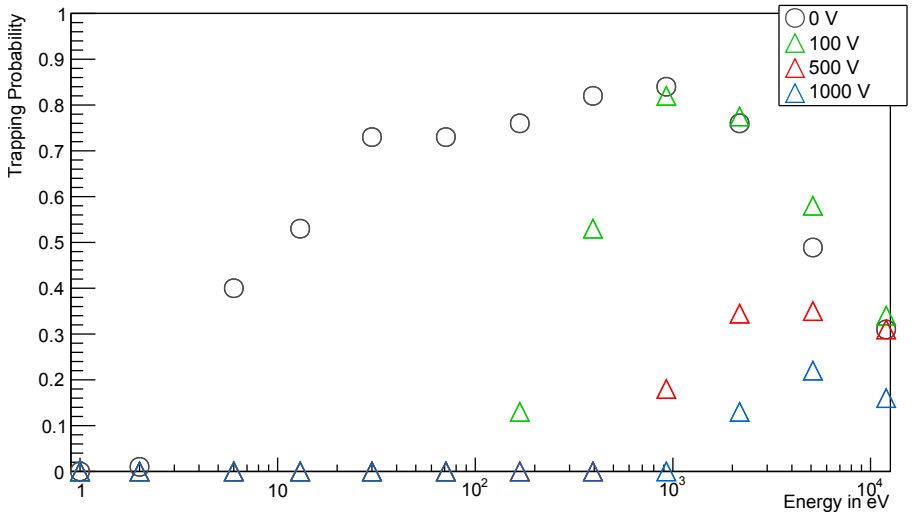

Figure 5.3: Simulation of trapping probabilities for different starting kinetic energies and dipole field strengths. Subdivision and numbering scheme of implemented electrode rings (sketch contains second wire layer). Figure adapted from [Ste16].

5.2 Influence of static dipole fields on intrinsic background

An extensive suite of measurements with static electric dipole fields was conducted to first commission the operation of the inner electrode system in a dipole potential configuration over longer time scales of $\mathcal{O}(\text{min})$. A dipole field can be established either by setting the eastern part or the western part of the electrode system onto a more negative potential. Due to the $\boldsymbol{E} \times \boldsymbol{B}$-drift, it is expected that particles from the vessel surface will drift into the sensitive flux tube volume. As the magnetic field of the setup always points into source direction, in case of the west half being more negative ("dipole-west"), secondary particles are expected to drift from the bottom between the two electrode sides to the top. If the eastern side ("dipole-east") is elevated onto a more negative potential, secondaries are expected to drift from the top down into the flux tube.

After discussion of the specific measurement settings, the difference between an eastern and western dipole setting is evaluated. During the measurements with static dipole fields, drastic reductions of the detector background rates were observed due to induced blocking potentials. This novel and previously neglected systematic transmission effect was confirmed by dedicated measurements together with corresponding simulations.

5.2.1 Measurement configuration and methodology

The electro-magnetic configuration for the following investigations is based on non-standard settings. It was used extensively in the context of background investigations in the SDS-II measurement campaign [Har15]. In this particular case, the transmission of signal electrons is not guaranteed due to the effect of early retardation [Gro15]. This effect implies that electrons are reflected due to a too negative potential present before the minimum magnetic field is reached which collimates the longitudinal momentum. This configuration is implemented for steep cone potentials, which are too negative. As the steep cone voltage is controlled by positive offset potentials, which add to the common inner electrode potential, an early retardation can happen in case of an insufficient positive offset potential. For transmission of signal electrons this effect has to be prevented, whereas for background investigations this effect can usually be neglected.

In the context of static dipole measurements, the steep cone offsets were set to an offset of 1 V only resulting in a non-negligible early retardation effect. For comparison, a single measurement was performed with a more positive offset (97 V), which prevents early

Table 5.1: Measurement configurations with static electric dipole fields.

Run number	Dipole side	U_{dipole} (V)	$U_{\text{steepcone}}$ (V)	Measurement time (s)
22177	east	-5	+1	7200
22178	east	-10	+1	3600
22179	east	-20	+1	10800
22180	east	-50	+1	3600
22200	west	-10	+1	3600
22201	west	-20	+1	7200
22202	west	-30	+1	3600
22203	west	-40	+1	3600
22204	west	-50	+1	7200
22205	west	-60	+1	3600
22206	west	-70	+1	3600
22207	west	-80	+1	3600
22208	west	-90	+1	3600
22209	west	-100	+1	7200
22385	west	-100	+97	3600

retardation. In both configurations, the vessel was elevated to −18.5 kV, while the inner electrode was set to be 100 V more negative. As the dipole potential is added to both voltages, it results in a maximal potential of −18.7 kV in the context of the dipole measurements. For the magnetic field configuration, SDS-II standard values for the EMCS currents were chosen. The LFCS system was set to a current setting to generate a 5 G magnetic field at the analyzing plane. Since a dual minimum configuration was chosen, the flux tube is more homogeneous as compared to a single minimum setting [Wan13]. The common values are summarized in the following:

- EMCS currents: 50 A (horizontal) and 9 A (vertical)
- LFCS configuration: 5 G (two magnetic field minima)
- Vessel potential: −18.5 kV
- Inner electrode potential: −18.6 kV
- Steep cone electrode offset: 1 V and 97 V
- Dipole offset potentials: −10 V ... −100 V

Table 5.1 lists all measurements together with the run number, the dipole location, the value of the dipole field, and the positive offset voltages of the steep cones.

5.2.2 Detector rate asymmetry with eastern and western dipole field

Over the course of the first measurements, the difference between eastern and western dipole configurations was tested by applying dipole voltages ranging from −5 V to −50 V. In table 5.2, the different mean detector rates are listed together with the ratio for the four dipole settings.

If the western electrode is set to a more negative potential, the resulting mean detector rate generally is lower than in the opposite case. For increasing dipole potentials the rate factor between the eastern and western dipole configurations increases by up to a factor of 1.5.

Table 5.2: Measurement configurations with static electric dipole fields.

Dipole voltage U_{dipole} (V)	Rate R_{east} (mcps)	Rate R_{east} (mcps)	$\frac{R_{\text{east}}}{R_{\text{west}}}$
-5	601.0 ± 0.9	484.1 ± 8.3	1.24
-10	766.3 ± 1.5	578.6 ± 1.3	1.32
-20	668.9 ± 7.9	489.1 ± 9.2	1.37
-50	372.6 ± 10.32	240.8 ± 5.8	1.55

Based on this observation, it can be concluded that more secondary particles are drifting from the top into the flux tube than from the bottom. This asymmetry has already been mentioned in [Har15] for measurements with an asymmetric magnetic field configuration. The different rates for eastern and western dipole fields tend to confirm these results. In principle, the cause of the observed asymmetry could be due to local variations of environmental or intrinsic radiation of field electron emission or due to cosmic muon induced secondaries. A large number of measurements was carried out in order to determine the primary source of secondary emission from the vessel surface. In these investigations, the effect of environmental radiation could be excluded as a result of dedicated measurements [Mül16]. Currently the most promising theory of secondary electron emission by the vessel surface is the decay of implanted ^{210}Po. This scenario is currently under investigation in [Tro17].

Because a western dipole configuration typically results in a smaller background contribution due to secondary particles from the vessel surface, this mode is used as standard one for all future dipole measurements.

5.2.3 Detector rate reduction by blocking potentials

For almost all static dipole measurements, an unexpected one-sided rate reduction was observed. In case of a western dipole, the FPD pixels covering the eastern part of the flux tube, show a strong rate reduction (fig. 5.7, left). This leads to the first order assumption that the electric dipole field is indeed very effective in removing stored background electrons. In the context of the measurements #22200 - #22209, this rate reduction effect was investigated for different static electric dipole field strengths (west). A dipole voltage of 100 V will typically generate a field of approx. 10 V/m in the central flux tube volume. As expected, the reduction effect evidently is proportional to the applied dipole voltage as can been seen in fig. 5.4.

In addition, the signature of incoming secondary particles from the vessel surface can clearly be seen experimentally. The measured detector pixel pattern confirms qualitatively previous simulations, carried out in [Wan13]. Figure 5.5 (right) shows exemplary the pixel pattern obtained for a -10 V dipole setting. As expected in case of a western dipole, electrons from the bottom drift into the flux tube due to the resulting $\boldsymbol{E} \times \boldsymbol{B}$-drift.

The removal of electrons with an electric dipole would indicate that a large fraction of the background stems from stored particles with kinetic energies above 1.5 eV. However, the current background model [DM16, Dre15a, Dre15c] strongly disfavors and even contradicts this hypothesis. The background model proposes a dominant contribution due to very low energetic (orer of 10^{-2} eV) non-trapped electrons which was independently confirmed in [Tro17, Mül16].

In order to explain the visible rate reduction at the detector, the potential configuration of the dipole measurements had to be investigated further. Interestingly, a suite of in-depth

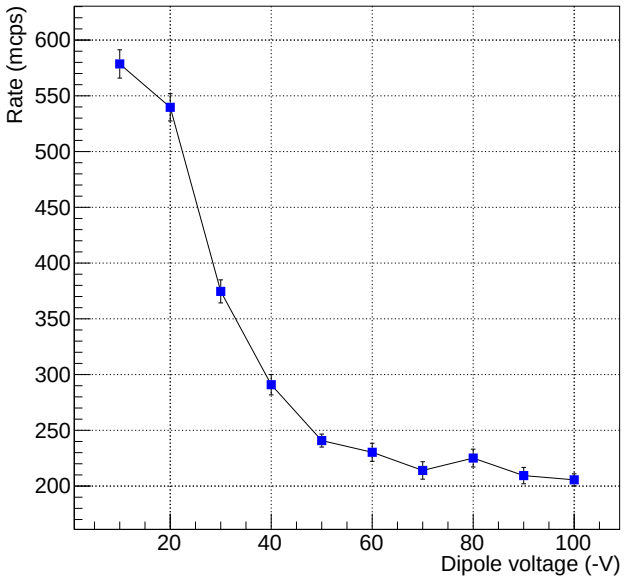

Figure 5.4: Detector rates as measured for different static electric dipole fields (west). The steeply decreasing detector rates in case of higher static electric dipole fields shown here amount to up to a factor 2.8.

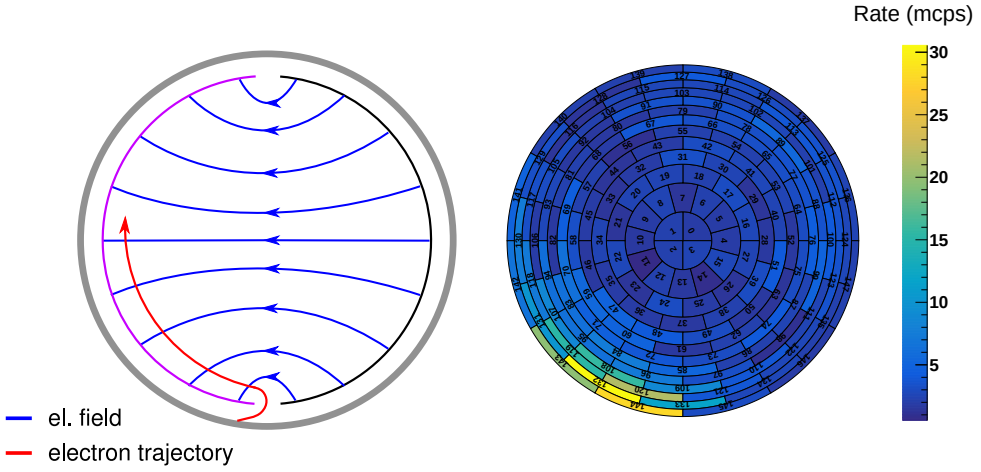

(a) Simulation of particles drifting into the flux tube due to a dipole field on the west side

(b) Pixel pattern of a measurement with −10 V dipole potential

Figure 5.5: Illustration of particle drift from the bottom side due to a western electric dipole and pixel pattern of a -10 V dipole configuration. Left illustration adapted from [Wan13].

simulations has revealed that small Penning traps will block electrons in detector direction in cases when the steep cone electrode is not elevated to a more positive potential. As already mentioned, all corresponding measurements were carried out with a steep cone which was not elevated to a more positive potential. Consequently, a blocking potential was created during the static dipole measurements. Figure 5.6 shows the underlying principle of a blocking potential.

In case of dipole configurations, the blocking potentials will occur on the opposite side of the applied dipole electrode with the more negative potential. In case of a western dipole,

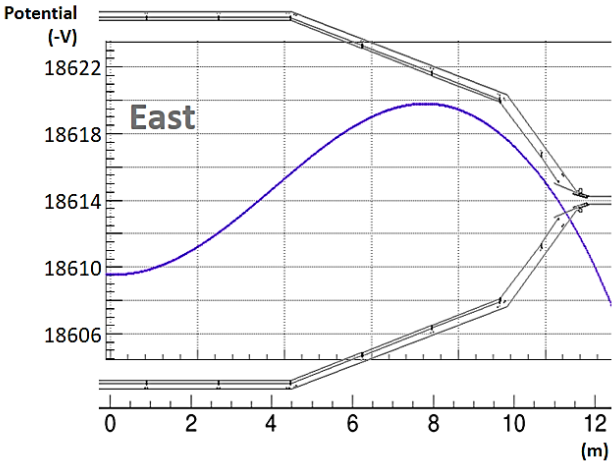

Figure 5.6: Sketch of a blocking potential. The picture illustrates the underlying principle of a blocking potential. If a dipole field is applied, characteristic potential hills can occur if the steep cones are not set to a more positive potential on the opposite side of the more negative dipole electrode. For example in case of a dipole voltage applied at the western electrode, the blocking potentials occur at the eastern volume. These small Penning traps prevent electrons from being registered at the detector.

the traps thus will occur on the eastern side, where the potential is more positive than on the western side. This explains why the rate reduction was visible only at one detector half, namely at the eastern pixels. In order to validate the assumption of blocking potentials, the dipole configuration was operated also with a more positive steep cone, hence with a setting which fulfills the transmission condition. Interestingly the transmission condition itself is not the crucial point. It is a rather the potential compensation which is important in this case. In a dipole configuration, one side is more negative than the other, so this negative potential penetrates to the more positive part. In the region of the small flat cone and steep cone the electrodes are relative close to each other. Accordingly, the negative potential has a significant influence here. The Penning trap occurs since this negative potential is enclosed by the more positive potential coming from the ground electrode and a blocking occurs. By setting the steep cones to more positive values, the negative potential from the western half has no longer a significant effect since the entire steep cone and flat cone areas (where the electrodes are close to each other) are more positive.

Figure 5.7 compares the detector pixel map of a 100 V dipole without (left) and with (right) positive steep cone electrodes. It is clearly visible that in case of more positive steep cones, the "removal" effect vanishes (note the difference in the scaling).

It can thus be concluded that the effect of lower rates in case of a dipole configuration is not an indication for the removal of stored electrons by an $\boldsymbol{E} \times \boldsymbol{B}$-drift. It can however be traced back to be due to the emergence of small Penning traps which block electrons from reaching the detector region. In the following, detailed potential configurations are computed along magnetic field lines in order to investigate the depth and the location of the resulting Penning traps.

5.2.4 Calculation of blocking potentials

In order to localize the emergence of Penning traps by means of dedicated simulations, specific field lines were simulated for different detector pixels in the eastern (130, 82, 34, 10) and in the western FPD hemisphere (nos. 124, 76, 28, 4). In both cases the electric and magnetic configuration from runs #22209 (without positive steep cones) and #22385

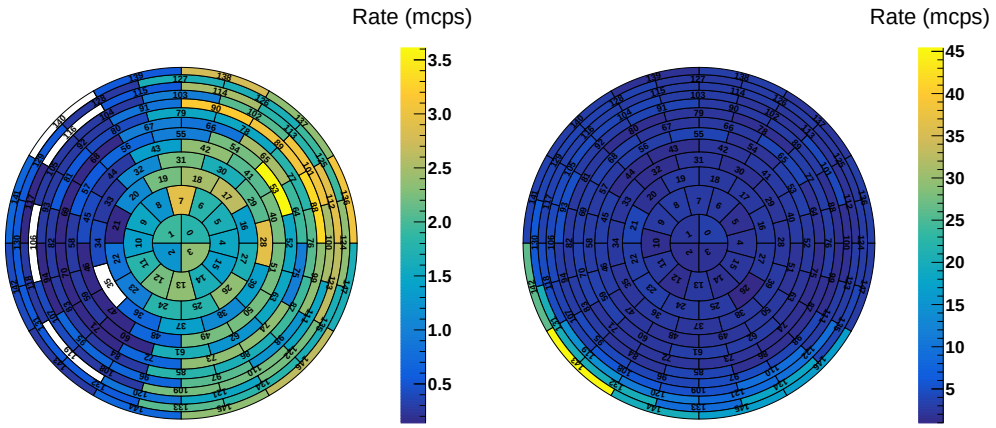

(a) Static dipole (west, -100V) with more positive steep cones (97 V) which fulfills the transmission condition

(b) Static dipole (west, -100V) with more positive steep cones (97 V) which fulfills the transmission condition

Figure 5.7: Pixel distribution for static dipole measurements with different steep cone offset potentials. Left: Here the effect of blocking potentials can be recognized by the drastic decrease of count rate at the eastern half (left). This effect results from a too negative steep cone potential. **Right:** The pixel distribution of a correctly set steep cone offset shows no effect on the spectrum by a static dipole field. Here almost no electrons are blocked.

Table 5.3: Location and depth of blocking potentials.

Pixel	Depth (V)	z_{block} (m)
130	7.822797	-9.114631
82	5.764673	-8.798667
34	2.977971	-8.256392
10	0.769079	-7.171936

(with positive steep cones) was chosen. In all cases the field lines start from the detector wafer. The legend of the following different plots denotes the radial position of the field line at $z = 0\,\text{m}$. Figure 5.8 first compares the effect of the blocking potential at the eastern and western sides both with and without positive steep cones. The blocking potentials will occur mainly on the eastern side for outer pixels. However, even on the western side small blocking potentials will occur. In general, the blocking potentials are not symmetric at $z = 0\,\text{m}$ because the pinch magnet has a higher magnetic field than the pre-spectrometer magnet. Interestingly, the minimum of the blocking potentials will move to $z = 0\,\text{m}$ for field lines starting at inner pixels.

Table 5.3 lists the depth of the blocking potentials for the eastern pixels in case of a negligible steep cone offset voltage from picture 5.8, top.

Over the course of this investigation an optimal dipole potential setting was found to gather information from the entire flux tube. In doing so, the western dipole configuration was chosen, as this configuration leads to a somewhat smaller influx of secondary particles from the vessel surface than the eastern configuration.

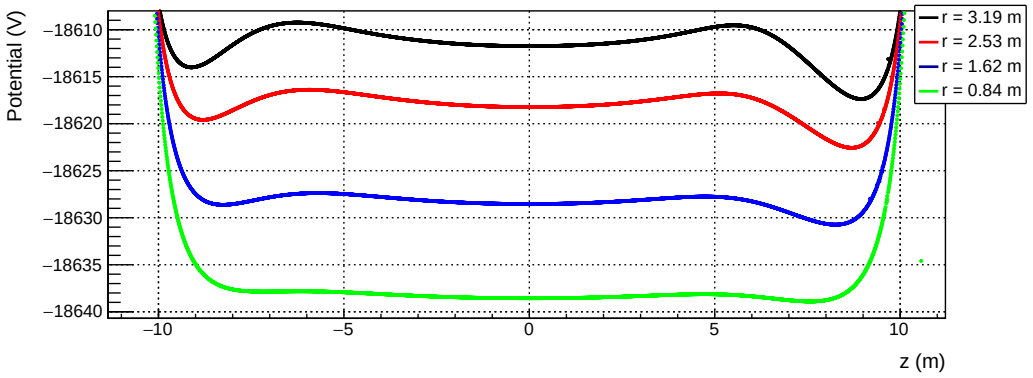

(a) East field lines, +1 V steep cone offset

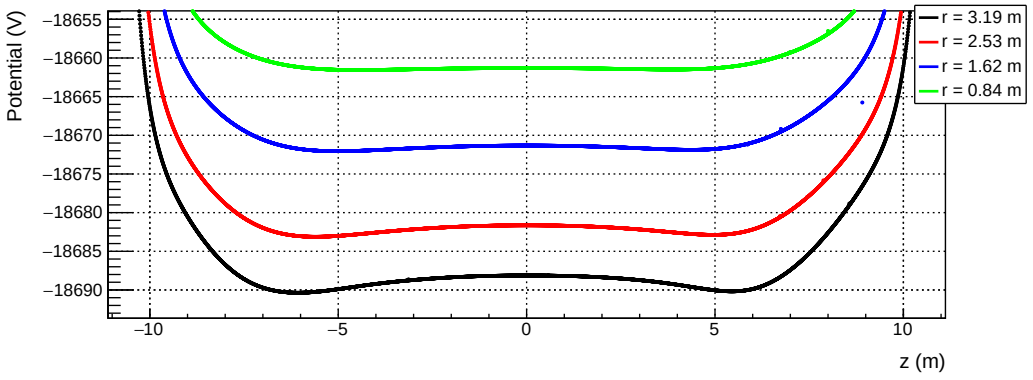

(b) West field lines, +1 V steep cone offset

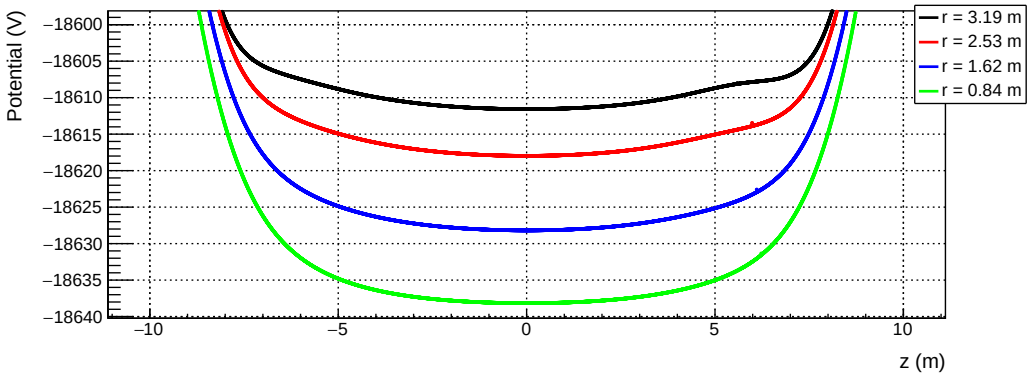

(c) East field lines, +97 V steep cone offset

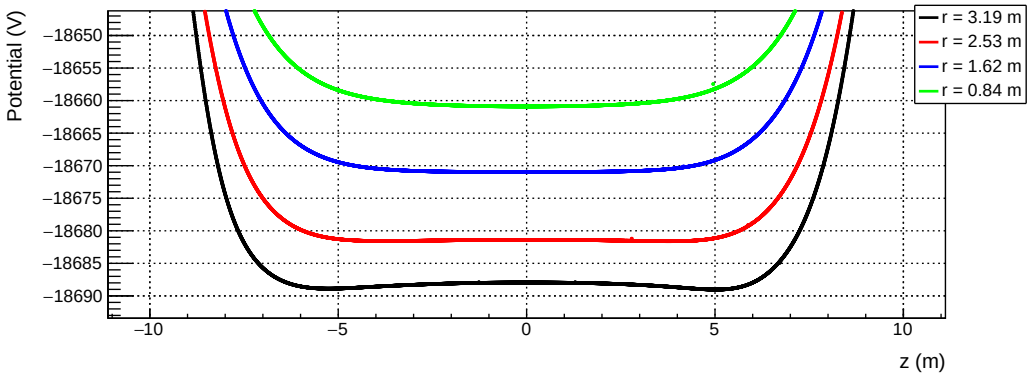

(d) West field lines, +97 V steep cone offset

Figure 5.8: Field lines for a west -100 V electric dipole with different positive steep cone offsets.

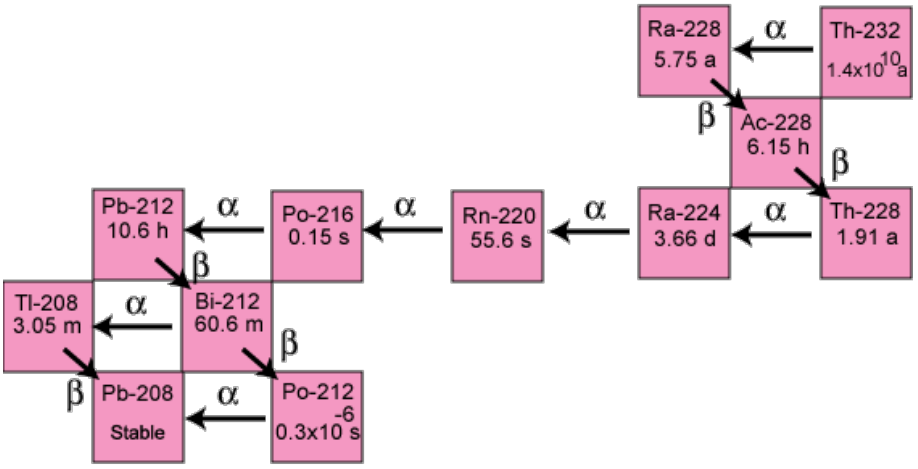

Figure 5.9: Decay scheme of ^{232}Th. A ^{220}Rn nucleus is created by the α-decay of ^{224}Ra and results itself in ^{216}Po. The different decay modes are indicated together with the half-life of the corresponding elements. Adapted from [Sur].

5.3 Influence of pulsed dipole fields on artificial stored particle background

As explained above, the technique of applying electric dipole pulses for short time periods ($\mathcal{O}(s)$) represents a highly effective method to remove stored low-energy electrons. To validate this, a ^{220}Rn source was attached to the spectrometer in order to artificially increase the stored-particle background in the SDS-II campaign. In this way the functionality and the efficiency of the electric dipole method could be studied for different dipole field configurations. In the following, the complex atomic deexcitation processes following the α-decay of ^{220}Rn are outlined. This is followed by a discussion of the energy spectrum of electrons following the nuclear α-decay. before the results of measurements with pulsed electric dipole fields are presented which were targeted to derive corresponding reduction factors for different dipole field strengths. Finally the background relaxation time scale is discussed in order to suggest an optimal pulse scheme for stored-particle background.

5.3.1 Stored electrons due to radon α-decay

When studying the removal efficiency of the electric dipole method, the goal is to actively remove both the stored primary and secondary electrons from radon α-decay. Benefiting from the increased event statistics due to the artificial source, the dipole technique can now be investigated in detail even for short pulse time scales. In the following the physical processes of the creation of primary electrons and secondary electrons following α-decay of ^{220}Rn are discussed. The ^{220}Rn isotope is part of the long ^{232}Th decay chain, which is illustrated in fig. 5.9. With a half-life time of 55.6 s, ^{220}Rn atoms will decay into ^{216}Po via an α-decay.

The emission of an α-particle does not lead directly to background, as this particle is very heavy and thus will not follow the rather weak magnetic field lines in the central parts of the main spectrometer. However electrons can be emitted after the decay due to various atomic deexcitation processes. There are several types of processes resulting in an electron emission:

- **Conversion electrons:** If the wave-function of a shell electron is non-vanishing at the nucleus, it can be emitted during de-excitation of the excited polonium nucleus. This class of electrons occurs with a rather low probability ($<10^{-5}$) in the case of

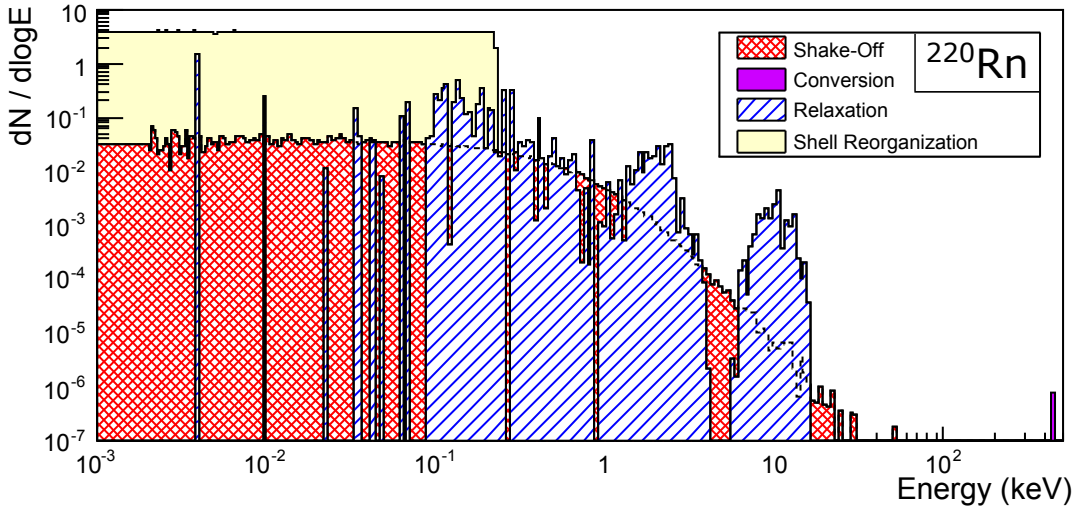

Figure 5.10: Energy spectrum of emitted electrons following ^{220}Rn decay. The plot shows the energy distribution of conversion, shake-off, relaxation and shake-off electrons. Adapted from [Wan13].

^{220}Rn decay, since there exists only a single excited state of polonium, which is populated via ^{220}Rn decay.

- **Shake-off electrons:** α-particles will propagate with a large speed of $\approx 10^7$ m/s and when colliding with atomic shell electrons, which typically have a speed which is lower by one order of magnitude, atomic electrons are emitted.
- **Shell reorganization electrons:** Electrons in the outer shells have a much lower speed than the emitted α-particle, hence instead of a collision the change of the charge of the nucleus will lead to a sudden emission of on average two shell reorganization electrons.
- **Auger electrons:** Shake-off and conversion electrons leave a vacancy in the atomic shell which is filled by electrons from outer shells. During the filling mechanism, a non-negligible number of X-ray photons or Auger electrons is emitted. The latter case can result in a chain reaction (Auger explosion) which leads to the emission of a specific number of Auger electrons [Mer12].

Figure 5.10 illustrates the electron energy spectrum of the ^{220}Rn α-decay and distinguishes the above mentioned different processes.

The primary stored high-energy electron released during α-decay will slowly cool down via ionization of residual gas molecules until it is finally no longer stored. The visible background signal at the detector will thus come predominantly from secondary electrons from ionization processes of the residual gas. These electrons are low-energetic and can leave the spectrometer over rather short time intervals of several minutes. The number of created secondary electrons N_e depends on the energy of the primary electron E_{prim} and its average energy loss per ionization process $< E_{\text{loss}} >$, which is in the order $\mathcal{O}(37\,\text{meV})$ [M$^+$, M$^+$13]:

$$N_e(E_{\text{prim}}) \approx \frac{E_{\text{prim}}}{< E_{\text{loss}} >}. \tag{5.1}$$

A very high-energy primary particle evidently will stay trapped over longer time periods in the spectrometer, as long as it is still adiabatic, leading to more secondary electrons. Figure 5.11 displays the number of created secondaries as a function of the kinetic energy

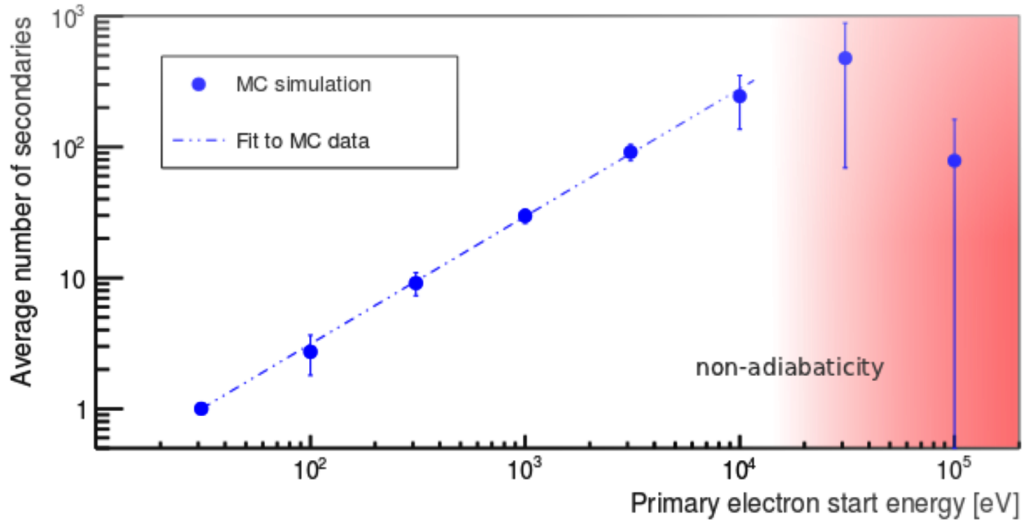

Figure 5.11: Number of secondary electrons from primary electrons of radon α-decay. Adapted from [Mer12].

of the primary electron. Both at the very low and very high energy end, the primary particles are not longer stored.

During ν-mass runs, the enhanced creation rate of secondary particles represents a non-Poisson background process which can significantly reduce the ν-mass sensitivity of KATRIN.

According to previous simulations, the electric dipole method is expected to remove both primary and secondary stored electrons with kinetic energies up to 1 keV (fig. 5.3). In the following dedicated measurements are discussed, which have demonstrated that the electric dipole method can indeed effectively remove this type of particles.

5.3.2 Measurement configuration and methodology

After warming-up of the baffle system to $T_{\text{baffle}} \approx 294\,\text{K}$ at pump port 3, an artificial ^{220}Rn source was attached behind the Cu-baffles. In this elevated temperature regime the emanated radon atoms are no longer cryosorbed on the baffle surface. All measurements performed and analyzed in the context of this investigation share the following standard setup of electro-magnetic fields:

- EMCS currents: 50 A (horizontal) and 9 A (vertical)
- LFCS configuration: 5 G (at $z = 0\,\text{m}$, two magnetic field minima)
- Vessel potential: $-18.5\,\text{kV}$
- Inner electrode potential: $-18.6\,\text{kV}$
- Steep cone electrode offset: 1 V
- Dipole potentials (west): $-5\,\text{V}$ ... $-100\,\text{V}$

Throughout the measurement campaign, the dipole offset voltage was applied exclusively to the western electrode part. In this case, electron drift processes are directed from the bottom to the top. For all settings, a dipole pulse of 1 s length ("on-time") was applied, followed by a 29 s long relaxation time window ("off-time"). The measurement time with different dipole field configurations is distributed according to table 5.4.

The large ensemble of pulse cycles was stacked to a single period of 30 s for analysis, with all events binned into 1 s long intervals.

Table 5.4: Measurement configurations with pulsed dipole fields and attached artificial ^{220}Rn source. The table below lists the dipole offset potentials applied on the western electrode part together with the measurement time and the dipole pulse cycles.

	Run number	$U_{\text{west-dipole}}$ (V)	Measurement time (s)	Stacked pulse cycles
1	#24134	-100	3600	120
2	#24135	-75	3600	120
3	#24136	-50	3600	120
4	#24137	-25	2700	90
5	#24138	-5	2400	80

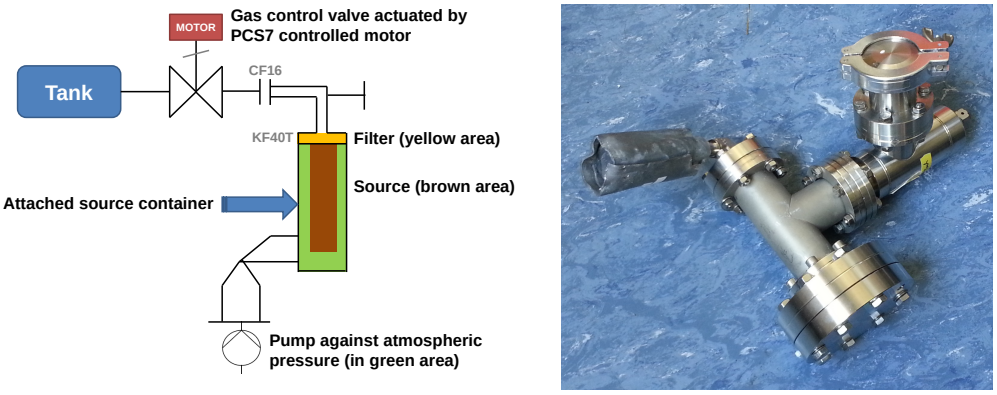

Figure 5.12: Source container for artifical sources. Left: Flowchart of the source container attachment. The system is separated from the main spec UHV by a PCS7-controlled leak valve and a manual operated valve. After opening all valves, the UHV is furthermore protected by a sintered filter from the attached source material. **Right:** On the picture the source container area is visible on top, right. Below the source container the manual-controlled valve is installed.

Installation of container system for artifical sources

The vacuum system of the spectrometer provides excellent UHV conditions and also comprises a dedicated gas-inlet system to release radon atoms in the inner volume.

In order to attach the source to the main spectrometer volume under UHV conditions, the source container has multiple vacuum regions, which are separated by different valves. At first the source chamber has to be pumped out through a fore-vacuum stand at pump port 2. Afterwards, a manually operated valve has to be closed to separate the source from the fore vacuum pump. Afterwards a second valve is opened manually in order to connect the source volume (separated by a sintered filter) to the main vacuum volume.

Pixel exclusion

As outlined above, the dipole field was consistently applied to the western side of the inner electrode system so that particles (under the influence of the $\boldsymbol{E}\times\boldsymbol{B}$-drift) will enter the flux tube from the bottom side of the electrode. In the analysis chain targeted to deduce the rate reduction of stored particles in the flux tube, detector pixels being dominated by these electrons were systematically excluded from the analysis. In order to gather information on the influence by electrons from the vessel wall, the determination of reduction factors and relaxation times was performed using two different pixel patterns which are facing to the bottom part of the electrode. Figure 5.13 illustrates the excluded pixel areas on the

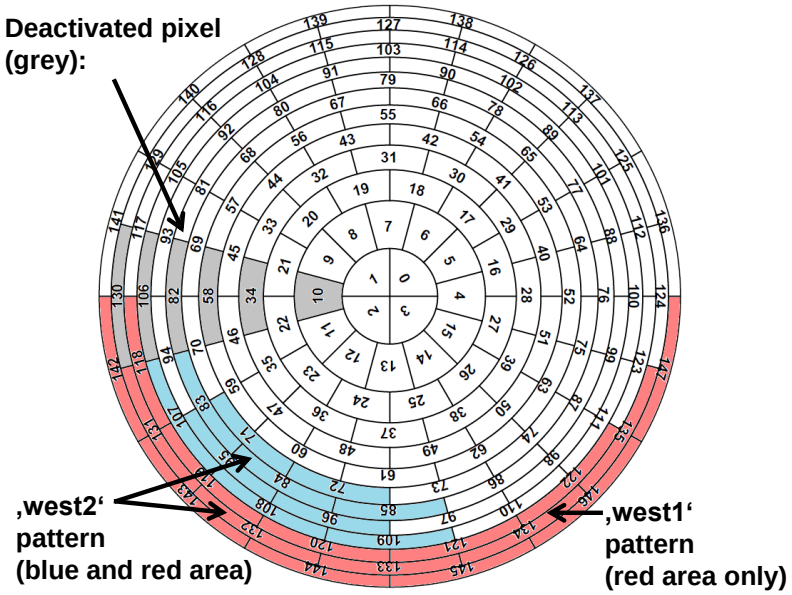

Figure 5.13: Excluded pixels for analysis of pulsed electric dipole fields. For the pixel exclusion three pixel pattern have been defined. **Grey:** A pre-amplifier of the detector has been deactivated due to instabilities and no rate information is delivered at these six pixels for all measurements with a pulsed dipole. **Red:** 16 pixels at the outer bottom of the FPD pixel map have been excluded for taking into account secondary electrons from the tank wall. **Blue:** A pattern of five pixels, which are located further inside, facing to the eastern electrode part, have been excluded additionally.

detector. First, only the centrally aligned red area was excluded (in the following labeled as “west1”) and then, secondly, in addition the blue-shaded area was excluded as well, consisting of a further six pixels, facing the eastern electrode part. The combination of both exclusion patterns is labeled as “west2”. For these particular pixel areas, an increase of electrons is expected due to a western dipole field as already shown by measurements with a static electric dipole field. With the help of these two pixel groups, the influence on the electron spectrum and the reduction efficiency of the dipole field can be studied in more detail. Due to non-nominal fluctuations of a pre-amplifier card, a total of six additional pixels (grey color) had to be excluded for the analysis described below.

5.3.3 Dipole field strength and background reduction factors

Each dipole pulse was applied over a time period of 1 s. Directly after the pulse, a rate relaxation was recorded. The following exponential fit function was used to model the characteristic relaxation time scale:

$$R(t) = R_0 \cdot \left(1 - \exp\left(-\frac{t}{\tau}\right)\right). \tag{5.2}$$

The relaxation function is adapted from the rather similar charging process of a capacitor in an RC-circuit. Here, R_0 is the maximal rate achieved after an infinitesimal relaxation time, whereas the parameter τ is the characteristic time constant which describes the rate relaxation time after the pulse. The goal now is to determine the reduction factor to examine the effect of different dipole field strengths on radon-induced secondary particles. Table 5.5 compares the fit parameters of the different dipole voltages together with different pixel exclusion patterns.

The errors given in the table are based on Poisson statistics and do not regard inherent non-Poisson nature of radon-induced background processes. In the latter case, the rate error

Table 5.5: Parameters for dipole fit function. The rate increase after a dipole pulse is described by an exponential function with two parameters. R_0 represents the infinitesimal rate to be achieved after a pulse and τ the time constant. The last column contains the χ^2-value over the number of degrees of freedom as an indicator for the fit quality.

Pixel pattern	R_0 (mcps)	τ (s)	χ^2/ndf
$U_{\text{dip}} = -100\,V$			
none	4286.26 ± 57.63	5.41 ± 0.26	65.11/27
west1	3877.63 ± 55.73	5.56 ± 0.28	68.18/27
west2	3605.04 ± 54.23	5.65 ± 0.29	56.9/27
$U_{\text{dip}} = -75\,V$			
none	3746.16 ± 47.34	4.06 ± 0.23	78.05/27
west1	3384.88 ± 44.18	4.02 ± 0.23	63.81/27
west2	3150.28 ± 42.34	4.04 ± 0.24	60.73/27
$U_{\text{dip}} = -50\,V$			
none	3483.07 ± 40.27	3.05 ± 0.19	51.32/27
west1	3145.00 ± 38.25	3.02 ± 0.20	55.54/27
west2	2914.10 ± 36.97	3.03 ± 0.21	52.22/27
$U_{\text{dip}} = -25\,V$			
none	3935.79 ± 46.54	2.22 ± 0.18	51.18/27
west1	3560.47 ± 44.33	2.20 ± 0.19	61.39/27
west2	3291.77 ± 42.91	2.21 ± 0.21	59.48/27
$U_{\text{dip}} = -5\,V$			
none	3759.05 ± 42.27	0.74 ± 0.16	30.84/27
west1	3373.51 ± 39.94	0.71 ± 0.17	37.08/27
west2	3130.81 ± 38.19	0.61 ± 0.19	33.15/27

between two dipole pulses has to be scaled due to the non-Poisson process of creation of radon-induced secondary electrons. In context of [Mer12, Wan13, Har15] radon-induced background processes were studied together with the expected error contribution. In context of this study, the quality of rate reduction is discussed in the context of the applied dipole field. The following conclusions can be extracted from the fitted data in table 5.5:

- The rates R_0, gathered at different dipole voltages, show a strong variation confirming the influence of the non-Poissonian creation of secondary particles of ^{220}Rn.
- The time constant increases for a higher applied dipole voltage. This implies that a higher dipole fields can remove higher energetic primary electrons of ^{220}Rn. Since these electrons are removed, it takes up a longer time to 'recover' the elevated level of low-energy secondary electrons from subsequent α-decays which release high-energy primaries, while the low dipole field strength is capable of removing only very low-energy secondary electrons. The primary electrons with higher energy will not be removed for lower dipole fields. The results confirm previous simulations, cf. fig. 5.3.
- At the first stage the different exclusion pattern lead to no visible effect regarding the determination of reduction factors.

In the next step, the count rate recovery time scales will be discussed.

5.3.4 Dipole pulse frequencies and background relaxation time

The time constants summarized in table 5.5 depend on the applied dipole voltage and therefore give a hint on how effective the specific dipole setting is to remove stored low-energy electrons. The time scale t_{relax} defines the time period after the dipole pulse, when the rate has 'recovered' to a fraction α of the original rate:

$$t_{\mathrm{relax}} = -\tau \ln\left(1 - \frac{R_{\mathrm{target}}}{R_0}\right) \tag{5.3}$$

$$= -\tau \ln\left(1 - \alpha\right) \tag{5.4}$$

The corresponding times were calculated for different dipole voltages and different pixel exclusion patterns, as summarized in table 5.8. The applied dipole voltage is proportional to observed relaxation time. The 100 V dipole configuration evidently is the most effective, in his case the 1 s pulse needs to be applied every 3.9 seconds to obtain a rate reduction of 50 %. For a long-term KATRIN measurement this value could be exemplary scaled up: During the one second pulse time, no measurement with tritium can be taken for analysis since a dipole field distorts the MAC-E principle. After this period, a 3.9 s long interval could be used to take data with a lower background rate. This would correspond to a fraction of 78.4 % of the total measurement time while profiting from a 50 % less background. However, this scenario would introduce additional systematics due to the non-constant background rate in between dipole pulses. To minimize systematic uncertainties due to this previously ignored effect, an excellent understanding of the recovery time periods after a single pulse would be needed. In general, the method of periodic dipole pulses needs a through understanding of the recovery time scales. This is one of the central realizations of this work.

Figure 5.14 compares the rate relaxation effects of the 5 V and 100 V dipoles. The two histograms contain the normalized counts per second for the stacked pulse intervals. For the 100 V dipole, a total of 120 intervals were stacked, whereas for the 5 V dipole an ensemble of 80 pulses was taken into account. The x-axis labels the time in seconds with bin sizes of one second. The y-axis denotes the counts, scaled in millicounts per second

Table 5.6: Rates during and after the dipole pulse at fixed times. The rates have been determined at fixed times

Pixel pattern	$R(t = 0\,\mathrm{s})$ (mcps)	$R(t = 1\,\mathrm{s})$ (mcps)	$R(t = 30\,\mathrm{s})$ (mcps)
$U_{\mathrm{dip}} = -100\,V$			
none	1917 ± 126	1317 ± 105	4825 ± 201
west1	1442 ± 110	1183 ± 99	4333 ± 190
west2	1350 ± 106	1067 ± 94	4017 ± 183
$U_{\mathrm{dip}} = -75\,V$			
none	1783 ± 122	1775 ± 122	3708 ± 176
west1	1450 ± 110	1558 ± 114	3342 ± 167
west2	1367 ± 107	1447 ± 110	3092 ± 161
$U_{\mathrm{dip}} = -50\,V$			
none	1733 ± 120	1975 ± 128	3550 ± 172
west1	1533 ± 113	1858 ± 124	3183 ± 163
west2	1483 ± 111	1717 ± 120	2992 ± 158
$U_{\mathrm{dip}} = -25\,V$			
none	2267 ± 159	2489 ± 166	4067 ± 213
west1	1989 ± 149	2289 ± 159	3722 ± 203
west2	1833 ± 143	2156 ± 155	3422 ± 195
$U_{\mathrm{dip}} = -5\,V$			
none	3188 ± 200	3363 ± 205	4050 ± 225
west1	2875 ± 190	3038 ± 195	3650 ± 214
west2	2638 ± 182	2913 ± 191	3325 ± 204

Table 5.7: Rate reduction factors as determined by rate at t=30 s and t=1 s.

Dipole voltage	No pixel exclusion	West1 exclusion	West2 exclusion
-100 V	3.66 ± 0.44	3.66 ± 0.47	3.77 ± 0.50
-75 V	2.09 ± 0.24	2.14 ± 0.26	2.14 ± 0.27
-50 V	1.80 ± 0.20	1.71 ± 0.20	1.74 ± 0.21
-25 V	1.63 ± 0.19	1.63 ± 0.20	1.59 ± 0.20
-5 V	1.20 ± 0.14	1.20 ± 0.15	1.14 ± 0.14

Table 5.8: Rates during and after the dipole pulse at fixed times.

Pixel pattern	$t_{\mathrm{relax}}(50\,\%)$ (s)	$t_{\mathrm{relax}}(90\,\%)$ (s)
$U_{\mathrm{dip}} = -100\,V$		
none	3.75 ± 0.18	12.46 ± 0.60
west1	3.85 ± 0.19	12.80 ± 0.64
west2	3.92 ± 0.20	13.02 ± 0.67
$U_{\mathrm{dip}} = -75\,V$		
none	2.82 ± 0.16	9.35 ± 0.53
west1	2.79 ± 0.16	9.26 ± 0.53
west2	2.80 ± 0.17	9.30 ± 0.55
$U_{\mathrm{dip}} = -50\,V$		
none	2.11 ± 0.13	7.02 ± 0.44
west1	2.09 ± 0.14	6.96 ± 0.46
west2	2.10 ± 0.16	6.98 ± 0.48
$U_{\mathrm{dip}} = -25\,V$		
none	1.54 ± 0.15	5.12 ± 0.41
west1	1.53 ± 0.13	5.07 ± 0.44
west2	1.53 ± 0.16	5.09 ± 0.48
$U_{\mathrm{dip}} = -5\,V$		
none	0.51 ± 0.11	1.71 ± 0.37
west1	0.49 ± 0.12	5.09 ± 0.39
west2	0.42 ± 0.13	1.41 ± 0.44

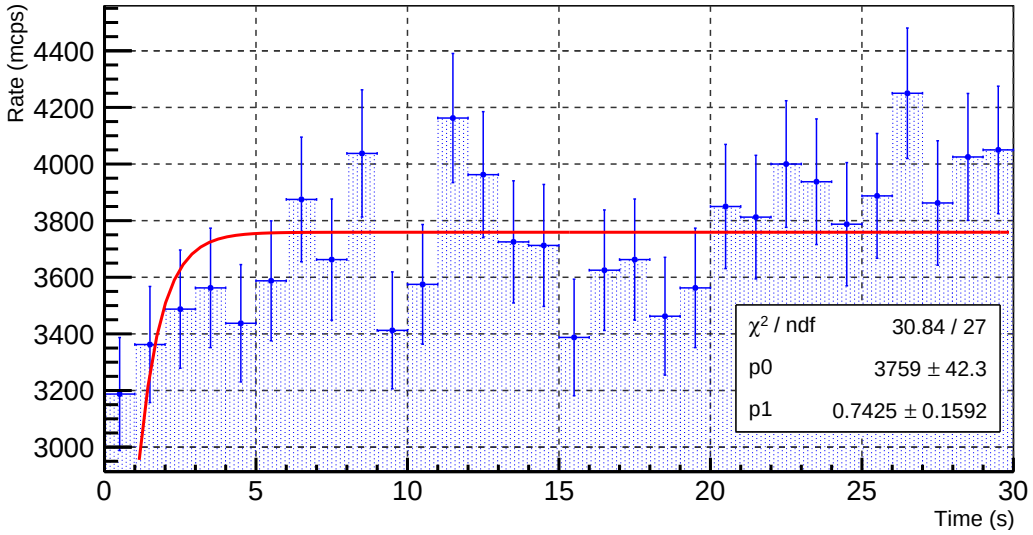

(a) Reduction of ^{220}Rn secondary electrons with a 5 V-dipole field

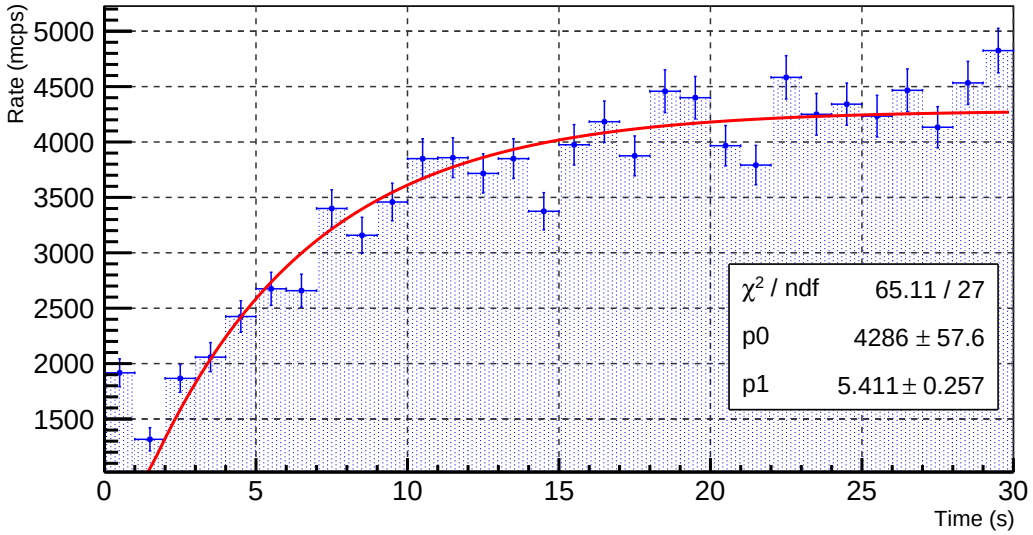

(b) Reduction of ^{220}Rn secondary electrons with a 100 V-dipole field

Figure 5.14: Reduction of ^{220}Rn secondary electrons with a 5 V and 100 V-dipole field. The two histograms show the rate reduction due to a 5 V- and 100 V-dipole field.

(mcps). In the graph additional information on the respective fit function can be found. Together with the normalized χ^2-value, the parameters $p_0(= R_0)$ and $p_1(= \tau)$ are given. The error bars are computed based on a Poissonian statistics with $\sigma = \sqrt{N}$.

The first bin is not incorporated into the fit function as in this time period the dipole is applied. It is clearly visible that the 100 V dipole gives the distinct advantage of a relatively long relaxation time. It also feature a very good rate reduction compared to the other field settings. Figure 5.15 shows a comparison of all different dipole field configurations.

5.4 Conclusion

In this chapter the electric dipole potential configuration of the main spectrometer was investigated at first with static dipole potentials of up to −100 V. The system works

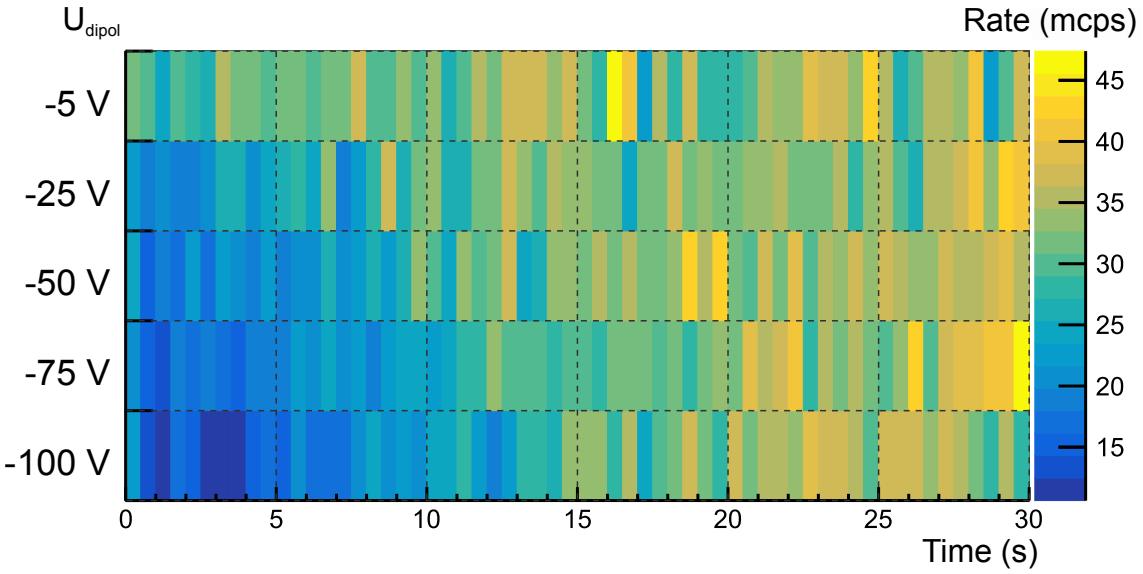

Figure 5.15: Illustration of rate reduction by all measured different dipole configurations. The stacked rates during and after dipole pulse are illustrated. The picture shows that a 100 V dipole has the largest time constant. As the time constant will be shorter for longer dipole fields, the reduction efficiency decreases as well.

reliably and the effects of different dipole field configurations were investigated. As one main result, measurements revealed a high background rate in case of an eastern negative dipole potential. In this case, secondary particles from the top enter the flux tube due to the induced $\boldsymbol{E} \times \boldsymbol{B}$-drift. This has been compared with a western dipole field which profits from a lower secondary rate. Furthermore measurements were performed with different dipole potential settings with negligible positive steep cone offset. In this steep cone configuration, the transmission of signal electrons is distorted and in case of an applied dipole potential, Penning traps occur which establish blocking potentials of up to $-7.8\,\mathrm{V}$. This could be demonstrated via measurements with different potential settings and corresponding simulations.

For the second part of this chapter the effect of the electric dipole was studied in the context of pulsed fields in order to remove stored particle background during normal operation. For this measurement series it was essential to artificially increase this background type in the main spectrometer with additional ^{220}Rn, which has been attached via a source chamber to the vacuum system. The α-decay of radon will lead to stored high-energy electrons which give rise to a high amount of stored secondary electrons. The dipole method can remove both types of electrons if their energy is below around 1 keV. Different dipole voltages were tested and an optimal dipole potential of $-100\,\mathrm{V}$ was determined. This setting would allow in an optimal case during normal scanning to reduce the stored particle induced background by 50 % by using still over 75 % of the available measurement time. However, the introduced pressure-dependent recovery times of the background in between dipole pulses would introduce a systematic effect over the net 3 years of measuring time. Therefor the application of dipole pulses should only proceed in case of a significant background reduction. At present, the limited rate of background electrons from non-trapped ^{219}Rn atoms released from the NEG stored does not necessitate this.

CHAPTER 6

Survey of background in the main spectrometer with special field configurations

In context of the second commissioning measurement phase of the main spectrometer and detector section from October 2014 to September 2015, the well-known radon-induced background component [Mer12, Wan13] was investigated and successfully reduced to a level of $R_0 = (36^{+18}_{-15})$ mcps together as a result of the continuous operation of the system of three cold baffle [Har15].

A much larger and at present irreducible background component of $R = (664 \pm 1)$ mcps (with 3.8 G setting) has however remained in case of an unbaked spectrometer and $R = (397 \pm 2)$ mcps in case of a fully baked-out vessel. Both background levels have a non-negligible impact on the sensitivity for the observables of the neutrino mass in the context of the long-term measurements with active tritium. Both values are originally reported in [Har15].

The cause for this background component has been deduced to stem from highly-excited, long-lived Rydberg states of hydrogen atoms which are released from the inner surface of the large spectrometer vessel. Thermal black body radiation then can ionize the propagating hydrogen atoms. This will release low-energy electrons of $\mathcal{O}$(meV) which will leave the spectrometer volume towards the detector and are thus indistinguishable from signal electrons.

The main focus of this chapter is to study the energy scale of electrons from Rydberg atoms with a dipole electrode configuration. After a brief outline of the theory of highly excited hydrogen Rydberg states and of the creation mechanism of low-energy electrons in section 6.1, the transmission and storage behavior of these electrons is investigated: As pulsed electric dipole fields represent a highly efficient and reliable method to remove stored particles in the main spectrometer flux tube, a long-term measurement was performed in order to study whether Rydberg-induced electrons can be removed via an $\boldsymbol{E} \times \boldsymbol{B}$ drift. The results of these measurements is compared to corresponding Monte-Carlo simulations (sec. 6.2).

As these measurements indeed confirm that these low-energetic particles are not stored at a high nominal HV setup of the main spectrometer and will escape the flux tube volume towards the detector or source without being drifted to the tank walls by the applied dipole field, finally dedicated electromagnetic configurations of the spectrometer are proposed in order to store this kind of particles. Together with a discussion of Monte Carlo simulation

results, section 6.3 closes with the presentation of a measurement strategy to perform even more stringent tests of the Rydberg characteristics.

6.1 Excited Rydberg atoms as novel source of background

Previously, a variety of different possible creation mechanisms of Rydberg atoms and electrons were outlined. In the following this is summarized briefly, these scenarios are explained in more detail in [Har15].

The SDS measurements in the standard configuration revealed an increased background level (in an SDS standard configuration, the electrodes were operated with generic settings which allowed the transmission of electrons. Since the passive background reduction by the cold baffle system was active during these runs, stored high-energy electrons by radon α-decay can be excluded as possible background source. Together with a high-pressure measurement, where individual α-decays were manifesting as time-correlated multi-hit events, any radon α-decay, correlated hypothesis can be excluded, too.

The following section 6.2 is targeted to explain in more detail that electric dipole pulses have no effect on this background. As a transversal energy limit can be deduced from equation 2.13, the remaining electrons will have a maximal transversal energy of 1.6 eV only in order not be stored. In addition, possible Penning traps can be excluded since they manifest as time-dependent and localized events and are pressure-dependent, in contrast to observations. The challenging task now is to determine the energy scale of the remaining background component.

As a possible source, secondary background electrons from inner vessel surfaces were examined first in more detail in the context of SDS-II. Here, the following items were investigated:

- Different inner electrode offset potentials were applied. It is expected that the background signals should show a radially-dependent signal, correlated with the applied offset potential. However, only a radially independent and rather moderate decrease of the background rate was measured with higher offset potentials.
- These electrons feature exceedingly small energies well below the storage conditions required for a radial drift via an $\boldsymbol{E} \times \boldsymbol{B}$ drift. Accordingly these electrons are not removed by the dipole method.
- High-pressure measurements would have reduced the storage times in the flux tube center, however the background rate is independent of the pressure.

The most likely reason for this background class is the ionization of Rydberg states of hydrogen atoms in the volume. In this way the energy of electrons well below 1.5 eV can easily be explained due to the kinematic of the photoelectric effect. These electrons should be distributed homogeneously in the flux tube, which nicely explains the observed volume dependence. Furthermore, the rate of background electrons in the volume depends from the inner electrode offset. After SDS-IIa, the spectrometer was baked out which led to a background decrease of 40 %. Rydberg atoms are characterized by a very high principal quantum number which results in very high Bohr radii. This explains the first effect of the inner electrode. Secondly the outbaking process changed the hydrogen content of the vessel surface, explaining the bake-out characteristics. The question is now if these atoms indeed emit low-energy electrons. Three possible mechanisms are discussed in the following [DM16, Dre15a, Dre15c, Dre15b]:

- Autoionization of excited hydrogen molecules: Hydrogen atoms are located in a large number on the inner surface of the main spectrometer. After desorption, molecular

hydrogen is created. A certain number of long-lived molecules or states will travel into the sensitive flux tube in excited molecular states. The lifetime of this state, is about 1 ms, and thus sufficient to travel through the flux tube.

- Interaction of Rydberg molecules with black-body radiation (BBR): The vessel wall emits BBR which can ionize the Rydberg atoms. The highly excited states are close to the ionization threshold and thus have a lifetime of up to ms.
- Furthermore they interact with any electrostatic fields since they have a large dipole moment.

In the following the second item is discussed in more detail: The interaction of a Rydberg state through BBR can happen by three different interaction processes:

- Stimulated photon emission due to induced transition to a lower principal quantum state (decay).
- Excitation to higher n state after absorption of BBR photon
- Ionization of a Rydberg atom, with an expected ionization rate of smaller than 1500 per second.

In the following, the third issue is discussed in more detail. In case of an inner electrode potential of $-100\,\mathrm{V}$, an electric field of $7\,\mathrm{V/cm}$ results between the vessel and the inner wire electrode. This field is sufficient to ionize all Rydberg states with $n \geq 82$. These Rydberg atoms are consequently ionized close to their point of origin at the inner surface or wire electrode and thus do not contribute to the spectrometer background. A radially independent background reduction as observed by different inner electrode offset potentials is thus a strong argument for the Rydberg hypothesis [Har15]. Furthermore, in case of very high electric fields at the upstream and downstream ends of the main spectrometer, selective field ionization (SFI) can happen. Figure 6.1 shows the slope of the electric magnitude directly along the z-axis at $x = y = 0\,\mathrm{m}$ and the volume where almost all Rydberg states are destroyed.

The BBR ionization process depends on the angular momentum quantum state l of the Rydberg atom on the surface. Hence a spontaneous decay before the induced ionization on the vessel wall is also possible. In total the creation of low-energy electrons in the flux tube is a complex interplay of different effects: spontaneous decay, BBR-induced excitation, deexcitation, ionization and finally the SFI. In the context of the creation of Rydberg atoms, a variety of desorption processes at the inner surfaces have to be taken into account. The following theoretical processes were considered to create Rydberg states:

- Electron-stimulated desorption (ESD): Electrons with an energy $E > 20\,\mathrm{eV}$ can lead to the emission of excited Rydberg atoms: $\mathrm{H_2} + e^- \longrightarrow \mathrm{H} + \mathrm{H}^* + e^-$. This is not a dominant process since only a small number of electrons at the surface will have these energies and only atomic hydrogen is adsorbed.
- Photon-stimulated desorption (PSD): Gamma rays or X-rays can also result in the desorption of hydrogen Rydberg states.
- Ion-induced desorption: The acceleration of positive ions (produced in the vicinity of the ground electrode) by the negative vessel potential could result in ion impacts onto the stainless steel vessel surface with energies up to 18.6 keV.

Distribution of principal quantum numbers and energy spectrum

The main contributing background process for electron creation is based on the BBR-induced photoionization. For this reason the interaction of a hydrogen atom with the

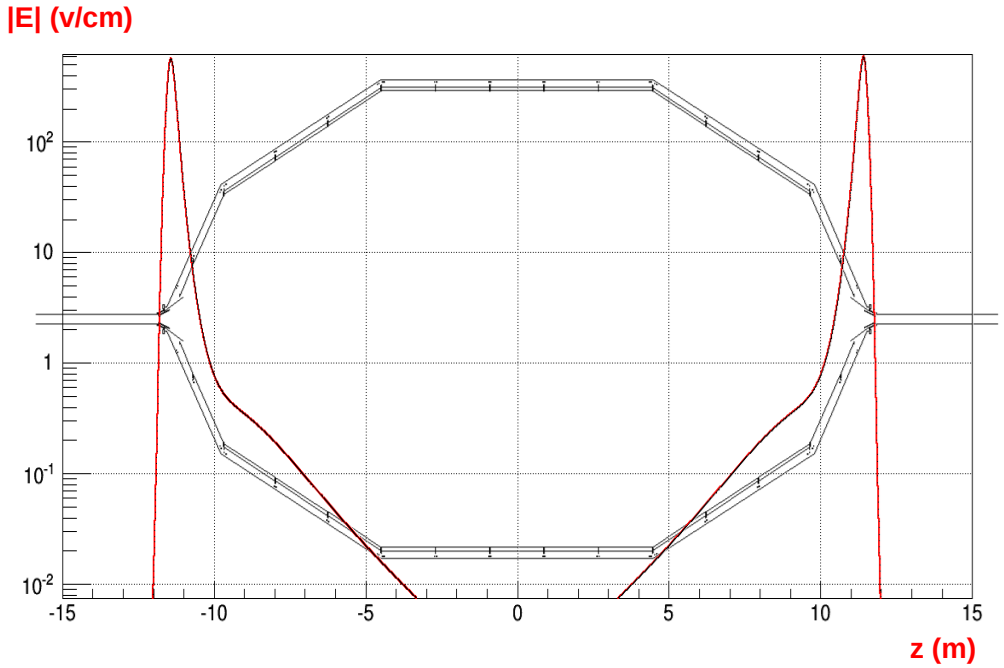

Figure 6.1: Calculation of electric fields inside the main spectrometer along the z-axis. At the upstream and downstream entrance very high field regions occur due to the frontier between components which are on HV and grounded elements.

black body radiation has to be calculated. As input a temperature of $T = 293\,\mathrm{K}$ is assumed, which equals to 500 million BBR photons per cm^3. The total power of these photons inside the main spectrometer is $P = 300\,\mathrm{kW}$. From the photo-ionization transition rate the corresponding cross section can be calculated. Consecutively, from the cross section, an energy spectrum can be calculated [Glü15]. For the following simulations, the principal quantum number n was diced from a corresponding distribution as given in [Tro15]. The diced n-value was taken to compute the electron energy spectrum as outlined in [Glü15]. Figure 6.2 sketches the used n-distribution and the energy spectrum for $n = 16$ as determined randomly from this given distribution.

The given energy spectrum is used to create a realistic particle spectrum inside the main spectrometer. This distribution ensures that mostly particles with a very low initial kinetic energy will be used.

6.2 Background characterization with the electric dipole method

The goal now is to investigate the remaining intrinsic background component from Rydberg ionizations in the context of static and dynamically pulsed electric dipole fields. In the SDS-IIa measurement phase, first static dipole fields were investigated in order to examine particle trajectories with an applied static dipole field. Over the course of a long-term measurement campaign over several hours, the influence of pulsed electric dipole fields on the intrinsic background is checked. The goal is to determine the storage behavior of the remaining Rydberg background. Due to the excellent energy resolution of the main spectrometer, the particle energy can be deduced from the division point of $1-2\,\mathrm{eV}$, where electrons start to get stored and thus become prone removal via dipole fields. Consequently, the application of electric dipole pulses allows to confirm or to rule out the theory of Rydberg-induced non-stored low-energy particle background.

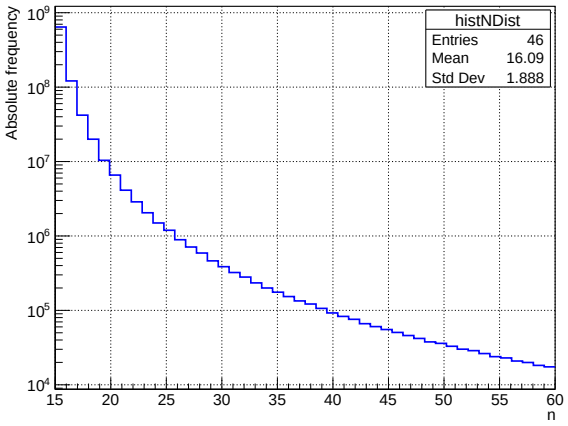

(a) Distribution of principal quantum numbers n of hydrogen atoms

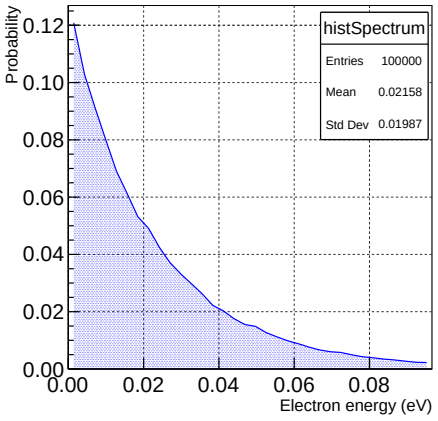

(b) Energy distribution from single diced n value ($n = 16$)

Figure 6.2: Distribution of principal quantum numbers and energy spectrum of Rydberg-induced electrons.

6.2.1 Measurement with static electric dipole fields

As already outlined in chapter 5, particular potential settings for the correct operation of static electric dipole fields have to be applied to investigate their effect on the intrinsic background component.
Steep cone potentials at the inner electrode potential with $U_{\text{steepcone}} \approx U_{\text{cylinder}}$ will typically result in the occurrence of blocking potentials, which manifest in pixel patterns with a drastically lower rate than the expected standard background one. By applying a more positive steep cone potential, no rate reduction was visible, confirming the absence of blocking potentials. Accordingly the rate per pixel was distributed as in the case of the standard background level without electric dipole fields. Together with a retarding potential of $U = -18.6\,\text{kV}$, a static dipole field of $-100\,\text{V}$ (west) and a $5\,\text{G}$ magnetic field, the following rates were recorded: A background level of 540 mcps was observed with and 530 mcps without dipole field. Consequently, a static dipole field has a negligible effect to the intrinsic background component, leading to the conclusion that the intrinsic background is not dominated by stored particles, as expected for Rydberg-dominated background.

6.2.2 Long-term measurement with electric dipole pulses

In the case of the following long-term measurements, the dipole was used in the following electro-magnetic configuration:

- EMCS currents: 50 A (horizontal) and 9 A (vertical)
- LFCS configuration: 3.8 G (single minimum)
- Vessel potential: $-18.5\,\text{kV}$
- Inner electrode potential: $-18.6\,\text{kV}$
- Steep cone electrode offset: 97 V
- Dipole offset potentials: $-100\,\text{V}$, west

The total run-time of the dipole measurements was 6 h and includes runs # 22379, #22380 and #22381. The measurements were taken in the context of the SDS-IIa measurement

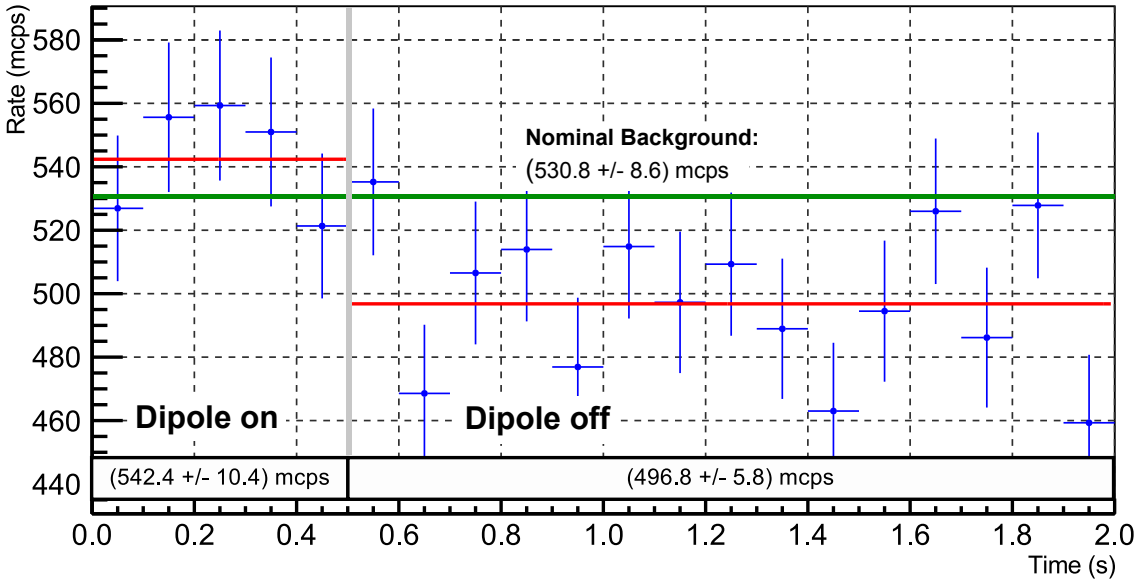

Figure 6.3: Stacked rates for long-term dipole measurements. These dipole measurements were performed with a dipole potential of −100 V and a retarding potential of −18.6 kV with a 3.8 G-magnetic field configuration. Visible are stacked rates comprising a run-time of 2 h.

campaign with an un-baked spectrometer. The reference background without a dipole field was taken from run #22377 with a total run-time of 2 h. The pressure in the vessel was 6×10^{-10} mbar and dominated by hydrogen and water molecules. The mean background rate in this configuration was determined to

$$R_0 = (530.8 \pm 8.6)\,\text{mcps}, \tag{6.1}$$

i.e. in a case where no dipole voltage was applied. For the later more detailed discussion of results, multi-cluster events were excluded. These are groups of detector events which are registered together within a short time frame of $\Delta t = 2\,\mu\text{s}$. These multi-cluster events do not carry information on the background itself. Furthermore all three baffles were kept cold in order to minimize radon-induced background.

Application of dipole pulses

As outlined in chapter 5, dipole pulses were stacked to increase statistics. After summing up a total of 6 h of measurement time, consisting of 10599 pulse cycles, a slight rate decrease is observed after comparison to the above given reference background value. The rate reduction of (45.6 ± 16.2) mcps is compatible with the results from [Har15], where a remaining radon-induced background of (36^{+18}_{-15}) mcps is reported. From this one can argue that the electric dipole pulses have successfully removed the stored low-energy particle background from non-trapped ^{219}Rn.

Finally, the impact of blocking potentials on measured spectra will be investigated and compared to simulation results. The goal here is to understand the pixel pattern during and after the application of an electric dipole field.

Characterization of dipole pixel pattern at standard background

At first, the different pixel patterns of different dipole modes are discussed qualitatively in a configuration with three cold baffles in order to suppress radon-induced background. The different pixel patterns are displayed in fig. 6.4. The pixel patterns in the first row

of figure 6.4 shows the different dipole modes (static, pulsed). The pixel pattern of the pulsed dipole method (0.5 s on-time and 1.5 s off-time) can be seen as a superposition of 75 % of the background pixel pattern and 25 % of the static dipole pixel map.

In addition, (in the second row) relative rates were computed from the standard background pixel map, both for static and pulsed dipole. The pixel rates of the static dipole relative to the standard background confirm that in case of a western dipole, particles from the bottom drift into the flux tube due to the $\boldsymbol{E} \times \boldsymbol{B}$-drift. This is indicated by yellow-colored pixels where the relative rate value is above 1. In the center, the pixel pattern of the static over the pulsed dipole is shown. In this case less particles drift into the flux tube than in the static mode from the bottom. The last picture shows again that less particles drift into the flux tube for a pulsed mode than in the static mode.

Taken together the pixel maps show that particles indeed enter the flux tube from the bottom of the vessel into the flux tube for a west dipole. The amount of particles drifting into the field of view depends on the specific setting of the dipole mode. Whereas a static dipole permanently allows particles to drift in from the bottom, the pulsed dipole only produces a smaller background rate which is localized at the bottom pixels, as only short time periods are present where electrons can drift. Consequently, when operating in a dipole mode, it is advantageous to apply the dipole fields for shortest time scales only.

Discussion of blocking potentials

The motivation of the following tracking simulation is to investigate possible blocking potentials in the present electro-magnetic setting. A blocking potential as outlined earlier, will imply that particular detector pixels "see" a lower electron rate rather due to a violation of the transmission condition than an actual removal through $\boldsymbol{E} \times \boldsymbol{B}$-drift. In this particular configuration, a western dipole was used, accordingly the electric potential along four field lines from the eastern side were computed. It is important to note that the steep cones have been set to a more positive potential in order to avoid blocking potentials (as tested for the 5 G dual minimum setting).

The field lines start from the same pixels as denoted in sec. 5.2. As the 3.8 G setting in a single minimum setting is characterized through larger curvatures of the field line than the dual minimum setting, fig. 6.5, blocking potentials will occur at the outer field lines.

The outer field line, which starts from pixel 130, has a radius of 3.5 m at the analyzing plane, experiences a blocking potential of 950 mV. Compared to the previously simulated blocking potentials this is a rather small value. However this value is large compared to the standard background electrons with energies of $\mathcal{O}$(meV) and the very shallow potential distribution along the central analyzing plane. A more detailed study is recommended together with measurements at different blocking potentials in order to investigate the effect on the detector rates.

Simulation of trapping probabilities

Experimentally, it could be proven that low-energy Rydberg electrons are not stored and directly escape the spectrometer. Corresponding simulations have confirmed these measurement results, underlining that no particles are stored. To simulate this effect, an ensemble of 1000 Rydberg-induced electrons with principal quantum number $n = 16$ and an electron energy distribution as illustrated in fig. 6.2 were started homogeneously in a 3.8 G flux tube (single minimum configuration). Next, the same configuration was simulated now with an additional electric dipole field. Since blocking potentials occur at this particular configuration, a very small fraction of electrons is expected to be stored. Indeed the simulation revealed that only 17.6 % of the low-energy electrons were stored.

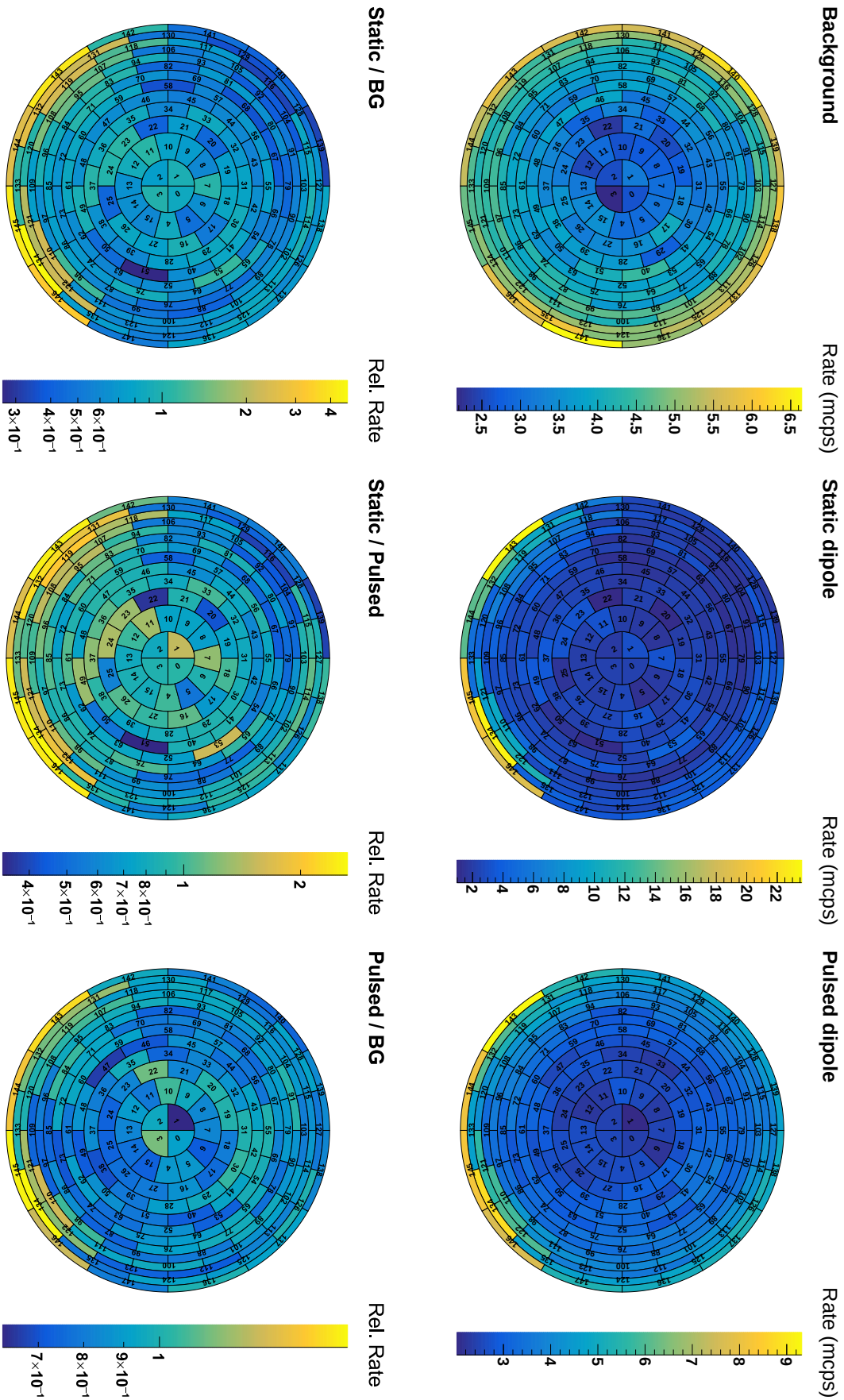

Figure 6.4: Comparison of different dipole modes.

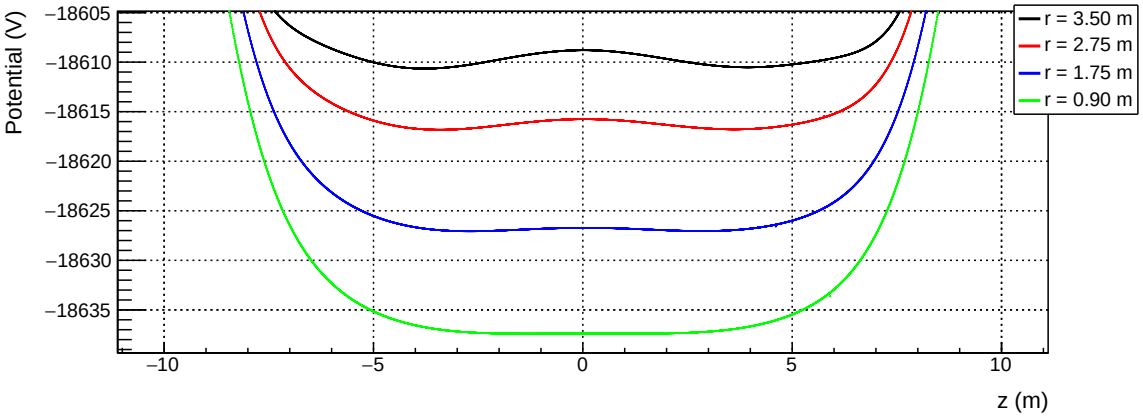

Figure 6.5: Simulation of electric potentials for a -100 V western dipole along magnetic field lines at 3.8 G-configurations. Visible are small blocking potentials at the outer field lines with a maximal depth of 950 mV. The legend denotes the field line radius at $z = 0$ m.

Discussion

As shown in chapter 5 by both data analysis and corresponding simulation, the electric dipole method is highly effective in removing stored particles from the sensitive flux tube volume. In the context of applying of long-term (static or pulsed) electric dipole pulses to the standard background, a rate decrease of approx. 30 mcps were observed. This result is compatible with the remaining radon background component. The systematic effect of blocking potentials can lead to a rate reduction via transmission breakdown due to the low-energy nature of Rydberg-induced background. In order to study Rydberg-induced background with the electric dipole method in more detail, the following background measurements should be carried out in the future:

- in order to avoid blocking potentials, the same series of measurements should be repeated with a dual minimum 5 G magnetic field setting in order to avoid blocking potentials during active dipole fields.
- Test if the rate reduction by ≈ 30 mcps results from remaining very shallow blocking potentials by applying *deeper blocking potentials*. In that case, especially at the outer pixel an even lower rate should be visible.
- During the dipole pulse operation, take into account *longer relaxation times*. This will allow to identify that the reduced background indeed results from radon-induced electrons.
- Complementary, the reduction of *artificial* ^{220}Rn *background could be studied on shorter time scales* in order to compare the rate signatures with the measurements for standard background.
- Take into account that the remaining background comes from both from radon- and from Rydberg-induced electrons.

As the Rydberg background is based on the kinematics of the photo effect, these background electrons cannot be removed by active methods.

The experimental investigations of this thesis have revealed that electrostatic dipoles only work on radon-induced electrons, but not on Rydberg electrons. In future dipole investigations, the time between the pulses should be longer in order to measure the recovery time constants of background electrons with an artificial radon source.

Table 6.1: Trapping probabilities of low-energy electrons at low retarding potentials. Given are the trapping probabilities for the 3.8 G and 5 G magnetic configuration.

U_0 (-V)	Steep Cone Offset (V)	P_{trap} (%) (3.8 G)	P_{trap} (%) (5 G)
40	0.0	69.1	61.0
80	0.5	52.3	43.3
120	0.6	43.2	36.0
200	1.0	27.2	17.6
500	2.7	7.6	3.5
750	4.0	2.6	1.5
1000	5.4	1.0	0.1
2000	10.8	0.0	0.0
4000	21.5	0.0	0.0
6000	32.3	0.0	0.0
10000	53.8	0.0	0.0

6.3 Storage of low-energy adiabatic electrons for active removal

A promising way to measure the energy scale of Rydberg-induced background electrons is to decrease the inner electrode potential or to decrease the magnetic field in the analyzing plane. In both cases, the energy resolution of the MAC-E filter will be improved which leads to trapping of even very low-energy electrons. If the background electrons are trapped, they can be removed by the electric dipole method. Simulations can be used to find the optimum different inner electrode potential configuration for these investigations. A first result is, that the steep cone should be always be 0.5 % more positive than the absolute inner electrode potential in order to avoid early retardation effects and to allow transmission of electrons. For each setting, a total of 1000 Rydberg-induced electrons was started over the entire flux tube volume. Different potentials have been tested with two different magnetic field settings, with table 6.1 listing the trapping probabilities for the different electro-magnetic settings.

It could be shown that electrons with a very low kinetic energy can be stored by setting the inner electrode to a very low (or elevated) retarding potential. In this way the absolute energy resolution is improved significantly so that more and more electrons are stored. The same effect can be obtained by applying a smaller magnetic field, as the comparison between the two setups show. As outlined these low-energy electrons can be removed by the electric dipole method. From the amount of removed particles for a certain dipole voltage one can conclude the energy scale of the electrons. As lower and lower count rates are expected at very small retarding potentials, a large amount of measurement time has to be invested, however. Also, one has to carefully mitigate blocking potentials at the spectrometer exit which are not related to the step cone potential.

Realization of low-potential settings

In order to store low-energy electrons with $\mathcal{O}$(meV) the above mentioned voltage and magnet settings have to be set up, which requires the following prerequisites:

- Floating potentials have to be avoided since these can lead to blocking potentials which distort the electron trajectories. A stable HV operation has to be guaranteed.

- The work function of steel has to be taken into account, since this effect may lead to a deviation between pre-set and the real potential of up to a few 100 mV. It might be that the potentials differ especially in the flat cone region, so a very blocking potential might be established in this region. Then the electron trajectory is highly distorted and the storage condition is broken.
- The storage of low energetic particle happens if the transversal energy is bigger than the energetic resolution of the MAC-E filter. Consequently, the ratio of the minimal and maximal magnetic field has a direct influence on the energy resolution.

6.4 Conclusion

In context of the second spectrometer and detector commissioning phase (SDS-II), a novel source of background electrons was revealed [DM16] in order to explain the increased background level in the main spectrometer. In this chapter, the results of a long-term measurement campaign with electric dipole pulses was discussed. The visible removal effect of electrons is compatible with the value of remaining radon-induced stored-particle background as reported in [Har15]. The dipole finally confirms the Rydberg hypothesis as these electrons are not stored and thus immune to the induced $\boldsymbol{E} \times \boldsymbol{B}$ drift by the dipole. A further characterization of the background can be performed by improving the energy resolution of the spectrometer with the target to store even $\mathcal{O}$(meV) background electrons over the entire flux tube. Consequently, the dipole could remove these particles and a rate reduction could be observed. However, the removal of Rydberg-induced electrons during normal data taking is beyond the scope of the electrostatic dipole method. This can only be achieved by removing or reducing adsorbed H-atoms on the inner vessel walls, much in the same way as radon atoms were successfully cryotrapped by the baffle system.

CHAPTER 7

Summary and outlook

In 1998 the discovery of neutrino flavor oscillations has significantly expanded our picture of the principles of elementary particle physics via the breakthrough discovery of non-vanishing neutrino masses. In the Standard Model of particle physics, neutrinos were described as massless particles, so that the discovery of massive neutrinos acts as gateway to new physics beyond the Standard Model. Due to their unique role in cosmology and astrophysics, moreover, neutrinos and their fundamental mass scale are of key importance for answering essential questions about the evolution of large-scale structures in our universe.

As neutrino oscillation experiments are only sensitive to neutrino mass splittings, they can not probe the absolute mass scale. By contrast, beta decay experiments allow to directly access this mass scale. The KATRIN experiment, being the key mission pursuing this kinematic / direct approach, is currently undergoing extensive commissioning measurements at the KIT Campus North site. The overall aim there is to launch high-precision spectroscopy close to the tritium endpoint region in the final quarter of 2017. The KATRIN experimental setup extends over 70 m, and consists of various major components, each pushing the technology to its limits.

The main objective of this thesis was to study and apply static and pulsed electric dipole fields in the KATRIN main spectrometer. From the simulation perspective, many open questions had to be solved with the aim to accomplish fast particle tracking within a non-axial dipole field configuration of the main spectrometer. This was the main motivation to develop a highly reliable and optimized electrode model specially suited for fast particle trajectory calculations. Together with the application of cubature and fast multipole methods, the simulation software is now able to accompany and guide measurements with variable electric dipole fields in the main spectrometer.

When operating the experiment in complex electromagnetic configurations, it is of key importance to obtain high statistics electron particle trajectories over all subcomponents in advance. This methodology allows to examine different physical effects and to directly compare them to measurements. For this purpose, the KATRIN collaboration takes advantage of the in-house developed toolkit called *Kasper*, which comprises different software modules for data analysis, sensitivity calculation and particle tracking with electromagnetic field simulations. For the latter, the programs *Kassiopeia* and *KEMField* were developed in an extensive team effort, involving several international collaborators of the KATRIN experiment. Both software modules have now been released in terms of an open-source software license for the public and are already used by many astroparticle physics experiments, like Project8 or XENON1T.

The elaborate interplay of electromagnetic fields needs to be fine-tuned to adiabatically guide β-electrons from the source to the detector. More specifically, transmission properties have a direct influence on the neutrino mass sensitivity. This requires the precise calculation of electrostatic fields and potentials as well as magnetic fields, both of which are of main importance for the operation of the two major MAC-E filter systems in the beam line of KATRIN. This serves two main purposes: on the one hand for in-depth background studies and on the other hand for the precision calculations of signal electron transmission properties. To do so, the *KEMField* package computes electrostatic potentials and fields with the boundary element method (BEM). Here, the geometry is discretized into small triangular, rectangular or linear patches. The direct field computation method requires a two-dimensional surface integration over all discretized elements. Because of analytical integration methods, former code versions suffered from non-negligible round-off errors, which in turn lead to rather imprecise and even un-physical results. Together with the application of numerical integration by Gaussian cubature the accuracy of electrostatic field computation has been pushed to the 'ultimate' accuracy of the floating-point number system, that is, to a remarkable level of $\mathcal{O}(10^{-15})$ where previous round-off errors have successfully been eliminated.

Over the course of this thesis fundamental properties of the intrinsic background components in the large volume spectrometer of the Karlsruhe Tritium Neutrino experiment (KATRIN) have been revealed for the first time by employing the electric dipole method. This method now can be routinely used as a reliable and powerful method to reduce stored-particle background while simultaneously providing information on background contributions of unknown origin. The results obtained mark a big step towards the targeted design neutrino mass sensitivity of the experiment of 200 meV for the effective electron (anti-)neutrino mass.

Corresponding experimental studies were carried out in the second phase of commissioning measurements of the main spectrometer and detector section (SDS) of KATRIN. In the context of these measurements many technical improvements were applied to the SDS apparatus which led to a very fruitful data-taking period. To investigate and test active background mitigation techniques based on the dipole method, the vacuum system was extended to temporarily include an artificial ^{220}Rn source to increase the stored-particle background. In this way, higher statistics could be gathered over a shorter period of time thus allowing to investigate a much larger region of parameter space of the dipole method. The underlying physics is related to the fact that the α-decay of the isotope ^{220}Rn in the entire flux tube volume leads to stored high-energy primary electrons with energies up to several 10^2 keV. Primary electrons stay trapped in the volume due to the magnetic bottle effect and thus can ionize residual gas molecules. Thereby hundreds of low-energy secondary electrons are produced, which can escape the spectrometer volume to the detector and thus contribute significantly to the background signals.

The measurements with the electric dipole method to eliminate this stored-particle background were carried out both in static and in pulsed mode. Whereas in the first phase dipole fields were applied over longer time scales ($\mathcal{O}$(min)) to the two separate electrode halves of the main spectrometer, the pulsed mode runs were driven by the fields applied over shorter time scales of $\mathcal{O}$(s). Both operation modes have exposed previously unknown characteristics of the MAC-E filter with respect to the removal efficiency of stored-particles. Static dipole measurements have revealed the presence of distorting blocking potentials which can inhibit the transmission of electrons to the outer pixels of the detector. Based on this new insight, this effect can no longer be classified as a rate reduction. However it can be used as a novel method to characterize background properties in the outer flux tube regions. Making use of the attached ^{220}Rn source, the most efficient field configuration of the dipole method was tested with a maximal rate reduction factor for the low-energy

stored particles of almost four. This achievement represents a crucial milestone in order to achieve the targeted neutrino mass sensitivity of the experiment. Dipole fields which are applied during only one quarter of the measurement time result in a long-term rate reduction of 50 %. This allows to largely eliminate stored high-energy electrons from radon migration to the flux tube, however at the price of introducing time-dependent background rates.

The dipole method has thus been successfully commissioned as a powerful method to reduce and to characterize stored-particle background in the main spectrometer. This method is however also suited to characterize the storage behavior of the remaining intrinsic background level of $\approx \mathcal{O}(500\,\mathrm{mcps})$ in the KATRIN main spectrometer which is not associated to radon α-decay. For this reason, long-term measurements over several hours were carried out to test if pulsed electric dipole fields allow to reduce the number of these background electrons. Surprisingly, the particle motion of the remaining background is not affected by electric dipole pulses. This outcome is an important corroboration of the existence of a novel background class consisting of non-stored electrons of $\mathcal{O}(\mathrm{meV})$, which are guided within $\mathcal{O}(\mathrm{ms})$ to the focal plane detector and which dominate the residual background component of $\mathcal{O}(500\,\mathrm{mcps})$. Consequently, the dipole method represents a further very strong proof of the theory of highly excited hydrogen Rydberg states desorbed from the large spectrometer surface, which can produce these electrons through photoionization by the spectrometer black-body radiation. This remarkable milestone completes the new background paradigm and thus provides key insight into physical processes in large-volume electrostatic retarding spectrometers.

In the future measurements with the KATRIN spectrometers, the dipole method can be used to further characterize the intrinsic background component. For example, the low-energy electrons can be stored in the main spectrometer when operating the MAC-E filter at rather low retarding potentials. Consequently, the low-energy electrons are expected to be removed by the electric dipole method. This novel technique represents a very promising technique to proof and validate the paradigm-changing background model based on excited hydrogen Rydberg atoms. In the context of the projected tritium measurements starting at the end of the year 2017, the dipole method will be used in a routine way to further reduce of the remaining stored-particle background by non cryo-trapped radon atoms underlying α-decay. If the Rydberg-dominated background component can be suppressed by other means, such as UV-illumination in combination with an extended spectrometer bake-out phase, the electric dipole method pioneered in this thesis could be essential to reduce the background below the targeted design goal of 10 mcps.

Appendix

A Adiabatic invariance

In the following adiabatic invariance is discussed briefly. The derivation and explanations made in this section are adapted from [Lon92] (physical approach) (chapter 11), [Val04] and [Jac02] (chapter 12.5) (adiabatic invariant approach) respectively.

A.1 Physical approach

The adiabatic motion of a charged particle in a time-varying magnetic field is discussed here. The particle's trajectory forms a helix which is given by

$$r = \frac{\gamma m_0 v \sin(\theta)}{zeB}, \tag{7.1}$$

where m_0 denotes the rest mass v the velocity, θ the polar angle, ze the charge and B the magnetic field strength. In this example the axis of the particle trajectory is parallel to the magnetic field lines. Adiabatic motion implies that the gradient of the magnetic field $\frac{\Delta B}{B}$ changes by only a small fraction within a single cyclotron period with time T and frequency ν_g. The movement of a charged particle around a magnetic field line establishes a current loop with current I and transversal velocity component $v_\perp$ relative to the magnetic field line: $I = \frac{zev_\perp}{2\pi r}$. The magnetic moment is given by the current times the area $A = \pi r^2$ which is enclosed by the moving charge. After plugging the definition of the radius r of a moving charge along a cyclotron orbit, one obtains:

$$\mu = I \cdot A = \frac{m_0 v_\perp^2}{2B} = \frac{E_\perp}{B}. \tag{7.2}$$

Finally the magnetic moment μ is given a the transversal energy component $E_\perp$ and the magnetic field B.
Furthermore a small change of the magnetic field creates an electric field $\mathcal{E}$ according to Maxwell's equation:

$$ze\mathcal{E} = ze(\pi r^2)\frac{\mathrm{d}B}{\mathrm{d}t} = ze(\pi r^2)\frac{\Delta B}{\Delta t}. \tag{7.3}$$

Regarding the change of kinetic energy within a single cyclotron turn $\Delta E_\perp$, one obtains the relation

$$\Delta\left(\frac{E_\perp}{B}\right) = 0. \tag{7.4}$$

This relation implies that in case of a slowly varying field, the magnetic moment is a constant as well. Furthermore this equation is equal to

$$\Delta\left(\frac{p_\perp^2}{B}\right) = 0. \tag{7.5}$$

A.2 Adiabatic invariant approach

Adiabatic invariance can be studied in context of classical Hamiltonian mechanics. In general, the action of a generalized coordinate q_k is defined as the integral

$$J_k = \oint p_k \mathrm{d}q_k. \tag{7.6}$$

The action J_k is constant for a defined set of system properties and the coordinate q_k is periodical while the canonical momentum p_k is integrated over a full period. If the system properties change very slowly relatively to a single period, the action still stays constant. This kind of motion is called adiabatic motion. In the KATRIN experiment, electrons move along magnetic field lines in a static magnetic field. The magnetic field is changing very slowly regarding one cyclotron period of the electron. For this case the action is defined as the integral over the perpendicular component of the momentum:

$$J = \oint \mathbf{p}_\perp \mathrm{d}\mathbf{s} \tag{7.7}$$

$$= \oint \gamma m \mathbf{v}_\perp \cdot \mathrm{d}\mathbf{s} + \frac{e}{c} \oint \mathbf{A} \mathrm{d}\mathbf{s} \tag{7.8}$$

Here $\mathbf{p}_\perp$ is the transversal component of the canonical momentum $\mathbf{p} = \gamma m \mathbf{v} + \frac{e}{c}\mathbf{A}$ and $\mathrm{d}\mathbf{s}$ is a line segment, which is parallel to the direction of $\mathbf{p}_\perp$. After several steps, the term can be expressed in terms of the cyclotron frequency ω_c and radius r_c:

$$J = \pi \gamma m \omega_c r_c^2 = \frac{e}{c}(B \pi r_c^2). \tag{7.9}$$

If J is an adiabatic invariant, e.g. in case of slowly changing magnetic fields, further adiabatic invariants result from this equation:

- The product $B r_c^2$ is constant and implies that for higher magnetic fields, a lower cyclotron radius is expected and vice versa.
- The quotient $\frac{p_\perp^2}{B}$ is constant over one cyclotron turn resulting in a lower cyclotron velocity per turn.
- The magnetic moment is $\gamma\mu$ is constant.

B *KGeoBag* shell areas

For computing of electric dipole fields, non-axial electrodes have to be modeled and discretized. In *KGeoBag* they are defined by the coordinates r, z together with two angular parameters `angle_start` and `angle_stop` for the definition of arbitrary opening angles. The other given parameters are equal to the rotational symmetric elements. In order to provide elements with arbitrary opening angles, a new class of *KGeoBag* elements has been developed in context of [Com15]. Together with the shell areas, conic and cylindrical electrodes can be modeled easily as needed by the non-axial main spectrometer model, which is explained in sec. 4.5.1. Also this element class is used for the electrode model of the differential pumping section [Com15]. In the following an excerpt of the XML definition of the geometric shell objects is given.

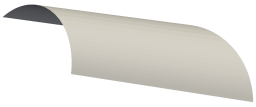

```
<!-- shell line segment surface -->

<shell_line_segment_surface name="shell_line_segment_surface"
  angle_start="240" shell_mesh_count="96" shell_mesh_power="6">

  <line_segment x1="0.15" y1="0.1" x2="-0.1" y2="0.05"
    line_mesh_count="36" line_mesh_power="2.2"/>

</shell_line_segment_surface
```

```
<!-- shell arc segment surface -->

<shell_arc_segment_surface name="shell_arc_segment_surface"
  angle_start="240" angle_stop="360" shell_mesh_count="128"
  shell_mesh_power="6">

  <arc_segment x1="0.15" y1="0.1" x2="-0.1" y2="0.05"
    radius="0.3" right="true" short="true" arc_mesh_count="64"/>

</shell_arc_segment_surface>
```

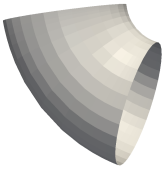

```
<!-- shell circle surface -->

<shell_circle_surface name="shell_circle_surface"
  angle_start="200" angle_stop="130" shell_mesh_count="32"
  shell_mesh_power="6">

  <circle x="0.1" y="0.5" radius="0.3" circle_mesh_count="32"/>

</shell_circle_surface>
```

```
<!-- shell poly line surface -->

<shell_poly_line_surface name="shell_poly_line_forward_surface"
  angle_start="270" angle_stop="120" shell_mesh_count="64"
  shell_mesh_power="6">

  <poly_line>
    <start_point x="0.2" y="0.3"/>
    <next_line x="0.1" y="0.1" line_mesh_count="36"
    line_mesh_power="4.5"/>
    <next_arc x="-0.1" y="0.1" radius="0.2" right="true"
      short="true" arc_mesh_count="96"/>
    <next_line x="-0.2" y="0.2" line_mesh_count="36"
      line_mesh_power="1."/>
    <next_line x="-0.3" y="0.1" line_mesh_count="24"
      line_mesh_power="4.5"/>
  </poly_line>

</shell_poly_line_surface>
```

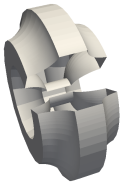

```
<!-- shell poly loop surface -->

<shell_poly_loop_surface name="shell_poly_loop_surface"
  angle_start="30" angle_stop="360" shell_mesh_count="64"
  shell_mesh_power="6">

  <poly_loop>
    <start_point x="0.3" y="0.3"/>
    <next_line x="0.3" y="0.5" line_mesh_count="64"
      line_mesh_power="2.5"/>
    <next_arc x="0.1" y="0.7" radius="0.25" right="false"
      short="true" arc_mesh_count="64"/>
    <next_line x="-0.1" y="0.7" line_mesh_count="64"
      line_mesh_power="2.5"/>
    <next_arc x="-0.3" y="0.5" radius="0.25" right="false"
      short="true" arc_mesh_count="64"/>
    <next_line x="-0.3" y="0.3" line_mesh_count="64"
      line_mesh_power="2.5"/>
    <next_arc x="-0.1" y="0.1" radius="0.25" right="false"
      short="true" arc_mesh_count="64"/>
    <next_line x="0.1" y="0.1" line_mesh_count="64"
      line_mesh_power="2.5"/>
    <last_arc radius="0.25" right="false" short="true"
      arc_mesh_count="64"/>
  </poly_loop>

</shell_poly_loop_surface>
```

C Gaussian points and weights for triangles

Table C.1: Barycentric coordinates and weights of the 4-point (degree 3) Gaussian cubature for triangle. See refs. [Str71, HS56, HS58].

λ_A	λ_B	λ_C	weight
1/3	1/3	1/3	-9/16
3/5	1/5	1/5	25/48
1/5	3/5	1/5	25/48
1/5	1/5	3/5	25/48

Table C.2: Barycentric coordinates and weights of the 7-point (degree 5) Gaussian cubature for triangle; $t = 1/3$, $s = (1 - \sqrt{15})/7$, $r = (1 + \sqrt{15})/7$. Both the second and the third row corresponds to three Gaussian points with equal weights, according to all possible different permutations of λ_A and $\lambda_B = \lambda_C$ (like the rows two to four in Table C.1). From refs. [Rad48, HMS56, Str71], [EMU96] (p. 420).

λ_A	λ_B	λ_C	weight
t	t	t	9/40
$t + 2ts$	$t - ts$	$t - ts$	$(155 + \sqrt{15})/1200$
$t + 2tr$	$t - tr$	$t - tr$	$(155 - \sqrt{15})/1200$

Table C.3: Barycentric coordinates and weights of the 12-point (degree 7) Gaussian cubature for triangle. Each row corresponds to three Gaussian points with equal weights: we get the second and third points by the permutations $(\lambda_A, \lambda_B, \lambda_C) \to (\lambda_B, \lambda_C, \lambda_A)$ and $(\lambda_A, \lambda_B, \lambda_C) \to (\lambda_C, \lambda_A, \lambda_B)$, respectively; taken from ref. [Gat88].

λ_A	λ_B	λ_C	weight
0.06238226509439084	0.06751786707392436	0.8700998678316848	0.05303405631486900
0.05522545665692000	0.3215024938520156	0.6232720494910644	0.08776281742889622
0.03432430294509488	0.6609491961867980	0.3047265008681072	0.05755008556995056
0.5158423343536001	0.2777161669764050	0.2064414986699949	0.13498637401961758

Table C.4: Barycentric coordinates and weights of the 19-point (degree 9) Gaussian cubature for triangle. Each of the rows two to five corresponds to three Gaussian points with equal weights, according to all possible different permutations of λ_A and $\lambda_B = \lambda_C$ (like in Table C.1). The last row corresponds to six Gaussian points with equal weights, according to all possible permutations of λ_A, λ_B and λ_C. Numbers taken from ref. [LJ75].

λ_A	λ_B	λ_C	weight
1/3	1/3	1/3	0.09713579628279610
0.02063496160252593	0.48968251919873704	0.48968251919873704	0.03133470022713983
0.1258208170141290	0.4370895914929355	0.4370895914929355	0.07782754100477543
0.6235929287619356	0.18820353561903219	0.18820353561903219	0.07964773892720910
0.9105409732110941	0.04472951339445297	0.04472951339445297	0.02557767565869810
0.03683841205473626	0.7411985987844980	0.22196298916076573	0.04328353937728940

Table C.5: Barycentric coordinates and weights of the 33-point (degree 12) Gaussian cubature for triangle. Each of the first five rows corresponds to three Gaussian points with equal weights, according to all possible different permutations of λ_A and $\lambda_B = \lambda_C$ (like in Table C.1). Each of the last three rows corresponds to 6 Gaussian points with equal weights, according to all possible permutations of λ_A, λ_B and λ_C. Numbers taken from ref. [Pap15].

λ_A	λ_B	λ_C	weight
0.4570749859701478	0.27146250701492611	0.27146250701492611	0.06254121319590276
0.1197767026828138	0.44011164865859310	0.44011164865859310	0.04991833492806094
0.0235924981089169	0.48820375094554155	0.48820375094554155	0.02426683808145203
0.7814843446812914	0.10925782765935432	0.10925782765935432	0.02848605206887754
0.9507072731273288	0.02464636343633558	0.02464636343633558	0.00793164250997364
0.1162960196779266	0.2554542286385173	0.62824975168355610	0.04322736365941421
0.02303415635526714	0.2916556797383410	0.68531016390639186	0.02178358503860756
0.02138249025617059	0.1272797172335894	0.85133779251024000	0.01508367757651144

D Gaussian points and weights for rectangles

Table D.6: Natural coordinates and weights of the 4-point (degree 3) Gaussian cubature for rectangle; $s = 1/\sqrt{3}$. From refs. [EMU96] (p. 417), [AC58] (p. 8).

x	y	weight
s	s	1/4
s	-s	1/4
-s	s	1/4
-s	-s	1/4

Table D.7: Natural coordinates and weights of the 7-point (degree 5) Gaussian cubature for rectangle; $t = \sqrt{14/15}$, $r = \sqrt{3/5}$, $s = \sqrt{1/3}$. The last row corresponds to four Gaussian points with equal weights, according to all possible sign changes (like in table D.6): $(x, y) \to (r, s)$, $(r, -s)$, $(-r, s)$, $(-r, -s)$. From refs. [Str71] (p. 246), [Rad48] (p. 298), [AC58] (p. 9).

x	y	weight
0	0	2/7
0	t	5/63
0	-t	5/63
r	s	5/36

Table D.8: Natural coordinates and weights of the 12-point (degree 7) Gaussian cubature for rectangle; $r = \sqrt{6/7}$, $s = \sqrt{(114 - 3\sqrt{583})/287}$, $t = \sqrt{(114 + 3\sqrt{583})/287}$, $B_1 = 49/810$, $B_2 = (178981 + 2769\sqrt{583})/1888920$, $B_3 = (178981 - 2769\sqrt{583})/1888920$. Each of the last two rows corresponds to four Gaussian points with equal weights, according to all possible sign changes of s and t, like in Tables D.6 and D.7. From refs. [Str71] (p. 253), [Tyl53] (p. 403).

x	y	weight
r	0	B_1
-r	0	B_1
0	r	B_1
0	-r	B_1
s	s	B_2
t	t	B_3

Table D.9: Natural coordinates and weights of the 17-point (degree 9) Gaussian cubature for rectangle. Each of the last four rows corresponds to four Gaussian points with equal weights, according to the transformations $(x, y) \rightarrow \pm(x, y)$, $\pm(-y, x)$ (rotations by 0°, 180° and ±90° in the $x - y$ plane). From refs. [Möl76] (p. 194), [Eng80] (p. 257), [EMU96] (p. 419).

x	y	weight
0	0	0.131687242798353921
0.968849966361977720	0.630680119731668854	0.022219844542549678
0.750277099978900533	0.927961645959569667	0.028024900532399120
0.523735820214429336	0.453339821135647190	0.099570609815517519
0.076208328192617173	0.852615729333662307	0.067262834409945196

Table D.10: Natural coordinates and weights of the 33-point (degree 13) Gaussian cubature for rectangle. Each of the last eight rows corresponds to four Gaussian points with equal weights, according to the transformations $(x, y) \rightarrow \pm(x, y)$, $\pm(-y, x)$ (rotations by 0°, 180° and ±90° in the $x - y$ plane). From ref. [CH88] (p. 145).

x	y	weight
0	0	0.075095528857806335
0.778809711554419422	0.983486682439872263	0.007497959716124783
0.957297699786307365	0.859556005641638928	0.009543605329270918
0.138183459862465353	0.958925170287534857	0.015106230954437494
0.941327225872925236	0.390736216129461000	0.019373184633276336
0.475808625218275905	0.850076673699748575	0.029711166825148901
0.755805356572081436	0.647821637187010732	0.032440887592500675
0.696250078491749413	0.070741508996444936	0.053335395364297350
0.342716556040406789	0.409304561694038843	0.064217687370491966

E Validation of spherical capacitor

Here the accuracy of the integration routines, as discussed in context chapter 4 are tested regarding accuracy with an analytical input model. The integrator classes have direct influence to the solution of the constant charge density value of each mesh element and to the potential and field values at arbitrary points in space. Note that in this example Dirichlet and Neumann boundary condition have to be taken into account. As a consequence, the Robin Hood field solver [FLC+12] has to compute potential and field values. The targeted accuracy of the charge density values is 10^{-6}. In order to validate the developed analytical and numerical integrator classes, the analytical solvable case of a spherical capacitor with two linear dielectric media, as discussed in many textbooks, has been modeled to determine the deviation of the computed field and potential values from the analytical solution. The spherical capacitor spheres have a radius of $r_1 = 1\,\mathrm{m}$, $r_2 = 2\,\mathrm{m}$ and $r_3 = 3\,\mathrm{m}$. The center sphere is a virtual sphere for the realization of the dielectric boundary for $\epsilon_1 = 2$ and $\epsilon_2 = 3$. The different boundaries have been discretized in total into 4112 triangles.

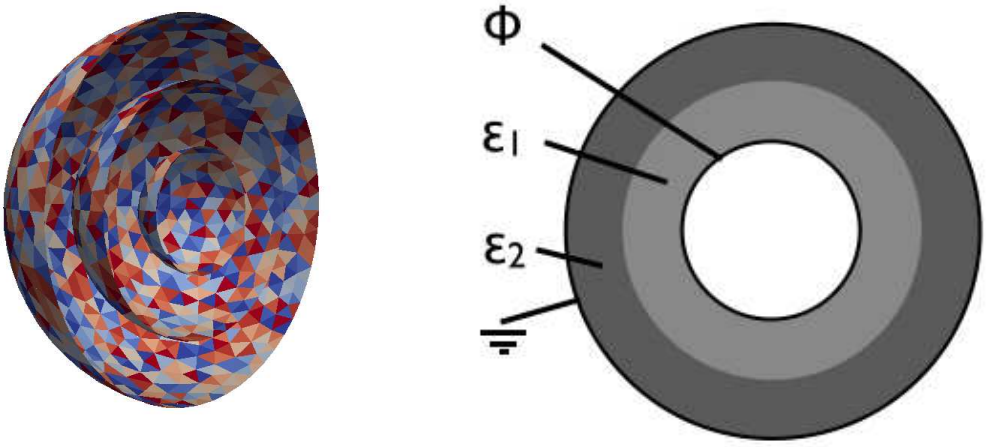

(a) Discretized triangular mesh elements (b) Potential distribution

Figure E.1: Layout of the spherical capacitor test case. Left: Illustration of surfaces of spherical capacitor surfaces into 4112 triangular mesh elements. **Right:** Illustration of the potential distribution on different spheres surrounded by two linear dielectric media. Illustrations taken from [Cor14].

Figure E.2 contains plots of the electric potential and field magnitude as calculated by the analytical formula and the numerical integrators. As explained in [Cor14], the numerical values can reproduce analytical results to a very high accuracy. The remaining error results from discretization effects of the meshed triangular geometry.

Table E.11 comprises the summary of the relative accuracies for potential and field values, whereas table E.12 comprises the summary of the absolute accuracies for potential and field values. The visible deviations result from discretization effects. The errors get reduced as soon as the count of meshed elements gets reduced.

Summarizing, the integration techniques, based on the Gaussian cubature and the RWG basis, correctly reproduce physical results with best accuracy and produce valid and reliable results in context of arbitrary simulations, even the spherical capacitor model is very sensitive to the number of meshed elements and only 4112 triangular patches have been used for discretization.

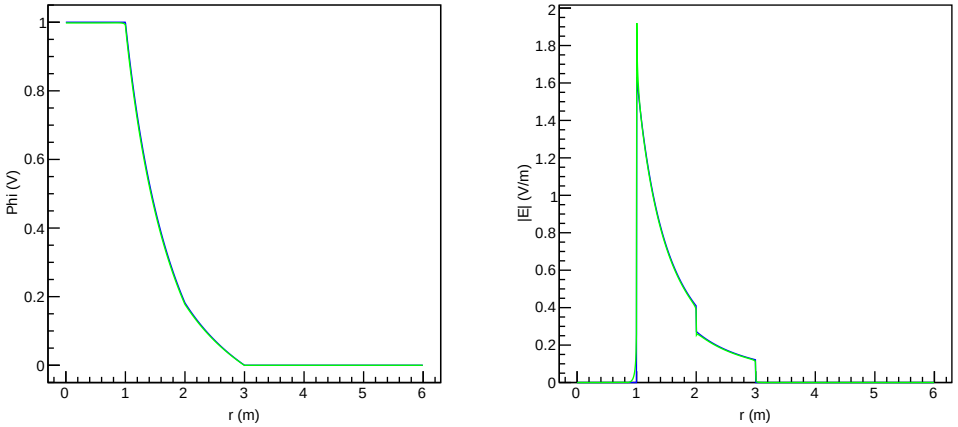

Figure E.2: Radial progress of electric potential and field of sperical capacitor. Left: The analytical potential value is plotted together with the numerical value as obtained by numerical integration routines. **Right:** The electric field magnitude as calculated by the analytical formula against the numerical integration routines.

Table E.11: Relative accuracy summary (analytic vs numeric) for spherical capacitor test. The relative accuracy is determined by comparison of analytical solution of the spherical capacitor problem with the numerical methods as explained in chapter 4 at 1000 diced field points.

	Average (%)	Max (%)	Min (%)
El. potential:	0.347325	3.612955	0.004470
El. field (x):	0.238503	6.144544	7.9×10^{-7}
El. field (y):	0.224556	3.002205	4.2×10^{-6}
El. field (z):	0.226108	3.058698	3.8×10^{-7}

Table E.12: Absolute accuracy summary (analytic vs numeric) for spherical capacitor test. The relative accuracy is determined by comparison of analytical solution of the spherical capacitor problem with the numerical methods as explained in chapter 4 at 1000 diced field points.

	Average	Max	Min
El. potential (V):	6.5389×10^{-4}	1.7566×10^{-2}	4.4700×10^{-5}
El. field (x):	3.9775×10^{-4}	3.0463×10^{-2}	7.9132×10^{-7}
El. field (y):	4.3350×10^{-4}	2.5457×10^{-2}	4.1971×10^{-8}
El. field (z):	3.6133×10^{-4}	1.8713×10^{-2}	3.7642×10^{-9}

F Effect of numerical accuracy to radial potential inhomogeneity in the analyzing plane

In context of a KATRIN toy measurement, the effect of numerical unstable potentials by analytical integration on the neutrino mass estimate is examined. The potentials have been computed with an accurate main spectrometer model as developed in context of [Cor14]. A electro-magnetic configuration has been chosen:

- Vessel potential: $U_{\text{vessel}} = -18.4\,\text{kV}$
- Inner electrode offset: $U_{\text{IE}} = -200\,\text{V}$
- Steep cone offset: $U_{\text{steepcone}} = 100\,\text{V}$
- Magnetic field configuration: 3.8 G in analyzing plane (dual minimum) with 6 T pinch magnet

The challenge of this investigation is to study different potentials in the analyzing plane, whereas the differences between analytical and numerical field solvers are expected in the range of $\mathcal{O}(\text{mV})$. Consequently the difference on the neutrino mass systematics may be in the order of numerical uncertainties.

To be able to report the systematic shift of the estimate, two different simulations have been prepared. As explained in section 3.5, in case of an ensemble test, the absolute signal rate N is drawn from a Poisson distribution with a well-defined expectation value. Since the effect is expected to be very small, the first simulation does not dice N randomly from a distribution, instead a single systematic shift will be calculated. Afterwards, this calculation is repeated 1000 times in order to determine the expected numerical error of the χ^2-fit from the minimization algorithm MINIUT.

For the simulations, KATRIN reference values as reported in the design report [A+04], will be used (e.g. tritium spectrum, model of response function, etc.). In the following, the input field inhomogeneities are discussed.

Input simulation parameter

Before starting the simulation, the radial inhomogeneity of the electric and magnetic field have to be determined at the position of the analyzing plane. For this reason a field line tracking simulation has been carried out, whereas the position of the analyzing plane has been set to the field point, where the retarding potential is minimal.

The magnetic field and the electric potential has been computed from the different detector pixels at their border.

Table F.13 lists the calculated z-positions of the analyzing plane together with magnetic field and electric potential values. The values in table F.13 have been computed with the numerical field solver. Here, a shift of the electric potentials of $\Delta U < 1.5\,\text{V}$ and the magnetic field $\Delta B < 0.2\,\text{G}$, as seen by different detector pixel rings, is visible.

The error for the z-value is given by the step length of the field line calculation $\Delta r = 1\,\text{cm}$ and the field values are given with numerical precision.

For the determination of the *KaFit* input radial inhomogeneities, the program is fed by the arithmetic mean of two following ring values. In that way a mean radial inhomogeneity, as seen by each pixel ring, is defined. Furthermore, a common offset of $U_{\text{offset}} = -2\,\text{V}$ has been added. The errors are the same as stated above.

Table F.13: Magnetic fields and electric potential in analyzing plane. The analyzing plane position has been determined as the point where the electric potential is minimal along each magnetic field line, starting from a detector ring (incl. center at $r = 0$).

FPD Ring	z (cm)	Magnetic field (G)	Electric potential (V)
0	2.4474	3.8106	-18597.7786
1	3.1517	3.8062	-18597.7946
2	3.3802	3.7949	-18597.8422
3	3.7939	3.7864	-18597.8876
4	5.4106	3.7808	-18597.9310
5	7.2541	3.7783	-18597.9724
6	9.3450	3.7789	-18598.0118
7	13.7155	3.7825	-18598.0493
8	26.4008	3.7877	-18598.0851
9	55.4536	3.7849	-18598.1213
10	75.9215	3.7783	-18598.1619
11	85.8917	3.7773	-18598.2098
12	90.4682	3.7827	-18598.2706
13	91.8149	3.7949	-18598.3599

Table F.14: Radial inhomogeneity of magnetic field and electric potential in analyzing plane as calculated with analytical methods. The analyzing plane position has been determined as the point where the electric potential is minimal along each magnetic field line, starting from a detector ring (incl. center at $r = 0$).

FPD Ring	z (cm)	$\mathrm{d}B_{\mathrm{radial}}$ (G)	$\mathrm{d}U_{\mathrm{radial}}$ (V)
0	2.4474	-0.0023	0.2132
1	3.1517	-0.0100	0.1815
2	-0.6198	-0.0199	0.1350
3	2.7939	-0.0270	0.0906
4	1.4106	-0.0311	0.0481
5	8.2541	-0.0323	0.0078
6	14.3450	-0.0304	-0.0307
7	17.7155	-0.0264	-0.0673
8	31.4008	-0.0250	-0.1033
9	55.4538	-0.0291	-0.1416
10	75.9215	-0.0343	-0.1859
11	87.8912	-0.0320	-0.2403
12	90.4682	-0.0219	-0.3152

Table F.15: Radial inhomogeneity of magnetic field and electric potential in analyzing plane as calculated with numerical methods. The analyzing plane position has been determined as the point where the electric potential is minimal along each magnetic field line, starting from a detector ring (incl. center at $r = 0$).

FPD Ring	z (cm)	$\mathrm{d}B_{\mathrm{radial}}$ (G)	$\mathrm{d}U_{\mathrm{radial}}$ (V)
0	2.4474	-0.0023	0.2134
1	3.1517	-0.0101	0.1816
2	3.3802	-0.0200	0.1351
3	3.7939	-0.0270	0.0907
4	5.4106	-0.0311	0.0483
5	7.2541	-0.0321	0.0079
6	9.3450	-0.0300	-0.0306
7	13.7155	-0.0255	-0.0672
8	26.4008	-0.0243	-0.1032
9	55.4538	-0.0291	-0.1416
10	75.9215	-0.0329	-0.1858
11	85.8917	-0.0307	-0.2402
12	90.4682	-0.0219	-0.3152

Shift of neutrino mass parameter

A final *KaFit* parameter fit with a direct comparison between analytical and numerical integration routines results into the parameters as given by tables F.14 and F.15. For the ensemble test 1000 fits with a statistical error on m_ν^2 of 0.017073 have been applied to the inhomogeneity values as mentioned above. A deviation of the neutrino mass estimate by the uncertainty of the analytical integrator is visible by the fit result. Following systematic shift has been calculated within 1-σ:

$$\Delta m_\nu^2 = 1.12 \times 10^{-4}\,\mathrm{eV}^2 \pm 0.01 \times 10^{-4}\,\mathrm{eV}^2, \text{ with} \tag{7.10}$$

$$\chi^2/\mathrm{DOF} = 0.0439/529 \tag{7.11}$$

Consequently the determination of the neutrino mass estimate has to be corrected by the above stated value if analytical integration routines have been used for the determination of the electric potential in the analyzing plane.

G Hardware equipment for computations

In the following, technical details about the computers, that have been used in context of accuracy and speed comparisons for both the implementation of analytical and numerical integrator classes in chapter 4 are mentioned together with details about the software equipment.

- Single-threaded C++ code from chapter 4 has been executed on an Intel(R) Xeon(R) CPU with 3.10 GHz clock speed (E5-2687W v3). In context of sec. 4.5 an Intel(R) Xeon(R) CPU (E5-2650 v2) running at 2.60 GHz has been used.
  All CPU programs have been compiled with GCC 4.8.4 with optimization flag O3 under Xubuntu 14.04 as operating system.
- In order to exploit dedicated capabilities of parallel hardware architectures, the code has been ported to OpenCL (version 1.1) as well.
  In order to test the speed on GPUs, a Tesla K40c card with a GK110b chip running at 875 MHz, installed in a dedicated system, has been used.
  The OpenCL programs have been compiled together with the card driver version 352.55. The operating system has been Xubuntu, version 14.04, as well.

List of Acronyms

ADEI	Advanced Data Extraction Infrastructure
BEM	Boundary Element Method
BIXS	Beta-Induced X-Ray Spectroscopy
BBR	Black-body Radiation
CAD	Computer-aided Design
CPS	Cryogenic pumping section
CPU	Central Processing Unit
CUDA	Compute Unified Device Architecture
DAQ	Data Acquisition
DPS	Differential Pumping Section
EMCS	Earth Magnetic Field Compensation System
FDM	Finite Difference Method
FEM	Finite Element Method
FFTM	Fast Fourier Transform on Multipoles
FMM	Fast Multipole Method
FPD	Focal-Plane Detector
FWHM	Full Width at Half Maximum
OpenCL	Open Computing Language
GPGPU	General-Purpose computing on Graphics Processing Units
GPU	Graphics Processing Unit
KATRIN	Karlsruhe Tritium Neutrino
KIT	Karlsruhe Institute of Technology
L2L	Local to local conversion
LARA	Laser Raman
LFCS	Low-Field Field Correction System
M2L	Multipole to local conversion
M2M	Multipole to multipole conversion
MAC-E	Magnetic Adiabatic Collimation combined with an Electrostatic Filter

MoM	Methods of Moments
MPI	Message Passing Interface
MTD	Measurement Time Distribution
OpenCL	Open Computing Language
ORCA	Object-Oriented Real-Time Control And Acquisition
PIN	P-type, i-type, n-type semiconductor
PS1	Pre-spectrometer magnet 1
PS2	Pre-spectrometer magnet 2
RAM	Random Access Memory
ROOT	Object-oriented data analysis software package
RWG	Rao-Wilton-Glisson
SDS	Spectrometer and Detector Section
SDS-IIa	Second spectrometer and detector section measurement campaign, first part
SDS-IIb	Second spectrometer and detector section measurement campaign, second part
SSC	Source and Spectrum Calculation
SSM	Standard Solar Model
UHV	Ultra-high vacuum
VTK	Visualization Toolkit
VTP	File format for serial vtkPolyData
WGTS	Windowless gaseous tritium source
XML	Extensible Markup Language

List of Figures

List of Tables

Bibliography

[A+04] J. Angrik *et al.*, "KATRIN Design Report," 2004. [Cited on pages 6, 43, 45, 80, 83, and 163.]

[A+09] I. Antcheva *et al.*, "ROOT - A C++ framework for petabyte data storage, statistical analysis and visualization," *Computer Physics Communications*, vol. 180, no. 12, pp. 2499 – 2512, 2009. [Online]. Available: http://www.sciencedirect.com/science/article/pii/S0010465509002550 [Cited on pages 50, 80, and 105.]

[A+11a] K. N. Abazajian *et al.*, "Cosmological and astrophysical neutrino mass measurements," *Astroparticle Physics*, vol. 35, no. 4, pp. 177 – 184, 2011. [Online]. Available: http://www.sciencedirect.com/science/article/pii/S0927650511001344 [Cited on page 13.]

[A+11b] S. Abe *et al.*, "Measurement of the ^{8}B solar neutrino flux with the KamLAND liquid scintillator detector," *Phys. Rev. C*, vol. 84, p. 035804, Sep 2011. [Online]. Available: http://link.aps.org/doi/10.1103/PhysRevC.84.035804 [Cited on page 7.]

[A+11c] V. N. Aseev *et al.*, "Upper limit on the electron antineutrino mass from the Troitsk experiment," *Phys. Rev. D*, vol. 84, p. 112003, Dec 2011. [Online]. Available: http://link.aps.org/doi/10.1103/PhysRevD.84.112003 [Cited on pages 19 and 43.]

[A+13] B. Aharmim *et al.*, "Combined analysis of all three phases of solar neutrino data from the Sudbury Neutrino Observatory," *Phys. Rev. C*, vol. 88, p. 025501, Aug 2013. [Online]. Available: http://link.aps.org/doi/10.1103/PhysRevC.88.025501 [Cited on page 7.]

[A+15a] J. F. Amsbaugh *et al.*, "Focal-plane detector system for the {KATRIN} experiment," *Nuclear Instruments and Methods in Physics Research Section A: Accelerators, Spectrometers, Detectors and Associated Equipment*, vol. 778, pp. 40 – 60, 2015. [Online]. Available: http://www.sciencedirect.com/science/article/pii/S0168900215000236 [Cited on pages 33 and 34.]

[A+15b] D. M. Asner *et al.*, "Single-Electron Detection and Spectroscopy via Relativistic Cyclotron Radiation," *Phys. Rev. Lett.*, vol. 114, p. 162501, Apr 2015. [Online]. Available: http://link.aps.org/doi/10.1103/PhysRevLett.114.162501 [Cited on page 17.]

[A+16a] P. A. R. Ade *et al.*, "Planck 2015 results. XIII. Cosmological parameters," vol. 594, p. A13, Sep. 2016. [Cited on page 13.]

[A+16b] M. Arenz *et al.*, "Commissioning of the vacuum system of the KATRIN Main Spectrometer," *Journal of Instrumentation*, vol. 11, no. 04, p. P04011, 2016. [Online]. Available: http://stacks.iop.org/1748-0221/11/i=04/a=P04011 [Cited on pages 21, 32, 38, and 83.]

[AC58] J. Albrecht and L. Collatz, "Zur numerischen Auswertung mehrdimensionaler Integrale," *ZAMM - Journal of Applied Mathematics and Mechanics / Zeitschrift für Angewandte Mathematik und Mechanik*, vol. 38, no. 1-2, pp. 1–15, 1958. [Online]. Available: http://dx.doi.org/10.1002/zamm.19580380102 [Cited on pages 98 and 159.]

[Ale01] A. Alexandrescu, *Modern C++ Design: Generic Programming and Design Patterns Applied*. Boston, MA, USA: Addison-Wesley Longman Publishing Co., Inc., 2001. [Cited on page 58.]

[B+87] R. M. Bionta *et al.*, "Observation of a neutrino burst in coincidence with supernova 1987A in the Large Magellanic Cloud," *Phys. Rev. Lett.*, vol. 58, pp. 1494–1496, Apr 1987. [Online]. Available: http://link.aps.org/doi/10.1103/PhysRevLett.58.1494 [Cited on page 14.]

[B+08] S. Baeßler *et al.*, "First measurements with the neutron decay spectrometer a SPECT," *The European Physical Journal A*, vol. 38, no. 1, pp. 17–26, 2008. [Online]. Available: http://dx.doi.org/10.1140/epja/i2008-10660-0 [Cited on page 83.]

[B+10] M. Beck *et al.*, "Effect of a sweeping conductive wire on electrons stored in the Penning trap between the KATRIN spectrometers," *Eur. Phys. J.*, vol. A44, pp. 499–511, 2010. [Cited on page 32.]

[B+12] M. Babutzka *et al.*, "Monitoring of the operating parameters of the KATRIN Windowless Gaseous Tritium Source," *New Journal of Physics*, vol. 14, no. 10, p. 103046, 2012. [Online]. Available: http://stacks.iop.org/1367-2630/14/i=10/a=103046 [Cited on page 27.]

[Bab14] M. Babutzka, "Design and development for the Rearsection of the KATRIN experiment," Ph.D. dissertation, Karlsruhe Institute of Technology, 2014. [Online]. Available: http://digbib.ubka.uni-karlsruhe.de/volltexte/1000045598 [Cited on pages 27 and 28.]

[Bar13] J. P. Barrett, "Fast Multipole Methods for KATRIN," Collaboration internal note, 2013. [Cited on pages 72 and 73.]

[Bar15] ——, "Optimized implementation of potential and field calculation in context of charge density solving," Private communication, 2015. [Cited on page 91.]

[Bar16] ——, "A Spatially Resolved Study of the KATRIN Main Spectrometer Using a Novel Fast Multipole Method," Ph.D. dissertation, Massachusetts Institute of Technology, 2016. [Cited on pages 71, 72, 106, 107, and 112.]

[BD92] C. A. Brebbia and J. Dominguez, *Boundary elements : an introductory course*, 2nd ed. Southampton: Computational Mechanics [u.a.], 1992. [Cited on page 83.]

[Beh16] J. Behrens, "Design and commissioning of a mono-energetic photoelectron source and active background reduction by magnetic pulse at the KATRIN spectrometers," Ph.D. dissertation, University of Münster, 2016. [Cited on pages 34, 37, and 115.]

[Bel03] E. Bellotti, *Neutrino Physics*. Societa italiana di fisica, 2003. [Cited on page 27.]

[Bel16] G. Bellini, "The impact of Borexino on the solar and neutrino physics," *Nuclear Physics B*, vol. 908, pp. 178 – 198, 2016, neutrino Oscillations: Celebrating the Nobel Prize in Physics 2015. [Online]. Available: http://www.sciencedirect.com/science/article/pii/S0550321316300499 [Cited on page 8.]

[BFC15] J. P. Barrett, J. A. Formaggio, and T. J. Corona, "A method to calculate the spherical multipole expansion of the electrostatic charge distribution on a triangular boundary elements," *Progress In Electromagnetics Research B*, vol. 63, pp. 123–143, 2015, doi:10.2528/PIERB15061904. [Online]. Available: http://www.jpier.org/pierb/pier.php?paper=15061904 [Cited on page 72.]

[BMB73a] A. B. Birtles, B. J. Mayo, and A. W. Bennett, "Computer technique for solving 3-dimensional electron-optics and capacitance problems," *Electrical Engineers, Proceedings of the Institution of*, vol. 120, no. 2, pp. 213–220, February 1973. [Cited on pages 93 and 96.]

[BMB73b] ——, "Erratum: Computer technique for solving 3-dimensional electron-optics and capacitance problems," *Electrical Engineers, Proceedings of the Institution of*, vol. 120, no. 5, p. 559, May 1973. [Cited on pages 93 and 96.]

[BPSM+08] T. Bray, J. Paoli, C. M. Sperberg-McQueen, E. Maler, and F. Yergeau, "Extensible Markup Language (xml) 1.0," 2008. [Online]. Available: http://www.w3.org/TR/xml [Cited on page 55.]

[Bre] P. Breeuwsma, "Cubic interpolation," accessed: 2016-09-14. [Online]. Available: http://www.paulinternet.nl/?page=bicubic [Cited on page 70.]

[BS79] I. N. Bronstein and K. A. Semendjajew, *Taschenbuch der Mathematik*, 19th ed., G. Grosche and V. Ziegler, Eds. Leipzig, Moskau: BSB B. G. Teubner Verlagsgesellschaft, Nauka-Verlag, 1979. [Cited on page 88.]

[BSB05] J. N. Bahcall, A. M. Serenelli, and S. Basu, "New Solar Opacities, Abundances, Helioseismology, and Neutrino Fluxes," *The Astrophysical Journal Letters*, vol. 621, no. 1, p. L85, 2005. [Online]. Available: http://stacks.iop.org/1538-4357/621/i=1/a=L85 [Cited on pages 4 and 10.]

[BSD08] G. Beer, I. M. Smith, and C. Dünser, *The boundary element method with programming : for engineers and scientists*. Wien: Springer, 2008. [Online]. Available: http://swbplus.bsz-bw.de/bsz267863101cov.htm [Cited on page 83.]

[BTW84] C. A. Brebbia, J. C. Telles, and L. C. Wrobel, *Boundary element techniques : theory and applications in engineering*. Berlin: Springer, 1984. [Cited on page 83.]

[Car13] M. J. Carley, "Analytical Formulae for Potential Integrals on Triangles," *Journal of Applied Mechanics*, vol. 80, pp. 1–7, 2013. [Cited on pages 93 and 96.]

[Cat10] B. Catanzaro, "OpenCL Optimization Case Study: Simple Reduction," http://developer.amd.com/resources/articles-whitepapers/opencl-optimization-case-study-simple-reductions/, Aug 2010, accessed: 2016-07-26. [Cited on page 70.]

[CBKV10] S. Chilingaryan, A. Beglarian, A. Kopmann, and S. Vöcking, "Advanced data extraction infrastructure: Web based system for management of time series data," *Journal of Physics: Conference Series*, vol. 219, no. 4, p. 042034, 2010. [Online]. Available: http://stacks.iop.org/1742-6596/219/i=4/a=042034 [Cited on page 41.]

[CH88] R. Cools and A. Haegemans, "Another step forward in searching for cubature formulae with a minimal number of knots for the square," *Computing*, vol. 40, no. 2, pp. 139–146, 1988. [Online]. Available: http://dx.doi.org/10.1007/BF02247942 [Cited on pages 98 and 160.]

[CLRZ99] D. Cubric, B. Lencova, F. H. Read, and J. Zlamal, "Comparison of FDM, FEM and BEM for electrostatic charged particle optics," *Nuclear*

Instruments and Methods in Physics Research Section A: Accelerators, Spectrometers, Detectors and Associated Equipment, vol. 427, no. 1-2, pp. 357 – 362, 1999. [Online]. Available: http://www.sciencedirect.com/science/article/pii/S0168900298015630 [Cited on page 64.]

[CMP89] R. D. Cook, D. S. Malkus, and M. E. Plesha, *Concepts and applications of finite element analysis*, 3rd ed. New York [u.a.]: Wiley, 1989. [Online]. Available: http://digitool.hbz-nrw.de:1801/webclient/DeliveryManager?pid=2361906&custom_att_2=simple_viewer [Cited on pages 83 and 97.]

[Com15] R. Combe, "Design optimization of the KATRIN transport section and investigation of related background contribution," *Master thesis*, 2015, Karlsruhe Institute of Technology. [Online]. Available: https://fuzzy.fzk.de/bscw/bscw.cgi/964402 [Cited on pages 56, 106, and 155.]

[Coo] R. Cools, "Encyclopaedia of Cubature Formulas, web page." [Online]. Available: http://nines.cs.kuleuven.be/ecf [Cited on page 98.]

[Coo99] ——, "Monomial cubature rules since Stroud: a compilation - part 2," *Journal of Computational and Applied Mathematics*, vol. 112, no. 1-2, pp. 21 – 27, 1999. [Online]. Available: http://www.sciencedirect.com/science/article/pii/S0377042799002290 [Cited on page 98.]

[Coo02] ——, "Advances in multidimensional integration," *Journal of Computational and Applied Mathematics*, vol. 149, no. 1, pp. 1 – 12, 2002, scientific and Engineering Computations for the 21st Century - Methodologies and Applications Proceedings of the 15th Toyota Conference. [Online]. Available: http://www.sciencedirect.com/science/article/pii/S0377042702005174 [Cited on page 98.]

[Coo03] ——, "An encyclopaedia of cubature formulas," *Journal of Complexity*, vol. 19, no. 3, pp. 445–453, 2003, oberwolfach Special Issue. [Online]. Available: http://www.sciencedirect.com/science/article/pii/S0885064X03000116 [Cited on page 98.]

[Cor09] T. J. Corona, "Tools for Electromagnetic Field Simulation in the KATRIN Experiment," 2009. [Online]. Available: http://inspirehep.net/record/1375890/files/mth-corona.pdf [Cited on pages 83, 84, 85, 91, and 103.]

[Cor11] ——, "Penning trap searches in the detector region," *Talk at the 21. KATRIN collaboration meeting*, 10 2011. [Cited on page 75.]

[Cor14] ——, "Methodology and application of high performance electrostatic field simulation in the KATRIN experiment," p. 149, 2014, copyright - Database copyright ProQuest LLC; ProQuest does not claim copyright in the individual underlying works; Last update - 2016-06-06. [Online]. Available: http://search.proquest.com/docview/1648168745?accountid=11793 [Cited on pages 50, 65, 83, 84, 85, 91, 93, 95, 96, 103, 104, 105, 106, 107, 161, and 163.]

[CR93] R. Cools and P. Rabinowitz, "Monomial cubature rules since Stroud: a compilation," *Journal of Computational and Applied Mathematics*, vol. 48, no. 3, pp. 309 – 326, 1993. [Online]. Available: http://www.sciencedirect.com/science/article/pii/0377042793900279 [Cited on page 98.]

[CS00] M. V. K. Chari and S. J. Salon, *Numerical methods in electromagnetism*, ser. Academic Press series in electromagnetism. San Diego [u.a.]: Academic Press, 2000. [Cited on page 83.]

[D+14] S. Dyba *et al.*, "Repair of electrical short-circuits in wire electrode system - status and perspectives," Tech. Rep., 2014. [Cited on page 40.]

[DAR14] B. Dawes, D. Abrahams, and R. Rivera, *boost C++ libraries*, 2014. [Cited on page 50.]

[DH89] K. Davey and S. Hinduja, "Analytical integration of linear three-dimensional triangular elements in BEM," *Applied Mathematical Modelling*, vol. 13, no. 8, pp. 450 – 461, 1989. [Online]. Available: http://www.sciencedirect.com/science/article/pii/0307904X89900930 [Cited on pages 93 and 96.]

[DM16] G. Drexlin and S. Mertens, "Hydrogen Rydberg atoms as a novel source of background in the very large electrostatic spectrometer of KATRIN," *to be published*, 2016. [Cited on pages 120, 138, and 147.]

[DR06] F. Delfino and M. Rossi, *FEM (Finite Element Modeling) Techniques for Electrostatic Microactuators*. Boston, MA: Springer US, 2006, pp. 1145–1176. [Online]. Available: http://dx.doi.org/10.1007/0-387-25786-1_30 [Cited on page 64.]

[Dre15a] G. Drexlin, "Excited Molecules and Atoms as background source," *Presentation*, 03 2015, 28th KATRIN Collaboration Meeting. [Cited on pages 120 and 138.]

[Dre15b] ——, "Origin of Rydberg background a survey of current investigations," *Presentation*, 10 2015, 29th KATRIN Collaboration Meeting. [Cited on page 138.]

[Dre15c] ——, "Rydberg states of hydrogen atoms a novel source of background," *Presentation*, 10 2015, 29th KATRIN Collaboration Meeting. [Cited on pages 120 and 138.]

[Dre17] ——, "Ryderg atoms as a novel source of background (to be published)," 2017. [Cited on page 46.]

[Duf82] M. G. Duffy, "Quadrature Over a Pyramid or Cube of Integrands with a Singularity at a Vertex," *SIAM Journal on Numerical Analysis*, vol. 19, no. 6, pp. 1260–1262, 1982. [Online]. Available: http://dx.doi.org/10.1137/0719090 [Cited on page 101.]

[Dun85] D. A. Dunavant, "High degree efficient symmetrical Gaussian quadrature rules for the triangle," *International Journal for Numerical Methods in Engineering*, vol. 21, no. 6, pp. 1129–1148, 1985. [Online]. Available: http://dx.doi.org/10.1002/nme.1620210612 [Cited on page 98.]

[Dur64] E. Durand, *Electrostatique*. Paris: Masson, 1964, vol. 1: Les distributions. [Cited on pages 90, 93, and 96.]

[Dyb17] S. Dyba, "In preparation," Ph.D. dissertation, University of Münster, 2017. [Cited on page 31.]

[E+14] M. Erhard *et al.*, "High-voltage monitoring with a solenoid retarding spectrometer at the KATRIN experiment," *Journal of Instrumentation*, vol. 9, no. 06, p. P06022, 2014. [Online]. Available: http://stacks.iop.org/1748-0221/9/i=06/a=P06022 [Cited on page 32.]

[EMU96] G. Engeln-Müllges and F. Uhlig, *Numerical algorithms with C*. Berlin: Springer, 1996. [Online]. Available: http://digitool.hbz-nrw.de:1801/webclient/DeliveryManager?pid=2371417&custom_att_2=simple_viewer;http://swbplus.bsz-bw.de/bsz053517814cov.htm [Cited on pages 97, 98, 157, 159, and 160.]

[Eng80] H. Engels, *Numerical quadrature and cubature*, ser. Computational mathematics and applicatfons. London [u.a.]: Acad. Pr., 1980. [Online]. Available: http://digitool.hbz-nrw.de:1801/webclient/DeliveryManager?pid=2331877&custom_att_2=simple_viewer [Cited on pages 97, 98, and 160.]

[Erh12] M. Erhard, "Untersuchung der Langzeitstabilität des nuklearen Standards für die Energieskala des KATRIN-Experiments," *Diploma thesis*, 2012, Karlsruhe Institute of Technology. [Online]. Available: http://www.katrin.kit.edu/publikationen/dth-erhard.pdf [Cited on page 33.]

[Erh16] ——, "Influence of the magnetic field on the transmission characteristics and the neutrino mass systematic of the KATRIN experiment, to be published," Ph.D. dissertation, Karlsruhe Institute of Technology, 2016. [Cited on pages 34, 35, 37, 47, and 107.]

[Eup85] M. Eupper, *Eine verbesserte Integralgleichungsmethode zur numerischen Lösung dreidimensionaler Dirichletprobleme und ihre Anwendung in der Elektronenoptik*. na, 1985. [Cited on pages 93 and 96.]

[Eva93] G. Evans, *Practical numerical integration*. Chichester [u.a.]: Wiley, 1993. [Online]. Available: http://www.gbv.de/dms/ilmenau/toc/122325613.PDF [Cited on pages 93, 94, 96, and 97.]

[Fis14] S. Fischer, "Commissioning of the KATRIN Raman system and durability studies of optical coatings in glove box and tritium atmospheres," Ph.D. dissertation, Karlsruhe Institute of Technology, 2014. [Online]. Available: http://digbib.ubka.uni-karlsruhe.de/volltexte/1000043697 [Cited on page 29.]

[Fla05] B. Flatt, "Voruntersuchungen zu den Spektrometern des KATRIN-Experiments," Ph.D. dissertation, University of Mainz, 2005. [Online]. Available: http://ubm.opus.hbz-nrw.de/volltexte/2005/715/pdf/diss.pdf [Cited on page 116.]

[FLC+12] J. A. Formaggio, P. Lazic, T. J. Corona, H. Stefancic, H. Abraham, and F. Glück, "Solving for micro- and macro-scale electrostatic configurations using the robin hood algorithm," *Progress In Electromagnetics Research B*, vol. 39, pp. 1 – 37, 2012. [Online]. Available: http://www.jpier.org/pierb/pier.php?paper=11112106 [Cited on pages 65, 66, 83, 85, 90, 93, 95, 96, 103, 104, 105, and 161.]

[Frä10] F. Fränkle, "Background Investigations of the KATRIN Pre-Spectrometer," Ph.D. dissertation, Karlsruhe Institute of Technology, 2010. [Online]. Available: http://digbib.ubka.uni-karlsruhe.de/volltexte/1000019392 [Cited on pages 25, 33, and 34.]

[Fur13] D. L. Furse, "Derivations of Equations of Motion in the Kassiopeia Package," Internal KATRIN report, February 2013. [Cited on page 54.]

[Fur15] ——, "Techniques for direct neutrino mass measurement utilizing tritium β-decay," Ph.D. dissertation, Masssachusetts Institute of Technology, 2015. [Online]. Available: http://inspirehep.net/record/1418279/files/Thesis-2015-Furse.pdf [Cited on pages 50, 51, 52, 53, and 83.]

[G+05] F. Glück *et al.*, "The neutron decay retardation spectrometer aSPECT: Electromagnetic design and systematic effects," *The European Physical Journal A - Hadrons and Nuclei*, vol. 23, no. 1, pp. 135–146, 2005. [Online]. Available: http://dx.doi.org/10.1140/epja/i2004-10057-1 [Cited on page 83.]

[Gar63] M. W. Garrett, "Calculation of Fields, Forces, and Mutual Inductances of Current Systems by Elliptic Integrals," *Journal of Applied Physics*,

vol. 34, no. 9, pp. 2567–2573, 1963. [Online]. Available: http://scitation.aip.org/content/aip/journal/jap/34/9/10.1063/1.1729771 [Cited on page 60.]

[Gat88] K. Gatermann, "The construction of symmetric cubature formulas for the square and the triangle," *Computing*, vol. 40, no. 3, pp. 229–240, 1988. [Online]. Available: http://dx.doi.org/10.1007/BF02251251 [Cited on pages 98 and 157.]

[GDL+13] F. Glück, G. Drexlin, B. Leiber, S. Mertens, A. Osipowicz, J. Reich, and N. Wandkowsky, "Electromagnetic design of the large-volume air coil system of the KATRIN experiment," *New Journal of Physics*, vol. 15, no. 8, p. 083025, 2013. [Online]. Available: http://stacks.iop.org/1367-2630/15/i=8/a=083025 [Cited on pages 36 and 63.]

[GF+16] S. Groh, D. L. Furse *et al.*, "Kassiopeia: A Modern, Extensible C++ Particle Tracking Package," *to be published*, 2016. [Cited on pages 52, 53, 55, 83, and 108.]

[GGMS16] M. C. Gonzalez-Garcia, M. Maltoni, and T. Schwetz, "Global analyses of neutrino oscillation experiments," *Nuclear Physics B*, vol. 908, pp. 199 – 217, 2016, neutrino Oscillations: Celebrating the Nobel Prize in Physics 2015. [Online]. Available: http://www.sciencedirect.com/science/article/pii/S0550321316000778 [Cited on pages 10 and 11.]

[GK90] K. Grotz and H. V. Klapdor, *The Weak Interaction in Nuclear, Particle and Astrophysics*. Taylor & Francis, 1990. [Cited on page 12.]

[GKW03] L. Gaul, M. Kögl, and M. Wagner, *Boundary element methods for engineers and scientists : an introductory course with advanced topics*, ser. Engineering online library. Berlin [u.a.]: Springer, 2003. [Online]. Available: http://swbplus.bsz-bw.de/bsz104167890cov.htm [Cited on page 83.]

[Glü06] F. Glück, "The 3-dimensional magnetic field calculation program package magfield3," 2006. [Cited on page 60.]

[Glü11a] ——, "Axisymmetric electric field calculation with zonal harmonic expansion," *Progress In Electromagnetics Research B*, vol. 32, pp. 319–350, 2011. [Online]. Available: http://www.jpier.org/pierb/pier.php?paper=11042106 [Cited on pages 67 and 69.]

[Glü11b] ——, "Axisymmetric magnetic field calculation with zonal harmonic expansion," *Progress In Electromagnetics Research B*, vol. 32, pp. 351–388, 2011. [Online]. Available: http://www.jpier.org/pierb/pier.php?paper=11042108 [Cited on pages 60 and 62.]

[Glü15] ——, "Calculation of H atom Rydberg state transitions," 2015, Internal note. [Cited on page 140.]

[Glü16] ——, "Axisymmetric electric field calculation with BEM and elliptic integrals," *to be published*, 2016. [Cited on pages 61, 67, and 68.]

[Gol91] D. Goldberg, "What Every Computer Scientist Should Know About Floating-point Arithmetic," *ACM Comput. Surv.*, vol. 23, no. 1, pp. 5–48, Mar. 1991. [Online]. Available: http://doi.acm.org/10.1145/103162.103163 [Cited on pages 92, 93, and 94.]

[Gör14] S. Görhardt, "Background Reduction Methods and Vacuum Technology at the KATRIN Spectrometers," Ph.D. dissertation, Karlsruhe Institute of Technology, 2014. [Online]. Available: http://digbib.ubka.uni-karlsruhe.de/volltexte/1000038050 [Cited on pages 39 and 115.]

[Gos15] W. Gosda, "A new Preconditioning Approach using the Fast Fourier Transformation on Multipoles," *Diploma thesis*, 2015, Karlsruhe Institute of Technology. [Cited on pages 28, 65, 72, and 106.]

[GR88] L. Greengard and V. Rokhlin, *The rapid evaluation of potential fields in three dimensions.* Berlin, Heidelberg: Springer Berlin Heidelberg, 1988, pp. 121–141. [Online]. Available: http://dx.doi.org/10.1007/BFb0089775 [Cited on page 72.]

[GR97] ——, "A new version of the Fast Multipole Method for the Laplace equation in three dimensions," *Acta Numerica*, vol. 6, pp. 229–269, 1 1997. [Online]. Available: http://journals.cambridge.org/article_S0962492900002725 [Cited on page 72.]

[Gro10] S. Groh, "Untersuchung von UV-Laser induziertem Untergrund am KATRIN Vorspektrometer," *Diploma thesis*, 2010, Karlsruhe Institute of Technology. [Cited on page 25.]

[Gro15] ——, "Modeling of the response function and measurement of transmission properties of the KATRIN experiment," Ph.D. dissertation, Karlsruhe Institute of Technology, 2015. [Online]. Available: http://digbib.ubka.uni-karlsruhe.de/volltexte/1000046546 [Cited on pages 24, 37, 50, 51, 54, 55, 57, 83, 107, and 118.]

[Gup99] O. P. Gupta, *Finite and boundary element methods in engineering.* Rotterdam [u.a.]: Balkema, 1999. [Cited on page 83.]

[H$^+$] M. A. Howe *et al.*, "ORCA webpage," Tech. Rep. [Cited on page 41.]

[H$^+$87] K. Hirata *et al.*, "Observation of a neutrino burst from the supernova SN1987A," *Phys. Rev. Lett.*, vol. 58, pp. 1490–1493, Apr 1987. [Online]. Available: http://link.aps.org/doi/10.1103/PhysRevLett.58.1490 [Cited on page 14.]

[Han07] V. Hannen, "Production of the wire electrode for the KATRIN main spectrometer," *Talk at the 13. KATRIN collaboration meeting*, 2007. [Online]. Available: http://fuzzy.fzk.de/bscw/bscw.cgi/d425777/95-TRP-4303-S1-VHannen.pdf [Cited on pages 23 and 102.]

[Har07] M. Harris, "Optimizing Parallel Reduction in CUDA," http://developer.download.nvidia.com/compute/cuda/1.1-Beta/x86_website/projects/reduction/doc/reduction.pdf, Oct 2007, accessed: 2016-07-26. [Cited on page 70.]

[Har15] F. Harms, "Characterization and Minimization of Background Processes in the KATRIN Main Spectrometer," Ph.D. dissertation, Karlsruhe Institute of Technology, 2015. [Online]. Available: http://digbib.ubka.uni-karlsruhe.de/volltexte/1000050027 [Cited on pages 23, 25, 30, 33, 35, 39, 41, 43, 46, 115, 118, 120, 131, 137, 138, 139, 142, and 147.]

[Hei15] F. Heizmann, "Optimization of a KATRIN source analysis tool and investigations of the potential to constrain the relic neutrino background," *Master thesis*, 2015, Karlsruhe Institute of Technology. [Online]. Available: http://www.katrin.kit.edu/publikationen/mth_heizmann.pdf [Cited on pages 63 and 106.]

[HK89] P. W. Hawkes and E. Kasper, *Principles of electron optics.* London: Academic Pr., 1989, vol. 1: Basic geometrical optics. [Cited on pages 64 and 83.]

[HMS56] P. C. Hammer, O. J. Marlowe, and A. H. Stroud, "Numerical Integration Over Simplexes and Cones," *Mathematical Tables and Other Aids to Computation*, vol. 10, no. 55, pp. 130–137, 1956. [Online]. Available: http://www.jstor.org/stable/2002483 [Cited on pages 98 and 157.]

[Höt12] M. Hötzel, "Simulation and analysis of source-related effects for KATRIN," Ph.D. dissertation, Karlsruhe Institute of Technology, 2012. [Online]. Available: http://digbib.ubka.uni-karlsruhe.de/volltexte/1000031259 [Cited on pages 50, 78, 79, and 81.]

[HP76] A. Haegemans and R. Piessens, "Construction of cubature formulas of degree eleven for symmetric planar regions, using orthogonal polynomials," *Numerische Mathematik*, vol. 25, no. 2, pp. 139–148, 1976. [Online]. Available: http://dx.doi.org/10.1007/BF01462267 [Cited on page 98.]

[HP77] ——, "Construction of Cubature Formulas of Degree Seven and Nine Symmetric Planar Regions, Using Orthogonal Polynomials," *SIAM Journal on Numerical Analysis*, vol. 14, no. 3, pp. 492–508, 1977. [Online]. Available: http://dx.doi.org/10.1137/0714029 [Cited on page 98.]

[HS56] P. C. Hammer and A. H. Stroud, "Numerical Integration Over Simplexes," *Mathematical Tables and Other Aids to Computation*, vol. 10, no. 55, pp. 137–139, 1956. [Online]. Available: http://www.jstor.org/stable/2002484 [Cited on pages 98 and 157.]

[HS58] ——, "Numerical Evaluation of Multiple Integrals II," *Mathematical Tables and Other Aids to Computation*, vol. 12, no. 64, pp. 272–280, 1958. [Online]. Available: http://www.jstor.org/stable/2002370 [Cited on pages 98 and 157.]

[HTS06] I. Hänninen, M. Taskinen, and J. Sarvas, "Singularity subtraction integral formulae for surface integral equations with rwg, rooftop and hybrid basis functions," *Progress In Electromagnetics Research*, vol. 63, pp. 243–278, 2006. [Online]. Available: http://dx.doi.org/10.2528/PIER06051901 [Cited on pages 83, 85, 86, 88, 93, 95, 96, 99, 100, 103, 104, and 105.]

[Hue75] K. H. Huebner, *The finite element method for engineers*, ser. A Wiley-Interscience publication. New York [u.a.]: Wiley, 1975. [Cited on pages 83 and 97.]

[Hug10] K. Hugenberg, "An angular resolved pulsed UV LED photoelectron source for KATRIN," *Progress in Particle and Nuclear Physics*, vol. 64, no. 2, pp. 288 – 290, 2010, neutrinos in Cosmology, in Astro, Particle and Nuclear PhysicsInternational Workshop on Nuclear Physics, 31st course. [Online]. Available: http://www.sciencedirect.com/science/article/pii/S0146641009001094 [Cited on page 27.]

[Hwu11] W.-m. W. Hwu, *GPU Computing Gems Emerald Edition*, 1st ed. San Francisco, CA, USA: Morgan Kaufmann Publishers Inc., 2011. [Cited on pages 75 and 103.]

[Jac99] J. D. Jackson, *Classical electrodynamics*, 3rd ed. New York: Wiley, 1999. [Cited on page 71.]

[Jac02] ——, *Klassische Elektrodynamik*, 3rd ed. Berlin [u.a.]: de Gruyter, 2002. [Online]. Available: http://www.gbv.de/dms/ilmenau/toc/334724740.PDF [Cited on page 153.]

[Jan15] A. Jansen, "The Cryogenic Pumping Section of the KATRIN Experiment : Design Studies and Experiments for the Commissioning," Ph.D. dissertation, Karlsruhe Institute of Technology, 2015. [Online]. Available: http://digbib.ubka.uni-karlsruhe.de/volltexte/1000047146 [Cited on page 31.]

[Jin14] J. Jin, *The Finite Element Method in Electromagnetics*, 3rd ed. Wiley-IEEE Press, 2014. [Cited on page 64.]

[K+05] C. Kraus *et al.*, "Final results from phase II of the Mainz neutrino mass search in tritium β decay," *The European Physical Journal C - Particles and Fields*, vol. 40, no. 4, pp. 447–468, 2005. [Online]. Available: http://dx.doi.org/10.1140/epjc/s2005-02139-7 [Cited on pages 19, 43, and 83.]

[Käf12] W. Käfer, "Sensitivity Studies for the KATRIN experiment," Ph.D. dissertation, Karlsruhe Institute of Technology, 2012. [Online]. Available: http://digbib.ubka.uni-karlsruhe.de/volltexte/1000026021 [Cited on page 81.]

[Kah65] W. Kahan, "Pracniques: Further Remarks on Reducing Truncation Errors," *Commun. ACM*, vol. 8, no. 1, pp. 40–, Jan. 1965. [Online]. Available: http://doi.acm.org/10.1145/363707.363723 [Cited on page 103.]

[KL13] S. F. King and C. Luhn, "Neutrino mass and mixing with discrete symmetry," *Reports on Progress in Physics*, vol. 76, no. 5, p. 056201, 2013. [Online]. Available: http://stacks.iop.org/0034-4885/76/i=5/a=056201 [Cited on page 12.]

[Kle14] M. Kleesiek, "A Data-Analysis and Sensitivity-Optimization Framework for the KATRIN Experiment," Ph.D. dissertation, Karlsruhe Institute of Technology, 2014. [Online]. Available: http://digbib.ubka.uni-karlsruhe.de/volltexte/1000043301 [Cited on pages 41, 49, 50, 78, 79, 80, and 81.]

[Kle17] M. Klein, "In preparation," Ph.D. dissertation, Karlsruhe Institute of Technology, 2017. [Cited on page 29.]

[Kra92] L. M. Krauss, "Supernova neutrinos and the signal from the next galactic supernova," *Nuclear Physics B - Proceedings Supplements*, vol. 28, no. 1, pp. 106 – 115, 1992. [Online]. Available: http://www.sciencedirect.com/science/article/pii/092056329290153J [Cited on page 14.]

[Kra16] M. Kraus, "Energy-scale systematics at the KATRIN main spectrometer," Ph.D. dissertation, Karlsruhe Institute of Technology, 2016. [Online]. Available: https://publikationen.bibliothek.kit.edu/1000054447/3841410 [Cited on pages 34, 40, and 42.]

[KS05] P. K. Kythe and M. R. Schäferkotter, *Handbook of computational methods for integration*. Boca Raton [u.a.]: Chapman & Hall/CRC, 2005. [Online]. Available: http://www.gbv.de/dms/ilmenau/toc/386128006.PDF [Cited on pages 93, 94, 96, and 97.]

[Kuc16] L. Kuckert, "The windowless gaseous tritium source - Characterisation of gas dynamical and plasma properties," Ph.D. dissertation, Karlsruhe Institute of Technology, 2016. [Cited on pages 27 and 29.]

[Kyt95] P. K. Kythe, *An introduction to boundary element methods*. Boca Raton [u.a.]: CRC Press, 1995. [Online]. Available: http://www.gbv.de/dms/goettingen/183041410.pdf [Cited on page 83.]

[LC94] J. N. Lyness and R. Cools, "A Survey of Numerical Cubature over Triangles," *Preprint MCS-P410-0194, Argonne National Laboratory*, 1994. [Online]. Available: http://ftp.mcs.anl.gov/pub/tech_reports/reports/P410.pdf [Cited on pages 98 and 101.]

[Lei14] B. Leiber, "Investigations of background due to secondary electron emission in the KATRIN-experiment," Ph.D. dissertation, Karlsruhe Institute of

Technology, 2014. [Online]. Available: http://digbib.ubka.uni-karlsruhe.de/volltexte/1000042415 [Cited on pages 63, 67, and 70.]

[LeV07] R. LeVeque, *Finite Difference Methods for Ordinary and Partial Differential Equations: Steady-State and Time-Dependent Problems (Classics in Applied Mathematics)*. Philadelphia, PA, USA: Society for Industrial and Applied Mathematics, 2007. [Cited on page 64.]

[LG78] M. E. Laursen and M. Gellert, "Some criteria for numerically integrated matrices and quadrature formulas for triangles," *International Journal for Numerical Methods in Engineering*, vol. 12, no. 1, pp. 67–76, 1978. [Online]. Available: http://dx.doi.org/10.1002/nme.1620120107 [Cited on page 98.]

[LJ75] J. N. Lyness and D. Jespersen, "Moderate Degree Symmetric Quadrature Rules for the Triangle," *IMA Journal of Applied Mathematics*, vol. 15, no. 1, pp. 19–32, 1975. [Online]. Available: http://imamat.oxfordjournals.org/content/15/1/19.abstract [Cited on pages 98 and 158.]

[LL02] T. J. Loredo and D. Q. Lamb, "Bayesian analysis of neutrinos observed from supernova SN 1987A," *Phys. Rev. D*, vol. 65, p. 063002, Feb 2002. [Online]. Available: http://link.aps.org/doi/10.1103/PhysRevD.65.063002 [Cited on page 14.]

[Lob03] V. M. Lobashev, "The search for the neutrino mass by direct method in the tritium beta-decay and perspectives of study it in the project KATRIN," *Nuclear Physics A*, vol. 719, pp. C153 – C160, 2003. [Online]. Available: http://www.sciencedirect.com/science/article/pii/S0375947403009850 [Cited on page 83.]

[Lon92] M. Longair, *High Energy Astrophysics: Volume 1, Particles, Photons and their Detection*. Cambridge University Press, 1992. [Cited on page 153.]

[LP14] J. Lesgourgues and S. Pastor, "Neutrino cosmology and Planck," *New Journal of Physics*, vol. 16, no. 6, p. 065002, 2014. [Online]. Available: http://stacks.iop.org/1367-2630/16/i=6/a=065002 [Cited on page 13.]

[LPPM11] S. Lopez-Pena, A. G. Polimeridis, and J. R. Mosig, "On the analytic-numeric treatment of weakly singular integrals on arbitrary polygonal domains," *Progress In Electromagnetics Research B*, vol. 117, pp. 339–355, 2011. [Online]. Available: http://www.jpier.org/pier/pier.php?paper=11050504 [Cited on pages 93 and 96.]

[LS85] V. M. Lobashev and P. E. Spivak, "A method for measuring the electron antineutrino rest mass," *Nuclear Instruments and Methods in Physics Research Section A: Accelerators, Spectrometers, Detectors and Associated Equipment*, vol. 240, no. 2, pp. 305 – 310, 1985. [Online]. Available: http://www.sciencedirect.com/science/article/pii/0168900285906400 [Cited on pages 19 and 20.]

[LSA06] P. Lazic, H. Stefancic, and H. Abraham, "The Robin Hood method - A novel numerical method for electrostatic problems based on a non-local charge transfer," *Journal of Computational Physics*, vol. 213, no. 1, pp. 117 – 140, 2006. [Online]. Available: http://www.sciencedirect.com/science/article/pii/S0021999105003712 [Cited on pages 49, 65, and 66.]

[LSA08] ——, "The Robin Hood method - A new view on differential equations," *Engineering Analysis with Boundary Elements*, vol. 32, no. 1, pp. 76 – 89, 2008. [Online]. Available: http://www.sciencedirect.com/science/article/pii/S0955799707001026 [Cited on pages 65 and 66.]

[M+] S. Mertens *et al.*, "Storage of electrons with energies below the H2 ionization threshold in the KATRIN spectrometers," *to be published.* [Cited on page 126.]

[M+13] ——, "Background due to stored electrons following nuclear decays in the KATRIN spectrometers and its impact on the neutrino mass sensitivity," *Astroparticle Physics*, vol. 41, pp. 52 – 62, 2013. [Online]. Available: http://www.sciencedirect.com/science/article/pii/S0927650512001892 [Cited on page 126.]

[Mer12] S. Mertens, "Study of Background Processes in the Electrostatic Spectrometers of the KATRIN Experiment," Ph.D. dissertation, Karlsruhe Institute of Technology, 2012. [Online]. Available: http://digbib.ubka.uni-karlsruhe.de/volltexte/1000027058 [Cited on pages 25, 26, 115, 126, 127, 131, and 137.]

[MF09] B. Monreal and J. A. Formaggio, "Relativistic cyclotron radiation detection of tritium decay electrons as a new technique for measuring the neutrino mass," *Phys. Rev. D*, vol. 80, p. 051301, Sep 2009. [Online]. Available: http://link.aps.org/doi/10.1103/PhysRevD.80.051301 [Cited on page 17.]

[MH03] K. Martin and B. Hoffman, "Mastering CMake: A Cross-Platform Build System," 01 2003. [Cited on page 50.]

[MM07] S. Mukherjee and N. Majumdar, "Use of Triangular Elements for Nearly Exact BEM Solutions," *ArXiv e-prints*, Apr. 2007. [Cited on pages 93 and 96.]

[Möl76] H. M. Möller, "Minimum-point cubature formulas," *Numerische Mathematik*, vol. 25, no. 2, pp. 185–200, 1976. [Online]. Available: http://dx.doi.org/10.1007/BF01462272 [Cited on pages 98 and 160.]

[MPI94] MPI Forum, "MPI: A Message-Passing Interface Standard," Knoxville, TN, USA, Tech. Rep., 1994. [Cited on page 50.]

[MS86] S. P. Mikheyev and A. Y. Smirnov, "Resonant amplification of ν oscillations in matter and solar-neutrino spectroscopy," *Il Nuovo Cimento C*, vol. 9, no. 1, pp. 17–26, 1986. [Online]. Available: http://dx.doi.org/10.1007/BF02508049 [Cited on page 6.]

[Mül02] B. Müller, "Umbau des Mainzer Neutrinomassenexperiments und Untergrunduntersuchungen im Hinblick auf KATRIN," *Diploma thesis*, 2002, University of Mainz. [Online]. Available: http://www.katrin.kit.edu/publikationen/dth-mueller.pdf [Cited on page 116.]

[Mül16] A. Müller, "Investigation of the secondary emission characteristics of the KATRIN main spectrometer," *Master thesis*, 2016, Karlsruhe Institute of Technology. [Cited on page 120.]

[NBGS08] J. Nickolls, I. Buck, M. Garland, and K. Skadron, "Scalable Parallel Programming with CUDA," *Queue*, vol. 6, no. 2, pp. 40–53, Mar. 2008. [Online]. Available: http://doi.acm.org/10.1145/1365490.1365500 [Cited on page 50.]

[NFB+06] S. Nagy, T. Fritioff, M. Björkhage, I. Bergström, and R. Schuch, "On the Q-value of the tritium β-decay," *EPL (Europhysics Letters)*, vol. 74, no. 3, p. 404, 2006. [Online]. Available: http://stacks.iop.org/0295-5075/74/i=3/a=404 [Cited on page 22.]

[Nor61] T. G. Northrop, "The guiding center approximation to charged particle motion," *Annals of Physics*, vol. 15, no. 1, pp. 79 – 101, 1961. [Online]. Available: http://www.sciencedirect.com/science/article/pii/0003491661901671 [Cited on page 54.]

[Nor63] ——, "Adiabatic charged-particle motion," *Reviews of Geophysics*, vol. 1, no. 3, pp. 283–304, 1963. [Online]. Available: http://dx.doi.org/10.1029/RG001i003p00283 [Cited on page 54.]

[Not14] Center for Experimental Nuclear Physics and Astrophysics, University of Washington, Annual Report, 2014. [Cited on pages 49 and 50.]

[O+14] K. A. Olive *et al.*, "Review of Particle Physics," *Chin. Phys.*, vol. C38, p. 090001, 2014. [Cited on pages 3, 5, and 52.]

[OBW06] E. W. Otten, J. Bonn, and C. Weinheimer, "The Q-value of tritium β-decay and the neutrino mass," *International Journal of Mass Spectrometry*, vol. 251, no. 2-3, pp. 173 – 178, 2006, Ultra-accurate mass spectrometry and related topics - Dedicated to H.-J. Kluge on the occasion of his 65th birthday anniversary - Jürgen Kluge Special Issue. [Online]. Available: http://www.sciencedirect.com/science/article/pii/S1387380606000741 [Cited on page 22.]

[OH82] E. E. Okon and R. F. Harrington, "The potential due to a uniform source distribution over a triangular domain," *International Journal for Numerical Methods in Engineering*, vol. 18, no. 9, pp. 1401–1411, 1982. [Online]. Available: http://dx.doi.org/10.1002/nme.1620180911 [Cited on pages 93 and 96.]

[OS06] I. P. Omelyan and V. B. Solovyan, "Improved cubature formulae of high degrees of exactness for the square," *Journal of Computational and Applied Mathematics*, vol. 188, no. 2, pp. 190 – 204, 2006. [Online]. Available: http://www.sciencedirect.com/science/article/pii/S0377042705002165 [Cited on page 98.]

[Ost16] R. Ostertag, "Testmessung und Inbetriebnahme eines automatisierten Magnetfeldmesssystems am KATRIN Hauptspektrometer," *Bachelor thesis, to be published*, 2016, Karlsruhe Institute of Technology. [Cited on page 47.]

[OW08] E. W. Otten and C. Weinheimer, "Neutrino mass limit from tritium β decay," *Reports on Progress in Physics*, vol. 71, no. 8, p. 086201, 2008. [Online]. Available: http://stacks.iop.org/0034-4885/71/i=8/a=086201 [Cited on page 46.]

[P+92] A. Picard *et al.*, "A solenoid retarding spectrometer with high resolution and transmission for keV electrons," *Nuclear Instruments and Methods in Physics Research Section B: Beam Interactions with Materials and Atoms*, vol. 63, no. 3, pp. 345 – 358, 1992. [Online]. Available: http://www.sciencedirect.com/science/article/pii/0168583X9295119C [Cited on pages 19 and 20.]

[Pap15] S.-A. Papanicolopulos, "Computation of moderate-degree fully-symmetric cubature rules on the triangle using symmetric polynomials and algebraic solving," *Computers & Mathematics with Applications*, vol. 69, no. 7, pp. 650 – 666, 2015. [Online]. Available: http://www.sciencedirect.com/science/article/pii/S089812211500067X [Cited on pages 98 and 158.]

[PRG+12] M. Prall, P. Renschler, F. Glück *et al.*, "The KATRIN pre-spectrometer at reduced filter energy," *New Journal of Physics*, vol. 14, no. 7, p. 073054, 2012. [Online]. Available: http://stacks.iop.org/1367-2630/14/i=7/a=073054 [Cited on page 83.]

[PTVF07] W. H. Press, S. A. Teukolsky, W. T. Vetterling, and B. P. Flannery, *Numerical Recipes 3rd Edition: The Art of Scientific Computing*, 3rd ed. New York, NY, USA: Cambridge University Press, 2007. [Cited on pages 61 and 70.]

[R+13] M. Röllig *et al.*, "Activity monitoring of a gaseous tritium source by beta induced X-ray spectrometry," *Fusion Engineering and Design*, vol. 88, no. 6-8, pp. 1263 – 1266, 2013, proceedings of the 27th Symposium On Fusion Technology (SOFT-27); Liege, Belgium, September 24-28, 2012. [Online]. Available: http://www.sciencedirect.com/science/article/pii/S0920379612004632 [Cited on page 27.]

[Rad48] J. Radon, "Zur mechanischen Kubatur," *Monatshefte für Mathematik*, vol. 52, no. 4, pp. 286–300, 1948. [Online]. Available: http://dx.doi.org/10.1007/BF01525334 [Cited on pages 98, 157, and 159.]

[Rei12] J. Reich, "Internal communication, CAD drawing of main spec air coil system," 2012. [Cited on page 37.]

[Res17] O. Rest, "In preparation," Ph.D. dissertation, University of Münster, 2017. [Cited on page 31.]

[RGWV79] S. Rao, A. Glisson, D. Wilton, and B. Vidula, "A simple numerical solution procedure for statics problems involving arbitrary-shaped surfaces," *IEEE Transactions on Antennas and Propagation*, vol. 27, no. 5, pp. 604–608, Sep 1979. [Cited on pages 93 and 96.]

[Röt16] C. Röttele, "Simulations of commissioning measurements with the Cryogenic Pumping Section CPS at KATRIN experiment," *Master thesis*, 2016, Karlsruhe Institute of Technology. [Online]. Available: https://fuzzy.fzk.de/bscw/bscw.cgi/d1044396/mth_roettele.pdf [Cited on page 58.]

[RR69] P. Rabinowitz and N. Richter, "Perfectly Symmetric Two-Dimensional Integration Formulas with Minimal Numbers of Points," *"Mathematics of Computation"*, vol. 23, pp. 765–779, 1969. [Online]. Available: http://dx.doi.org/10.1090/S0025-5718-1969-0258281-4 [Cited on page 98.]

[RS05] M. Rumpf and R. Strzodka, *Graphics Processor Units: New Prospects for Parallel Computing*, ser. Lecture Notes in Computational Science and Engineering. Springer, 2005, vol. 51, p. 89–134. [Online]. Available: http://asc.ziti.uni-heidelberg.de/sites/default/files/research/papers/public/RuSt05PPDE.pdf [Cited on page 75.]

[RWG82] S. Rao, D. Wilton, and A. Glisson, "Electromagnetic scattering by surfaces of arbitrary shape," *IEEE Transactions on Antennas and Propagation*, vol. 30, no. 3, pp. 409–418, May 1982. [Cited on page 85.]

[Sch13] M. R. H. Schlösser, "Accurate calibration of the Raman system for the Karlsruhe Tritium Neutrino Experiment," Ph.D. dissertation, Karlsruhe Institute of Technology, 2013. [Online]. Available: http://digbib.ubka.uni-karlsruhe.de/volltexte/1000034967 [Cited on pages 16 and 29.]

[Sch14] J. S. Schwarz, "The Detector System of the KATRIN Experiment : Implementation and First Measurements with the Spectrometer," Ph.D. dissertation, Karlsruhe Institute of Technology, 2014. [Online]. Available: http://digbib.ubka.uni-karlsruhe.de/volltexte/1000042772 [Cited on pages 20, 25, 32, and 33.]

[Sco35] F. A. Scott, "Energy Spectrum of the Beta-Rays of Radium E," *Phys. Rev.*, vol. 48, pp. 391–395, Sep 1935. [Online]. Available: http://link.aps.org/doi/10.1103/PhysRev.48.391 [Cited on page 2.]

[Seg84] L. J. Segerlind, *Applied finite element analysis*, 2nd ed. New York [u.a.]: Wiley, 1984. [Cited on pages 83 and 97.]

[SEH+14] S. Streubel, T. Eronen, M. Höcker, J. Ketter, M. Schuh, R. S. Van Dyck, and K. Blaum, "Toward a more accurate Q value measurement of tritium: status of THe-Trap," *Applied Physics B*, vol. 114, no. 1, pp. 137–145, 2014. [Online]. Available: http://dx.doi.org/10.1007/s00340-013-5669-x [Cited on page 22.]

[SGS10] J. E. Stone, D. Gohara, and G. Shi, "OpenCL: A Parallel Programming Standard for Heterogeneous Computing Systems," *Computing in Science Engineering*, vol. 12, no. 3, pp. 66–73, May 2010. [Cited on pages 50 and 103.]

[SM17] H. Seitz-Moskaliuk, "In preparation," Ph.D. dissertation, Karlsruhe Institute of Technology, 2017. [Cited on page 29.]

[Smi03] A. Y. Smirnov, "The MSW effect and solar neutrinos," in *Neutrino telescopes. Proceedings, 10th International Workshop, Venice, Italy, March 11-14, 2003. Vol. 1+2*, 2003, pp. 23–43. [Online]. Available: http://alice.cern.ch/format/showfull?sysnb=2375336 [Cited on page 7.]

[SML06] W. Schroeder, K. Martin, and B. Lorensen, *The Visualization Toolkit (4th ed.)*. Kitware, 2006. [Cited on page 50.]

[Ste16] S. Stern, "Untersuchung der Untergrundeigenschaften des KATRIN-Hauptspektrometers mit gepulsten elektrischen Dipolfeldern," *Bachelor thesis, to be published*, 2016, Karlsruhe Institute of Technology. [Cited on pages 70, 74, 106, 107, 116, 117, and 118.]

[Str71] A. H. Stroud, *Approximate calculation of multiple integrals*, ser. Prentice-Hall series in automatic computation. Englewood Cliffs, NJ: Prentice-Hall, c 1971. [Cited on pages 97, 98, 157, and 159.]

[Sur] U. G. Survey, "The Thorium-232 Decay Scheme," accessed: 2016-10-26. [Online]. Available: http://pubs.usgs.gov/of/2004/1050/Th-232-Decay-Chain.gif [Cited on page 125.]

[Szi88] M. Szilágyi, *Electron and ion optics*, ser. Microdevices: physics and fabrication technologies. New York [u.a.]: Plenum Pr., 1988. [Cited on pages 64 and 83.]

[THT02] A. Tatematsu, S. Hamada, and T. Takuma, "Analytical expressions of potential and electric field generated by a triangular surface charge with a high-order charge density distribution," *Electrical Engineering in Japan*, vol. 139, no. 3, pp. 9–17, 2002. [Online]. Available: http://dx.doi.org/10.1002/eej.1155 [Cited on pages 93 and 96.]

[Thü02] T. Thümmler, "Entwicklung von Methoden zur Untergrundreduzierung am Mainzer Tritium-β-Spektrometer," *Diploma thesis*, 2002, Universität Mainz. [Online]. Available: http://www.katrin.kit.edu/publikationen/dth-thuemmler.pdf [Cited on pages 54 and 116.]

[Tro15] N. Trost, "Rydberg summary," 2015, Internal note. [Cited on page 140.]

[Tro17] ——, "In preparation," Ph.D. dissertation, Karlsruhe Institute of Technology, 2017. [Cited on pages 46 and 120.]

[Tyl53] G. W. Tyler, "Numerical integration of functions of several variables," *Canad. J. Math.*, vol. "5", pp. "393–412", "1953". [Online]. Available: http://dx.doi.org/10.4153/CJM-1953-044-1 [Cited on pages 98 and 159.]

[Übe97] C. W. Überhuber, *Numerical computation*. Berlin: Springer, 1997, vol. 1:. [Cited on pages 92, 93, 94, and 103.]

[V+11] K. Valerius *et al.*, "Prototype of an angular-selective photoelectron calibration source for the KATRIN experiment," *Journal of Instrumentation*, vol. 6, no. 01, p. P01002, 2011. [Online]. Available: http://stacks.iop.org/1748-0221/6/i=01/a=P01002 [Cited on page 27.]

[Val04] K. Valerius, "Elektromagnetisches Design für das Hauptspektrometer des KATRIN Experiments," *Diploma thesis*, 2004, university of Bonn. [Online]. Available: http://www.uni-muenster.de/Physik.KP/AGWeinheimer/Files/theses/Diplom_Katrin_Valerius.pdf [Cited on page 153.]

[Val09] ——, "Spectrometer-related background processes and their suppression in the KATRIN experiment," Ph.D. dissertation, University of Münster, 2009. [Online]. Available: http://repositorium.uni-muenster.de/document/miami/93137705-73f4-404a-a438-09d487cbff63/diss_valerius.pdf [Cited on page 32.]

[Val10] ——, "The wire electrode system for the KATRIN main spectrometer," *Progress in Particle and Nuclear Physics*, vol. 64, no. 2, pp. 291–293, 2010, neutrinos in Cosmology, in Astro, Particle and Nuclear PhysicsInternational Workshop on Nuclear Physics, 31st course. [Online]. Available: http://www.sciencedirect.com/science/article/pii/S0146641009001100 [Cited on pages 23 and 102.]

[Val16] ——, "Direct mass searches: KATRIN and Project 8 and searches with Holmium," *Presentation, session Neutrino properties II*, 07 2016, XXVII International Conference on Neutrino Physics and Astrophysics (Neutrino 2016). [Online]. Available: http://neutrino2016.iopconfs.org/IOP/media/uploaded/EVIOP/event_948/kvalerius_directnumass_v4_web.pdf [Cited on page 47.]

[Wan09] N. Wandkowsky, "Design and Background Simulations for the KATRIN Main Spectrometer and Air Coil System," *Diploma thesis*, 2009, Karlsruhe Institute of Technology. [Online]. Available: http://www.katrin.kit.edu/publikationen/dth-wandkowsky.pdf [Cited on page 36.]

[Wan13] ——, "Study of background and transmission properties of the KATRIN spectrometers," Ph.D. dissertation, Karlsruhe Institute of Technology, 2013. [Online]. Available: http://digbib.ubka.uni-karlsruhe.de/volltexte/1000036631 [Cited on pages 15, 25, 26, 31, 37, 115, 116, 117, 119, 120, 121, 126, 131, and 137.]

[Wol78] L. Wolfenstein, "Neutrino oscillations in matter," *Phys. Rev. D*, vol. 17, pp. 2369–2374, May 1978. [Online]. Available: http://link.aps.org/doi/10.1103/PhysRevD.17.2369 [Cited on pages 6 and 7.]

[Wul14] J. Wulf, "Electrostatic Field Simulations and Low-Temperature Measurements for a Xenon-based Dual-Phase Noble Gas Dark Matter Detector," *Master thesis*, 2014, Karlsruhe Institute of Technology. [Online]. Available: http://www.physik.uzh.ch/groups/groupbaudis/darkmatter/theses/xenon/master_wulf.pdf [Cited on pages 58 and 85.]

[WX03] S. Wandzurat and H. Xiao, "Symmetric quadrature rules on a triangle," *Computers & Mathematics with Applications*, vol. 45, no. 12, pp. 1829 – 1840, 2003. [Online]. Available: http://www.sciencedirect.com/science/article/pii/S0898122103900046 [Cited on page 98.]

[ZCL09] L. Zhang, T. Cui, and H. Liu, "A SET OF SYMMETRIC QUADRATURE RULES ON TRIANGLES AND TETRAHEDRA," *Journal of Computational Mathematics*, vol. 27, no. 1, pp. 89–96, 2009. [Online]. Available: http://www.jstor.org/stable/43693493 [Cited on page 98.]

[Zub11] K. Zuber, *Neutrino Physics, Second Edition*, ser. Series in High Energy Physics, Cosmology and Gravitation. Taylor & Francis, 2011. [Cited on pages 6, 8, 9, 14, and 15.]

Danksagung

Abschließend möchte ich mich herzlichst bei allen bedanken, die mich während der Zeit meiner Doktorarbeit unterstützt und zum Gelingen dieser Arbeit beigetragen haben. Ein ganz herzliches Dankeschön gilt insbesondere folgenden Personen:

- Vielen Dank Prof. Dr. Guido Drexlin für die Möglichkeit, in dem sehr spannenden Umfeld des KATRIN Experimentes zu promovieren, die sehr interessante und abwechslungsreiche Aufgabenstellung und die sehr gute Betreuung und Unterstützung während der Promotion.
- Vielen Dank Prof. Dr. Wim de Boer für sein großes Engagement bei der Ausarbeitung dieser Arbeit und die Übernahme des Koreferats.
- Vielen Dank der Prüfungskommission für die Begutachtung und Beurteilung meiner Doktorarbeit.
- I am grateful to Prof. Dr. Joe Formaggio for valuable input for the work on numerical integration routines and the possibility to work in the Neutrino and Dark Matter Physics group at MIT.
- Vielen Dank Dr. Ferenc Glück für seine große Hilfe und Unterstützung bei allen physikalischen und mathematischen Fragen.
- Vielen Dank dem Karlsruhe House Of Young Scientists (KHYS) für die finanzielle Unterstützung meines zweimonatigen Auslandsaufenthaltes am MIT, Cambridge.
- Vielen Dank Armen Beglarian, Jan Behrens, Dr. Florian Fränkle, Holger Frenzel, Julius Hartmann, Dr. Marcel Kraus, Martin Mark, Klaus Mehret, Dr. Klaus Schlösser, Dr. Johannes Schwarz, Dr. Thomas Thümmler, Dr. Sascha Wüstling und Dr. Joachim Wolf für die Unterstützung und Hilfe bei den Messungen am Hauptspektrometer.
- Vielen Dank Dr. Stefan Groh und Dr. Marco Kleesiek für die Hilfe mit dem *Kassiopeia* und *KaFit* Software Paket.
- Many thanks Dr. John Barrett and Dr. Thomas Corona for their support regarding the usage and extension of the *KEMField* software tool.
- Vielen Dank Dr. Martin Babutzka, Thomas Csabo, Dr. Florian Fränkle, Florian Heizmann und Nikolaus Trost für die Administration des Instituts-Rechencluster.
- Vielen Dank Dr. Suren Chilingaryan und Dr. Matthias Vogelgesang für die Hilfe bei der Konfiguration und Optimierung des GPU Rechensystems.
- Für das Korrekturlesen dieser Arbeit bedanke ich mich bei Prof. Dr. Guido Drexlin, Prof. Dr. Wim de Boer, Dr. John Barrett, Dr. Florian Fränkle, Dr. Ferenc Glück, Dr. Fabian Harms, Dr. Alexander Jansen, Dr. Marco Kleesiek, Dr. Marcel Kraus und Dr. Kathrin Valerius.

- Vielen Dank den Sekretariaten von IKP und IEKP, insbesondere Katharina Fischer und Brigitte Gering für die Unterstützung und Abwicklung jeglicher administrativen Aufgaben.
- Vielen Dank Dr. Kathrin Valerius für das Organisieren des Institutslauftreffs.
- Vielen Dank Dr. Moritz Erhard, Dr. Fabian Harms und Dr. Marcel Kraus für die sehr gute Zusammenarbeit während der Promotion.
- Vielen Dank Dr. Alexander Jansen und Dr. Laura Kuckert für die schöne gemeinsame Zeit –vor allem außerhalb der Arbeit.
- Vielen Dank an meine ehemaligen Studenten Rodolphe Combe, Johannes Ding, Wolfgang Gosda, Sebastian Stern, Herbert Ullrich, Johannes Weis und Julien Wulf.

Der größte Dank geht an dieser Stelle an meine Eltern, die mich in allen Höhen und Tiefen meiner Studienzeit unterstützt haben und jederzeit für mich da sind.
Vielen Dank für Eure Unterstützung während der Promotion, insbesondere für die liebevollen Worte, die mich aufgebaut haben!